Springer Theses
Recognizing Outstanding Ph.D. Research

Andy Nowacki

Plate Deformation from Cradle to Grave

Seismic Anisotropy and Deformation at Mid-Ocean Ridges and in the Lowermost Mantle

Springer

Springer Theses

Recognizing Outstanding Ph.D. Research

For further volumes:
http://www.springer.com/series/8790

Aims and Scope

The series "Springer Theses" brings together a selection of the very best Ph.D. theses from around the world and across the physical sciences. Nominated and endorsed by two recognized specialists, each published volume has been selected for its scientific excellence and the high impact of its contents for the pertinent field of research. For greater accessibility to non-specialists, the published versions include an extended introduction, as well as a foreword by the student's supervisor explaining the special relevance of the work for the field. As a whole, the series will provide a valuable resource both for newcomers to the research fields described, and for other scientists seeking detailed background information on special questions. Finally, it provides an accredited documentation of the valuable contributions made by today's younger generation of scientists.

Theses are accepted into the series by invited nomination only and must fulfill all of the following criteria

- They must be written in good English.
- The topic should fall within the confines of Chemistry, Physics, Earth Sciences, Engineering and related interdisciplinary fields such as Materials, Nanoscience, Chemical Engineering, Complex Systems and Biophysics.
- The work reported in the thesis must represent a significant scientific advance.
- If the thesis includes previously published material, permission to reproduce this must be gained from the respective copyright holder.
- They must have been examined and passed during the 12 months prior to nomination.
- Each thesis should include a foreword by the supervisor outlining the significance of its content.
- The theses should have a clearly defined structure including an introduction accessible to scientists not expert in that particular field.

Andy Nowacki

Plate Deformation from Cradle to Grave

Seismic Anisotropy and Deformation at Mid-Ocean Ridges and in the Lowermost Mantle

Doctoral Thesis accepted by
the University of Bristol, United Kingdom

Springer

Author
Dr. Andy Nowacki
School of Earth Sciences
University of Bristol
Bristol
UK

Supervisors
Dr. James Wookey
School of Earth Sciences
University of Bristol
Bristol
UK

Prof. J.-Michael Kendall
School of Earth Sciences
University of Bristol
Bristol
UK

ISSN 2190-5053 ISSN 2190-5061 (electronic)
ISBN 978-3-642-34841-9 ISBN 978-3-642-34842-6 (eBook)
DOI 10.1007/978-3-642-34842-6
Springer Heidelberg New York Dordrecht London

Library of Congress Control Number: 2012952581

Printed on acid-free paper

Springer is part of Springer Science+Business Media (www.springer.com)

Parts of this thesis have been published in the following journal articles:

1. Nowacki, A., Wookey, J., & Kendall, J. M., 2010. Deformation of the lowermost mantle from seismic anisotropy, *Nature*, **467**(7319), 1091–1095, doi: 10.1038/nature09507.

2. Nowacki, A., Wookey, J., & Kendall, J. M., 2011. New advances in using seismic anisotropy, mineral physics and geodynamics to understand deformation in the lowermost mantle, *Journal of Geodynamics*, **52**(3-4), 205–228, doi: 10.1016/j.jog.2011.04.003.

3. Walker, A. M., Forte, A. M.,Wookey, J., Nowacki, A.,&Kendall, J. M., 2011. Elastic anisotropy of D″ predicted from global models of mantle flow, *Geochem Geophy Geosy*, **12**(10), Q10006, doi: 10.1029/2011GC003732.

4. Nowacki, A., Kendall, J. M., & Wookey, J., 2012. Mantle anisotropy beneath the Earth's mid-ocean ridges, *Earth Planet Sci Lett*, **317-318**, 56–67, doi: 10.1016/j.epsl.2011.11.044.

Supervisors' Foreword

The rocky mantle convects on timescales of centimetres each year in order to release heat from the Earth's deep interior. Thermal boundary layers lie at the top and bottom of this convective system: the bottom layer is the enigmatic D″ region that serves to buffer the slowly moving mantle from the more vigorously convecting liquid outer-core; the top layer comprises the more familiar tectonic plates that shape the Earth's surface. Seismology provides our best tools for studying these regions. As the polymineralic mantle moves and deforms, the lattice preferred orientation of the constituent mineral preserves the signature of mantle flow and leads to directional variations in seismic velocities, or seismic anisotropy. In a seminal paper in 1964, Harry Hess showed how azimuthal variations in seismic P-wave velocities supported ideas of plate formation and spreading at mid-ocean ridges. Nearly 50 years later we are now able to map anisotropy in less accessible parts of the Earth. In this thesis, Andy Nowacki develops a methodology for studying seismic anisotropy in the Earth's deep interior. He then draws on novel techniques for modeling mantle flow and new constraints from mineral physics to interpret these seismic observations.

Andy studies anisotropy in the lowermost mantle using seismic phases that turn above the D″ region and those that reflect from the core-mantle boundary. He uses clever and careful observations of shear-wave splitting in these phases, which is our least ambiguous evidence of anisotropy. Mantle flow models, based on density models derived from seismic velocity tomography, can be used to test plausible mineralogies and their associated deformation mechanisms. In 2004, in what was perhaps the most exciting discovery in mineral physics in the past few decades, a new phase transition in perovskite—the most abundant mineral in the mantle—to a denser 'post-perovskite' form was observed at near core-mantle boundary pressures. Andy shows that the presence of this mineral phase is consistent with his observations of anisotropy and takes significant steps in constraining the dislocation slip system for this mineral.

Andy's technique for studying shear-wave splitting also provides a new remote sensing tool for studying anisotropy near the source regions of earthquakes. He uses this approach to study the Earth's mid-ocean ridge system using earthquakes

recorded at distant stations. The results reveal variations that correlate with factors such as the spreading rate and proximity to transform faults. Andy shows that the anisotropy near oceanic spreading centers can be explained with aligned crystals in mantle peridotites, but also requires an additional contribution from thin layers of partially melted mantle that align parallel to the base of newly formed lithosphere.

The techniques Andy develops and invokes in this thesis are both challenging and novel. They offer us insights into the dynamical processes at play in the regions where new plates are formed, and where they reach the base of the mantle some 3000 km beneath our feet. Andy is now a well-known practitioner of the study of anisotropy in the Earth's deep interior. This work was supported by the UK Natural Environment Research Council and the European Research Council, and has been published in leading journals, including Nature. As seismic datasets grow, our knowledge of mantle mineralogy improves, and geodynamical models of convection become more complete, Andy has provided a methodology template that will be used to link these developments in an exciting field of scientific discovery.

Bristol, August 2012

Dr. James Wookey
Prof. J.-Michael Kendall

Preface

There are a few good reasons to conduct scientific research. One is merely to find out for yourself how things work. I am interested in how the inside of the Earth works: how its evolving, churning deep interior has shaped the planet we live on now, and how it made it possible for us to live on it in the first place. I believe there is an inherent worth in the creation and growth of knowledge about our environment, and I also argue that the only way we can understand ourselves—let alone the rest of the universe—is in the careful, steady, progressive analysis of our surroundings. Without committing to these means, the end cannot be achieved.

As important as science is for its own sake, however, there is no gain to be had if this understanding is not passed on. Scientists do not publish their research simply to have it challenged, improved, and checked, but also to have it read and—hopefully—ingested into the wider canon of knowledge. Therefore, all we scientists must strive to teach and reach out to anyone who has an interest in that which we are ourselves often extremely so interested. I therefore would like to warn the reader of this thesis that there may sometimes be digressions into the more arcane of points regarding observing and interpreting the Earth; but as I apologize, I also eulogize, because without these digressions we would struggle to make any progress at all.

It is with some thanks to Springer, therefore, that I end this preface. I am grateful that the body of work presented in this thesis—some of which is available in other forms already—can be presented to a wider audience together and somewhat coherently. I hope it is of some use to the reader.

Acknowledgments

Studying for a Ph.D. in Earth Sciences at Bristol has been an exceptionally rewarding experience, for which I am incredibly grateful to a number of people.

First, I thank my supervisors, James Wookey and Mike Kendall, for their intellectual and personal encouragement, support, and challenging. Obviously, none of this work could have been done without their role. I particularly want to say 'thank you' to both for the stimulating environment they provided during my studies and for the occasional bungs of cash to spend widening my horizons at conferences around the world. I really have benefited from the perfect double-act, reminiscent of Reeves and Mortimer, or Cannon and Ball in their stature.

Second, my funders the Natural Environment Research Council (and by extension all UK taxpayers) have made the whole thing possible, and afforded me a very comfortable standard of living—without the generous stipend Ph.D. students now get in the natural sciences, I could not have enjoyed the city of Bristol anywhere as much, and that would have made for a much more miserable and much less productive time studying for my doctorate.

Vitally, I am very grateful to Mark Panning and Matt Watson for examining me, externally and internally respectively, and for their insightful comments and suggestions for improvement. Without their generously agreeing to give their valuable time, attention, and discernment, this thesis would after all not be worth very much.

I thank Donna Blackman for making available the elastic constants which are used in Chap. 3, and Alessandro Forte for the flow model used in Chap. 5. Alessandro was also an entertaining and stimulating host when James and I visited him in Montréal. Seismic data have come from the IRIS DMC, the CNDC, but also the fair hands of James Hammond, Ian Bastow and Dave Thompson, with Mike and James's prints on it as well. Additionally, the authors of the free GMT software package and the maintainers of LaTeX have made my life a lot easier, if at times frustrating too.

I also want to thank those people who have shared their company, time, and experience with me while I have been in the office. In no particular order: Andy Wüstefeld, Ricardo Ramalho, Dave Thompson, James Verdon, Glenn

Jones, James Hammond, Ian Bastow, Doug Angus, Alan Baird, Freya Sterling, Anna Horleston, Kit Chambers, Elspeth Robertson, Jack Walpole. I especially want to thank Andrew Walker, who did all the above and also collaborated on some good science. You and all geophysicists have been a complete delight to have coffee with every day.

Last of all, even though it *is* customary to thank one's partner in the acknowledgments, I have plenty of good reasons to do so. Thank you, Jude.

Contents

Chapter 1
Introduction

1.1 The Dynamic Interior of the Earth

The primary paradigm at work in studying the Earth today is that its mantle and core (Figs. 1.1 and 1.2) are in constant motion, driven by the need to lose the heat generated in the core from its crystallisation. The motion in the liquid outer core is very rapid (tens of km a^{-1}), whilst that of the solid, silicate mantle above is much slower (a few cm a^{-1}). Nonetheless, the mantle's properties are shaped by this convective cooling, which determines the conditions at the surface of the Earth on which we live.

Here, the motion of the mantle is accommodated by the creation and spreading of cold, rigid tectonic plates at the surface (at mid-ocean ridges), and their subduction at destructive plate boundaries. Recently, a consensus has started to emerge that some of these plates, at least, sink deep into the lower mantle (Fig. 1.2) and perhaps to the core–mantle boundary (CMB), where the silicate and iron parts of the Earth meet (Grand 2002). The counterpart to slab subduction is the rising of thermally buoyant plumes of material, perhaps initiated at the CMB.

Our primary means of imaging the three-dimensional variation of the Earth's interior is seismology. Seismic tomography in particular can retrieve the present-day response of the mantle in terms of its seismic wave speed. Frequently, the presence of hot or cold regions are inferred from regions of the mantle which are slower or faster respectively than the radial average velocity. However, isotropic wave speed tomography can only yield an instantaneous (relatively, in terms of mantle motion) snapshot of how the interior behaves. To move further and observe the true dynamics at play inside the Earth, we must look for more information.

1.2 Anisotropy

Some of that information can come from seismic anisotropy. Anisotropy refers to the variation with direction of any property within a material, and in the case of seismic anisotropy this implies a variation of seismic wave speed with direction of

A. Nowacki, *Plate Deformation from Cradle to Grave*, Springer Theses,
DOI: 10.1007/978-3-642-34842-6_1, © Springer-Verlag Berlin Heidelberg 2013

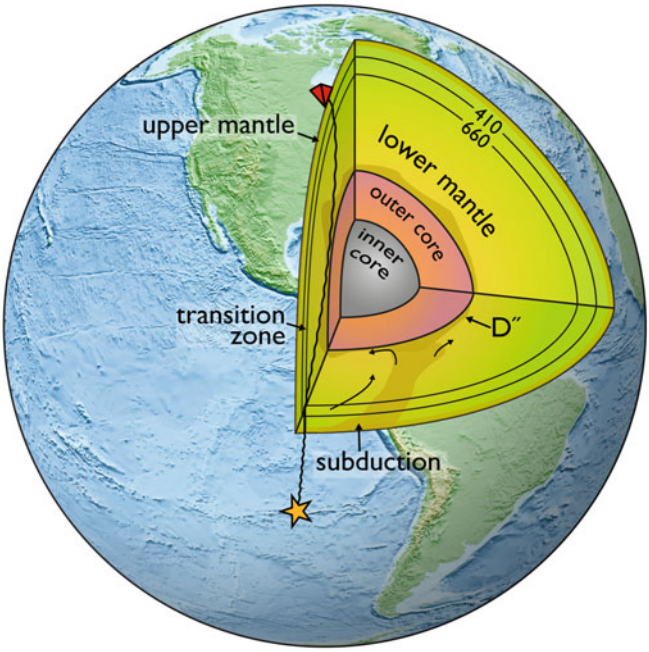

Fig. 1.1 Cartoon depicting internal structure of the Earth and major seismic discontinuities. Also shown is an example ray path for an ScS wave from an earthquake on the East Pacific Rise (*yellow star*) detected at a seismic station in North America (*red tetrahedron*), which reflects off the core–mantle boundary. '410' and '660' discontinuities are shown, as are the solid upper and lower mantle, transition zone and inner core. The outer core is liquid

the wave propagation. The presence of this then causes the absolute compressional wave velocity to vary with direction. Shear waves, in certain circumstances, not only vary in velocity with direction but also split into two orthogonal waves which travel at different speeds—a phenomenon known as 'shear wave splitting' (described in Chap. 2) which is analogous to optic birefringence. It is this property which gives perhaps the clearest indication that a shear wave has traversed a region of anisotropy, and the method which I will pursue mainly in this thesis.

The study of anisotropy in the Earth has developed radically over the last decades. Whilst earth scientists have long appreciated its significance, the first rigorous observations of its presence in the mantle were made in the second half of the twentieth century. Hess (1964), observed anisotropy beneath the oceanic crust near the Mendocino Fracture Zone in the eastern Pacific in seismic refraction experiments, showing P waves travel fastest parallel to the fracture zone. He interpreted this as due to the alignment of olivine crystals, which individually are strongly anisotropic. In sedimentary basins, anisotropy has been considered to be dominated instead by the gross structure of mainly horizontal beds of contrasting properties, with theories developed by many. Thomson (1950), and Backus (1962), amongst others, developed

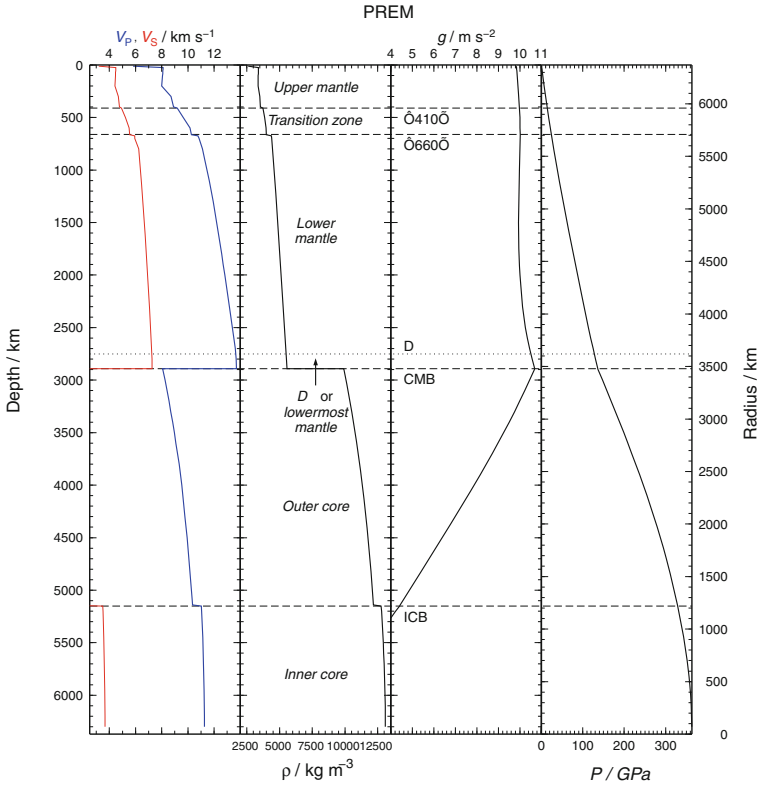

Fig. 1.2 P-wave and S-wave velocities, V_P and V_S, density, ρ, acceleration due to gravity, g, and pressure, P, in the Earth as given by the Preliminary Reference Earth Model (Dziewoński and Anderson 1981). The major seismic discontinuities are shown by *dashed lines* and labelled on the g plot. At ∼410 km, Mg_2SiO_4-olivine changes to wadsleyite. Near 660 km depth, Mg_2SiO_4-ringwoodite decomposes into $MgSiO_3$-perovskite and MgO. The D″ discontinuity is shown with *fine dashing* to indicate that it is observed at variable height and often not observed at all. Other abbreviations are the core–mantle boundary (CMB) and inner core boundary (ICB). Not shown is the Mohorovičić discontinuity at the base of the crust, usually between 6 and 50 km depth. g decreases monotonically to zero at the centre of the Earth from the CMB. The D″ region will interchangeably be referred to also as the lowermost mantle. Note that the largest change in material properties in the Earth occurs just below the D″ region at the CMB

effective-medium theories to describe the behaviour of relatively long wavelengths in such situations.

Global measurements of seismic anisotropy also have a long history. The Preliminary Reference Earth Model (PREM; Dziewoński and Anderson 1981) included anisotropy in the top 220 km as part of a radially-symmetric description of seismic wave speed and density in the Earth, whilst recently Montagner and Kennett (1996) inferred the presence of anisotropy in the deepest part of the mantle using whole-Earth oscillations. Whilst the first-order changes in the Earth occur with depth,

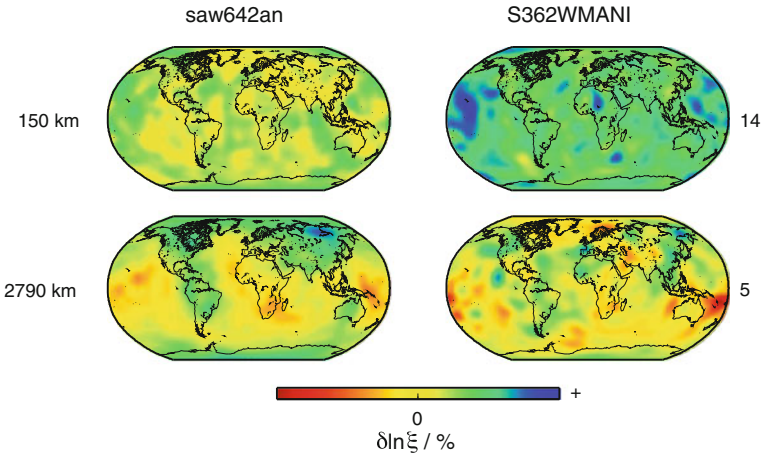

Fig. 1.3 Two global models of seismic anisotropy in the mantle: saw642an (Panning and Romanowicz 2004) and S362WMANI (Kustowski et al. 2008). These two models characterise the seismic wave speed in terms of 'radial anisotropy', where the only change in local seismic properties occurs with a change in wave propagation angle from the vertical. The plot shows the ξ parameter, which is the ratio of the squared velocities of horizontally- and vertically-polarised shear waves travelling horizontally. Because it deviates little from 1, $\delta\ln\xi$ is reported as a percentage deviation. Positive values (*cool colours*) indicate the horizontally-polarised waves travel faster in the region. Two depths are shown for each model: 150 and 2,790 km (100 km above the CMB). The numbers on the *right* indicate the maximum value of $\delta\ln\xi$ for that depth. The values are the total perturbation relative to an isotropic mantle, including the background, one-dimensional reference model

however, these approaches cannot give us much insight into the dynamics of the mantle. Hence a long-standing goal has been to measure the anisotropy in the mantle everywhere, and this has begun to be addressed. Anisotropic tomographic studies are now becoming available, with models being produced by Panning and Romanowicz (2004, 2006), Panning et al. (2010), and Kustowski et al. (2008). These models (Fig. 1.3) discriminate between the wave speed in the radial and horizontal directions as a first approximation, a necessary simplification. However, as I argue in this thesis, relieving ourselves of such constraints using regional techniques can give us yet more information about the type and cause of anisotropy.

Whilst effective-medium theories describing how anisotropy relates to small-scale heterogeneous structure such as layering have existed for over a century, some advances are much more recent. A key cause of anisotropy observed seismically is thought to be the alignment of individual mineral grains, which are themselves often inherently anisotropic because of the crystal lattice structure. Hess could explain his observations in terms of the alignment of olivine because mineral physical experiments by Birch had determined the seismic velocities of the phase in the laboratory. These methods continue to inform our understanding, and are being added to. The mineral physical repertoire now also encompasses measurements of seismic velocities of phases not stable at the Earth's surface, but the achievable range of

conditions is still highly restricted. Equally, new techniques to deform polymineralic samples are in development, also subject to strong shortcomings when attempting to reproduce the conditions of the deepest mantle. Complimentary to lab experiments, first-principles, 'ab initio' computer simulations of mineral structures at conditions of the deep Earth have progressed alongside huge advances in computer power in recent decades. All of these improvements in our understanding set the stage for their integration alongside seismic observations to image the mantle's dynamic interior.

1.3 The Boundary Layers of the Mantle

Because the mantle convects to efficiently deliver heat to the surface, much of its interior varies slowly in temperature in the radial direction. However, at the base and the surface, huge gradients in temperature are found where conduction dominates. At the surface, the lithosphere is the expression of this, giving rise to continental and oceanic plates. At the base of the mantle, the so-called 'D″' layer (which I also call here the 'lowermost mantle') similarly constitutes the bottom boundary layer, yet its structure, composition and dynamic processes are still poorly known.

These two boundaries control the motion of material in the mantle, and hence the dominant signal of the mantle's motion is to be found there. Therefore, these are the most fruitful areas to study if we wish to observe such dynamic processes today in the form of anisotropy.

1.4 Thesis Motivation

The first-order stratification of the Earth into core and mantle is a result of the segregation of denser and lighter elements shortly after the Earth's accretion (e.g., Allègre et al. 2008); however the second-order stratification of the mantle into the upper and lower mantle and the transition zone between 410 and 660 km depth is a result of phase changes in the mineral phases present in the mantle. This may also be responsible for another stratification in the D″ region (e.g., Shim 2008). Seismic anisotropy may develop in response to flow due to the alignment of mineral grains or the layering of seismically distinct material, as explained in Chap. 2, but in either case its origin and nature reflect the dynamics processes in the region. Hence we may use measurements of seismic anisotropy as a measure of the strength, direction and type of flow in the mantle's boundary layers. This is the first step towards observing the signs of flow which are lacking in existing methods.

Here I focus on observing and testing hypotheses of the causes and formation of seismic anisotropy in the lowermost mantle, a region of great current interest and uncertainty. In order to examine the deepest parts of the Earth, however, we must use seismic waves which pass through the shallowest parts. We are, in effect, trying to observe the deep Earth with blurry vision, and we require spectacles of the correct

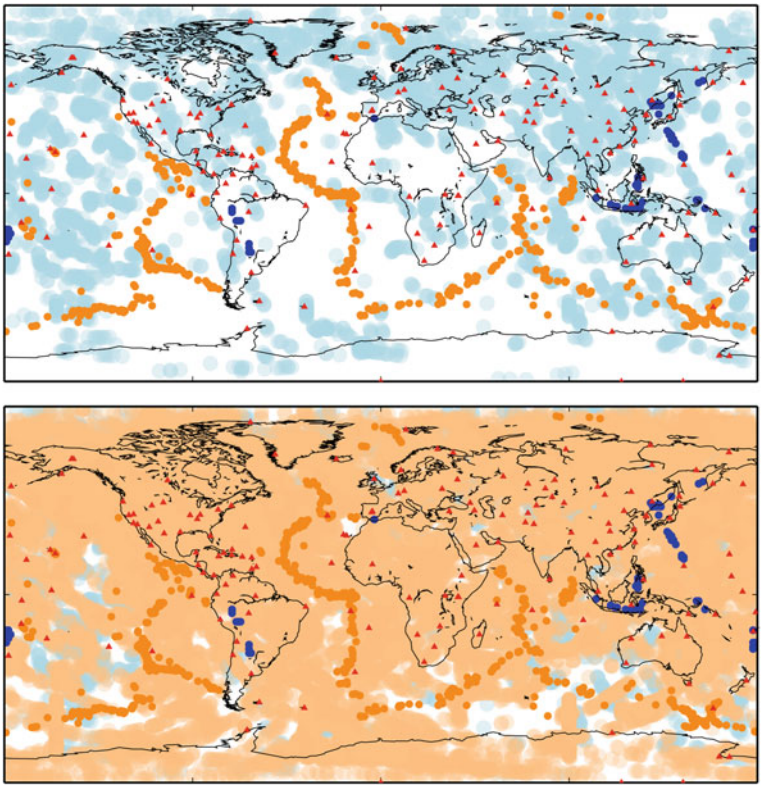

Fig. 1.4 Bouncepoints of ScS waves detected at IRIS GSN seismic stations from (*top*) earthquakes with depth ≥400 km and (*bottom*) earthquakes on mid-ocean ridges, in each case of events of magnitude ≥5.8. *Red triangles* show the seismic stations. *Dark blue circles* show deep earthquakes, whilst transparent *light blue circles* show CMB bouncepoints for ScS waves within a distance range of $55° \leq \Delta \leq 80°$ of the stations. Similarly, *dark orange circles* show events on the mid-ocean ridges and transparent *light orange circles* indicate the corresponding ScS bouncepoints for the same distance range and set of stations. The coverage without MOR events is far from complete, whilst just including MOR events (let alone other shallow events at other types of plate boundaries) significantly improves our ability to sample D″. The *circles* show the approximate first Fresnel zone of ScS waves of period 10 s at the equator

prescription. Figure 1.4 shows the contrasting view of the lowermost mantle we get from ScS waves from only deep events (>400 km; top), and those on mid-ocean ridges as well (bottom). We must therefore also investigate the topmost boundary layer, and to this end I present novel observations of a certain element of the Earth's surface—its mid-ocean ridges—which will be vital in developing our understanding of D″.

1.5 Thesis Outline

In this thesis, I present four chapters which are an original contribution to the study of deformation and structure in the Earth's mantle in its upper- and lowermost parts. The chapters advance logically, presenting a comprehensive review of recent studies of lowermost mantle anisotropy; then making measurements at mid-ocean ridges, providing the corrections needed to look deeper; subsequently using these to measure shear wave splitting in D″; and finally testing theories of deformation in D″ by comparing forward models with these measurements. Each chapter has been published, is under review, or is being prepared for publication.

- Chapter 2 reviews the recent and prevailing methods and understanding of the use of seismic anisotropy to infer deformation in D″.
- In Chap. 3, I provide a brief review of previous studies related to the field, and analyse the anisotropy beneath mid-ocean ridges. I performed a systematic study of 'source-side' splitting beneath all mid-ocean ridges to produce an entirely novel set of measurements at constructive plate margins worldwide. They revealed a discrepancy between reality and the shear wave splitting predictions of current models of mid-ocean ridge dynamics. Using these data and one such model of deformation, I examined the possibility that a near-ubiquitous seismic discontinuity beneath oceanic plates is compatible with my observations, and with receiver function and surface wave studies by other authors. Knowledge of upper mantle anisotropy beneath these ridges then allows us to use mid-ocean ridges as a seismic source when probing the deepest mantle.
- Chapter 4, presented in Nowacki et al. (2010), uses the methodologies described the previous chapters to infer seismic anisotropy in a large region in D″ beneath North and Central America. Shear wave splitting measurements are made along several ray paths, using corrections for upper mantle anisotropy to retrieve the signal of splitting in D″; some from the previous chapter. The hypothesis that the observed anisotropy is caused by LPO of mineral phases in response to deformation is tested by comparing the orientation these measurements would predict for a range of LPO textures in different mineral phases which may be present in D″.
- In Chap. 5 I combine the observations of the previous chapter with the methods of Chap. 3. A model of texture development in a candidate D″ phase, post-perovskite, created from a global model of mantle flow derived from observations, is used to re-examine the hypothesis of this thesis, that lowermost mantle anisotropy can be caused by LPO. I again calculate the ray-theoretical splitting for event-receiver ray paths where observations have previously been made, and find an enigmatic pattern of shear wave splitting, which suggests one of three things: that LPO is not always the primary cause of anisotropy at the bottom boundary layer of the mantle; we do not yet have a good enough understanding of how material deforms above the core–mantle boundary; or that our out current models of flow in the mantle are not a true reflection of how the Earth behaves.
- The final chapter concludes by summarising the findings laid out in previous chapters, and suggests which might next be fruitful avenues of research to further

the advances made in the course of producing this thesis. It identifies the key contributions made herein and outlines the methodologies employed to make them.

References

Allègre, C., Manhes, G., & Gopel, C. (2008). The major differentiation of the earth at similar to 4.45 Ga. *Earth Planet Science Letters*, *267*(1–2), 386–398. doi:10.1016/j.epsi.2007.11.056.

Backus, G. (1962). Long-wave elastic anisotropy produced by horizontal layering. *Journal of Geophysical Resereach*, *67*(11), 4427–4440. doi:10.1029/JZ067i011p04427.

Dziewoński, A., & Anderson, D. (1981). Preliminary reference Earth model. *Physics of the Earth and Planetary Interiors*, *25*(4), 297–356. doi:10.1016/0031-9201(81)90046-7.

Grand, S. P. (2002). Mantle shear-wave tomography and the fate of subducted slabs. *Philosophical Transactions of the Royal Society A*, *360*(1800), 2475–2491. doi:10.1098/rsta.2002.1077.

Hess, H. (1964). Seismic anisotropy of uppermost mantle under oceans. *Nature*, *203*(494), 629–631. doi:10.1038/203629a0.

Kustowski, B., Ekström, G., & Dziewoński, A. (2008). Anisotropic shear-wave velocity structure of the Earth's mantle: A global model. *Journal of Geophysical Research-Solid Earth,113*(B6), B06306. doi:10.1029/2007JB005169.

Montagner, J.-P., & Kennett, B. (1996). How to reconcile body-wave and normal-mode reference Earth models. *Geophysical Journal International*, *125*(1), 229–248. doi:10.1111/j.1365-246X.1996.tb06548.x.

Nowacki, A., Wookey, J., & Kendall, J. M. (2010). Deformation of the lowermost mantle from seismic anisotropy. *Nature*, *467*(7319), 1091–1095. doi:10.1038/nature09507.

Panning, M., & Romanowicz, B. (2004). Inferences on flow at the base of Earth's mantle based on seismic anisotropy. *Science*, *303*(5656), 351–353. doi:10.1126/science.1091524.

Panning, M., & Romanowicz, B. (2006). A three-dimensional radially anisotropic model of shear velocity in the whole mantle. *Geophysical Journal International*, *167*(1), 361–379. doi:10.1111/j.1365-246X.2006.03100.x.

Panning, M., Lekić, V., & Romanowicz, B. (2010). Importance of crustal corrections in the development of a new global model of radial anisotropy. *Journal of Geophysical Research-Solid Earth*, *115*, B12325. doi:10.1029/2010JB007520.

Shim, S.-H. (2008). The postperovskite transition. *Annual Review of Earth and Planetary Sciences*, *36*, 569–599. doi:10.1146/annurev.earth.36.031207.124309.

Thomson, W. (1950). Transmission of elastic waves through astratified solid medium. *Journal of Applied Physics*, *21*(2), 89–93. doi:10.1063/1.1699629.

Chapter 2
Seismic Anisotropy and Deformation in the Lowermost Mantle

2.1 Introduction

2.1.1 D″ and the Lowermost Mantle

The primary evidence for stratification of the Earth's interior comes from seismology. For nearly three quarters of a century seismologists have used changes in velocity gradients to map out the concentric shells that constitute the Earth's interior. Some changes are dramatic, like that seen at the core-mantle boundary (CMB), whilst others are more subtle, like that seen at the base of the lithosphere. Not long after Bullen's (1940) original classification of the lower mantle as the 'D' layer, it became apparent that the bottom few hundred kilometres of the mantle were seismically distinct from the bulk of the lower mantle. The lower mantle was split into D′—the top—and D″—the bottom (Bullen 1949). Whilst much of the original nomenclature used to label the layers of the Earth has been abandoned, D″ retains the name given to it over 60 years ago.

The D″ region encompasses a thermal boundary layer between the hot and vigorously convecting outer core and the colder, more slowly convecting mantle. It marks the terminus of downwelling mantle material and the place where upwelling plumes most probably originate. It is often bounded by a seismic discontinuity that lies on average 250 km above the CMB (e.g., Wysession et al. 1998), in many places contains ultra-low velocity zones at its base (e.g., Garnero et al. 1998), and generally exhibits fine-scale structure revealed through scattered seismic energy (e.g., Hedlin et al. 1997). The focus of this review is the observation and interpretation of seismic anisotropy in this region: in contrast to the overlying lower mantle, it exhibits significant seismic anisotropy (Meade et al. 1995; Montagner and Kennett 1996; Panning and Romanowicz 2006).

The implications of these observations are far reaching, as the CMB region plays a fundamental role in the dynamics of the mantle above and the core below. For example, core convection controls the generation of the Earth's magnetic field; mantle convection is the driving force behind plate tectonics. Making sense of the seismic

A. Nowacki, *Plate Deformation from Cradle to Grave*, Springer Theses,
DOI: 10.1007/978-3-642-34842-6_2, © Springer-Verlag Berlin Heidelberg 2013

observations requires a linked analysis of mineral physics, geodynamics and seismology. Here we present recent advances in each of these fields and show how they can be used to constrain the interpretation of measurements of seismic anisotropy.

2.1.2 Seismic Anisotropy

Seismic anisotropy—the variation of seismic wave speed with direction—appears to be commonplace in the upper- and lowermost mantle (see e.g. Savage 1999), and is probably present in the inner core (for a review, see Tromp 2001). Anisotropy may be related to the inherent, wavelength-independent nature of the medium through which a wave travels, such as within the crystal structure of many minerals in the Earth; or it may be due to extrinsic, wavelength-dependent ordering of heterogeneous material, such as sedimentary layering in basins. In either case, the propagation of an elastic wave through the medium is described by the elasticity tensor.

The elasticity tensor c_{ijkl} gives the relationship between the applied stress σ_{ij} and the resulting strain ε_{kl} according to a linear relationship (Hooke's Law $\sigma_{ij} = c_{ijkl}\,\varepsilon_{kl}$; for instance, see Nye 1985 or Hudson 1980b). The infinitesimal strain is

$$\varepsilon_{kl} = \frac{1}{2}\left(\frac{\partial u_k}{\partial x_l} + \frac{\partial u_l}{\partial x_k}\right), \tag{2.1}$$

where u_n is displacement and x_n is the corresponding cartesian direction. The $3 \times 3 \times 3 \times 3$ c_{ijkl} tensor can be reduced by symmetry ($\sigma_{ij} = \sigma_{ji}$, $\varepsilon_{ij} = \varepsilon_{ji}$) to a 6×6 matrix using the Voigt notation,

$$ij \to \alpha,\ kl \to \beta,\ c_{ijkl} \to C_{\alpha\beta},$$

$$11 \to 1\,,\ 22 \to 2\,,\ 33 \to 3\,,\ 32 = 23 \to 4\,,\ 31 = 13 \to 5\,,\ 12 = 21 \to 6\,,$$

$$C_{\alpha\beta} = \begin{bmatrix} C_{11} & C_{12} & C_{13} & C_{14} & C_{15} & C_{16} \\ & C_{22} & C_{23} & C_{24} & C_{25} & C_{26} \\ & & C_{33} & C_{34} & C_{35} & C_{36} \\ & & & C_{44} & C_{45} & C_{46} \\ & & & & C_{55} & C_{56} \\ & & & & & C_{66} \end{bmatrix}. \tag{2.2}$$

The matrix is symmetrical, hence the lower elements are not shown, and there are 21 independent elastic constants which describe a minimally symmetrical, fully anisotropic system, an example of which would be a triclinic crystal. Increasing symmetry within a system reduces the number of independent elastic constants. For orthorhombic symmetries, there are nine; for hexagonal symmetry, there are five (C_{11}, C_{33}, C_{44}, C_{66} and C_{13}); for cubic there are three (C_{11}, C_{44} and C_{12}); and for isotropic media, there are only two (C_{11} and C_{44}). (For this special case,

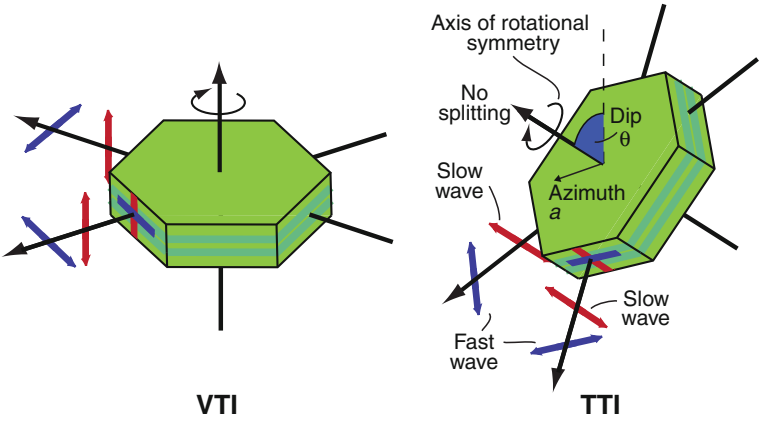

Fig. 2.1 Transverse isotropy, or hexagonal symmetry, and wave propagation through such a medium. On the *left*, the rotational axis of symmetry is vertical, leading to vertical transverse isotropy (VTI). On the *right*, the axis is tilted away from the vertical, leading to tilted transverse isotropy (TTI), or simply a general case of transverse isotropy (TI). Waves within the plane of isotropy are split into orthogonal fast (*blue*) and slow (*red*) waves. The dip θ and azimuth a (the dip direction) of the plane of isotropy define the TTI orientation

$C_{11} = C_{22} = C_{33}$, $C_{12} = C_{13} = C_{23}$, and $C_{44} = C_{55} = C_{66} = (C_{11} - C_{12})/2$.) A visual summary of the independent terms in the matrix $C_{\alpha\beta}$ for each crystal symmetry class can be found on p. 148 in Royer and Dieulesaint (2000). The second-rank tensor is often also subscripted ij (C_{ij}) rather than $\alpha\beta$ ($C_{\alpha\beta}$) because of the convenience in representing elastic constants with the reduced notation.

Because the full tensor is so complicated, it is usual to make assumptions about the kind of symmetry present in the Earth; hexagonal symmetries are a good approximation where sedimentary layering or oriented cracks or inclusions are present. Where the layering is horizontal, the hexagonal symmetry can be described by a vertical axis of rotational symmetry; if it is inclined, then so is the symmetry axis (Fig. 2.1). The plane normal to the symmetry axis is the plane of isotropy. When the plane of isotropy is horizontal (the axis of symmetry vertical), this is often referred to as vertical transverse isotropy (VTI), whereas a more general case where the plane inclined is termed tilted transverse isotropy (TTI).

In order to calculate the phase velocity along any particular direction given an elastic tensor, one solves the Christoffel equation,

$$\det|c_{ijkl}\, n_i\, n_j - \rho v_n^2\, \delta_{il}| = 0\ , \tag{2.3}$$

where n_i is the unit normal to the plane wavefront, ρ is the density, v_n is the phase velocity along the plane wavefront normal, and δ is the Kronecker delta. The three eigenvalues of the solution correspond to the P and S wave velocities, V_P, V_{S1} and V_{S2}, along this direction (strictly, to the phase velocities of the quasi-compressional and -shear waves, which are not necessarily parallel and orthogonal respectively to n_i).

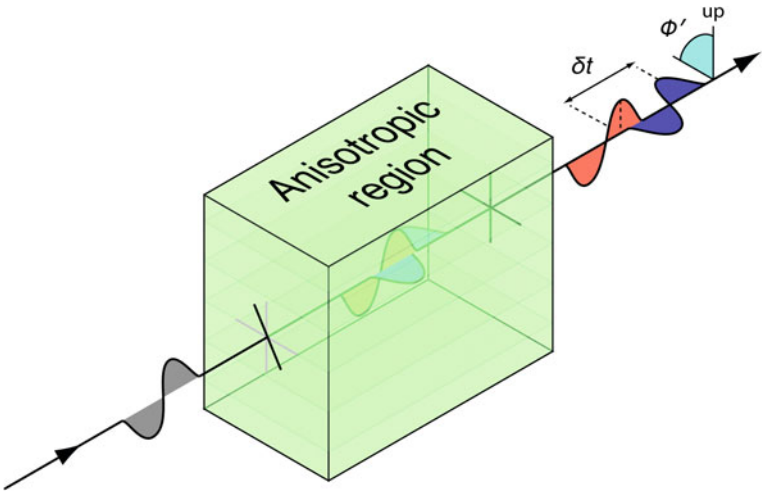

Fig. 2.2 Shear wave splitting in an anisotropic medium. The unsplit incoming shear wave encounters the anisotropic medium, and is split into two orthogonal waves, fast (S_1, *blue*) and slow (S_2, *red*). The delay between the two is measured as δt, and the fast orientation in the ray frame (measured relative to the vertical) is ϕ'

2.1.3 Shear Wave Splitting

Shear wave splitting occurs when a transverse wave travels through an anisotropic medium. Analogous to optic birefringence, this creates two orthogonally-polarised waves (the fast wave, S_1 and slow, S_2) (Fig. 2.2). Depending on the distance travelled in the anisotropic medium, s, and the two velocities, V_{S1} and V_{S2}, the slow wave will be delayed by some time $\delta t = s\left(\frac{1}{V_{S2}} - \frac{1}{V_{S1}}\right)$. The measured polarisation of S_1 is termed the fast orientation, ϕ, and this is measured at the seismic station, hence ϕ is usually in the geographic frame and measured as an azimuth from north. The fast orientation in the ray frame, ϕ', is measured relative to the intersection between the Earth radial plane (vertical) and the ray normal plane, and therefore ϕ' is constant whilst the ray is not being actively split in an anisotropic region.

The strength of the S-wave anisotropy along a certain direction in the anisotropic medium is generally expressed as $\delta V_S = 2(V_{S1} - V_{S2})/(V_{S1} + V_{S2}) \approx (V_S\,\delta t)/s$. Hence in making measurements of splitting, normally one must assume a background 'average' V_S (from global 1–D or tomographic models) and distance travelled in the anisotropic region, in order to calculate δV_S, with these uncertainties inherent. There is clearly a tradeoff between the path length in the anisotropic region and the strength of the anisotropy in that direction, hence in D″—where the layer thickness determines the path length—our knowledge of δV_S in any particular direction is limited by the uncertainty in exactly where in the lowermost mantle the anisotropy lies.

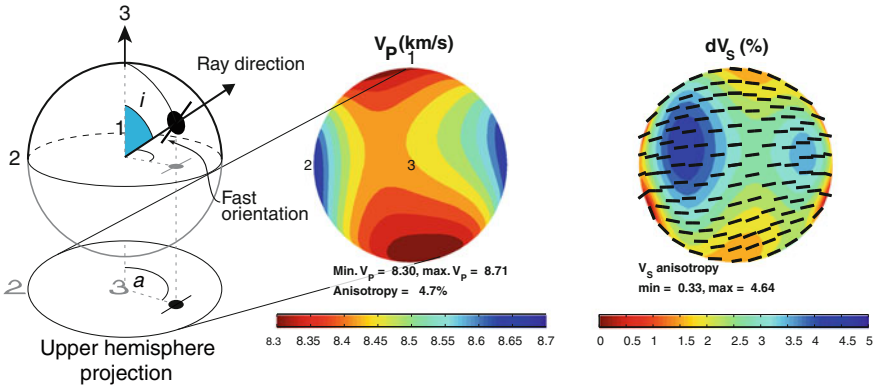

Fig. 2.3 Representation of elasticity tensor by the variation of V_P and V_S with direction. The leftmost diagram explains the wave anisotropy plots on the *right*. The tensor in the three cartesian directions 1, 2 and 3 is represented by an upper hemisphere projection of the variation of wave speed with direction. The *top* of the projection is the 1-direction, left the 2-direction, and out of the page the 3-direction. At each point (each inclination from the 3-axis, i, and azimuth clockwise away from 1 in the 1–2 plane, a), V_P (km s^{-1}) and δV_S (onto the upper hemisphere is shown by the *black ticks*. Shown are the average C_{ij} for a selection of five kimberlites from Mainprice and Silver (1993), where the X-, Y- and Z-directions are oriented to the 1-, 2- and 3-directions respectively

The elasticity tensor can be visualised by examining V_P and V_S as a function of direction. We present the elastic behaviour of materials using upper hemisphere diagrams, explained in Fig. 2.3. For all directions, we calculate the phase velocities as described above and show V_P and δV_S with colour. Additionally, the orientation of the fast shear wave, S_1, is shown by black ticks. In these diagrams, we show the variation in elastic properties with respect to the three cartesian axes, 1, 2 and 3. Figure 2.3 shows the elastic constants for a set of mantle peridotites taken from Mainprice and Silver (1993). The 1–2 plane corresponds to the foliation in the sample, which probably results from a shear fabric. The 1-direction is aligned with the lineation, which probably shows the shear direction.

2.2 Measuring Seismic Anisotropy

The measurement of seismic anisotropy in the Earth has become routine for a limited number of techniques. In the deep mantle, work has mostly been directed towards observing the primary, unambiguous product of the presence of anisotropy: shear wave splitting in phases which traverse the D″ region. However new approaches are becoming available which can directly invert for anisotropic structure within the lowermost mantle using a broader range of data. Previous reviews of observations of D″ anisotropy are in Lay et al. (1998), Kendall and Silver (2000), Moore et al. (2004) and Wookey and Kendall (2007)

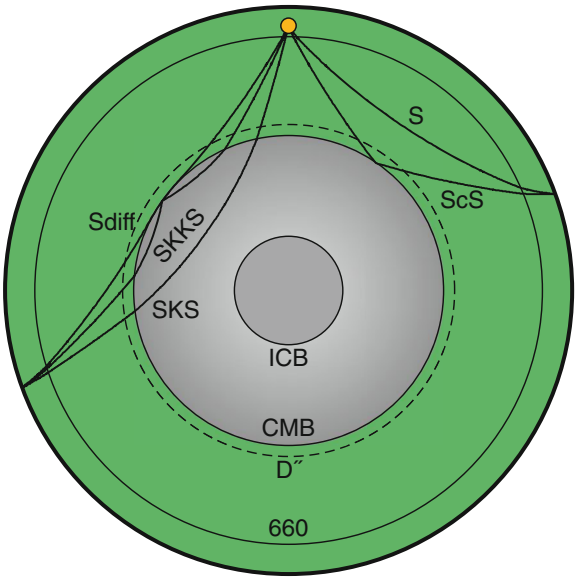

Fig. 2.4 Raypaths of some of the body wave phases used to study D″ anisotropy

2.2.1 Correcting for the Upper Mantle

Measuring anisotropy in the deepest part of the mantle is not straightforward, as the upper mantle is known to be widely anisotropic itself (for a review, see Savage 1999). The most common means of accounting for the effect of upper mantle anisotropy on D″-traversing phases is to use a correction based on SKS splitting measurements. This phase traverses the outer core as a P wave and converts to a vertically polarised S wave (SV) at the CMB, hence is unsplit upon re-entering the lower mantle (Fig. 2.4). Making the assumption of lower mantle isotropy, SKS should only split when encountering D″ and the upper mantle.

SKS studies are now numerous and successfully explain many features of upper mantle dynamics, on the basis that SKS's path length in D″ is relatively small because the phase travels nearly vertically, and anisotropy in the lowermost mantle should not affect splitting in SKS much. Niu and Perez (2004) and Restivo and Helffrich (2006) compared SKS and SKKS phases globally to investigate whether the lowermost mantle has an effect on such phases. In some individual cases in regions of high shear velocity, such as beneath eastern Canada, some discrepancy between SKS and SKKS was seen, which the authors attribute to D″ anisotropy related to LPO of post-perovskite or some other non-VTI mechanism. Overall, however, they found no significant departure from a mechanism in which SKS is not split in D″. This implies one of three things: anisotropy is not strong in D″, which does not appear to be the case from other measurements; anisotropy in D″ is not strong enough to be noticeable for near-vertical rays like SKS-SKKS, which have a relatively short path there; or the style of anisotropy (e.g., VTI) means that radially polarised rays are not

split, as azimuthal anisotropy may cause splitting in SKS-SKKS phases (Hall et al. 2004). This presents a puzzle for future studies of lowermost mantle anisotropy, as shall be explored.

If we continue with the assumption that SKS splitting reflects only upper mantle anisotropy, then it can be used to remove the receiver-side splitting which occurs in a D″-traversing phase when reaching the seismometer. The ray paths in the upper mantle of S, ScS and Sdiff are close to that of SKS for the distances discussed here, and their Fresnel zones at periods of 10 s all overlap significantly down to ∼300 km, so the effect of heterogeneity beneath the receiver is addressed. This does not account for anisotropy beneath the earthquake, however. One approach to address this is to use very deep-focus events (e.g., >500 km), which presumably do not experience much of the upper mantle anisotropic fabric as olivine is only stable down to ∼410 km. However, Wookey et al. (2005a), Rokosky et al. (2006) and Wookey and Kendall (2008), for instance, show that there is observable splitting beneath even some deep events (<600 km), so this assumption may increase uncertainties in observations of lowermost mantle splitting where no source-side corrections are made.

Further difficulties with SKS splitting-based corrections when examining lowermost mantle-traversing phases are that in order to adequately correct for anisotropy beneath the receiver, one must have a good knowledge of the type of anisotropy present there, as dipping or multiple layers of anisotropy will lead to observed splitting having a strong dependence of the incoming polarisation of S-ScS-Sdiff. Choosing recording stations with many SKS measurements from a wide range of backazimuths can help alleviate this. A 90° or 180° periodicity in the splitting parameters ϕ and δt compared to the backazimuth betray the presence of complex upper mantle anisotropy Silver and Savage (1994), which should be avoided. Equally, stations which show little or no splitting across all backazimuths may be used with no correction. For especially well studied regions, it may be possible to correct for even complicated types of anisotropy (Wookey and Kendall 2008), but the ability to uniquely interpret such SKS splitting measurements is rare.

An additional factor to consider in using SKS measurements as an upper mantle correction is that S and SKS phases are of different slowness, so their incidence angles beneath the receiver differ by up to ∼20°, depending on the epicentral distances being investigated. In general, this will lead to a difference in the splitting accrued along the rays in the upper mantle, hence an SKS-derived correction may not be appropriate. However, for an assumed hexagonal anisotropy with a horizontal symmetry axis beneath the station, the difference is small, and it appears in many studies the correction is adequate. Figure 2.5 shows the receiver-side upper mantle splitting which occurs in SKS and S in a 250 km-thick anisotropic layer. The elastic constants are of those shown in Fig. 2.3 (Mainprice and Silver 1993) with an imposed hexagonal symmetry. For SKS in the distance range $90° \leqslant \Delta \leqslant 120°$ (typical for upper mantle SKS splitting studies), the range of incidence angles is small (10–6°), and consequently there is almost no variation of splitting parameters with backazimuth. For S in the distance range $60° \leqslant \Delta \leqslant 80°$, incidence angles are ∼23–18°, and splitting in S shows some small variation with backazimuth. However, because the style of anisotropy is relatively simple, the difference in splitting parameters

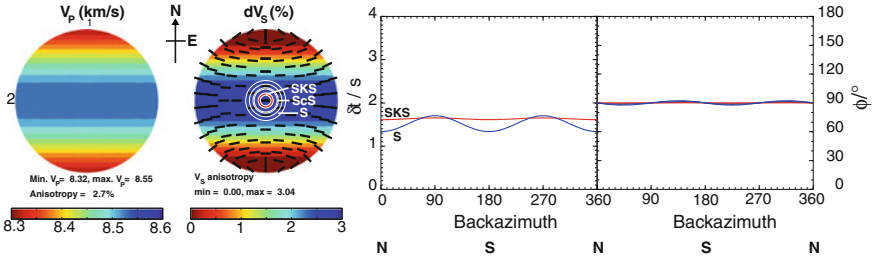

Fig. 2.5 Shear wave splitting parameters of SKS and S phases from upper mantle anisotropy. The two phases have slightly different slownesses, corresponding to a different incidence angle beneath the station. The upper hemisphere phase velocity plots, left, show the case of TI with a symmetry axis parallel to 1 (representing north). The 2-axis points west and 3 is up (out of the page). The elastic constants are those of Mainprice and Silver (1993) as shown in Fig. 2.3, but with an imposed hexagonal symmetry. The *circles* at the centre of the V_S plot show the range of incidence angles of SKS (*red*, innermost), S (*blue*, outermost) and ScS (*black*) phases at distances described in the text. The splitting parameters corresponding to these distances and backazimuths and a 250 km-thick layer are shown on the *right* for SKS (*red*) and S (*blue*). There is almost no variation in SKS, and for ϕ the two phases experience indistinguishable splitting. For δt, the largest difference is about 0.3 s, and within typical errors the two phases would exhibit the same splitting parameters. The parameters for ScS lie between the two other phases

between S and SKS is very small—the fast orientations ϕ are indistinguishable, and the delay times are less than 0.3 s different, which is similar to the typical error in δt.

2.2.2 SH-SV Traveltime Analysis

The most straightforward way to infer anisotropy in D″ is to compare the arrival times of the two components of a shear phase when polarised horizontally (SH) and vertically (SV) (or, respectively, the tangential and radial components), after correcting for upper mantle anisotropy. The phases studied are usually S, ScS and Sdiff, and the assumption is made that the wave travels approximately horizontally (CMB-parallel) when bottoming in D″. Therefore, if SH arrives first, one can infer that along this azimuth the velocity is faster in the tangential direction than the radial ($V_{SH} > V_{SV}$). Figure 2.6 gives an example of this method.

In any study, constraining the source of the anisotropy to D″ is the main difficulty. There is good reason to suggest that the lower mantle above D″ is isotropic (*e.g.,* Meade et al. 1995; Montagner and Kennett 1996; Panning and Romanowicz 2006), therefore taking pairs of phases—where one spends some time in D″ and the other avoids it—can be used to remove upper mantle effects. Figure 2.4 shows ray paths for the major phases used: S, ScS, and Sdiff.

Some of the earliest studies (e.g., Lay and Young 1991; Vinnik et al. 1995) inferred anisotropy by looking at the retardation (relative to SHdiff), amplitudes and phase shifts of SV waves diffracted along the CMB (SVdiff). However, anisotropy is not the

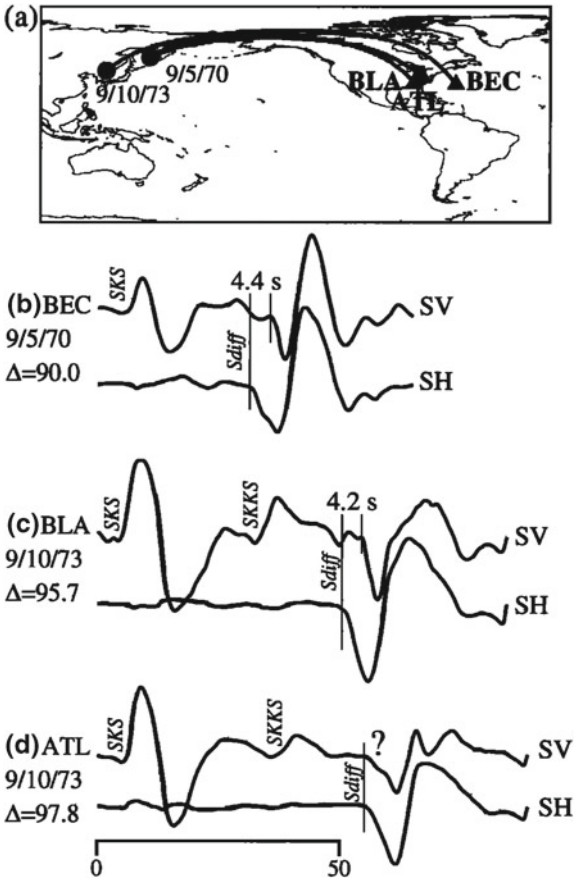

Fig. 2.6 SH-SV traveltime analysis, Figure 5 from Garnero and Lay (1997). The authors examine shear waves travelling along the CMB beneath Alaska from two events in 1970 and 1973, at distances $90.0° \leqslant \Delta \leqslant 97.8°$. The onset of the S wave on the transverse component (SH) is around 4 s before that of the radial component (SV). Because there is minimal energy on the transverse component for the SKS arrival, it appears that negligible upper mantle anisotropy affects the signal. Hence the authors conclude that the two components have experienced different velocities in the lowermost mantle ($V_{SH} > V_{SV}$)

only possible cause of these effects for waves diffracted past distances of $\Delta \gtrsim 95°$, as shown by Maupin (1994) and Komatitsch et al. (2010). They model shear wave propagation in isotropic Earth models using the Langer approximation with perturbation theory, and spectral element method respectively, to show the early onset of SHdiff relative to SVdiff because of SV's coupling with the outer core, hence caution is needed in ascribing anisotropy to D″ on the basis of measurements of Sdiff at large distances: detailed full-waveform modelling and accurate isotropic Earth models are needed.

The majority of observations comparing SH and SV traveltimes show $V_{SH} > V_{SV}$, with $0.5\% \leqslant \delta V_S \leqslant 3\%$, particularly in higher-than-average V_S regions, such as beneath subduction zones. Table 2.1 and Fig. 2.7 summarise the observations for regional measurements of splitting in D″. In general, however, it seems that around the Pacific rim, $V_{SH} > V_{SV}$. Beneath the central Pacific, the pattern is more variable: some studies find $V_{SH} > V_{SV}$, some $V_{SH} < V_{SV}$.

Table 2.1 Summary of previous studies of anisotropy in the lowermost mantle

Study	Phases used	Observation	δV_S / %[a]	Suggested style of anisotropy
1. Caribbean				
Lay and Helmberger (1983)	ScS	$V_{SH} > V_{SV}$	5	Isotropic velocity structure
Kendall and Silver (1996)	S,Sdiff	$V_{SH} > V_{SV}$	1.8	VTI
Ding and Helmberger (1997)	ScS	$V_{SH} > V_{SV}$	2.5	VTI
Rokosky et al. (2004)	ScS	$V_{SH} > V_{SV}$	0.6	VTI
Garnero et al. (2004a)	S,ScS,Sdiff	$\leqslant$20° dip east-west		TTI
Maupin et al. (2005)	S,ScS,Sdiff	$\leqslant$20° dip east-west	1.5–2.2	TTI
Rokosky et al. (2006)	ScS	Mostly $V_{SH} > V_{SV}$	0.0–2.0[b,c]	Varying TTI
Nowacki et al. (2010)	ScS	~50° dip ~south	0.8–1.5	TTI or orthorhombic
2. Central Pacific				
Vinnik et al. (1995)	Sdiff	$V_{SH} > V_{SV}$	0.6[b]	VTI
Vinnik et al. (1998)	Sdiff	$V_{SH} > V_{SV}$	~10	VTI
Pulliam and Sen (1998)	S	$V_{SH} < V_{SV}$	−2	VTI
Ritsema et al. (1998)	S,Sdiff	$V_{SH} < V_{SV}$	−2.1–−1.4	VTI
Kendall and Silver (1998)	S,Sdiff	$V_{SH} \approx V_{SV}$		Isotropic
Russell et al. (1998, 1999)	ScS	$V_{SH} > V_{SV}$, $V_{SH} < V_{SV}$	2–3	VTI
Fouch et al. (2001)	S,Sdiff	$V_{SH} > V_{SV}$	0.3–5.3	VTI
Kawai and Geller (2010)	S,ScS,SKS	$V_{SH} < V_{SV}$	−3	VTI
3. Alaska				
Lay and Young (1991)	S,ScS,Sdiff	$V_{SH} > V_{SV}$		VTI
Matzel et al. (1996)	S,ScS,Sdiff	$V_{SH} > V_{SV}$	1.5–3	VTI
Garnero and Lay (1997)	S,ScS,Sdiff	Mainly $V_{SH} > V_{SV}$	−1–3	VTI
Wysession et al. (1999)	Sdiff	$V_{SH} > V_{SV}$	0.2–0.6	VTI or TTI
Fouch et al. (2001)	S,Sdiff	$V_{SH} > V_{SV}$	0–0.9	VTI
4. South East Pacific				
Ford et al. (2006)	S,Sdiff	$V_{SH} > V_{SV}$, $V_{SH} < V_{SV}$	−1.0–0.9	VTI

(continued)

Table 2.1 (continued)

Study	Phases used	Observation	δV_S / %[a]	Suggested style of anisotropy
5. North West Pacific				
Wookey et al. (2005a)	ScS	~40° dip southeast	0.8–2.3	TTI
6. East Pacific				
Long (2009)	SKS-SKKS	Differential $\delta t \approx 2$ s [d]	0.5[b]	TTI
7. Western USA				
Nowacki et al. (2010)	ScS	26° dip southwest	1.2	VTI or TTI
8. Atlantic Ocean				
Garnero et al. (2004b)	S,Sdiff	$V_{SH} \approx V_{SV}$	$\leqslant 0.5$	Isotropy or weak VTI
9. Antarctic Ocean				
Usui et al. (2008)	S	$V_{SH} > V_{SV}$	1[b]	VTI
10. Southern Africa				
Wang and Wen (2007)	SKS-SKKS	Differential $\delta t \approx 1$ s[d]	~2[b]	Varying HTI
11. Indian Ocean				
Ritsema (2000)	S	$V_{SH} > V_{SV}$	1.4–1.7	VTI
12. Siberia				
Thomas and Kendall (2002)	S,ScS,Sdiff	Mainly $V_{SH} > V_{SV}$	−0.8–1.4	Mainly VTI
Wookey and Kendall (2008)	ScS	55° dip ~south	0.7–1.4	TTI or othorhombic
13. Southeast Asia				
Thomas et al. (2007)	ScS	9° dip southwest	0.5	VTI or TTI

[a] +ve: $V_{SH} > V_{SV}$; −ve: $V_{SH} < V_{SV}$
[b] Calculated from the study's stated δt using $\langle V_S \rangle$ from a global isotropic V_S model (Ritsema et al. 1999) for a uniform 250 km thick D″ layer
[c] Upper limit on δt of 2.5 s imposed
[d] Differential δt refers to $\delta t_{SKKS} - \delta t_{SKS}$

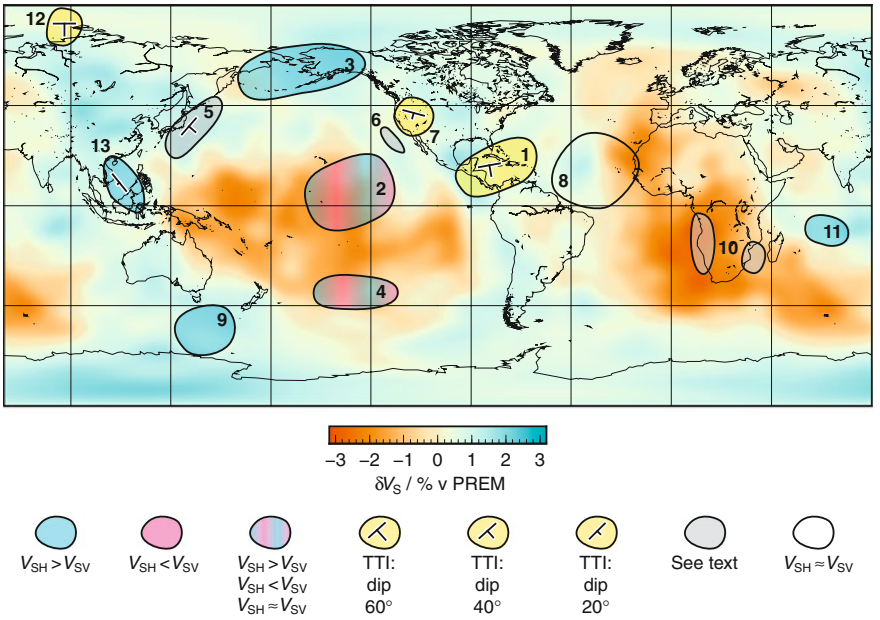

Fig. 2.7 Summary of previous studies of D″ anisotropy. Numbered regions corresponding to Table 2.1 are shown in outline, plotted on top of a global tomographic model of V_S at 2750 km (Becker and Boschi 2002) (colour indicates the variation away from PREM (Dziewoński and Anderson 1981) as per the legend). Regions where the dominant signal is $V_{SH} > V_{SV}$ are shown in *blue*; those where $V_{SH} < V_{SV}$ are in *purple*. Where a region is shown with *red* and *blue* stripes, both situations have been seen, as well as isotropy. *Yellow* areas indicate regions where the orientation of an assumed TTI fabric has been determined: this symbol shows the dip direction of the plane of isotropy with a tick of varying length, as shown in the legend (longer is steeper dip). In regions where one azimuth of raypaths show fast directions which are not CMB-parallel or -perpendicular, they also have a dip symbol as for the TTI regions, with the long bar parallel to the ray path in D″. Regions with no fill show isotropy, and *grey-filled regions* show complex isotropy, either from SKS-SKKS differential splitting (see Table 2.1), or because no studies comparing V_{SH} to V_{SV} have been undertaken

2.2.3 Global Inversion for Anisotropy

An extension of the above technique that can be made—in terms of searching for a VTI structure—is to produce a global inversion for a ratio of V_{SH} and V_{SV}; usually the parameter $\xi = V_{SH}^2/V_{SV}^2$ is sought. Whilst global 1-D models of V_S such as PREM (Dziewoński and Anderson 1981) sometimes include radial anisotropy in the upper mantle, at greater depths the inversions are generally isotropic. Montagner and Kennett (1996) used normal mode and body wave data to infer that $\xi > 1$ (i.e., $V_{SH} > V_{SV}$) in D″ on a global scale. This matches the majority of local observations of SH-SV traveltimes. Recently, Panning and Romanowicz (2004, 2006) have inverted a global dataset of long-period three-component S waveforms to obtain a 3-D model

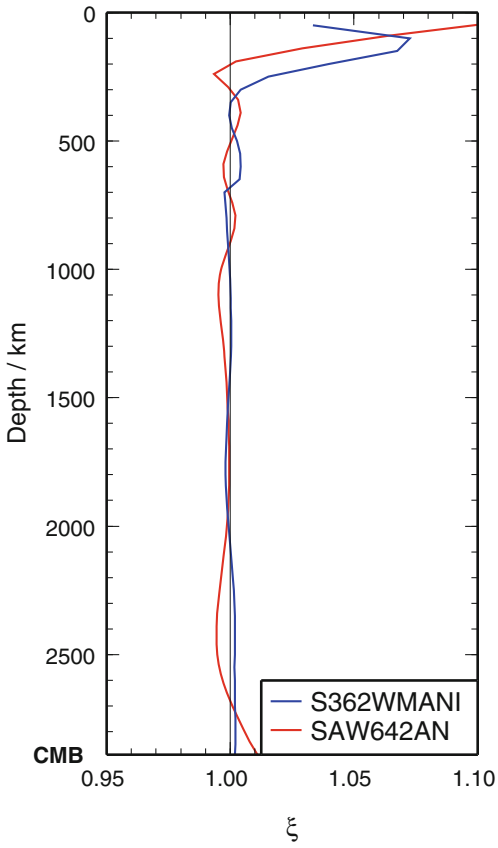

Fig. 2.8 Average depth profile of $\xi = V_{SH}^2/V_{SV}^2$ from the SAW642AN model of Panning and Romanowicz (2006) (*red*) and S362WMANI of Kustowski et al. (2008) (*blue*). For SAW642AN The uppermost and lowermost mantle show $\xi > 1$, whilst most of the lower mantle is approximately isotropic. S362WMANI does not show the same dominant signal in D″

of V_P,V_S, source parameters and ξ throughout the entire mantle. Any such study will be prone to difficulties in correcting for the strongly anisotropic crust and upper mantle, however, so great care is necessary to ensure that this does not contaminate the resulting model (Lekić et al. 2010). Equally, such models will necessarily suffer from sampling bias associated with the location of earthquakes and seismometers because of potentially limited azimuthal coverage of D″. With observations along only one ray path, it is not possible to resolve whether VTI is a good approximation. However, the model agrees with regional observations, showing $V_{SH} > V_{SV}$ where V_S is higher than average, especially around the Pacific rim subduction zones. Where V_S is relatively low, such as beneath the central Pacific and beneath Africa, $V_{SV} > V_{SH}$. Similarly to the work of Montagner and Kennett (1996), it also predicts $\xi > 1$ for D″ on average (Fig. 2.8). Kustowski et al. (2008) invert surface and body waves for 3-D anisotropic mantle velocities using similar data, but find strong tradeoffs in the lowermost mantle between V_S and ξ, and the anisotropic structure in D″ correlates poorly between the two models. It seems that at present there is still some room to improve on current global models.

2.2.4 Regional Full-Waveform Inversion

An alternative to producing a global map of anisotropy is to conduct regional full-waveform inversion of seismic data from phases which traverse D″. However, current studies are limited to assuming VTI in the lowermost mantle for computational and theoretical convenience. Using Tonga–USA raypaths, Kawai and Geller (2010) employ a full-waveform inversion for ξ beneath the central Pacific and find that $\xi < 1$ in D″, though there is little sensitivity to structure below about 150 km above the CMB. This agrees with other studies along similar raypaths, with $\xi \approx 0.97$, which is at the lower end of the range of values found previously. Here, it was necessary to impose a discontinuity of arbitrary depth at the top of the model, and upper mantle anisotropy was not included, so this may have a large impact on the uncertainty.

2.2.5 Waveform Analysis

Whilst relatively straightforward to implement, a weakness of any study which compares SH and SV waves is the assumption of VTI. Recently, efforts have been made to relax this constraint and infer more complex type of anisotropy.

An approach used by Garnero et al. (2004a) and Maupin et al. (2005) is regional forward waveform modelling of S–ScS waves beneath the Cocos plate and the Caribbean. They infer small deviations of a TI symmetry of $\leqslant 20°$ away from VTI as the raypaths move east to west across the region. Using an SH-SV traveltime approach, this would and does appear as $V_{SH} > V_{SV}$, though energy will appear on both radial and transverse components for both fast and slow arrivals.

2.2.6 Measurements of Shear Wave Splitting

Another recent advance towards allowing more complex forms of anisotropy to be studied is to apply the measurement of both ϕ and δt by grid search over the splitting parameters (Fukao 1984; Silver and Chan 1991) to lower mantle-traversing shear phases (Fig. 2.9). [This and other techniques such as the splitting intensity method (Chevrot 2000; Vinnik et al. 1989) are summarised by Long (2009)]. This allows one to determine a more general form of anisotropy, as the fast orientation is not limited to being either parallel or perpendicular to the CMB. In principle, with measurements along one azimuth, one can distinguish whether VTI is a possible mechanism for D″ anisotropy or not, two azimuths can define a TTI-type fabric, whilst three can define an orthorhombic symmetry of anisotropy.

One application of the measurement of shear wave splitting is to examine differential splitting between the S and ScS, usually investigated at epicentral distances $55° < \Delta < 82°$ [with details of the method given by Wookey et al. (2005a)]. Here,

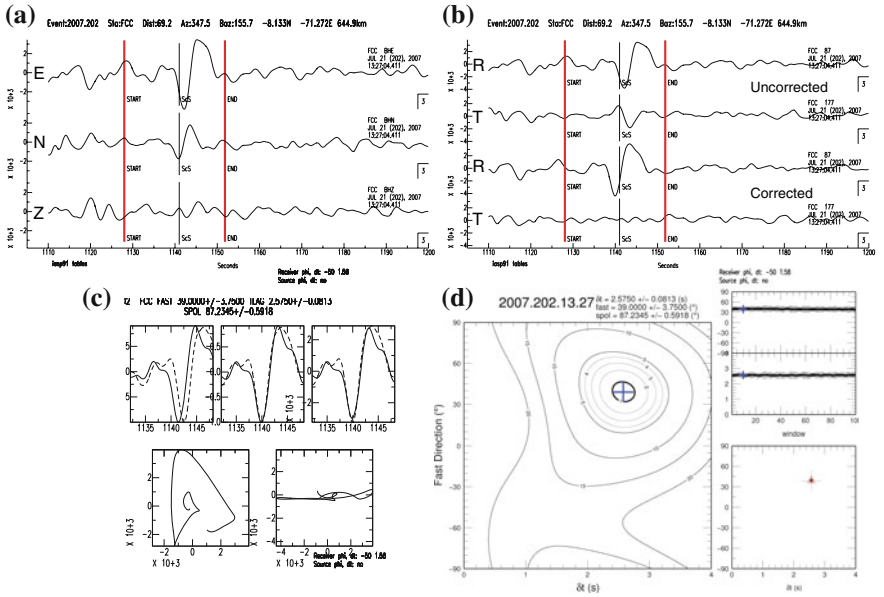

Fig. 2.9 Example of a shear wave splitting measurement, slightly modified from Supplementary Figure 3 of Nowacki et al. (2010). The measurement is made at FCC (Fort Churchill, Manitoba, Canada) on the ScS phase from an 645 km-deep earthquake beneath Brazil at 13:27 on 21 July, 2007, and pre-corrected for upper mantle anisotropy beneath the receiver. **a** Shows the original three component seismogram, with the predicted ScS arrival time for a 1-D global velocity model, and the arrival itself. **b** Shows the horizontal components when rotated to the fast orientation ϕ, as found in the analysis, before and after time-shifting the slow component forward by the delay time found in the analysis. **c** Shows the fast and slow waves before (*upper left*) and after (*upper right*) shifting by dt. The lower subpanels show the horizontal particle motion before and after correction with the optimum (ϕ, δt). **d** Shows the λ_2 surface (corresponding to misfit) in $\phi - \delta t$ space, with the optimum splitting parameters given by the blue cross, and surrounding 95 % confidence interval (thick contour). Subplots to the *right* show the result of cluster analysis (Teanby et al. 2004)—the single cluster shows this is a stable result

ScS samples D″, S turns above it, and both phases share a very similar path in the upper mantle. Because the ScS phase is approximately horizontal for most of its travel in D″ at these distances, the ray frame fast orientation ϕ' (also ϕ^*) is used (Wookey et al. 2005a). This measures the angle away from the Earth radial direction (i.e., vertical) when looking along the ray. Hence, for VTI with $V_{SH} > V_{SV}$, $\phi' = 90°$. If $\phi' \neq 90°$, then another mechanism such as TTI must be responsible.

Single-azimuth S–ScS studies beneath the northwest Pacific (Wookey et al. 2005a), Cocos plate (Rokosky et al. 2006) and southeast Asia (Thomas et al. 2007) have been conducted. Beneath the Cocos plate and southeast Asia, whilst there is some variability, in general fast directions do not depart much from being horizontal. Wookey et al. (2005a), however, found that the fast orientations dipped southeast towards the central Pacific by about 45°, which is a significant departure within the stated error of 7°. Assuming a TTI fabric, this actually provides a lower limit to

the dip of the plane of isotropy, so clearly VTI in this region cannot explain the observations.

Recently, studies using two azimuths of S–ScS paths have been conducted. Beneath northern Siberia, Wookey and Kendall (2008) find that for waves travelling north from Hindu Kush events to stations in Canada, $\phi' = 89°$ (the fast orientation is approximately horizontal in D″), whilst east-west paths from the Kuril arc to stations in Germany show $\phi' = 35°$ (the fast direction dips 55° to the south). Beneath the Caribbean and North America, Nowacki et al. (2010) examine three regions with uncertainties of $\leqslant 10°$ for all azimuths. For ray paths travelling north to stations in North America from events in South America, $\phi' \approx 90°$, within error, which agrees with previous single-azimuth observations (Kendall and Nangini 1996; Garnero and Lay 2003; Garnero et al. 2004a). However, ray paths which cross these are not compatible with VTI: paths travelling northeast from the East Pacific Rise show $\phi' = -42°$ (dipping to the southeast), whilst those travelling northwest from the Mid-Atlantic Ridge show $\phi' = 45°$ (dipping south). A third region off the coast of northwest USA shows two paths with fast orientations $\geqslant 10°$ different to horizontal.

In the cases outlined above, where $\phi' \approx 45°$, the traditional SH-SV traveltime method would not observe any effects of anisotropy (Wookey and Kendall 2007) (Fig. 2.10). Equally, cases where $0° < \phi' < 45°$ cannot be distinguished from simple VTI where $V_{SH} > V_{SV}$. Hence the importance of not only resolving the fast orientation, but also incorporating a large range of azimuths, is hard to understate if we wish to make inferences about the nature and origin of seismic anisotropy from analysis of shear waves. It seems that, in contrast to our previously simple idea of horizontal fast directions beneath subduction zones, and vertical ones beneath upwellings, the picture is more complex. If VTI is not a good approximation to the type of anisotropy in D″, then multiple-azimuth studies must become the norm, otherwise we are at the mercy of the specific, single event-receiver geometry as to whether we can resolve the true effect of CMB dynamics. At the same time, however, the Earth does not give up its secrets easily, as the location of landmasses and large earthquakes poses limitations on which regions of the lowermost mantle we can probe at present.

Given that several studies have now implied that D″ does not everywhere show VTI-type behaviour, it is prudent to assess the discrepancy between this knowledge and the conclusions of Niu and Perez (2004) and Restivo and Helffrich (2006) (Sect. 2.2.1). Because azimuthal anisotropy appears to be present beneath at least Siberia, the Caribbean, western USA, the eastern and northwest Pacific and southern Africa, we should expect that studies comparing SKS and SKKS should exhibit differential splitting between the two phases which emerge from the outer core in these regions. In fact, as pointed out, Long (2009) and Wang and Wen (2007) do observe this in regional studies. In addition, Restivo and Helffrich (2006), for example, also show strong anomalous splitting between the two phases beneath western USA and the eastern Pacific, whilst southern Africa is poorly sampled because of event-receiver geometries. Furthermore, the Caribbean is not well covered: anomalous splitting in SKS-SKKS is evident there also, even if the global trend does not show significant departure from VTI for the whole dataset. Another factor is that because SKS and

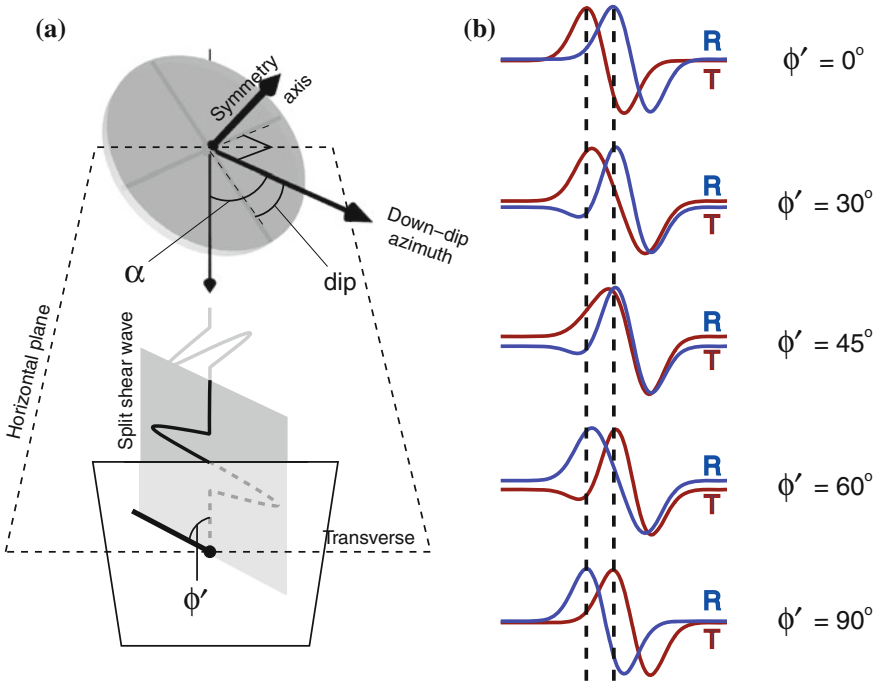

Fig. 2.10 Comparison of SH–SV traveltime analysis and shear wave splitting for a transversely isotropic (TI) medium. On the *left* (**a**), the plane of isotropy is shown by the *grey circle*, dipping at an angle from the horizontal. This defines the orientation of the anisotropy. The ray frame fast orientation of the split shear wave, ϕ', is controlled by the angle between the ray and the dip direction of the plane of isotropy, α, so that ϕ' is along the line of intersection between the plane of isotropy and the plane normal to the ray path. On the right (**b**) is shown the radial (R) and transverse (T) components of the split shear wave for various ϕ'. For all cases $\delta t = 1.5$ s, as shown by the *dashed lines*. Measuring the delay time directly on the two components only gives the correct amount and orientation of splitting for the special cases of $\phi' = 0°$ or 90°. Within ∼15° of 0 or 90°, such measurements are still useful for detecting the presence of anisotropy, but do not provide much information about the symmetry. Slightly modified from Wookey and Kendall (2007)

SKKS are polarised vertically upon exiting the outer core, they will not be split by TTI where the dip direction is closely parallel or anti-parallel to the wave propagation direction. Perhaps the largest difference is that even SKKS at $\Delta = 110°$ spends around 350 km in a 250 km-thick D″ with $\langle V_S \rangle = 7.3\,\mathrm{km\,s^{-1}}$, whereas ScS at 70° has a path over 1000 km. It may therefore be not so surprising that SKS-SKKS differential splitting is hard to observe. However, the small number of cases where it is seen [5 % of observations by Restivo and Helffrich (2006)] requires a good explanation that is still lacking.

2.3 Chemistry and Mineralogy of the Lower Mantle

The properties of the lowermost mantle are of course determined by the bulk composition and which phases are stable at the pressures and temperatures there. In order to interpret seismic observations using geodynamic inferences, we must understand the single- and polycrystal behaviour of the solid phases present, and the possibility of the presence of melt. There are a number of steps which are necessary to use mineral physics data to predict flow from anisotropy. Firstly, which phases are present must be established. Then, single-crystal elastic properties and deformation mechanisms must be evaluated. These can then be used to determine polycrystalline behaviour in deformation, which can allow an aggregate anisotropic fabric to be predicted on the basis of a given deformation history. Often it is hard to separate these in experiments, for instance, which involve many crystals, and authors attempt to find single-crystal properties from polycrystalline measurements. However successful modelling of texturing and hence anisotropy requires knowledge of all of these properties.

Lowermost mantle mineralogy can be investigated with mineral physics experiments at CMB pressures and temperatures using apparatuses such as the laser-heated diamond anvil cell (LHDAC), but there are of course limitations. An important source of error in experiments is the pressure scales used (the Au scale of Tsuchiya (2003), versus the MgO standard of Speziale et al. (2001), amongst others). This means the stated pressure, and hence depth, of the transition from pv to ppv in experiments can range by as much as ± 10 GPa (± 200 km in the lower mantle) depending on the scale, which is an ongoing problem (Hirose 2007). Another significant source of error comes from the high thermal gradients created in the cell by focussed laser heating and diamond's excellent thermal conduction.

Numerical calculations of the properties of materials at high pressure and temperature are another important technique. As for physical experiments, however, uncertainties are present, due to the approximations necessary in performing the calculations. Density functional theory (DFT; Kohn and Sham 1965) provides the basis for most of the studies we mention, which determines material properties by solving Schrödinger's wave equation. DFT gives an exact solution to the problem, but relies on an unknown term (the exchange-correlation energy). Different approximations to this term lead to different biases in the calculations. For a review, see Perdew and Ruzsinszky (2010).

2.3.1 Composition and D″ Mineralogy

The Earth's mantle is generally believed to be pyrolitic in composition (Ringwood 1962; McDonough and Sun 1995). This chemistry determines which mineral phases are present under the conditions of the lowermost mantle, though some experimental evidence suggests that a representative pyrolitic material, the KLB-1 peridotite, may not alone be able to reproduce the seismically-observed density in the lower

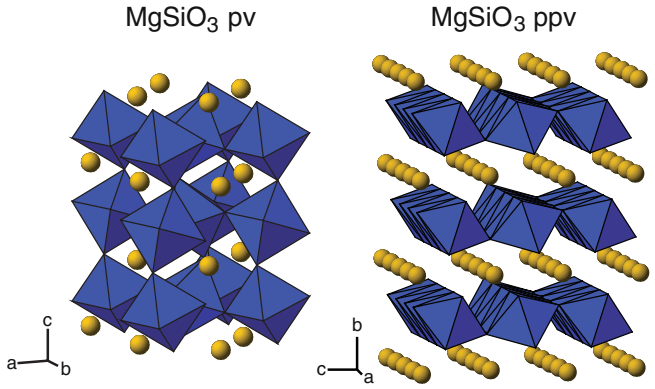

Fig. 2.11 Structure of $MgSiO_3$-perovskite and -post-perovskite. *Yellow spheres* are Mg ions; SiO_6 octahedra are shown in *blue*

mantle (Ricolleau et al. 2009). Input of other material such as mid-ocean ridge basalt (MORB) from subducting slabs must therefore play a role.

The phases present above D″ in a pyrolite composition are orthorhombic $MgSiO_3$ perovskite, with the likely incorporation of some Fe and Al (pv; Fig. 2.11), cubic (Mg,Fe)O (ferropericlase, fpc) and $CaSiO_3$-perovskite (Ca-pv). Experiments suggest they are in the proportions 75, 20 and 5 % respectively (Kesson et al. 1998; Murakami et al. 2005) (Fig. 2.12). For MORB, which is much richer in Al and Si, experiments show a very different mineralogy (Hirose et al. 1999; Ono et al. 2001; Hirose et al. 2005), with about 40 % pv, no fpc and 20 % Ca-pv. Significant amounts of a Na- and Al-rich phase, and a silica phase (∼20 % each) are present.

In 2004, several authors discovered another phase transition in $MgSiO_3$ to the orthorhombic $CaIrO_3$ structure at about 125 GPa (around 2700 km depth) and 2500 K (Murakami et al. 2004; Oganov and Ono 2004). The post-perovskite phase (ppv) has a structure of layers of SiO_6 octahedra parallel to (010), intercalated with layers of Mg ions (Fig. 2.11, right).

Recently, studies have been carried out on pyrolite and MORB samples up to CMB conditions. In pyrolite, Murakami et al. (2005) observe the pv–ppv transition at ∼113 GPa (equivalent to ∼2500 km) and 2500 K, where the phase assemblage is ppv (72 %), fpc (21 %) and tetragonal or cubic Ca-pv (7 %). In MORB compositions, Ono and Oganov (2005) investigated pressures up to 143 GPa (Au standard) and temperatures of 3000 K. They observed ppv, Ca-pv, α-PbO_2-type (also called columbite) silica and a $CaTi_2O_4$-type aluminous phase. Ohta et al. (2008) also investigated MORB samples with similar results, except they found a Ca-ferrite ($CaFe_2O_4$)-type aluminous phase at lowermost mantle conditions. They suggest a transition in silica from the $CaCl_2$ to α-PbO_2 structure at around 115 GPa and 2000 K. Figure 2.12 summarises our current understanding of the phase proportions in the lower mantle.

Whilst we do not focus in this review on the gross variability of the phase assemblage at D″ conditions because of compositional changes other than pyrolite versus

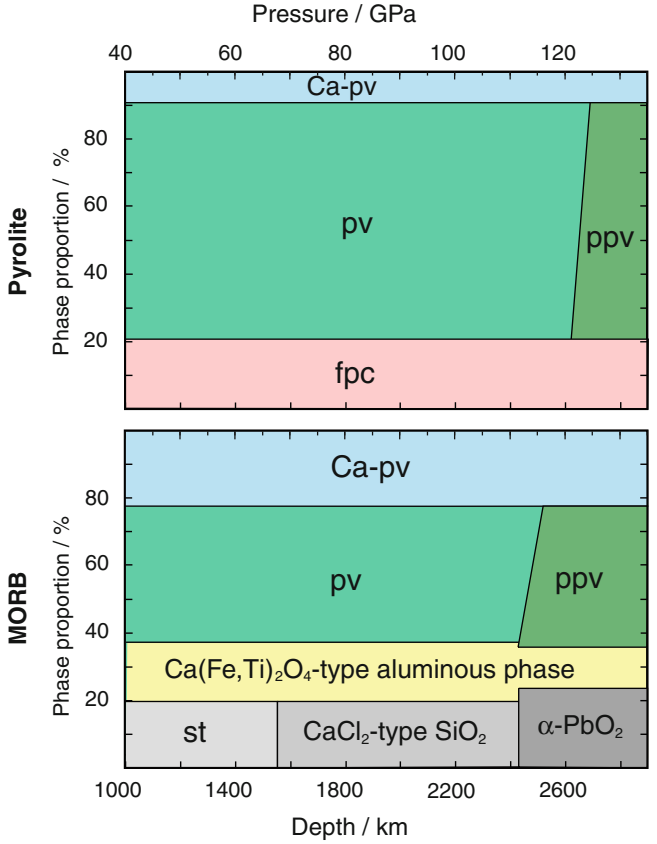

Fig. 2.12 Proportions of phases present in the lower mantle for pyrolite and MORB compositions (after Ono and Oganov 2005 and Hirose 2006, and partly based on Trønnes 2010). *Yellow regions* show aluminous phase regions, whilst *grey regions* show phases of silica. Sloping phase boundaries represent the range of depths over which the transition between the phases probably occurs. $Ca(Fe,Ti)_2O_4$-type Al-bearing phase refers to the uncertainty over the structure of the phase. Abbreviations are: Ca-pv: $CaSiO_3$- perovskite; pv: $(Mg,Fe)(Si,Al)SiO_3$-perovskite; ppv: $(Mg,Fe)(Si,Al)SiO_3$-post-perovskite; st: staurolite; α-PbO_2: SiO_2 in the α-PbO_2 form (also called columbite structure)

MORB, it is obviously important in the behaviour of the lowermost mantle, and there is increasing evidence that chemical heterogeneity must play a part in creating the seismic variability observed in D″ (e.g., Simmons et al. 2009).

Pv–ppv Phase Boundary

How much pv or ppv is present in the lowermost mantle is still unresolved. For pure $MgSiO_3$, the phase boundary is of course sharp and occurs at ∼110–120 GPa, or

2400–2600 km, hence D″ would be mainly composed of ppv. However with realistic amounts of Fe and Al, the phase boundary will be spread out over a range of pressures. Whether the region of costability is extended upward in the Earth by the addition of Fe and Al, or downwards, depends on the partition coefficient of the element between the two phases. If Fe, for instance, partitions more favourably into pv, then it will be stabilised down into the ppv stability field, and costability of the two phases will occur to greater depths than for the pure Mg endmember. Partitioning into ppv would conversely increase the mixed phase region upwards into pv's stability field. Thus this controls the amount of pv and ppv which are present in D″. Additionally, Fe^{2+} and Fe^{3+} will behave differently, and how much iron is ferrous (Fe^{2+}) depends on the oxidation state of the lowermost mantle. It might also be that if another phase like fpc is present into which Fe (or Al) partitions preferentially over pv and ppv, then this will buffer the Fe content and decrease the width of the two-phase region.

Pv and ppv do include Fe and Al in their structure in a pyrolitic composition (Murakami et al. 2005), so the phase boundary between pv and ppv in various compositions is important. Whilst progress is being made, there has yet to emerge a consensus on the partitioning of Fe in particular between fpc and ppv, versus fpc and pv, hence there remains uncertainty in the pressure range across which pv and ppv are both stable. It seems that the partition coefficient of Fe between pv and ppv, $K_{\mathrm{Fe}}^{\mathrm{pv/ppv}}$, is strongly dependent on Fe and Al content of the phases. Recent work at CMB conditions suggests $K_{\mathrm{Fe}}^{\mathrm{pv/ppv}} \approx 4$ (see Andrault et al. 2010, and their introduction for a recent concise review), and the phase boundary is predicted to be about 15 GPa or 300 km thick. Catalli et al. (2009) measure the transition width to be about 20 GPa (~400 km) in a synthesised sample of $(Mg_{0.9}Fe_{0.1})(Al_{0.1}Si_{0.9})O_3$, and less than that in a sample without Al ($(Mg_{0.91}Fe_{0.09})SiO_3$), though this of course does not include the buffering effects of any other phases which are present in the Earth. Both studies suggest costability begins at pressures equivalent to 400–600 km above the CMB.

Sinmyo et al.'s (2008) study highlights the uncertainties in the measurements of K_{D}, finding that the large temperature gradient in the sample may cause the variability between studies. Further, uncertainties in the pressure scales mean it is hard to define at exactly what depth the beginning of the mixed-phase region starts. Notably, actual peridotite samples (Murakami et al. 2005) apparently contain ppv at D″ conditions.

An additional factor to consider is that the phase proportion curve may not be linear across the transition, so larger or smaller amounts of ppv may be present than expected for a given pressure. One attempt to quantify this (Hernlund 2010) suggests ppv is likely to exist in significant proportions (>50 % of the mantle) after just a few tens of kilometres of the transition.

Measurements of the Clapeyron slope of the pv–ppv show it likely lies in the range 7–14 MPa K^{-1} (Oganov and Ono 2004; Tsuchiya et al. 2004; Ono and Oganov 2005; Hirose et al. 2006; Tateno et al. 2009). This positive value implies that colder areas of the lowermost mantle will be enriched in ppv relative to hotter ones, and also offers the possibility that because of the steep geotherm near the CMB, so-called 'double-crossings' of the phase boundary might occur, leading to lenses of ppv-rich

mantle bounded above and below by pv-rich areas (Hernlund et al. 2005; Wookey et al. 2005b). The effect this might have on the development of anisotropy from LPO of ppv is intriguing but poorly understood at present.

2.3.2 Single-Crystal Elasticity of D″ Minerals

With knowledge of the approximate proportions of phases present in the lowermost mantle, an understanding of the individual minerals' properties and relative stabilities is necessary to make predictions about the behaviour of seismic waves passing through this region. Hence there has been much interest in using both experimental and theoretical methods to investigate these properties. Recent reviews of some of the work done on lowermost mantle phases—mainly pv, ppv and fpc—can be found in Hirose (2007), Shim (2008), Ohtani and Sakai (2008) and Trønnes (2010), amongst others. Here we discuss the most basic property of the phases in D″ for our purposes, their elasticity, which provides a first-order idea of their contribution to seismic anisotropy.

Perovskite

Magnesium silicate perovskite (with about 10 % Fe and a few percent Al in the structure) is the most abundant mineral phase in the Earth, and is likely present in some portions of the bottom few hundred kilometres of the mantle. Because pv and ppv make up most of the lower mantle, they are the primary phases to affect seismic waves, and thus most important to understand well. Although perfect perovskites are cubic, pv is orthorhombic due to the rotation of the SiO_6 octahedra (Fig. 2.11, left).

Single-crystal elastic constants for pv at lowermost mantle conditions are shown in Fig. 2.13. Elastic constants for pv have been calculated by Oganov et al. (2001), Wentzcovitch et al. (2004), Wookey et al. (2005b) and Wentzcovitch et al. (2006) at CMB pressure, the latter two at high T. Figure 2.13 shows that there is some discrepancy between the calculations, which appears to be due to differences in the C_{12}, C_{22} and C_{33} terms. The maximum δV_S is between about 13–20 %, which is moderately but not very strongly anisotropic.

Post-perovskite

With the discovery of ppv (Iitaka et al. 2004; Murakami et al. 2004; Oganov and Ono 2004; Tsuchiya et al. 2004), there has been an understandable focus on its elasticity, phase stability, and so on, as explanations of lowermost mantle observations.

Intuitively, the orthorhombic ppv structure should be more seismically anisotropic than pv due to the layering of the SiO_6 octahedra, and this appears to be the case: the b-axis is more compressible than the a- and c-axes (Guignot et al. 2007; Mao et al.

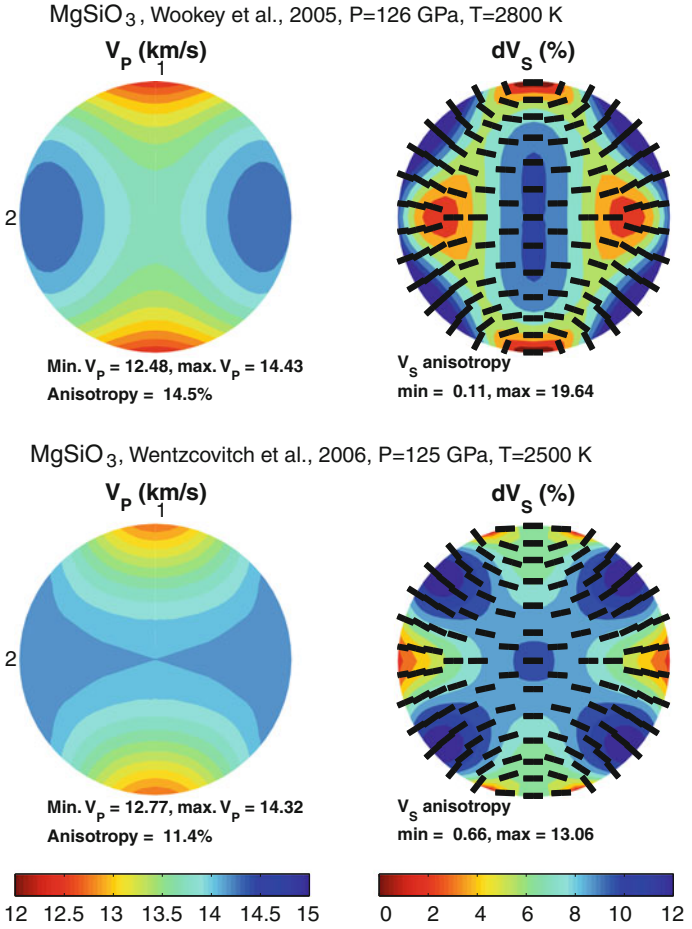

Fig. 2.13 Elastic P and S wave anisotropy for pv from calculations at lower mantle conditions. (*Top* Wookey et al. 2005b; *bottom* Wentzcovitch et al. 2006.) Plots on the left show upper hemisphere, equal area projections of V_P with direction within the orthorhombic crystal. The 1, 2 and 3 axes are shown, corresponding to the [100], [010] and [001] directions respectively: 1 is up, 2 is left and 3 is out of the page. Colour indicates V_P as shown in the scale bar at the *bottom*. Plots on the *right* show δV_S (colour as per the scale bar) and the fast shear wave orientation with direction (*black ticks*). Because of the orthorhombic symmetry, each plot only varies within each quadrant

2010). Elastic constants at D″ P and T have been calculated from experiments for ppv (Mao et al. 2010); *ab initio* calculations have recently been made by Wookey et al. (2005b), Stackhouse et al. (2005b) and Wentzcovitch et al. (2006).

Figure 2.14 shows the elastic anisotropy for ppv at high temperature, comparing the theoretical calculations ($MgSiO_3$) at 4000 K to those of Mao et al. (2010) ($(Mg_{0.6}Fe_{0.4})SiO_3$) at 2000 K. It is clear that there is some variation between the calculations. The experimentally-derived results show the largest δV_S, with $\delta V_S = 42\,\%$

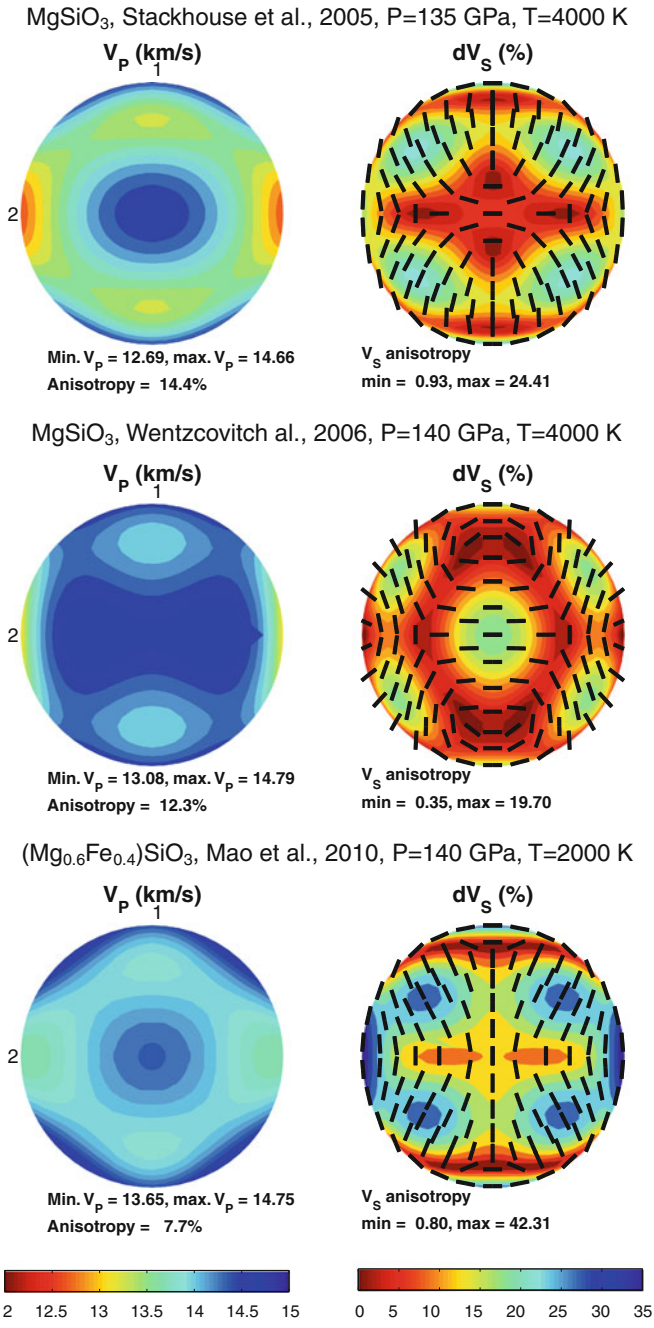

Fig. 2.14 Elastic P and S wave anisotropy for ppv from experiments and calculations at $T = 4000$ K (*top to bottom* Stackhouse et al. 2005b; Wentzcovitch et al. 2006; Mao et al. 2010). Features as for Fig. 2.13

along [010]. Otherwise, the pattern is quite similar between the studies of Stackhouse et al. (2005b) and Mao et al. (2010), despite the difference in Mg#. This agrees with the analysis of Wookey and Kendall (2007), who suggest from combining *ab initio* elastic constants for the $MgSiO_3$, $FeSiO_3$ (Stackhouse et al. 2006) and $AlSiO_3$ (Stackhouse et al. 2005a) ppv endmembers in pyrolitic proportions that they do not differ significantly from those of pure Mg case. The general pattern of anisotropy differs slightly when considering the constants of Wentzcovitch et al. (2006), mainly due to differences in C_{11}, C_{33} and C_{13}; the reason for this discrepancy is still unclear and hopefully future work will better constrain our knowledge of the single-crystal elasticity of ppv. It is notable that theoretical calculations with realistic amounts of Fe and Al in Mg-pv and -ppv are difficult because the number of atoms in the simulations becomes large, hence the effect of their incorporation is uncertain.

Ferropericlase

As the second most abundant mineral phase in the lowermost mantle, fpc is an important control on the behaviour of seismic waves in D″. Assuming a pyrolitic mantle, an approximate Mg# of 0.9 with Fe# = 0.1 is the likely composition. (Mg,Fe)O is stable throughout the lower mantle, though much recent interest has been shown in a possible change of its properties due to the change in the spin state in Fe which may occur at midmantle pressure and temperatures. We do not discuss in detail the spin transition in fpc further as it appears this occurs higher in the mantle than D″ (∼2200 km; e.g., Komabayashi et al. 2010); of relevance is that Fe in fpc is likely in the low-spin state in the lowermost mantle. (For a recent review of the spin transition in fpc, see Lin and Tsuchiya 2008.)

Because fpc is cubic, the three constants required to describe the elastic behaviour of the structure are C_{11}, C_{12} and C_{44}. Single-crystal elastic constants for fpc $(Mg_{0.9}Fe_{0.1})O$ have recently been determined from experiment by Marquardt et al. (2009) up to 81 GPa (∼1900 km) at ambient temperatures. Karki et al. (1999) calculate the elastic constants up to 150 GPa (greater than mantle depths) and 3000 K using *ab initio* methods for the pure Mg endmember, whilst Koci et al. (2007) perform calculations at 0 K up to 150 GPa for a range of Fe proportions up to 25 % ($(Mg_{0.75}Fe_{0.25})O$). Figure 2.15 shows a selection of single-crystal elastic constants for MgO from theoretical calculations and $(Mg_0 0.9Fe_{0.1})O$.

It appears that the main effect of Fe in fpc is to decrease C_{11} and C_{44}, and increase C_{12} (Fig. 2.15; Koci et al. 2007), which in general will decrease the anisotropy of the crystal (C_{12} becomes closer to $(C_{11} - 2\,C_{44})$, as for the isotropic case). Little work has been conducted with Fe in the structure at high pressure, however, so these results are for high- or intermediate-spin states of Fe, and it is not clear what effect low-spin Fe might have on the anisotropy of fpc. As with pv and ppv, a large unknown at present is the partition coefficient between these phases, hence our knowledge of the likely Fe content of any of them at a particular pressure and temperature is limited.

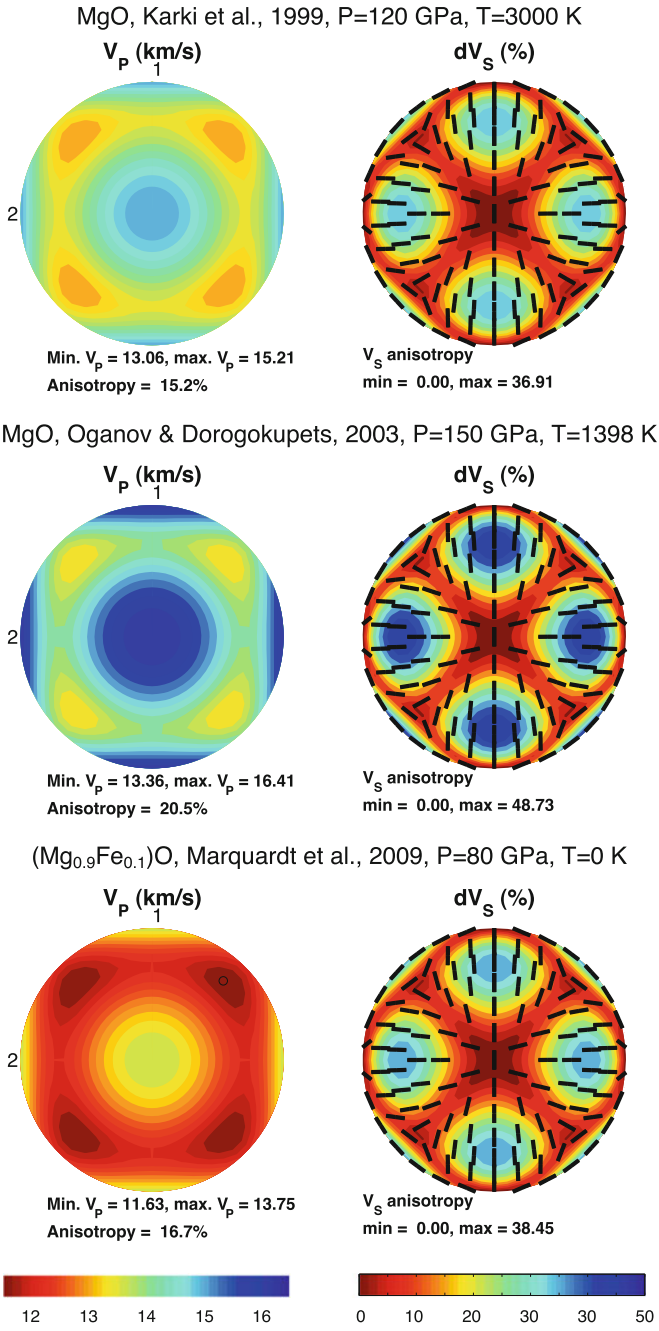

Fig. 2.15 Elastic P and S wave anisotropy for fpc from ab initio calculations and experiment at lower mantle conditions. The three axes (1, 2 and 3) each corresponds to the ⟨100⟩ directions—because of the cubic symmetry the plots only vary within each eighth of the upper hemisphere

Other Phases

Whilst pv–ppv and fpc are the dominant phases in a pyrolitic composition at D″ conditions, Ca-pv along with silica and aluminous phases are present in much larger proportions in a MORB composition, hence knowledge of these phases is still important.

Ca-pv is predicted to undergo a transition from cubic to tetragonal due to rotation of the SiO_6 octahedra at around 2000–2500 K at the CMB on the basis of *ab initio* molecular dynamics (MD) simulations (Adams and Oganov 2006; Stixrude et al. 2007), so potentially in cold regions of the mantle this lower symmetry phase may exist. In contrast, Li et al. (2006b) suggest—also from MD—that the tetragonal phase is stable throughout the lower mantle. However, experiments at both pressures and temperatures of the lowermost mantle have yet to be conducted, so the phase diagram of Ca-pv is uncertain. Li et al. (2006a), Adams and Oganov (2006) and Stixrude et al. (2007) report elastic constants for Ca-pv at CMB conditions. Cubic Ca-pv appears to be moderately anisotropic, showing maximum δV_S of ∼20 %, comparable to ppv and fpc, however the fact that it is a minor constituent of the lowermost mantle means it is often neglected as a possible contributor to seismic anisotropy.

The silica phases most likely present in D″ are in the orthorhombic $CaCl_2$ or α-PbO_2 (also called columbite) forms, with the transition occurring at about 110–120 GPa (2500–2600 km). The implications for the presence of mainly the α-PbO_2-type in D″ are not clear, as there are as yet no measurements of velocities or elastic constants for it at lowermost mantle temperatures and pressures. Karki et al. (1997a) do report constants at high pressure and 0 K from *ab initio* calculations (based on structure parameters reported in Karki et al. (1997b)). At least at 0 K, the α-PbO_2-type silica shows a maximum δV_S of ∼15 %, so appears unlikely to be a major candidate anisotropic phase in D″, given its low abundance. Future high-T work to elucidate the properties of free silica in the lowermost mantle will have important repercussions for models where subducted MORB at the CMB plays a large role in seismic anisotropy.

2.3.3 Lattice Preferred Orientation and Slip Systems in D″ Phases

In order to generate anisotropy, individual anisotropic crystals must be aligned over large lengthscales in a lattice- (or crystal-) preferred orientation (LPO, or CPO) (Fig. 2.16a). Assuming that the phase undergoes deformation which is accommodated by slip on a crystallographic plane (such as dislocation glide), the relative strengths of the slip systems active in the crystal determine how the mineral aligns. Furthermore, how an aggregate of individual crystals deforms depends on the phases present and their orientations.

At present, our understanding of slip systems and aggregate texture development for mono- and polymineralic assemblages of phases at CMB conditions is poor, mainly because it is currently impossible to recreate mantle temperatures, pressure

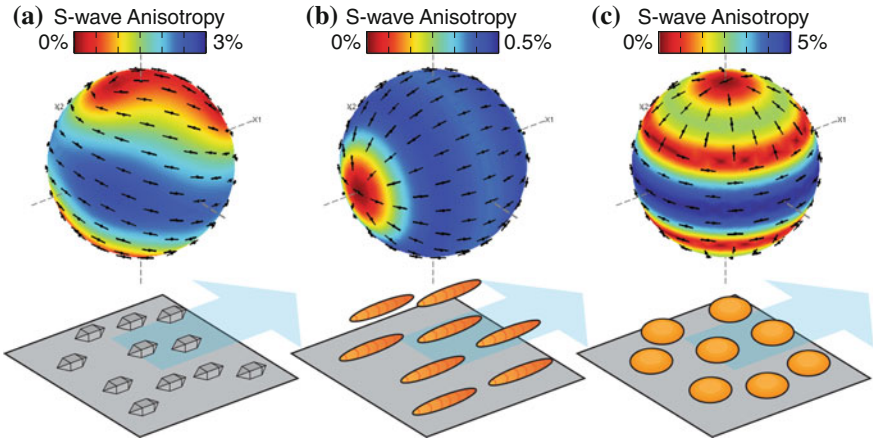

Fig. 2.16 Lattice preferred orientation (LPO) of crystals (**a**) and shape preferred orientation (SPO) of prolate (**b**) and oblate (**c**) slower isotropic inclusions in a faster anisotropic matrix (schematic). Spheres above are 3-D versions of the plots explained in Fig. 2.3. They show the amount of shear wave anisotropy δV_S by colour, and the fast shear wave orientation by *black ticks*. Note that the colour scales are different. *Blue arrows* show a direction of flow which may align the crystals or inclusions, and thus how this might be interpreted from measuring the anisotropy

(both very large) and strain rates (very low) on large polycrystalline samples in the laboratory. However, various experimental and theoretical methods have been used to examine the likely deformation mechanisms.

There are two main approaches to evaluating the LPO caused by deformation in mantle minerals. Firstly, one can investigate the phases at D″ conditions in the LHDAC, compressing the sample by increasing the confining pressure during the course of the experiment, leading to uniaxial deformation in the cell. Typically, radial X-ray diffraction data are taken and the intensity of the individual diffraction lines is taken to correspond to the number of crystals which are aligned in the orientation appropriate to cause the diffraction. The ellipticity of the diffraction rings is a measure of the differential stress within the sample. Thus a pole figure (orientation distribution function, ODF) can be calculated for the crystallographic directions and a dominant slip system inferred. There are a number of limitations to this technique, however—primarily, the sample size is very small (a few μm^3), hence the amount of shortening is limited, and the sample is rarely actually at D″ temperatures when observations are made: it is usually heated beforehand for some time, but is cooling when lattice parameters are measured.

Alternatively, one can look at structural analogues of lowermost mantle phases which are stable at conditions more easily achieved in the laboratory. Hence larger samples ($\sim$20 mm^3) can be compressed, and the texture created examined directly. $CaIrO_3$, $MgGeO_3$ and $MnGeO_3$ have been used in this way, for instance, to investigate the slip system in ppv as they share the same structure. So far, the Kawai and D-DIA (differential-DIA) apparatuses have been used to compress samples with a shear plane imposed at an angle to the compression direction. (For a review of terminology

and methods, see Durham et al. 2002.) The sample is typically sheared to a shear strain of $\gamma \sim \mathcal{O}(1)$, and the sample recovered and analysed with electron backscatter diffraction (EBSD) to determine the crystallographic orientation of potentially thousands of crystals. An ODF can be calculated, and slip systems inferred. Note that in such experiments, complex behaviour of polycrystalline material can be investigated, and several slip systems may operate. It is also notable that the presence of other phases as compared to a single-phase assemblage can change the deformation behaviour of an aggregate. This means that our long-term understanding of how material deforms in D″ must rely on calculations or experiments on likely lowermost mantle compositions.

Theoretical methods are also used to investigate deformation mechanisms, typically using the generalised stacking fault (GSF) within a Peierls-Nabarro dislocation model. Often, *ab initio* methods are used to find the GSF energy, feeding the Peierls-Nabarro model. Walker et al. (2010) summarise the main techniques used. Others, such as Oganov et al. (2005), use metadynamics to find new structures by perturbing the structure being studied, and allowing it to relax to another, effectively pushing the structure over an energy barrier to a new arrangement.

The purpose for this review of understanding single-crystal deformation mechanisms is that we require such knowledge in order to infer deformation from measurements of seismic anisotropy. With values for the relative strengths of slip systems, one can predict the aggregate ODF and subsequent anisotropy of a polycrystalline assemblage. The predicted slip systems may be used, for example, in a viscoplastic self-consistent model (Lebensohn and Tomé 1993; Wenk et al. 1991) and subjected to a known strain history, resulting in predictions which can be compared to observations.

Perovskite

For pv, theoretical calculations have been combined with experiment to determine the relative strengths of the dominant slip systems by Mainprice et al. (2008). Using a Peierls-Nabarro dislocation model, they infer that the [010](100) system is easiest at lowermost mantle conditions. This agrees qualitatively with experiments performed at lower pressures than present at the CMB (Cordier et al. 2004; Merkel et al. 2003), though high-temperature studies are still awaited. Even with 100 % alignment of the phase, the maximum δV_S is ∼2 %, which is significantly less than is the case for ppv or fpc. Hence it seems that, compared to fpc and ppv, pv is a poor candidate phase to explain the near-ubiquitous observation of D″ anisotropy.

Post-perovskite

Table 2.2 summarises the experimental studies to date on slip systems in ppv and its structural analogues. It is clear that little consensus exists regarding the dominant slip system, with slip on (100), (010), (001) and {110} all suggested by at least one

Table 2.2 Summary of inferred slip systems in $MgSiO_3$ post-perovskite and structural analogues from deformation experiments using the diamond-anvil cell (DAC), laser-heated diamond-anvil cell (LHDAC), Kawai-type and deformation-DIA (D-DIA) apparatuses

Study	Method	P (GPa)	T (K)	Differential stress (GPa)	Dominant slip system[a]	Remarks
(Mg, Fe)SiO_3						
Merkel et al. (2007)	LHDAC	145–157	1800	7–9	(100) or (110)	Mg#=0.9; opx starting material
Miyagi et al. (2010)	LHDAC	148–185	3500	5–10	[100](001) or [010](001)	Mg#=1.0; glass starting material
Mao et al. (2010)	LHDAC	140	2000	[b]	{100} or {110}	Mg#=0.6; opx starting material
$CaIrO_3$						
Yamazaki et al. (2006)	Kawai	1	1173		[100](010)	γ=0.4–1 [c]
Walte et al. (2007)	D-DIA	3	1000	[b]	[100](010)	γ=0.8–1
Niwa et al. (2007)	DAC	0–6	300	[b]	(010)	
Miyagi et al. (2008)	D-DIA	2–6	300–1300	−2–2	[100](010)	
Walte et al. (2009)	D-DIA	1-3	1300	[b]	[100]{010}	γ=0.5–1
$MgGeO_3$						
Merkel et al. (2006)	LHDAC	104–124	1600	3–8	(100) or (110)	Opx starting material
Kubo et al. (2008)	LHDAC	83–99	1600	0.1–1	(010)	Opx starting material
Okada et al. (2010)	LHDAC	78–110	300	1–3	(001)	4 runs: opx and pv starting material
$MnGeO_3$						
Hirose et al. (2010)	LHDAC	77–111	2000	2–10	(001)	Opx starting material

[a] Where no slip vector is given in the study, only the slip plane is shown
[b] Not stated
[c] Shear strain γ as stated in the study

study. However, there is agreement for the slip system in $CaIrO_3$. Recent DAC and large-volume deformation experiments seem to confirm (010) as the likely slip plane for relatively large strains, with perhaps [100] the slip direction. Most studies also detect a different texturing associated with the transformation from the pv to ppv structure—a so-called 'transformation texture'—consistent with slip on $\langle \bar{1}10 \rangle \{110\}$ (Walte et al. 2009; Okada et al. 2010; Hirose et al. 2010). However, whether $CaIrO_3$ is a 'good' analogue for ppv—in the sense that it deforms in the same way—is under debate (Walte et al. 2009; Hirose et al. 2010; Miyagi et al. 2010; Mao et al. 2010; Okada et al. 2010). Hence whilst the advantages of using relatively large, polycrystalline samples are obvious, care is needed in directly applying the results of analogues to the case of the lowermost mantle.

Earliest theoretical work suggested on the basis of structural arguments that slip on (010) should be easiest, as this is the plane in which the SiO_6 octahedra lie, and indeed this agrees with experiments on $CaIrO_3$. Carrez et al. (2007) suggest the system [100](010) on the basis of Peierls-Nabarro modelling. Metsue et al. (2009) also find the same, though point out that despite the similarity between the predicted slip systems in ppv and $CaIrO_3$, the starting single-crystal properties for the two phases are quite different, so drawing conclusions from such bases is difficult.

The observed 'transformation texture' of slip on {110} (e.g., Walte et al. 2009; Okada et al. 2010) adds complexity to our picture of the relation of deformation to anisotropy. If it is replicated in the pv–ppv transition, then it may be that descending mantle will acquire a certain texture for a time, which changes as strain increases. Hence future work to pin down whether such a process occurs in the Earth is important.

Ferropericlase

As the reader might have come to expect, great difficulties in experiments and theoretical calculations at extreme conditions mean there is disagreement between authors regarding the likely slip system in fpc. For NaCl-type cubic crystals, slip along $\langle 110 \rangle$ is expected to dominate, hence one might expect {110} to be the likely slip planes for fpc (Karato 1998). However, other slip planes may also be dominant, and high temperatures will affect the activation energies of the slip planes. *Ab initio* calculations for MgO and Peierls-Nabarro modelling (Carrez et al. 2009) suggests that the active slip system at low temperature is $\frac{1}{2}\langle 110 \rangle \{110\}$, though the $\frac{1}{2}\langle 110 \rangle \{100\}$ system becomes relatively easier with increasing pressure.

Experiments on the pure-Mg endmember at 47 GPa and ambient temperature by Merkel et al. (2002) in the LHDAC suggest slip on {110}. Contrasting results were found by Long et al. (2006), who used a large-volume press to deform a sample at 300 MPa and ~1400 K for a range of compositions ($0 \leqslant \text{Mg\#} \leqslant 1$). For pure MgO, [001] tends to align with the shear direction, whilst [110] aligns for FeO. Even for $\gamma \approx 4$, though, the development of LPO was fairly weak.

Yamazaki and Karato (2002) used compositions of Mg# = 0.25 and 1.0 at P = 300 MPa, $T \approx 1000$ K with a very similar experimental setup to that of Long et al. (2006). They find slip on {100} or {111} is likely.

Whilst knowledge of individual slip systems is important, in the long term we require experiments and calculations on polycrystalline, multi-phase assemblages of the kind we expect to exist at D″, as experience suggests monomineralic assemblages at vastly different conditions are not necessarily accurate proxies for the real thing. An improvement would be knowledge of the relative strengths of the several slip systems operating in the single crystal of any given phase. This would then allow one to calculate the development of texture under a known strain. An issue which seems very difficult to resolve experimentally is the vast difference in strain rates between studies and the Earth. It seems likely that strain rates in the deep mantle are $\dot{\varepsilon} \approx \mathcal{O}(10^{-16})$–$\mathcal{O}(10^{-14})$ s^{-1}, whilst at present we achieve $\dot{\varepsilon} \gtrsim 10^{-4}$ s^{-1}, so whether we can ever recreate such strains is a hard question to answer positively.

2.4 Shape-Preferred Orientation

Thus far we have only considered the LPO of mineral phases as a potential cause of lower mantle anisotropy. An entirely separate cause of anisotropy is the sub-wavelength layering or ordering of material with contrasting elastic properties (Fig. 2.16b, c). The anisotropy may be due to the periodic layering of different materials or the preferred alignment of inclusions like melt pockets.

If SPO is the cause of lowermost mantle anisotropy, it may still be a result of deformation processes. To infer the link between deformation and observed anisotropy we must appeal to effective medium theories that predict the anisotropy. A number of approaches exist, but they can be divided into those that assume constant strain (e.g., Hudson 1980a) or those that assume constant stress (e.g., Tandon and Weng 1984; Sayers 1992). A further complication involves the degree of interconnectivity between fluid inclusions, which leads to frequency dependent anisotropy (for a review see Hall and Kendall 2001). Assuming an effective medium theory, an aggregate elastic tensor can be constructed and then used to predict the seismic observables along a given ray path. Holtzmann and Kendall (2010) describe such an approach for linking a number of anisotropy mechanisms to strain partitioning at plate boundaries.

Spheroidal inclusions lead to a hexagonal symmetry or TTI (see examples in Fig. 2.16b, c). A more complex orthorhombic medium results if the inclusions are scalene ellipsoids (three axes of different lengths). However, on the basis of natural samples, which tend to contain either elongate (prolate spheroidal) or flat (oblate spheroidal) inclusions, it seems that in most settings one axis will be significantly different from the other two. An example of each are L- and S-tectonites in subduction settings (Tikoff and Fossen 1999).

With respect to the lower mantle, Kendall and Silver (1996, 1998), for example, model the effects of spheroidal inclusions of contrasting velocity. They show that small volume-fractions of oblate or disk-shaped inclusions of melt are highly efficient

in generating seismic anisotropy. In order for periodic layering or aligned inclusions to produce an effective anisotropy, and not simply heterogeneity, the wavelength of the layering must be less than the dominant seismic wavelength. Indeed a way of discriminating between LPO and SPO anisotropy may be through observations of frequency dependent effects. For example, small-scale heterogeneity may scatter high-frequency seismic energy, but such a medium may be effectively anisotropic to long wavelength energy (Rümpker et al. 1999).

Also compatible with observations might be the complementary presence of both SPO and LPO. If, for instance, strain partitions into one weaker phase in a multi-phase mixture (e.g., a solid and liquid, or two solid phases with contrasting strengths; e.g., Holtzmann et al. 2003a), then we might expect shear bands to form, as is frequently observed in surface geology. If the bands are of the appropriate length scale, they might have an SPO contribution to seismic anisotropy, whilst the highly deforming material in the bands—or even outside, for the case of melt-rich bands—may still deform to produce LPO. Hence the division between LPO and SPO is not necessarily clear whilst our knowledge of the lowermost mantle is at this limited stage.

A major unknown in this sort of analysis is that the plausibility of melt in the lowermost mantle is still speculative. Furthermore, much work is needed to better establish the material properties of such melt, be they primordial in origin, the remains of subducted palaeo-oceanic crust (basalt) or material derived from the outer core.

2.5 Geodynamics

While knowledge of the deformation mechanism of lowermost mantle materials is limited (see Sect. 2.3.3), one approach to assessing how likely they are to be realistic is to consider the first-order flow exptected just above the CMB. Topography on the CMB is limited to a few kilometres at most (e.g., Tanaka 2010), and the outer core is liquid with a free-slip surface above, so it seems highly likely that flow just above the CMB is mainly horizontal. If we assume this, we might be able to mark as unlikely some of the proposed deformation mechanisms for ppv, and then use the remainder to suggest slightly more nuanced flow situations in D″. We explore this further in Sect. 2.6.

Global models of mantle flow have matured rapidly with increasing computer power and new techniques over recent years, and inferring the first-order flow field at the CMB by including geophysical observables such as recent plate motions and likely phase stabilities and rheologies is now possible. Alongside this, models of mantle flow have developed which are derived from seismic tomography, with the constraints of mineral physics, geoid and plate motion data.

Where there is good evidence from seismic wave speed tomography (e.g., Ritsema et al. 1999; Montelli et al. 2004) of subducting slabs reaching the lowermost mantle, such as the Farallon slab beneath North America, we can make slightly more detailed inferences regarding the likely large-scale flow field. A simple approach used frequently (e.g., Wookey and Kendall 2007; Yamazaki and Karato 2007; Miyagi et al.

2010) is to assume horizontal flow occurs at the CMB, and hence slip systems which produce fast orientations within the slip plane are the likeliest to match the majority of observations which suggest $V_{SH} > V_{SV}$ in D″. As Sect. 2.2.6 shows, however, requiring horizontal fast directions in all directions does not match with observations, so such assumptions must be revisited.

One constraint on the kind of deformation experienced in such a situation is to construct models of mantle flow with an imposed subduction of a thermally negatively buoyant slab. McNamara et al. (2003), for example, use a general 2D cylindrical model with diffusion and dislocation creep to search the parameter space of variables such as slab thickness and strength, and relative activation energies of the two creep regimes. They find that dislocation creep dominates around the slab, and at the base of the mantle beneath the slab, whilst the rest of the mantle is likely deforming in diffusion creep, hence not producing significant LPO. They also claim that LPO in such a model requires $\gamma \gtrsim 4$ to develop. With this method, where the whole Earth's mantle is modelled, but without imposing the constraints of observed plate motions, the results can be qualitatively, and to some extent quantitatively compared to deformation mechanisms in lowermost mantle mineral phases.

In order to construct models which are useful in understanding how the mantle flows in D″, a huge number of parameters are necessary, only some of which are known well. One-dimensional radial viscosity profiles (e.g., Mitrovica and Forte 2004), for instance, place a strong control on the depth and extent of subduction, which would then affect the flow field above the CMB. Although these are constrained from present-day observables (mainly isostatic glacial rebound of the surface for shallow depths, and mineral physics data much deeper), obviously there is likely to be lateral variations in viscosity as well—such as that introduced by a cold slab—which can only be modelled with accurate understanding of the effect on viscosity of temperature, composition, mineralogy, and so forth. Other large unknowns are the temperature at the CMB and the effect of composition and temperature on the density of mantle phases.

In some studies (e.g., Wenk et al. 2006; Merkel et al. 2006, 2007), workers take 'general' models of flow of this kind and test for the type of anisotropy produced by a given deformation mechanism when traced through the flow field. Assuming a certain flow field as suggested by the convection model, they trace particles through the field and apply a viscoplastic self-consistent (VPSC) model (e.g., Lebensohn and Tomé 1993; Wenk et al. 1991) to calculate the texture developed for a polycrystalline aggregate using a set of slip system activities relevant to the phases being tested. The resulting aggregate elastic tensor is constructed from the single crystal constants and the orientation distribution function (ODF) of the phases in the aggregate, and can then be compared with seismic observations from similar settings—that is, beneath subducting slabs.

Another approach to modelling flow in the mantle is to seek a 'true' picture of what is happening at present. Using seismic travel time picks, plate motion reconstructions (Lithgow-Bertelloni and Richards 1998), gravity measurements, dynamic topography and other constraints, various authors (e.g., Tackley 2000; Trampert et al. 2004; Simmons et al. 2009) have attempted to invert for the present-day or recent flow

field in the mantle. Much of this work depends on the particular relationship between seismic wave speed and density in order to asses whether only thermal, or thermal and compositional effects are being seen by the seismic velocities. With knowledge of the density anomalies which are thermal and compositional (or mineralogical), one can produce a model of mantle flow. This seems a promising approach to take, if we wish to assess whether we can use measurements of anisotropy to determine flow in the mantle. For instance, if the flow is fairly constant over time and shear strains are fairly large ($\gtrsim$1, perhaps) then current mineral physics understanding suggests we could observe LPO, providing the strain rate is high enough and dislocation creep is occurring. If, on the other hand, strain rates predicted by such inversions are much lower, then perhaps SPO is the likely mechanism.

A further step to take with such an approach is to directly incorporate experimentally or theoretically derived slip system activities for a mono- or polymineralic assemblage of grains and perform VPSC calculations as above. The texture will be more complicated, and likely weaker, but in theory more 'realistic'. This does depend hugely on the flow model being used, though tests on producing a synthetic seismic model from a global flow model by Bull et al. (2010) suggest that the input and recovered strain fields are usually $<20°$ apart. This is encouraging from the perspective of hoping to be able to one day map deformation from anisotropy, but adequate seismic coverage will long be a problem, as discussed in Sect. 2.6.1.

2.6 Linking Observations to Physical Processes

If the measurement of seismic anisotropy is to be useful in studying the dynamics of the lowermost mantle, then we need a close understanding of the rheology of mantle materials at CMB conditions. Section 2.3 discussed that we are still some way from fully understanding how to 'measure' dynamics in D″ using seismic anisotropy, but we are now at the stage where our inferences are informed by a great deal of work on the properties of lowermost mantle minerals. In the first instance, seismic anisotropy can be used to evaluate a number of different mechanisms which might cause it.

2.6.1 Inferring SPO and TTI

A simple mechanism to produce lower mantle anisotropy which cannot at present be ruled out is SPO. This has been the preferred interpretation in a number of studies (e.g., Kendall and Silver 1998; Lay et al. 1998; Karato 1998), which model the expected bulk anisotropy for isotropic inclusions of material with a contrasting V_S in an isotropic medium. Kendall and Silver (1998), for instance, use the effective medium theory of Tandon and Weng (1984) to predict the shear wave splitting caused by horizontal rays travelling through a medium with oriented spheroidal inclusions. Whilst high-velocity inclusions are unlikely to be a mechanism which can match the

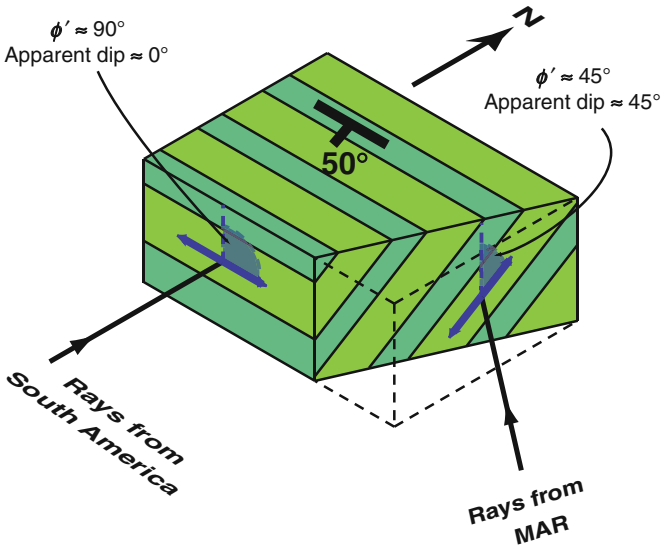

Fig. 2.17 TTI plane of isotropy in region 'E' of Nowacki et al. (2010), shown by schematic layering of the material. Rays from South America travelling north show $\phi' \approx 90°$, whilst those from the Mid-Atlantic Ridge (MAR) travelling northwest exhibit $\phi' = 45°$. Assuming hexagonal symmetry where $\delta \approx \varepsilon$, the fast orientation is in the plane of isotropy in each case. Whilst TTI is a possible explanation, it is only one type of anisotropy which can produce the observations with two azimuths of waves

observations (as the inclusions would need to have $V_{S_{inc}} \gtrsim 13\,\mathrm{km\,s^{-1}}$), melt-filled inclusions ($V_{S_{inc}} = 0$) can produce $\delta V_S = 2\,\%$ with a melt fraction of just 0.01 % for oblate spheroidal inclusions. Moore et al. (2004) show a D″ with horizontal sub-wavelength layering of heterogeneous material can produce synthetics compatible with observations in certain regions. Both studies suggest that SPO—especially of melt—is an efficient way of producing anisotropy without much reducing the bulk average V_S (Kendall and Silver 1996).

If we assume that SPO is the cause for an observed anisotropy, then this usually implies that the style of anisotropy is TTI (see Sect. 2.4). Because of the high symmetry of TTI, two near-perpendicular azimuths of shear waves are sufficient to characterise the orientation of the symmetry axis (or plane of isotropy), as five independent elastic constants describe such a system and the local $\langle V_S \rangle$ can be assumed.

One simplistic way to infer the orientation of the TTI fabric is to assume a case where Thomsen's (1986) parameters $\delta \approx \varepsilon$, hence the fast orientation of a wave split by such a medium is always in the plane of isotropy for waves not perpendicular to the plane. Therefore a simple geometrical calculation to find the common plane of the fast orientations in the ray frame ϕ' can be used. We use this to calculate the TTI planes of isotropy beneath the Caribbean and western USA in Chap. 4 (Fig. 4.16). Figure 2.17 illustrates the nominally simple geometry for region 'E' in this study.

An alternative method used by Wookey and Kendall (2008) to estimate the orientation of the TTI plane of isotropy for two orthogonal ray paths beneath Siberia can be summarised as: (1) take a set of elastic constants C_{ij} for a TI system, with vertical V_S and V_P defined by a global 1–D velocity model (Kennett et al. 1995); (2) rotate these constants about all three cartesian axes and compute δV_S (and hence δt) and ϕ' at each point; (3) output the orientations which produce $(\phi', \delta t)$ which are compatible with the observations. This inversion has the advantage that it can be simply extended for any set of elastic constants, and lies between analytic solutions from shear wave splitting measurements and inversions for the full elastic tensor, which would likely be poorly constrained.

2.6.2 Implications of SPO and TTI

If our assumption that the lowermost mantle shows a variable TTI type of anisotropy is correct—and it is worth noting that no studies as yet are incompatible with this symmetry—then what does this imply for the dynamics within and above D″? As discussed in the previous section, various authors have shown that SPO of melt pockets (or other low V_S inclusions) at the CMB could cause this, and this then begs the question as to where these melts come from. A possibility mooted by Knittle and Jeanloz (1987) was that reaction between core and mantle materials would lead to inclusions of Fe-rich products (e.g., FeO, FeSi) in D″ (Kendall and Silver 1998). However, the bulk reduction in V_{SH} from this does not match observations, hence is an unlikely scenario. As mentioned in Sect. 2.4, Stixrude et al. (2009), for example, suggest that silicate melts might be present in the lowermost mantle at temperatures as low as 4000 K. Just 0.01 % melt could be compatible with observations given the bulk sound velocity is predicted to be around 10.9 km s^{-1}.

If such models are accurate, then we require knowledge of how the inclusions—partially or wholly molten, or simply of contrasting velocity—align in response to flow, to make geodynamical inferences. To first order, weaker inclusions in a stronger matrix align parallel to the strain ellipse's long axis (i.e., the shear plane) when the strain is high ($\gamma > 1$). Hence for the cases where we have two azimuths (in the Caribbean and Siberia), we would predict flow dipping between 26–55° roughly to the south in D″. These steep angles seem somewhat unlikely for high strains, given that flow right at the CMB must be horizontal, but cannot necessarily be precluded.

Contrary to this first-order approximation, weak inclusions apparently rotate when sheared so that they are no longer parallel to the finite strain ellipse, as noted by Karato (1998). Numerous experiments—chiefly on olivine-MORB samples—indicate that shear bands of melt align antithetic to the shear plane at an angle of ∼20–40° (Kohlstedt and Zimmerman 1996; Holtzman et al. 2003a, b). Taking the example of the region studied by Wookey and Kendall (2008), this melt orientation predicts horizontal shear to the south in Siberia. Figure 2.18 shows this situation with the shear wave anisotropy predicted by sensible lowermost mantle parameters, where melt inclusions dip 25° southward, but due to northward flow. In the Caribbean,

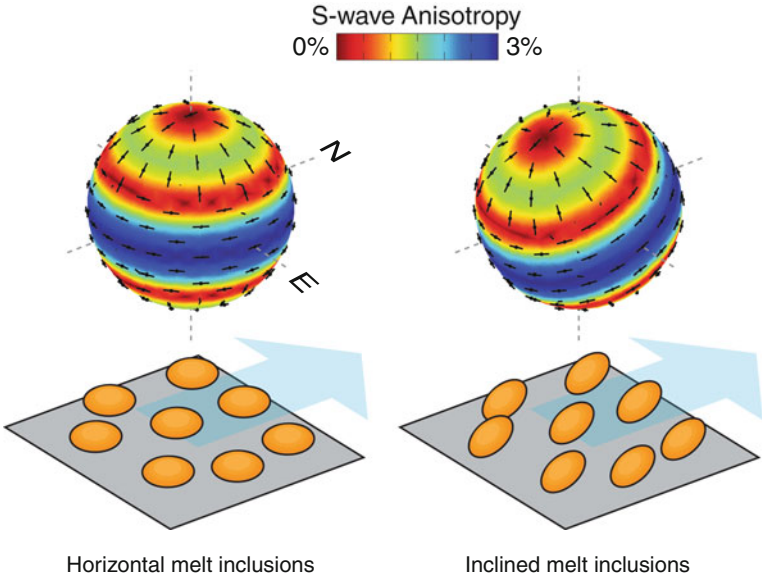

Fig. 2.18 Shear wave anisotropy for horizontal (*left*) and inclined (*right*) melt inclusions in D″. The *cartoons* below show the alignment of oblate spheroids which respond to the motion of the mantle differently. In both cases, the sense of shear is top to the north (approximately *right* here), shown by the *arrow*. On the *left*, the inclusions are aligned parallel to the horizontal flow and produce VTI. On the *right*, the melt inclusions dip at 25° towards the sense of shear, opposite the sense of flow. For most azimuths of horizontally-propagating shear waves, this produces splitting with the fast orientation parallel to the alignment of the oblate inclusions. As discussed in the text, this is compatible with observations beneath Siberia and the Caribbean. The elastic constants are calculated using effective medium theory (Tandon and Weng 1984) for an arbitrary set of lowermost mantle-like properties (matrix: $V_P = 14\,\mathrm{km\,s^{-1}}$, $V_S = 7.3\,\mathrm{km\,s^{-1}}$, $\rho = 5500\,\mathrm{kg\,m^{-3}}$; inclusions: $V_P = 7\,\mathrm{km\ s^{-1}}$, $V_S = 0\,\mathrm{km\,s^{-1}}$, $\rho = 5500\,\mathrm{kg\,m^{-3}}$, aspect ratio = 0.01, volume fraction = 0.005)

geodynamical calculations of the flow beneath subducting slabs would generally agree rather with east–west flow for a north–south-striking plate (McNamara et al. 2003), but at least this model seems physically possible.

The known mineral phases present at the CMB do not show hexagonal symmetry, however an alternative explanation for TTI would be the alignment of one crystallographic axis of some anisotropic mineral phase, with the other axes random. As an artificial example, Fig. 2.19 shows the case where an aggregate of ppv shows alignment of c-axes, but the a- and b-axes are otherwise randomly oriented. This might correspond to slip on the (001) plane along both the [100] and [010] directions. This leads to TI with the symmetry axis parallel to the c-axis, where the fast shear wave is within the TI plane.

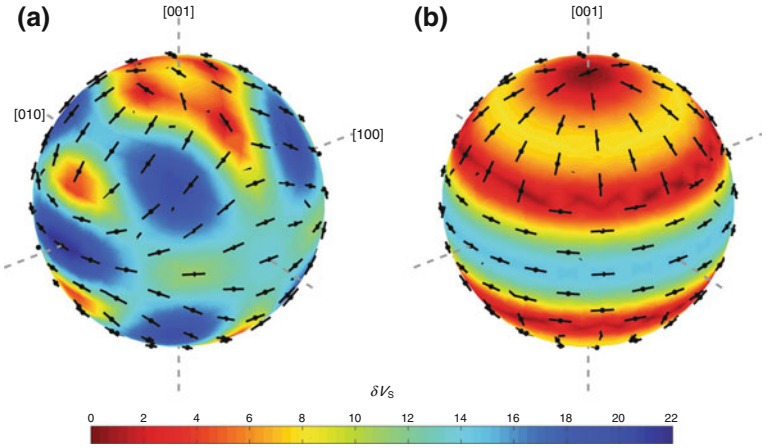

Fig. 2.19 Variation of shear wave splitting with direction for $MgSiO_3$ post-perovskite (elastic constants of Stackhouse et al. 2005b at 3000 K). Colour indicates the strength of shear wave anisotropy in a given direction (δV_S) as per the scale bar. The *black bars* show the orientation of the fast shear wave. The crystallographic directions are indicated. **a** Shear wave splitting for unaltered single-crystal constants. There is strong ($\delta V_S = 20\,\%$) anisotropy for rays along [100] and $\langle 111 \rangle$. **b** Anisotropy for a planar average of the constants when rotated around [001]. Strong ($\delta V_S = 15\,\%$) splitting occurs within the plane normal to [001], with fast directions also in the plane. However, this corresponds to an aggregate of perfect alignment of [001] directions of pure ppv, which does not occur in D″

2.6.3 Inferring Orthorhombic and Higher Symmetries

Whilst at present TTI cannot be ruled out as causative of the observed seismic anisotropy in D″, a more general orthorhombic symmetry—such as that caused by alignment of orthorhombic crystals—is a more likely mechanism. Equally, cubic and lower symmetries can also produce the observed patterns of anisotropy. However, it is unlikely that distinguishing such a highly symmetric type of anisotropy will be possible with the current earthquake and seismometer geometries for some time, so assuming that orthorhombic anisotropy is the lowest symmetry likely to exist is, for now, a necessary step.

So far, no studies have been able to uniquely infer the orientation of an orthorhombic symmetry, because only measurements of D″ anisotropy along two directions have been made. However, Wookey and Kendall (2008) use two azimuths and the technique described in Sect. 2.6.1 to test the orientations of different candidate orthorhombic systems beneath Siberia. In the case of using two azimuths of measurements, one normally finds that two sets of planes are compatible. Figure 2.20 shows an example of fitting possible orientations of different (orthorhombic) elastic constants to measurements made beneath Siberia (Wookey and Kendall 2008). They use several sets of constants obtained by deformation experiments for both the perovskite and post-perovskite structures. Here we show as examples two cases: first,

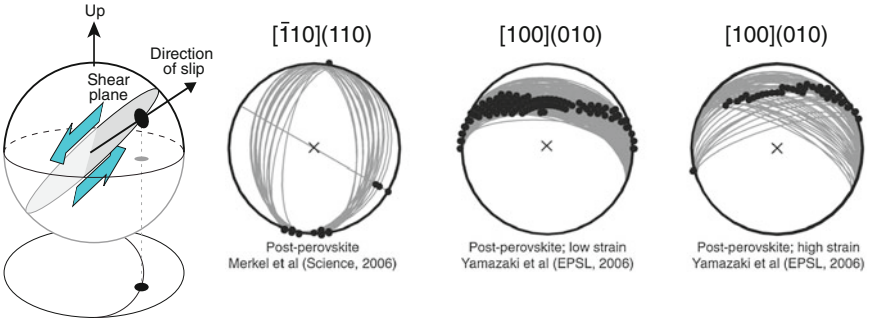

Fig. 2.20 Upper hemisphere diagrams showing shear planes and slip directions which are compatible with the measurements of sub- Siberia D″ shear wave splitting of Wookey and Kendall (2008). The schematic diagram on the *left* shows how to interpret the diagrams on the *right*: they show the upper hemisphere projection of the slip plane (*grey lines*) and slip direction (*black dots*), hence the centre of the plots corresponds to the vertical direction; in this case the *top* of the diagrams is north. The elastic constants tested are those of Merkel et al. (2007) and Yamazaki et al. (2006) (two cases for low and high strain), who deform ppv to produce aggregates consistent with the dominant slip system in the crystal of [$\bar{1}$10](110) and [100](010) respectively. For this region, the [$\bar{1}$10](110) slip system predicts shear dipping east or west at about 45° with slip north–south, whilst the [100](010) system suggests shear dipping south a similar amount, with poor constraint on the slip direction

the constants from Yamazaki et al. (2006), who deform $CaIrO_3$ (same structure as $MgSiO_3$-post-perovskite), and find that the [100](010) slip system is dominant. Secondly, we also show a case from Merkel et al. (2007), who deform post-perovskite and find that the slip system [$\bar{1}$10](110) may be dominant. The elastic constants are referenced to the shear plane and slip direction imposed upon the deformation, so we can directly infer in which direction a material which behaves in this way is being sheared.

2.6.4 Inferring Deformation in D″

We measure D″ anisotropy in the hope that it can provide information about the manner in which it is deforming, and hence how the mantle moves at depths. In order to estimate flow or strain from anisotropy, we must integrate our understanding of the cause of anisotropy, the orientation of the assumed anisotropy type, our knowledge of the rheology of the medium, and the response of the shear direction to the potentially changing flow field. Figure 2.21 illustrates the many steps involved in getting from observations to predictions of deformation, and the many assumptions which are made along the way.

At present, the response of D″ materials to deformation is not well known, hence early attempts at inferring flow from measurements of seismic anisotropy were necessarily general. Beneath the circum-Pacific subduction zones where flow is assumed to

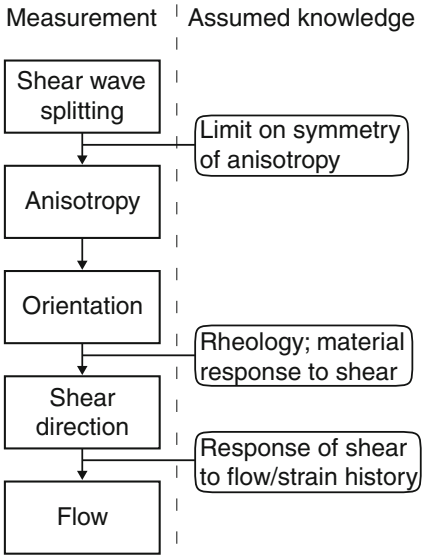

Fig. 2.21 Flow chart showing the progression of calculations and assumptions required to predict flow from measurements of shear wave splitting

be horizontal at the CMB, the global ξ models of Panning and Romanowicz (2004, 2006) show $V_{SH} > V_{SV}$, and thus it has been interpreted that likely mechanisms in response to shear in D″ mineral should produce fast orientations parallel to the shear plane. This then may lead to the inference that beneath the central Pacific, the change of $\xi > 1$ to $\xi < 1$ corresponds to vertical flow (e.g., Kawai and Geller 2010) or some sort of shearing in different horizontal directions (e.g., Pulliam and Sen 1998). Clearly, whilst there is short scale variability in the signal anyway, determining the first-order flow field from an educated guess is an understandable first step which we should attempt to improve upon.

In fact, this point highlights one of the current shortcomings in our addressing of the problem of using seismic anisotropy to map deformation. At present, we are limited to using 'best guess' estimates of the flow field in certain areas at the CMB (specifically, where the ancient Farallon slab is presumed to be sinking to the CMB beneath North and Central America, and to some extent other circum-Pacific subduction zones) to argue for and against different mechanisms for producing seismic anisotropy. For instance, Yamazaki and Karato (2007) prefer an explanation for D″ anisotropy of the LPO of a mixture of (Mg,Fe)O and $MgSiO_3$-post-perovskite because horizontal shear would give a horizontally-polarised fast shear wave for this case, which is the sort of deformation postulated beneath deep slabs. They then argue that SPO of melt inclusions oriented vertically is the likeliest case for the central Pacific, because flow there is probably vertical and in higher-temperature material. If the CMB is considered an impenetrable free slip surface, then why should flow not also be mainly vertical in the very lowermost mantle beneath a downwelling as

well as an upwelling? Whilst these first-order explanations are sensible, they are only an initial idea about flow, hence using this to constrain LPO and infer the presence of melt makes a large stride in assumptions which we must eventually address with direct observations of lowermost mantle rheology.

Nonetheless, many authors have inferred different flow regimes at the CMB based on seismic anisotropy. Early work (e.g., Vinnik et al. 1995; Lay and Young 1991; Ritsema et al. 1998) attributed anisotropy to stratification or LPO on the basis of the expected flow field near the CMB. Later, Kendall and Silver (1996), for instance, identify slab material which is laid down in piles parallel to the CMB as a cause of SPO. Recently, dual-azimuth splitting measurements were used in combination with global V_S tomography to infer that north–south flow beneath Siberia is the likely cause of anisotropy due to LPO of ppv (Wookey and Kendall 2008).

Future advances in incorporating all our current understanding of the behaviour of the constituents of the lowermost mantle into linking observations and dynamics will become incrementally better. These early attempts at measuring the flow of the deepest mantle should be surpassed as we use new information which becomes available from increasingly advanced experimental and numerical techniques for studying seismic anisotropy, flow, geodynamics and mineral physics.

2.7 Conclusions and Future Directions

In this review, we have presented the current state of studies which aim to use seismic anisotropy to discover the flow in the deepest mantle, and the many other fields which feed into this. It seems that we are moving from an early phase of D″ study into a more mature field, where the number of observations is now becoming limited by the location of seismic stations. As we look to the future, projects to increase global coverage of seismometers will benefit all studies of the Earth's interior, but especially that of the lowermost mantle. With this increased coverage, the prospect of using more advanced techniques to take advantage is an exciting one which may yet yield even harder questions than we currently try to answer.

One such technique that must be further explored with new datasets is the full inversion for the elastic tensor using the full seismic waveform. Recent advances towards this necessarily assume a simple anisotropy, but this can be relaxed as data coverage improves. However, as for global inversions for simple anisotropy, upper mantle and crustal corrections will be a problem. At the same time, existing global datasets—as used for global tomography, for example—might be exploited to move from regional shear wave splitting studies to global ones. This will require either a new, robust way of analysing shear wave splitting, which is still the most unequivocal of observations of anisotropy, or the further automation and quality control of standard techniques. Shear wave splitting 'tomography' is another technique which will likely prove important in the future.

Whilst seismological observations will be our primary test of models of D″ flow and anisotropy for some time, advances must be made in mineral physics and

geodynamics if we are to improve. Studies of deformation in likely lowermost mantle mineral assemblages will hopefully go some way in the future to reducing the ambiguity regarding how to translate anisotropy to flow, and global mantle flow models may be able to become predictors of anisotropy with such knowledge.

References

Adams, D., & Oganov, A. (2006). Ab initio molecular dynamics study of $CaSiO_3$ perovskite at *P-T* conditions of Earth's lower mantle. *Physical Review B*, *73*(18), 184106. doi:10.1103/PhysRevB.73.184106.

Ammann, M. W., Brodholt, J. P., Wookey, J., & Dobson, D. P. (2010). First-principles constraints on diffusion in lower-mantle minerals and a weak D″ layer. *Nature*, *465*(7297), 462–465. doi:10.1038/nature09052.

Andrault, D., Muñoz, M., Bolfan-Casanova, N., Guignot, N., Perrillat, J.-P., Aquilanti, G., et al. (2010). Experimental evidence for perovskite and post-perovskite coexistence throughout the whole D″ region. *Earth and Planetary Science Letters*, *293*(1–2), 90–96. doi:10.1016/j.epsl.2010.02.026.

Becker, T. W., & Boschi, L. (2002). A comparison of tomographic and geodynamic mantle models. *Geochemistry, Geophysics, Geosystems*, *3*, 1003. doi:10.1029/2001GC000168.

Bull, A. L., McNamara, A. K., Becker, T. W., & Ritsema, J. (2010). Global scale models of the mantle flow field predicted by synthetic tomography models. *Physics of the Earth and Planetary Interiors*, *182*(3–4), 129–138. doi:10.1016/j.pepi.2010.03.004.

Bullen, K. (1940). The problem of the Earth's density variation. *Bulletin of the Seismological Society of America*, *30*(3), 235–250.

Bullen, K. (1949). Compressibility-pressure hypothesis and the Earth's interior. *Monthly Notices of the Royal Astronomical Society. Geophysical Supplement*, *5*(9), 335–368. doi:10.1111/j.1365-246X.1949.tb02952.x.

Carrez, P., Ferré, D., & Cordier, P. (2007). Implications for plastic flow in the deep mantle from modelling dislocations in $MgSiO_3$ minerals. *Nature*, *446*(7131), 68–70. doi:10.1038/nature05593.

Carrez, P., Ferré, D., & Cordier, P. (2009). Peierls-Nabarro modelling of dislocations in MgO from ambient pressure to 100 GPa. *Modelling and Simulation in Materials Science*, *17*(3), 035010. doi:10.1088/0965-0393/17/3/035010.

Catalli, K., Shim, S.-H., & Prakapenka, V. B. (2009). Thickness and Clapeyron slope of the post-perovskite boundary. *Nature*, *462*(7274), 782–785. doi:10.1038/nature08598.

Chevrot, S. (2000). Multichannel analysis of shear wave splitting. *Journal of Geophysical Research, [Solid Earth]*, *105*(B9), 21579–21590.

Cordier, P., Ungar, T., Zsoldos, L., & Tichy, G. (2004). Dislocation creep in $MgSiO_3$ perovskite at conditions of the Earth's uppermost lower mantle. *Nature*, *428*(6985), 837–840. doi:10.1038/nature02472.

Ding, X., & Helmberger, D. V. (1997). Modelling D″ structure beneath Central America with broadband seismic data. *Physics of the Earth and Planetary Interiors*, *101*(3–4), 245–270. doi:10.1016/S0031-9201(97)00001-0.

Durham, W., Weidner, D., Karato, S., & Wang, Y. (2002). New developments in deformation experiments at high pressure. *Reviews in Mineralogy and Geochemistry*, *51*, 21–49.

Dziewoński, A., & Anderson, D. (1981). Preliminary reference Earth model. *Physics of the Earth and Planetary Interiors*, *25*(4), 297–356. doi:10.1016/0031-9201(81)90046-7.

Ford, S., Garnero, E. J., & McNamara, A. K. (2006). A strong lateral shear velocity gradient and anisotropy heterogeneity in the lowermost mantle beneath the southern Pacific. *Journal of Geophysical Research, [Solid Earth]*, *111*(B3), B03306. doi:10.1029/2004JB003574.

Fouch, M. J., Fischer, K. M., & Wysession, M. (2001). Lowermost mantle anisotropy beneath the Pacific: Imaging the source of the Hawaiian plume. *Earth and Planetary Science Letters*, *190*(3–4), 167–180. doi:10.1016/S0012-821X(01)00380-6.

Fukao, Y. (1984). Evidence from core-reflected shear-waves for anisotropy in the Earth's mantle. *Nature*, *309*(5970), 695–698. doi:10.1038/309695a0.

Garnero, E. J. & Lay, T. (1997). Lateral variations in lowermost mantle shear wave anisotropy beneath the north Pacific and Alaska. *Journal of Geophysical Research, [Solid Earth]*, *102*(B4), 8121–8135. doi:10.1029/96JB03830.

Garnero, E. J., & Lay, T. (2003). D″ shear velocity heterogeneity, anisotropy and discontinuity structure beneath the Caribbean and Central America. *Physics of the Earth and Planetary Interiors*, *140*(1–3), 219–242. doi:10.1016/j.pepi.2003.07.014.

Garnero, E. J., Revenaugh, J., Williams, Q., Lay, T., & Kellogg, L. (1998). Ultralow velocity zone at the core-mantle boundary. In M. Gurnis, M. E. Wysession, E. Knittle, & B. A. Buffett (Eds.), *The Core-Mantle Boundary Region, Geodynamics Series* (pp. 319–334). Washington, D.C., USA: American Geophysical Union.

Garnero, E. J., Maupin, V., Lay, T., & Fouch, M. J. (2004a). Variable azimuthal anisotropy in Earth's lowermost mantle. *Science*, *306*(5694), 259–261. doi:10.1126/science.1103411.

Garnero, E. J., Moore, M., Lay, T., & Fouch, M. J. (2004b). Isotropy or weak vertical transverse isotropy in D″ beneath the Atlantic Ocean. *Journal of Geophysical Research, [Solid Earth]*, *109*(B8), B08308. doi:10.1029/2004JB003004.

Guignot, N., Andrault, D., Morard, G., Bolfan-Casanova, N., & Mezouar, M. (2007). Thermoelastic properties of post-perovskite phase $MgSiO_3$ determined experimentally at core-mantle boundary *P-T* conditions. *Earth and Planetary Science Letters*, *256*(1–2), 162–168. doi:10.1016/j.epsl.2007.01.025.

Hall, S. & Kendall, J.-M. (2001). Constraining the interpretation of AVOA for fracture characterisation. In L. Ikelle & A. Gangi (Eds.), *Anisotropy 2000: Fractures, Converted Waves, and Case Studies. Proceedings of 9th International Workshop on Seismic Anisotropy (9IWSA)* (vol. 6 of Open File Publications, pp. 107–144). Tulsa, USA: Society of Exploration Geophysicists.

Hall, S. A., Kendall, J. M., & der Baan, M. V. (2004). Some comments on the effects of lower-mantle anisotropy on SKS and SKKS phases. *Physics of the Earth and Planetary Interiors*, *146*(3–4), 469–481. doi:10.1016/j.pepi.2004.05.002.

Hedlin, M., Shearer, P. M., & Earle, P. (1997). Seismic evidence for small-scale heterogeneity throughout the Earth's mantle. *Nature*, *387*(6629), 145–150. doi:10.1038/387145a0.

Hernlund, J. W. (2010). On the interaction of the geotherm with a post-perovskite phase transition in the deep mantle. *Physics of the Earth and Planetary Interiors*, *180*(3–4), 222–234. doi:10.1016/j.pepi.2010.02.001.

Hernlund, J. W., Thomas, C., & Tackley, P. (2005). A doubling of the post-perovskite phase boundary and structure of the Earth's lowermost mantle. *Nature*, *434*(7035), 882–886. doi:10.1038/nature03472.

Hirose, K. (2006). Postperovskite phase transition and its geophysical implications. *Reviews of Geophysics*, *44*(3), RG3001. doi:10.1029/2005RG000186.

Hirose, K. (2007). Discovery of post-perovskite phase transition and the nature of D″ layer. In K. Hirose, J. Brodholt, T. Lay & D. A. Yuen (Eds.), *Post-Perovksite: The Last Mantle Phase Transition, Geophysical Monograph* (pp. 19–35). Washington, D.C., USA: American Geophysical Union.

Hirose, K., Fei, Y., Ma, Y., & Mao, H. (1999). The fate of subducted basaltic crust in the Earth's lower mantle. *Nature*, *397*(6714), 53–56. doi:10.1038/16225.

Hirose, K., Takafuji, N., Sata, N., & Ohishi, Y. (2005). Phase transition and density of subducted MORB crust in the lower mantle. *Earth and Planetary Science Letters*, *237*(1–2), 239–251. doi:10.1016/j.epsl.2005.06.035.

Hirose, K., Sinmyo, R., Sata, N., & Ohishi, Y. (2006). Determination of post-perovskite phase transition boundary in $MgSiO_3$ using Au and MgO pressure standards. *Geophysical Research Letters*, *33*(1), L01310. doi:10.1029/2005GL024468.

Hirose, K., Nagaya, Y., Merkel, S., & Ohishi, Y. (2010). Deformation of $MnGeO_3$ post-perovskite at lower mantle pressure and temperature. *Geophysical Research Letters*, *37*(L20302), 1–5. doi:10.1029/2010GL044977.

Holtzmann, B. K. & Kendall, J. M. (2010). Organized melt, seismic anisotropy, and plate boundary lubrication. *Geochemistry, Geophysics, Geosystems*, *11*, Q0AB06. doi:10.1029/2010GC003296.

Holtzmann, B. K., Groebner, N., Zimmerman, M. E., Ginsberg, S., & Kohlstedt, D. L. (2003a). Stress-driven melt segregation in partially molten rocks. *Geochemistry, Geophysics, Geosystems*, *4*, 8607. doi:10.1029/2001GC000258.

Holtzmann, B. K., Kohlstedt, D. L., Zimmerman, M. E., Heidelbach, F., Hiraga, T., & Hustoft, J. W. (2003b). Melt segregation and strain partitioning: Implications for seismic anisotropy and mantle flow. *Science*, *301*(5637), 1227–1230. doi:10.1126/science.1087132.

Hudson, J. (1980a). Overall properties of a cracked solid. *Mathematical Proceedings of the Cambridge Philosophical Society*, *88*, 371–384.

Hudson, J. (1980b). *The excitation and propagation of elastic waves*. Cambridge, U.K.: Cambridge University Press.

Iitaka, T., Hirose, K., Kawamura, K., & Murakami, M. (2004). The elasticity of the $MgSiO_3$ post-perovskite phase in the Earth's lowermost mantle. *Nature*, *430*(6998), 442–445. doi:10.1038/nature02702.

Karato, S. (1998). Some remarks on the origin of seismic anisotropy in the D″ layer. *Earth Planets Space*, *50*, 1019–1028.

Karki, B. B., Stixrude, L., & Crain, J. (1997a). Ab initio elasticity of three high-pressure polymorphs of silica. *Geophysical Research Letters*, *24*(24), 3269–3272. doi:10.1029/97GL53196.

Karki, B. B., Warren, M., Stixrude, L., Ackland, G., & Crain, J. (1997b). Ab initio studies of high-pressure structural transformations in silica. *Physical Review B*, *55*(6), 3465–3471. doi:10.1103/PhysRevB.56.2884.

Karki, B. B., Wentzcovitch, R. M., de Gironcoli, S., & Baroni, S. (1999). First-principles determination of elastic anisotropy and wave velocities of MgO at lower mantle conditions. *Science*, *286*(5445), 1705–1707. doi:10.1126/science.286.5445.1705.

Kawai, K., & Geller, R. J. (2010). The vertical flow in the lowermost mantle beneath the Pacific from inversion of seismic waveforms for anisotropic structure. *Earth and Planetary Science Letters*, *297*(1–2), 190–198. doi:10.1016/j.epsl.2010.05.037.

Kendall, J. M., & Nangini, C. (1996). Lateral variations in D″ below the Caribbean. *Geophysical Research Letters*, *23*(4), 399–402. doi:10.1029/95GL02659.

Kendall, J. M., & Silver, P. G. (1996). Constraints from seismic anisotropy on the nature of the lowermost mantle. *Nature*, *381*(6581), 409–412. doi:10.1038/381409a0.

Kendall, J.-M. & Silver, P. G. (1998). Investigating causes of D″ anisotropy. In M. Gurnis, M. E. Wysession, E. Knittle & B. A. Buffett (Eds.), *The Core-Mantle Boundary Region, Geodynamics Series* (pp. 97–118). Washington, D.C., USA: American Geophysical Union.

Kendall, J.-M. & Silver, P. G. (2000). Seismic anisotropy in the boundary layers of the mantle. In S. Karato, A. Forte, R. C. Liebermann, G. Masters & L. Stixrude (Eds.), *Earth's Deep Interior: Mineral Physics and Tomography from the Atomic to the Global Scale* (vol. 117 of Geophysical Monograph, pp. 133–159). Washington, D.C., USA: American Geophysical Union.

Kennett, B., Engdahl, E., & Buland, R. (1995). Constraints on seismic velocities in the Earth from travel-times. *Geophysical Journal International*, *122*(1), 108–124. doi:10.1111/j.1365-246X.1995.tb03540.x.

Kesson, S., Gerald, J. F., & Shelley, J. (1998). Mineralogy and dynamics of a pyrolite lower mantle. *Nature*, *393*(6682), 252–255. doi:10.1038/30466.

Knittle, E., & Jeanloz, R. (1987). Synthesis and equation of state of (Mg, Fe)SiO_3 perovskite to over 100 gigapascals. *Science*, *235*(4789), 668–670. doi:10.1126/science.235.4789.668.

Koci, L., Vitos, L., & Ahuja, R. (2007). Ab initio calculations of the elastic properties of ferropericlase $Mg_{1-x}Fe_xO$ ($x \leq 0.25$). *Physics of the Earth and Planetary Interiors*, *164*(3–4), 177–185. doi:10.1016/j.pepi.2007.06.012.

Kohlstedt, D. L., & Zimmerman, M. E. (1996). Rheology of partially molten mantle rocks. *Annual Review of Earth and Planetary Sciences*, *24*, 41–62. doi:10.1146/annurev.earth.24.1.41.

Kohn, W., & Sham, L. (1965). Self-consistent equations including exchange and correlation effects. *Physical Review*, *140*, A1133–A1138. doi:10.1103/PhysRev.140.A1133.

Komabayashi, T., Hirose, K., Nagaya, Y., Sugimura, E., & Ohishi, Y. (2010). High-temperature compression of ferropericlase and the effect of temperature on iron spin transition. *Earth and Planetary Science Letters*, *297*(3–4), 691–699. doi:10.1016/j.epsl.2010.07.025.

Komatitsch, D., Vinnik, L. P., & Chevrot, S. (2010). SHdiff-SVdiff splitting in an isotropic Earth. *Journal of Geophysical Research, [Solid Earth]*, *115*, B07312. doi:10.1029/2009JB006795.

Kubo, A., Kiefei, B., Shim, S.-H., Shen, G., Prakapenka, V. B., & Duffy, T. S. (2008). Rietveld structure refinement of $MgGeO_3$ post-perovskite phase to 1 Mbar. *American Mineralogist*, *93*(7), 965–976. doi:10.2138/am.2008.2691.

Kustowski, B., Ekström, G., & Dziewoński, A. (2008). Anisotropic shear-wave velocity structure of the Earth's mantle: A global model. *Journal of Geophysical Research, [Solid Earth]*, *113*(B6), B06306. doi:10.1029/2007JB005169.

Lay, T. & Helmberger, D. V. (1983). The shear-wave velocity-gradient at the base of the mantle. *Journal of Geophysical Research*, *88*(NB10), 8160–8170. doi:10.1029/JB088iB10p08160.

Lay, T., & Young, C. (1991). Analysis of seismic SV waves in the core's penumbra. *Geophysical Research Letters*, *18*(8), 1373–1376. doi:10.1029/91GL01691.

Lay, T., Williams, Q., Garnero, E. J., Kellogg, L., & Wysession, M. E. (1998). Seismic wave anisotropy in the D″ region and its implications, In M. Gurnis, M. E. Wysession, E. Knittle, & B. A. Buffett (Eds.), *The Core-Mantle Boundary Region, Geodynamics Series* (vol. 28, pp. 299–318). Washington, D.C., USA: American Geophysical Union.

Lebensohn, R., & Tomé, C. (1993). A self-consistent anisotropic approach for the simulation of plastic-deformation and texture development of polycrystals-application to zirconium alloys. *Acta Metallurgica Et Materialia*, *41*, 2611–2624. doi:10.1016/0956-7151(93)90130-K.

Lekić, V., Panning, M., & Romanowicz, B. (2010). A simple method for improving crustal corrections in waveform tomography. *Geophysical Journal International*, *182*(1), 265–278. doi:10.1111/j.1365-246X.2010.04602.x.

Li, L., Weidner, D. J., Brodholt, J. P., Alfè, D., Price, G. D., Caracas, R., et al. (2006a). Elasticity of $CaSiO_3$ perovskite at high pressure and high temperature. *Physics of the Earth and Planetary Interiors*, *155*(3–4), 249–259. doi:10.1016/j.pepi.2005.12.006.

Li, L., Weidner, D. J., Brodholt, J. P., Alfè, D., Price, G. D., Caracas, R., et al. (2006b). Phase stability of $CaSiO_3$ perovskite at high pressure and temperature: Insights from ab initio molecular dynamics. *Physics of the Earth and Planetary Interiors*, *155*(3–4), 260–268. doi:10.1016/j.pepi.2005.12.007.

Lin, J.-F., & Tsuchiya, T. (2008). Spin transition of iron in the Earth's lower mantle. *Physics of the Earth and Planetary Interiors*, *170*(3–4), 248–259. doi:10.1016/j.pepi.2008.01.005.

Lithgow-Bertelloni, C., & Richards, M. (1998). The dynamics of Cenozoic and Mesozoic plate motions. *Reviews of Geophysics*, *36*(1), 27–78. doi:10.1029/97RG02282.

Long, M. D. (2009). Complex anisotropy in D″ beneath the eastern pacific from SKS-SKKS splitting discrepancies. *Earth and Planetary Science Letters*, *283*(1–4), 181–189. doi:10.1016/j.epsl.2009.04.019.

Long, M. D., Xiao, X., Jiang, Z., Evans, B., & Karato, S. (2006). Lattice preferred orientation in deformed polycrystalline (Mg, Fe)O and implications for seismic anisotropy in D″. *Physics of the Earth and Planetary Interiors*, *156*(1–2), 75–88. doi:10.1016/j.pepi.2006.02.006.

Mainprice, D., & Silver, P. (1993). Interpretation of SKS-waves using samples from the subcontinental lithosphere. *Physics of the Earth and Planetary Interiors*, *78*(3–4), 257–280. doi:10.1016/0031-9201(93)90160-B.

Mainprice, D., Tommasi, A., Ferré, D., Carrez, P., & Cordier, P. (2008). Predicted glide systems and crystal preferred orientations of polycrystalline silicate Mg-perovskite at high pressure: Implications for the seismic anisotropy in the lower mantle. *Earth and Planetary Science Letters*, *271*(1–4), 135–144. doi:10.1016/j.epsl.2008.03.058.

Mao, W. L., Meng, Y., & Mao, H. (2010). Elastic anisotropy of ferromagnesian post-perovskite in Earth's D″ layer. *Physics of the Earth and Planetary Interiors*, *180*(3–4), 203–208. doi:10.1016/j.pepi.2009.10.013.

Marquardt, H., Speziale, S., Reichmann, H. J., Frost, D. J., & Schilling, F. R. (2009). Single-crystal elasticity of $(Mg_{0.9}Fe_{0.1})O$ to 81 GPa. *Earth and Planetary Science Letters*, *287*(3–4), 345–352. doi:10.1016/j.epsl.2009.08.017.

Matzel, E., Sen, M., & Grand, S. P. (1996). Evidence for anisotropy in the deep mantle beneath Alaska. *Geophysical Research Letters*, *23*(18), 2417–2420. doi:10.1029/96GL02186.

Maupin, V. (1994). On the possibility of anisotropy in the D″ layer as inferred from the polarization of diffracted S waves. *Physics of the Earth and Planetary Interiors*, *87*(1–2), 1–32. doi:10.1016/0031-9201(94)90019-1.

Maupin, V., Garnero, E. J., Lay, T., & Fouch, M. J. (2005). Azimuthal anisotropy in the D″ layer beneath the Caribbean. *Journal of Geophysical Research, [Solid Earth]*, *110*(B8), B08301. doi:10.1029/2004JB003506.

McDonough, W., & Sun, S. (1995). The composition of the Earth. *Chemical Geology*, *120*(3–4), 223–253.

McNamara, A. K., van Keken, P., & Karato, S. (2003). Development of finite strain in the convecting lower mantle and its implications for seismic anisotropy. *Journal of Geophysical Research, [Solid Earth]*, *108*(B5), 2230. doi:10.1029/2002JB001970.

Meade, C., Silver, P. G., & Kaneshima, S. (1995). Laboratory and seismological observations of lower mantle isotropy. *Geophysical Research Letters*, *22*(10), 1293–1296. doi:10.1029/95GL01091.

Merkel, S., Wenk, H.-R., Shu, J., Shen, G., Gillet, P., Mao, H., & Hemley, R. (2002). Deformation of polycrystalline MgO at pressures of the lower mantle. *Journal of Geophysical Research, [Solid Earth]*, *107*(B11), 2271. doi:10.1029/2001JB000920.

Merkel, S., Wenk, H.-R., Badro, J., Montagnac, G., Gillet, P., Mao, H., et al. (2003). Deformation of $(Mg_{0.9}, Fe_{0.1})SiO_3$ Perovskite aggregates up to 32 GPa. *Earth Planet Sci Lett*, *209*(3–4), 351–360. doi:10.1016/S0012-821X(03)00098-0.

Merkel, S., Kubo, A., Miyagi, L., Speziale, S., Duffy, T. S., Mao, H., et al. (2006). Plastic deformation of $MgGeO_3$ post-perovskite at lower mantle pressures. *Science*, *311*(5761), 644–646. doi:10.1126/science.1121808.

Merkel, S., McNamara, A. K., Kubo, A., Speziale, S., Miyagi, L., Meng, Y., et al. (2007). Deformation of (Mg, Fe)SiO_3 post-perovskite and D″ anisotropy. *Science*, *316*(5832), 1729–1732. doi:10.1126/science.1140609.

Metsue, A., Carrez, P., Mainprice, D., & Cordier, P. (2009). Numerical modelling of dislocations and deformation mechanisms in $CaIrO_3$ and $MgGeO_3$ post-perovskites-Comparison with $MgSiO_3$ post-perovskite. *Physics of the Earth and Planetary Interiors*, *174*(1–4), 165–173. doi:10.1016/j.pepi.2008.04.003.

Mitrovica, J. X., & Forte, A. M. (2004). A new inference of mantle viscosity based upon joint inversion of convection and glacial isostatic adjustment data. *Earth and Planetary Science Letters*, *225*(1–2), 177–189. doi:10.1016/j.epsl.2004.06.005.

Miyagi, L., Nishiyama, N., Wang, Y., Kubo, A., West, D. V., Cava, R. J., et al. (2008). Deformation and texture development in $CaIrO_3$ post-perovskite phase up to 6 GPa and 1300 K. *Earth and Planetary Science Letters*, *268*(3–4), 515–525. doi:10.1016/j.epsl.2008.02.005.

Miyagi, L., Kanitpanyacharoen, W., Kaercher, P., Lee, K. K. M., & Wenk, H.-R. (2010). Slip systems in $MgSiO_3$ post-perovskite: Implications for D″ anisotropy. *Science*, *329*(5999), 1639–1641. doi:10.1126/science.1192465.

Montagner, J.-P., & Kennett, B. (1996). How to reconcile body-wave and normal-mode reference earth models. *Geophysical Journal International*, *125*(1), 229–248. doi:10.1111/j.1365-246X.1996.tb06548.x.

Montelli, R., Nolet, G., Dahlen, F., Masters, G., Engdahl, E., & Hung, S. (2004). Finite-frequency tomography reveals a variety of plumes in the mantle. *Science*, *303*(5656), 338–343. doi:10.1126/science.1092485.

Moore, M., Garnero, E. J., Lay, T., & Williams, Q. (2004). Shear wave splitting and waveform complexity for lowermost mantle structures with low-velocity lamellae and transverse isotropy. *Journal of Geophysical Research, [Solid Earth]*, *109*(B2), B02319. doi:10.1029/2003JB002546.

Murakami, M., Hirose, K., Kawamura, K., Sata, N., & Ohishi, Y. (2004). Post-perovskite phase transition in $MgSiO_3$. *Science*, *304*(5672), 855–858. doi:10.1126/science.1095932.

Murakami, M., Hirose, K., Sata, N., & Ohishi, Y. (2005). Post-perovskite phase transition and mineral chemistry in the pyrolitic lowermost mantle. *Geophysical Research Letters*, *32*(3), L03304. doi:10.1029/2004GL021956.

Niu, F., & Perez, A. (2004). Seismic anisotropy in the lower mantle: A comparison of waveform splitting of SKS and SKKS. *Geophysical Research Letters*, *31*(24), L24612. doi:10.1029/2004GL021196.

Niwa, K., Yagi, T., Ohgushi, K., Merkel, S., Miyajima, N., & Kikegawa, T. (2007). Lattice preferred orientation in $CaIrO_3$ perovskite and post-perovskite formed by plastic deformation under pressure. *Physics and Chemistry of Minerals*, *34*(9), 679–686. doi:10.1007/s00269-007-0182-6.

Nowacki, A., Wookey, J., & Kendall, J. M. (2010). Deformation of the lowermost mantle from seismic anisotropy. *Nature*, *467*(7319), 1091–1095. doi:10.1038/nature09507.

Nye, J. (1985). *Physical properties of crystals: Their representation by tensors and matrices*. Oxford, UK: Oxford Science Publications, Oxford University Press.

Oganov, A., & Ono, S. (2004). Theoretical and experimental evidence for a post-perovskite phase of $MgSiO_3$ in Earth's D″ layer. *Nature*, *430*(6998), 445–448. doi:10.1038/nature02701.

Oganov, A., Brodholt, J. P., & Price, G. D. (2001). The elastic constants of $MgSiO_3$ perovskite at pressures and temperatures of the Earth's mantle. *Nature*, *411*(6840), 934–937. doi:10.1038/35082048.

Oganov, A., Martonak, R., Laio, A., Raiteri, P., & Parrinello, M. (2005). Anisotropy of Earth's D″ layer and stacking faults in the $MgSiO_3$ post-perovskite phase. *Nature*, *438*(7071), 1142–1144. doi:10.1038/nature04439.

Ohta, K., Hirose, K., Lay, T., Sata, N., & Ohishi, Y. (2008). Phase transitions in pyrolite and MORB at lowermost mantle conditions: Implications for a MORB-rich pile above the core-mantle boundary. *Earth and Planetary Science Letters*, *267*(1–2), 107–117. doi:10.1016/j.epsl.2007.11.037.

Ohtani, E., & Sakai, T. (2008). Recent advances in the study of mantle phase transitions. *Physics of the Earth and Planetary Interiors*, *170*(3–4), 240–247. doi:10.1016/j.pepi.2008.07.024.

Okada, T., Yagi, T., Niwa, K., & Kikegawa, T. (2010). Lattice-preferred orientations in post-perovskite-type $MgGeO_3$ formed by transformations from different pre-phases. *Physics of the Earth and Planetary Interiors*, *180*(3–4), 195–202. doi:10.1016/j.pepi.2009.08.002.

Ono, S., & Oganov, A. (2005). In situ observations of phase transition between perovskite and $CaIrO_3$-type phase in $MgSiO_3$ and pyrolitic mantle composition. *Earth and Planetary Science Letters*, *236*(3–4), 914–932. doi:10.1016/j.epsl.2005.06.001.

Ono, S., Ito, E., & Katsura, T. (2001). Mineralogy of subducted basaltic crust (MORB) from 25 to 37 GPa, and chemical heterogeneity of the lower mantle. *Earth and Planetary Science Letters*, *190*(1–2), 57–63. doi:10.1016/S0012-821X(01)00375-2.

Panning, M., & Romanowicz, B. (2004). Inferences on flow at the base of Earth's mantle based on seismic anisotropy. *Science*, *303*(5656), 351–353. doi:10.1126/science.1091524.

Panning, M., & Romanowicz, B. (2006). A three-dimensional radially anisotropic model of shear velocity in the whole mantle. *Geophysical Journal International*, *167*(1), 361–379. doi:10.1111/j.1365-246X.2006.03100.x.

Perdew, J. P. & Ruzsinszky, A. (2010). Density functional theory of electronic structure: A short course for mineralogists and geophysicists. In R. Wentzcovitch & L. Stixrude (Eds.), Theoretical and Computational Methods in Mineral Physics: Geophysical Applications (vol. 71 of Reviews in Mineralogy & Geochemistry) (pp. 1–18). Chantilly, VA, USA: Mineralogical Society of America.

Pulliam, J., & Sen, M. (1998). Seismic anisotropy in the core-mantle transition zone. *Geophysical Journal International*, *135*(1), 113–128. doi:10.1046/j.1365-246X.1998.00612.x.

Restivo, A., & Helffrich, G. (2006). Core-mantle boundary structure investigated using SKS and SKKS polarization anomalies. *Geophysical Journal International*, *165*(1), 288–302. doi:10.1111/j.1365-246X.2006.02901.x.

Ricolleau, A., Fei, Y., Cottrell, E., Watson, H., Deng, L., Zhang, L., et al. (2009). Density profile of pyrolite under the lower mantle conditions. *Geophysical Research Letters*, *36*, L06302. doi:10.1029/2008GL036759.

Ringwood, A. (1962). A model for the upper mantle. *Journal of Geophysical Research*, *67*(2), 857–867. doi:10.1029/JZ067i002p00857.

Ritsema, J. (2000). Evidence for shear velocity anisotropy in the lowermost mantle beneath the Indian Ocean. *Geophysical Research Letters*, *27*(7), 1041–1044. doi:10.1029/1999GL011037.

Ritsema, J., Lay, T., Garnero, E. J., & Benz, H. (1998). Seismic anisotropy in the lowermost mantle beneath the Pacific. *Geophysical Research Letters*, *25*(8), 1229–1232. doi:10.1029/98GL00913.

Ritsema, J., van Heijst, H. J., & Woodhouse, J. H. (1999). Complex shear wave velocity structure imaged beneath Africa and Iceland. *Science*, *286*(5446), 1925–1928. doi:10.1126/science.286.5446.1925.

Rokosky, J. M., Lay, T., Garnero, E. J., & Russell, S. (2004). High-resolution investigation of shear wave anisotropy in D″ beneath the Cocos Plate. *Geophysical Research Letters*, *31*(7), L07605. doi:10.1029/2003GL018902.

Rokosky, J. M., Lay, T., & Garnero, E. J. (2006). Small-scale lateral variations in azimuthally anisotropic D″ structure beneath the Cocos Plate. *Earth and Planetary Science Letters*, *248*(1–2), 411–425. doi:10.1016/j.epsl.2006.06.005.

Royer, D., & Dieulesaint, E. (2000). *Elastic waves in solids I: Free and guided propagation*, Advanced texts in physics. Heidelberg: Springer.

Rümpker, G., Tommasi, A., & Kendall, J.-M. (1999). Numerical simulations of depth-dependent anisotropy and frequency-dependent wave propagation effects. *Journal of Geophysical Research, [Solid Earth]*, *104*, 23141–23153. doi:10.1029/1999JB900203.

Russell, S., Lay, T., & Garnero, E. J. (1998). Seismic evidence for small-scale dynamics in the lowermost mantle at the root of the Hawaiian hotspot. *Nature*, *396*(6708), 255–258. doi:10.1038/24364.

Russell, S., Lay, T., & Garnero, E. J. (1999). Small-scale lateral shear velocity and anisotropy heterogeneity near the core-mantle boundary beneath the central Pacific imaged using broadband ScS waves. *Journal of Geophysical Research, [Solid Earth]*, *104*(B6), 13183–13199, doi:10.1029/1999JB900114.

Savage, M. (1999). Seismic anisotropy and mantle deformation: What have we learned from shear wave splitting? *Reviews of Geophysics*, *37*(1), 65–106. doi:10.1029/98RG02075.

Sayers, C. (1992). Elastic anisotropy of short-fibre reinforced composites. *International Journal of Solids Structures*, *100*, 4149–4156. doi:10.1016/0020-7683(92)90150-R.

Shim, S.-H. (2008). The postperovskite transition. *Annual Review of Earth and Planetary Sciences*, *36*, 569–599. doi:10.1146/annurev.earth.36.031207.124309.

Silver, P. G. & Chan, W. W. (1991). Shear-wave splitting and subcontinental mantle deformation. *Journal of Geophysical Research, [Solid Earth]*, *96*(B10), 16429–16454. doi:10.1029/91JB00899.

Silver, P. G., & Savage, M. (1994). The interpretation of shear-wave splitting parameters in the presence of two anisotropic layers. *Geophysical Journal International*, *119*(3), 949–963. doi:10.1111/j.1365-246X.1994.tb04027.x.

Simmons, N. A., Forte, A. M., & Grand, S. P. (2009). Joint seismic, geodynamic and mineral physical constraints on three-dimensional mantle heterogeneity: Implications for the relative importance of thermal versus compositional heterogeneity. *Geophysical Journal International*, *177*(3), 1284–1304. doi:10.1111/j.1365-246X.2009.04133.x.

Sinmyo, R., Hirose, K., Nishio-Hamane, D., Seto, Y., Fujino, K., Sata, N., & Ohishi, Y. (2008). Partitioning of iron between perovskite/postperovskite and ferropericlase in the lower mantle. *Journal of Geophysical Research, [Solid Earth]*, *113*(B11), B11204. doi:10.1029/2008JB005730.

Speziale, S., Zha, C., Duffy, T., Hemley, R., & Mao, H. (2001). Quasi-hydrostatic compression of magnesium oxide to 52 GPa: Implications for the pressure-volume-temperature equation of state. *Journal of Geophysical Research, [Solid Earth]*, *106*, 515–528. doi:10.1029/2000JB900318.

Stackhouse, S., Brodholt, J. P., & Price, G. D. (2005a). High temperature elastic anisotropy of the perovskite and post-perovskite Al_2O_3. *Geophysical Research Letters*, *32*(13), L13305. doi:10.1029/2005GL023163.

Stackhouse, S., Brodholt, J. P., Wookey, J., Kendall, J. M., & Price, G. D. (2005b). The effect of temperature on the seismic anisotropy of the perovskite and post-perovskite polymorphs of $MgSiO_3$. *Earth and Planetary Science Letters*, *230*(1–2), 1–10. doi:10.1016/j.epsl.2004.11.021.

Stackhouse, S., Brodholt, J. P., & Price, G. D. (2006). Elastic anisotropy of $FeSiO_3$ end-members of the perovskite and post-perovskite phases. *Geophysical Research Letters*, *33*(1), L01304. doi:10.1029/2005GL023887.

Stixrude, L., Lithgow-Bertelloni, C., Kiefer, B., & Fumagalli, P. (2007). Phase stability and shear softening in $CaSiO_3$ perovskite at high pressure. *Physical Review B*, *75*(2), 024108. doi:10.1103/PhysRevB.75.024108.

Stixrude, L., de Koker, N., Sun, N., Mookherjee, M., & Karki, B. B. (2009). Thermodynamics of silicate liquids in the deep Earth. *Earth and Planetary Science Letters*, *278*(3–4), 226–232. doi:10.1016/j.epsl.2008.12.006.

Tackley, P. (2000). Mantle convection and plate tectonics: Toward an integrated physical and chemical theory. *Science*, *288*(5473), 2002–2007. doi:10.1126/science.288.5473.2002.

Tanaka, S. (2010). Constraints on the core-mantle boundary topography from P4KP-PcP differential travel times. *Journal of Geophysical Research, [Solid Earth]*, *115*, B04310. doi:10.1029/2009JB006563.

Tandon, G., & Weng, G. (1984). The effect of aspect ratio of inclusions on the elastic properties of unidirectionally aligned composites. *Polymer Composite*, *5*(4), 327–333. doi:10.1002/pc.750050413.

Tateno, S., Hirose, K., Sata, N., & Ohishi, Y. (2009). Determination of post-perovskite phase transition boundary up to 4400 K and implications for thermal structure in D″ layer. *Earth and Planetary Science Letters*, *277*(1–2), 130–136. doi:10.1016/j.epsl.2008.10.004.

Teanby, N., Kendall, J. M., & der Baan, M. V. (2004). Automation of shear-wave splitting measurements using cluster analysis. *Bulletin of the Seismological Society of America*, *94*(2), 453–463. doi:10.1785/0120030123.

Thomas, C., & Kendall, J. M. (2002). The lowermost mantle beneath northern Asia—II. Evidence for lower-mantle anisotropy. *Geophysical Journal International*, *151*(1), 296–308. doi:10.1046/j.1365-246X.2002.01760.x.

Thomas, C., Wookey, J., & Simpson, M. (2007). D″ anisotropy beneath Southeast Asia. *Geophysical Research Letters*, *34*(4), L04301. doi:10.1029/2006GL028965.

Thomsen, L. (1986). Weak elastic anisotropy. *Geophysics*, *51*(10), 1954–1966. doi:10.1190/1.1442051.

Tikoff, B., & Fossen, H. (1999). Three-dimensional reference deformations and strain facies. *Journal of Structural Geology*, *21*, 1497–1512. doi:10.1016/S0191-8141(99)00085-1.

Trampert, J., Deschamps, F., Resovsky, J., & Yuen, D. A. (2004). Probabilistic tomography maps chemical heterogeneities throughout the lower mantle. *Science*, *306*(5697), 853–856. doi:10.1126/science.1101996.

Tromp, J. (2001). Inner-core anisotropy and rotation. *Annual Review of Earth and Planetary Sciences*, *29*, 47–69. doi:10.1146/annurev.earth.29.1.47.

Trønnes, R. G. (2010). Structure, mineralogy and dynamics of the lowermost mantle. *Mineralogy and Petrology*, *99*(3–4), 243–261. doi:10.1007/s00710-009-0068-z.

Tsuchiya, T. (2003). First-principles prediction of the *P-V-T* equation of state of gold and the 660-km discontinuity in Earth's mantle. *Journal of Geophysical Research, [Solid Earth]*, *108*(B10), 2462. doi:10.1029/2003JB002446.

Tsuchiya, T., Tsuchiya, J., Umemoto, K., & Wentzcovitch, R. M. (2004). Phase transition in $MgSiO_3$ perovskite in the earth's lower mantle. *Earth and Planetary Science Letters*, *224*(3–4), 241–248. doi:10.1016/j.epsl.2004.05.017.

Usui, Y., Hiramatsu, Y., Furumoto, M., & Kanao, M. (2008). Evidence of seismic anisotropy and a lower temperature condition in the D″ layer beneath Pacific Antarctic Ridge in the Antarctic Ocean. *Physics of the Earth and Planetary Interiors*, *167*(3–4), 205–216. doi:10.1016/j.pepi.2008.04.006.

Vinnik, L. P., Kind, R., Kosarev, G., & Makeyeva, L. (1989). Azimuthal anisotropy in the lithosphere from observations of long-period S-waves. *Geophysical Journal International*, *99*(3), 549–559. doi:10.1111/j.1365-246X.1989.tb02039.x.

Vinnik, L. P., Romanowicz, B., Stunff, Y. L., & Makeyeva, L. (1995). Seismic anisotropy in the D″ layer. *Geophysical Research Letters*, *22*(13), 1657–1660. doi:10.1029/95GL01327.

Vinnik, L. P., Breger, L., & Romanowicz, B. (1998). Anisotropic structures at the base of the Earth's mantle. *Nature*, *393*(6685), 564–567. doi:10.1038/31208.

Walker, A., Carrez, P., & Cordier, P. (2010). Atomic-scale models of dislocation cores in minerals: Progress and prospects. *Mineralogical Magazine*, *74*(3), 381–413. doi:10.1180/minmag.2010.074.3.381.

Walte, N. P., Heidelbach, F., Miyajima, N., & Frost, D. J. (2007). Texture development and TEM analysis of deformed $CaIrO_3$: Implications for the D″ layer at the core-mantle boundary. *Geophysical Research Letters*, *34*(8), L08306. doi:10.1029/2007GL029407.

Walte, N. P., Heidelbach, F., Miyajima, N., Frost, D. J., Rubie, D. C., & Dobson, D. P. (2009). Transformation textures in post-perovskite: Understanding mantle flow in the D″ layer of the Earth. *Geophysical Research Letters*, *36*, L04302. doi:10.1029/2008GL036840.

Wang, Y. & Wen, L. (2007). Complex seismic anisotropy at the border of a very low velocity province at the base of the Earth's mantle. *Journal of Geophysical Research, [Solid Earth]*, *112*(B9), B09305. doi:10.1029/2006JB004719.

Wenk, H.-R., Bennett, K., Canova, G., & Molinari, A. (1991). Modeling plastic-deformation of peridotite with the self-consistent theory. *Journal of Geophysical Research-Solid Earth and Planets*, *96*, 8337–8349. doi:10.1029/91JB00117.

Wenk, H.-R., Speziale, S., McNamara, A. K., & Garnero, E. J. (2006). Modeling lower mantle anisotropy development in a subducting slab. *Earth and Planetary Science Letters*, *245*(1–2), 302–314. doi:10.1016/j.epsl.2006.02.028.

Wentzcovitch, R. M., Karki, B. B., Cococcioni, M., & de Gironcoli, S. (2004). Thermoelastic properties of $MgSiO_3$-perovskite: Insights on the nature of the Earth's lower mantle. *Physical Review Letters*, *92*(1), 018501. doi:10.1103/PhysRevLett.92.018501.

Wentzcovitch, R. M., Tsuchiya, T., & Tsuchiya, J. (2006). $MgSiO_3$ postperovskite at D″ conditions. *Proceedings of the National Academy of Sciences of the United States of America*, *103*(3), 543–546. doi:10.1073/pnas.0506879103.

Wookey, J., & Kendall, J.-M. (2007). Seismic anisotropy of post-perovskite and the lowermost mantle. In K. Hirose, J. Brodholt, T. Lay & D. A. Yuen (Eds.), *Post-perovksite: The last mantle phase transition* (vol. 174, pp. 171–189). Washington, D.C., USA: American Geophysical Union Geophysical Monograph.

Wookey, J., & Kendall, J. M. (2008). Constraints on lowermost mantle mineralogy and fabric beneath Siberia from seismic anisotropy. *Earth and Planetary Science Letters*, *275*(1–2), 32–42. doi:10.1016/j.epsl.2008.07.049.

Wookey, J., Kendall, J. M., & Rümpker, G. (2005). Lowermost mantle anisotropy beneath the north Pacific from differential S-ScS splitting. *Geophysical Journal International*, *161*(3), 829–838. doi:10.1111/j.1365-246X.2005.02623.x.

Wookey, J., Stackhouse, S., Kendall, J. M., Brodholt, J. P., & Price, G. D. (2005b). Efficacy of the post-perovskite phase as an explanation for lowermost-mantle seismic properties. *Nature*, *438*(7070), 1004–1007. doi:10.1038/nature04345.

Wysession, M., Langenhorst, A., Fouch, M. J., Fischer, K. M., Al-Eqabi, G., Shore, P., et al. (1999). Lateral variations in compressional/shear velocities at the base of the mantle. *Science*, *284*(5411), 120–125. doi:10.1126/science.284.5411.120.

Wysession, M. E., Lay, T., Revenaugh, J., Williams, Q., Garnero, E. J., Jeanloz, R., & Kellogg, L. (1998). The D″ discontinuity and its implications. In M. Gurnis, M. E. Wysession, E. Knittle & B. A. Buffett (Eds.), *The core-mantle boundary region, geodynamics series* (pp. 273–298). Washington, D.C., USA: American Geophysical Union.

Yamazaki, D., & Karato, S. (2002). Fabric development in (Mg, Fe)O during large strain, shear deformation: implications for seismic anisotropy in Earth's lower mantle. *Physics of the Earth and Planetary Interiors*, *131*(3–4), 251–267. doi:10.1016/S0031-9201(02)00037-7.

Yamazaki, D., & Karato, S. (2007). Lattice-preferred orientation of lower mantle materials and seismic anisotropy in the D″ layer. *Post-perovksite: The last mantle phase transition, geophysical monograph* (pp. 69–78). Washington, D.C., USA: American Geophysical Union.

Yamazaki, D., Yoshino, T., Ohfuji, H., Ando, J., & Yoneda, A. (2006). Origin of seismic anisotropy in the D″ layer inferred from shear deformation experiments on post-perovskite phase. *Earth and Planetary Science Letters*, *252*(3–4), 372–378. doi:10.1016/j.epsl.2006.10.004.

Chapter 3
Mantle Anisotropy Beneath the Earth's Mid-Ocean Ridges

3.1 Introduction

Although it is well known that mid-ocean ridges (MORs) mark sites where oceanic lithosphere is created, there is still considerable uncertainty about mantle processes near ridges and how melt is extracted to form new crust. It has been long understood that viscous shearing leads to the lattice-preferred orientation (LPO) of mantle minerals at spreading centres (e.g., Hess 1964; Blackman et al. 1996; Tommasi et al. 1999); additionally, upwelling and decompression lead to melt generation, and shearing and strain partitioning can cause melt segregation (Phipps Morgan 1987; Holtzman and Kendall 2010). Both effects can impart a significant anisotropic signature on seismic waves, measurements of which can therefore be used to probe the dynamics of the Earth's upper mantle (UM) beneath ridges.

Measurements of two orthogonally polarised and independent shear waves (i.e., shear wave splitting) are the most unambiguous observation of anisotropy, and are now routinely made in continental regions, or on oceanic islands (for reviews, see for instance Savage 1999; Long and Silver 2009). With UM anisotropy, the orientations of fast shear waves, as derived from splitting measurements, are usually interpreted in terms of LPO in peridotites, where olivine a-axes align roughly parallel to mantle flow directions (e.g., Mainprice 2007). The delay time between the fast and slow shear-waves is proportional to both the magnitude of the anisotropy and the extent of the anisotropic region.

Whilst subduction zones and orogens are well-sampled, MORs have not been routinely investigated because of significant logistical problems with placing seismometers on the seafloor. Experiments using ocean-bottom seismometers (OBSs) (Blackman et al. 1993, 1995b; Wolfe and Solomon 1998; Hung and Forsyth 1999; Barclay and Toomey 2003; Harmon et al. 2004) have provided vital insights into MOR processes, though there are still very few observations of shear wave splitting at MORs. Using teleseismic phases (e.g., SKS), these few studies generally reveal fast shear wave polarisations parallel to the direction of plate spreading, with increasing values in delay times moving away from the ridge axis (Wolfe and Solomon 1998;

A. Nowacki, *Plate Deformation from Cradle to Grave*, Springer Theses,
DOI: 10.1007/978-3-642-34842-6_3, © Springer-Verlag Berlin Heidelberg 2013

Hung and Forsyth 1999; Harmon et al. 2004). These observations are consistent with interpretations of olivine LPO as originally proposed by Hess (1964) (based on observations of P-wave anisotropy) and as modelled by Blackman et al. (1996). In contrast, shallow earthquakes measured within the axial valley show fast shear-wave orientations in the crust that are parallel to the ridge axis, which are attributed to aligned cracks and layered intrusions of volcanic material (Barclay and Toomey 2003). Blackman et al. (1993, 1995a, 1996) explained the early arrival of P-waves across the southern Mid-Atlantic Ridge in terms of the vertical alignment on olivine a-axes in a mantle wedge beneath the ridge axis. Subsequent modelling has suggested that the vertical alignment of melt in films, pockets or bands would also be very effective in generating shear-wave splitting in near-vertically arriving teleseismic phases (e.g., Kendall 1994; Blackman and Kendall 1997; Holtzman and Kendall 2010), and would also predict ridge-parallel fast shear-wave polarisations.

Previous studies of anisotropy beneath MORs in a global context have been undertaken using surface waves to infer azimuthal anisotropy (see e.g., Becker et al. 2007). Debayle et al. (2005), for instance, show that beneath MORs, fast orientations are generally similar to the spreading direction, however the behaviour beneath transform zones is more complex and such surface wave studies are limited in their horizontal resolution. It is also the case that even for the simpler case of global inversions for radial anisotropy in the UM, a priori corrections for the crust have a strong effect on the results of such inversions (Ferreira et al. 2010). Hence whilst this should be less of a problem in the region of MORs, where the crust is simple, caution in directly interpreting such results is still advisable. In a more localised study Gaherty (2001) and Delorey et al. (2007) mapped vertical and lateral variations in anisotropy beneath the Reykjanes Ridge. Using sources on the Gibbs fracture zone and receivers on Iceland, differences in Love and Rayleigh wave arrival times revealed faster vertically-polarised Rayleigh waves than horizontally-polarised Loves waves near the ridge axis and at depths less than 100 km. This observation is consistent with either the vertical alignment of olivine a-axes or a melt-induced anisotropy, but Holtzman and Kendall (2010) argue that the latter is more likely.

In this study we evaluate MOR anisotropy using measurements of shear wave splitting which occur beneath the earthquake, rather than the receiver, using direct S waves—a technique often termed 'source-side splitting' (e.g., Schoenecker et al. 1997; Nowacki et al. 2010; Foley and Long 2011). Using seismic stations with well-characterised anisotropy in the UM beneath the receivers, we can remove the effect of the splitting on the receiver side and measure only that which occurs beneath the source. We then attempt to interpret these observations in the context of previous observations and proposed mechanisms for anisotropy beneath a MOR.

As well as providing insight into MOR processes, our results also significantly increase the source region for measurements of D″ anisotropy and should provide a basis for future studies of deformation in the lowermost mantle.

3.2 Methods and Data

3.2.1 Shear Wave Splitting

We aim to measure the seismic anisotropy beneath MORs around the world using the primary observable it produces, shear wave splitting. We use the 'minimum eigenvalue' technique of Teanby et al. (2004) (which is an extension of that of Silver and Chan (1991)), which removes splitting by effectively maximising the linearity of the horizontal particle motion for a given pair of splitting parameters: the fast direction, ϕ, and the delay between the fast and slow waves, δt. Where measurements are available for an event at more than one station within an azimuthal range of 15°, we use the method of Wolfe and Silver (1998) to stack the small eigenvalue (λ_2) surfaces, with a backazimuth-independent implementation. This significantly reduces the errors when for some stations the measurement is very near null, as the initial polarisation is close to the fast direction beneath the event.

In this study, we make the common assumption that the lower mantle above D″ is not significantly anisotropic: several studies support this assumption (e.g., Meade et al. 1995; Montagner and Kennett 1996; Panning and Romanowicz 2006; Kustowski et al. 2008). Hence we can infer that any splitting is caused by anisotropy in the UM beneath the source and receiver. If we have prior knowledge of splitting in the UM beneath the receiver, we may correct for this and analyse the S phase, retrieving the splitting caused by anisotropy beneath the source. We interpret the fast direction of the receiver-corrected signal simply by considering the fast orientation at the source, $\phi'' = \text{azimuth} + \text{backazimuth} - \phi$. This simple geometric relationship is true for rays which are vertically incident at the surface, but is only less accurate by a few degrees than a fully slowness-dependent expression, for the range of slownesses in this study. This error is generally less than the uncertainty in the shear wave splitting measurements themselves.

3.2.2 SKS UM Splitting Corrections

Seismic anisotropy in the continental UM (where our stations are located) appears to be ubiquitous, and is typically measured using phases such as SKS, PKS and SKKS; SKS is the most commonly used. It converts from a compressional to an S wave upon exiting the outer core, so begins its ascent through the mantle with no splitting present. It is polarised radially, hence it is also polarised parallel to the backazimuth at the receiver. SKS also propagates steeply through D″, which is known to be anisotropic in various places in the lower mantle (see reviews by Kendall and Silver 1998, 2000; Lay et al. 1998; Nowacki et al. 2011). However, we assume that any contribution to splitting in the phase along this section is minor, as it has spent relatively little time in D″. Studies on a global scale support this approximation (Niu and Perez 2004; Restivo and Helffrich 2006), though any strong effects should be visible and display backazimuthal variation in splitting parameters (Hall et al. 2004).

Because we wish to remove UM anisotropy from the S phase, we choose seismic stations which have many SKS splitting measurements along a variety of backazimuths. If dipping or multiple layers of anisotropy exist beneath the station, then we expect the results to show a 90° or 180° periodicity to the measurements of ϕ and δt (Silver and Savage 1994). We do not use stations which exhibit such measurements, as complicated UM anisotropy beneath the receiver is difficult to infer uniquely, and therefore we cannot confidently remove its effects on direct S phases, as they will be arbitrarily polarised compared to the backazimuth, depending on the source mechanism and anisotropic fabric they have encountered near the source. Stations which exhibit backazimuthal variation in SKS splitting may also do so because of laterally heterogeneous anisotropy beneath them. We also avoid using such stations for similar reasons. Our approach is slightly different from some authors, who opt to use stations which appear to show no anisotropy beneath them (Foley and Long 2011), however these are rare and UM anisotropy appears to be the norm, rather than isotropy.

In order to be confident of our measurements, we wish to make several for each MOR event, and so we choose from sets of stations in North America and Ethiopia, where extensive SKS splitting studies have been conducted (Ayele et al. 2004; Barruol et al. 1997; Evans et al. 2006; Fouch et al. 2000; Kendall et al. 2005; Liu 2009; Niu and Perez 2004; J.O.S. Hammond, pers. comm., 2010). As explained, we reject stations with apparently complicated sub-station anisotropy. SKS measurements for two example stations used in this study are shown in Fig. 3.1. The stations used in this study and the SKS splitting parameters used as UM corrections are shown in Fig. 3.2.

We use these SKS-derived corrections and analyse the direct S phase from events beneath MORs, applying the correction during the analysis. We note that even though reciprocity must apply along the ray path (see, for example, Kendall et al. 1992), the splitting operators are not commutative (Wolfe and Silver 1998), so it is essential to make the corrections in the correct order (see Wookey and Kendall 2008; Wookey et al. 2005). As a further check that the correction is valid, after the measurement we check that the source polarisation of S matches that predicted by the event's focal mechanism (see Sect. 3.2.4). This helps mitigate against the possibility that the S phase we analyse is contaminated by depth phases (sS and pS), as these will generally alter the apparent source polarisation of the combined phase to be different to that expected from the CMT solution. A difference in the measured source polarisation may also occur due to the application of an incorrect receiver correction in the analysis (see below), which also leads us to reject measurements where the two are not in agreement within 15°.

3.2.3 Testing the Use of Receiver Corrections

Whilst we make every effort to ensure that we use seismic stations which have very well-characterised anisotropy beneath them, some error will be present in the

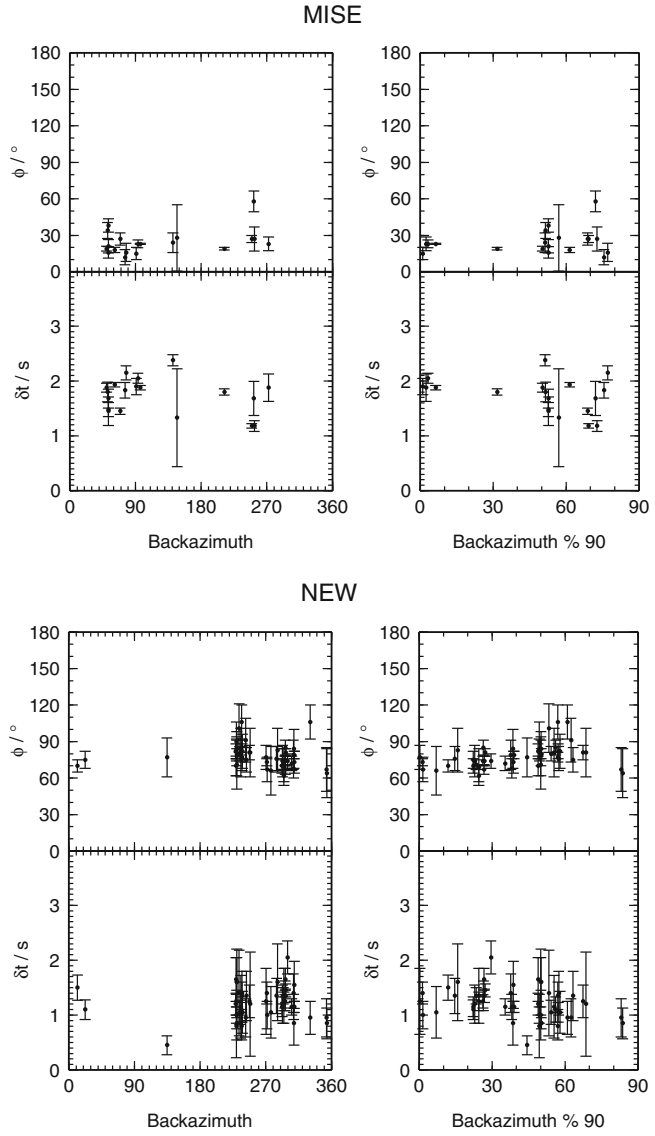

Fig. 3.1 SKS splitting measurements at stations MISE, Mieso, Oromia, Ethiopia (J.O.S. Hammond, pers. comm., 2010) and NEW, Newport, Washington, USA Liu (2009). Shown are measurements for backazimuths 0–360° (*left panels*), and backazimuth modulo 90° (*right panels*). *Errorbars* show 2σ uncertainties. Both stations show consistent splitting parameters across a range of backazimuths, with no apparent 90° periodicity

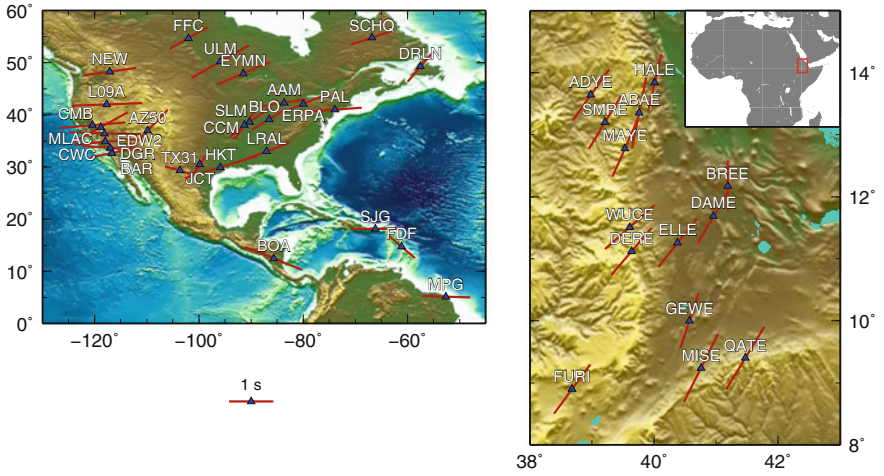

Fig. 3.2 Stations used in this study, with the SKS splitting parameters used as receiver corrections shown by *red bars*. Length is proportional to δt as shown by the legend, and ϕ is indicated by orientation. *Right*: *Inset* map shows location of larger-scale figure of Ethiopian stations. Station DRV (Base Dumont Durville, Terre-Adelie, Antarctica) is not shown

measurement. Part of the difference will result because of the different slownesses between the S waves we study and the SKS phases used to make the splitting measurements we use as station corrections, but the difference is usually negligible in ϕ and very small in δt (see discussion in Nowacki et al. 2011). The majority of the error therefore likely comes from the assumption that the anisotropy is simple beneath the station, and that the SKS splitting measurements are accurate.

We conduct synthetic tests to determine how large the uncertainty in the measured source splitting parameters are when an 'incorrect' receiver correction is used. We apply a known initial amount of splitting (the 'source-side' splitting, $\phi_s''^{\text{true}}$, δt_s^{true}) to a synthetic wave of dominant frequency 0.1 Hz, then a known receiver-side splitting, ϕ_r^{true}, δt_r^{true}. We then analyse the splitting in the wave with a range of receiver corrections (ϕ_r^{trial}, $\delta t_r^{\text{trial}}$) to obtain the 'observed' splitting parameters at the source ($\phi_s''^{\text{trial}}$, $\delta t_s^{\text{trial}}$) and compare the known and measured source-side splitting. The procedure can be repeated for any combination of true source and receiver splitting operators, and all receiver 'corrections'.

Figure 3.3 shows the difference between the true and measured splitting parameters where $\phi_s''^{\text{true}} = 20°$, $\delta t_s^{\text{true}} = 1.0\,\text{s}$, and $\phi_r^{\text{true}} = 0°$, $\delta t_r^{\text{true}} = 1.0\,\text{s}$. The difference in fast orientation, $\Delta(\phi'') = \left|\phi_s''^{\text{trial}} - \phi_s''^{\text{true}}\right|$, is within about 15° whilst the trial receiver correction is within about 40° and 0.4 s of the true receiver splitting parameters. In these limits, the absolute difference in source delay time, $\Delta(\delta t) = \left|\delta t_s^{\text{trial}} - \delta t_s^{\text{true}}\right|$, is up to 0.6 s. Consistent with previous tests using real data (Russo and Mocanu 2009), we find that errors in δt_r appear to cause the largest uncertainty in the 'observed' source-side splitting parameters. Figure 3.4 shows the case when $\phi_s''^{\text{true}} = 45°$, $\delta t_s^{\text{true}} = 1.0\,\text{s}$.

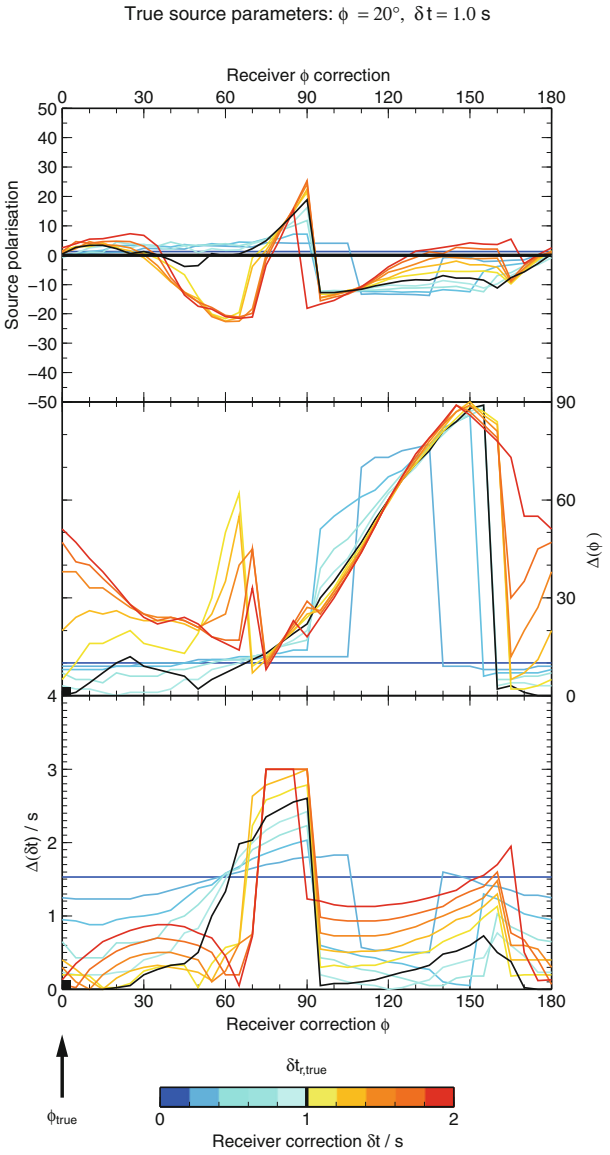

Fig. 3.3 Difference between true and recovered splitting parameters and measured initial source polarisations for synthetic shear waves with an imposed case of two-layer splitting and a range of trial values as corrections for the second layer. The coloured curves—where colour shows the trial receiver correction delay time, $\delta t_r^{\text{trial}}$—are the absolute difference between recovered and true splitting parameters for the source, $\Delta(\phi'')$ and $\Delta(\delta t)$, for a range of trial receiver fast orientations, ϕ_r^{trial}. The true receiver parameters are $\phi_r^{\text{true}} = 0°$, $\delta t_r^{\text{true}} = 1.0\,\text{s}$ (shown by the *black square* in the figure). The *black lines* represent the recovered splitting for the true receiver delay time (δt_r^{true}), and the *arrow* indicates the true receiver fast orientation (ϕ_r^{true}). True source parameters are $\phi_s''^{\text{true}} = 20°$, $\delta t_s^{\text{true}} = 1.0\,\text{s}$. See main text for further information

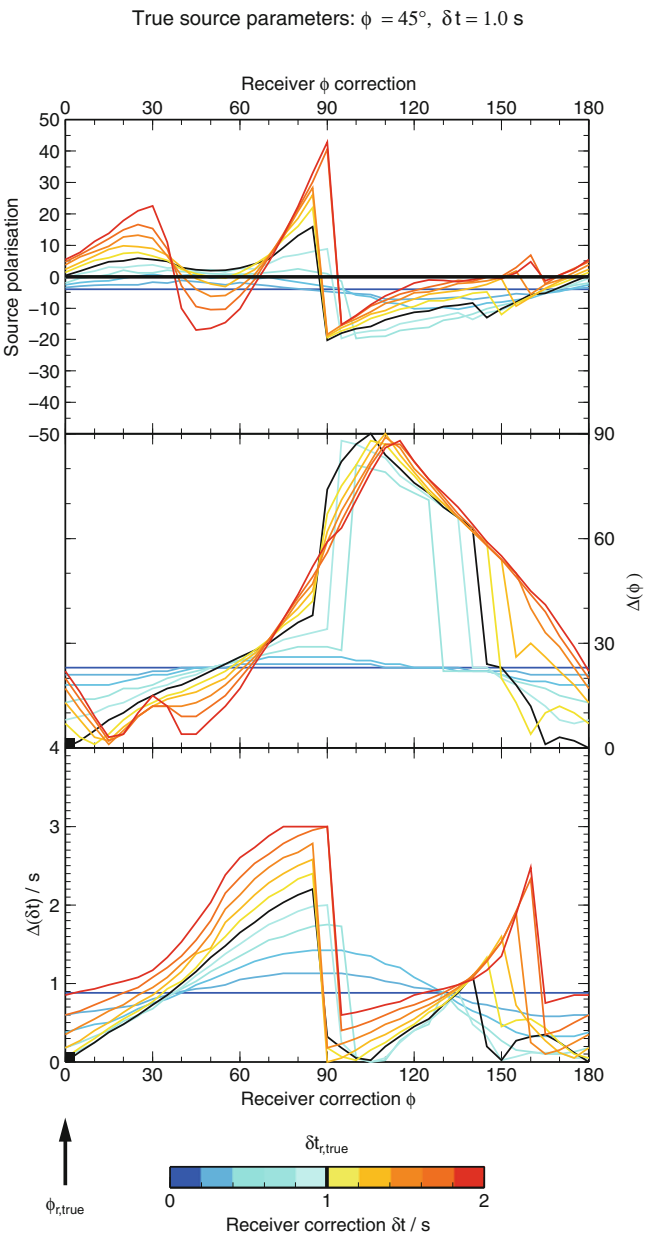

Fig. 3.4 As for Fig. 3.3, but for a case where $\phi_s''^{\text{true}} = 45°$, $\delta t_s^{\text{true}} = 1.0\,\text{s}$

We also show in Figs. 3.3 and 3.4 the difference between the known and measured source polarisation for a range of ϕ_r^{trial} and $\delta t_r^{\text{trial}}$. The initial polarisation is 0° in both cases. Again, the difference in the true and trial receiver delay times plays a large rôle, and when the 'observed' source-side splitting parameters are most inaccurate, the source polarisation is often incorrect by about 10–20°. Hence the use of the source polarisation as a diagnostic of the quality of the result is important and helpful.

Finally, manual inspection of the results indicates that in several instances the 'observed' source splitting parameters would be classified as null events, especially where the delay times are large as shown in Figs. 3.3 and 3.4. This also highlights the strength of using manual inspection or an automated null-classifying scheme to maintain the integrity of measurements (Wuestefeld et al. 2010). When all of these diagnostics are included, and the receiver corrections are within an acceptable uncertainty range of within about 20° for the fast direction and 0.4 s for the delay time, we can be confident that the source-side shear wave splitting measurement is a true reflection of the splitting which has affected the wave in the source anisotropic region.

3.2.4 Event Locations and Focal Mechanisms

In order to make inferences about anisotropy beneath MORs, it is obviously important to accurately know the earthquake location. Because MOR events typically have large uncertainties on their locations in time and space, where possible (for events before 2008) we take these parameters from the ISC's relocations using the EHB algorithm (Engdahl et al. 1998). The published horizontal uncertainty in the standard ISC locations is approximately 20 km; for the EHB locations in this study, the average uncertainty is 7 km.

The location of an event—whether beneath a ridge segment or transform zone—may affect the type of anisotropy we expect, hence each event was assigned to one of these categories based on its location relative to the bathymetry (Smith and Sandwell 1997), and in part its focal mechanism. These were taken from the Global CMT catalogue. Where there was ambiguity from bathymetry, the event was classified as being located on a ridge if the focal mechanism was mainly dip-slip, and as on a transform if mainly strike-slip.

3.2.5 Dataset

We consider events of $M > 5.0$, depth $\leq$35 km, in the epicentral distance range $55° \leq \Delta \leq 82°$, which are located on the East Pacific Rise (EPR), Mid-Atlantic Ridge (MAR), Gakkel Ridge, and the Southwest and Southeast Indian Ridges (IRs) (Fig. 3.5). At distances less than ∼55°, the difference in incidence angle between SKS and S becomes large enough that the vertical-incidence approximation may no

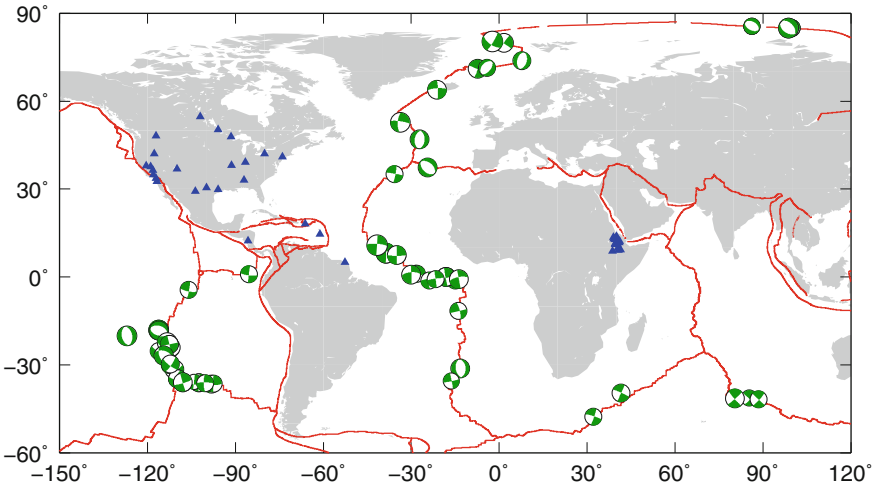

Fig. 3.5 Location of events used in this study with plate boundaries of Bird (2003). Lower-hemisphere focal mechanisms are the best-fitting double-couple solutions as given by the Global CMT project. *Blue triangles* are seismic stations. Magnitude range ($4.4 \leq M_b \leq 6.7$) shown by size of hemispheres

longer be appropriate, and increases the possibility that an SKS-correction for UM anisotropy is inaccurate; beyond ∼82°, the S phase interferes with ScS, or there may be a triplication due to the presence of the D″ layer, contaminating the S signal in the splitting analysis. We of course also wish to avoid D″-traversing rays due to the anisotropy present there. Events deeper than 35 km are unlikely to occur near MORs, and such depths may indicate a poor event location. The seismograms were band-pass filtered between 0.001 and 0.3 Hz.

After selection, over 2000 events matched the criteria between 1979 and 2009, according to the USGS National Earthquake Information Center (NEIC) and International Seismological Centre (ISC) catalogues. Due mainly to signal-to-noise requirements, ∼400 events were retained for analysis, leaving ∼820 event-station pairs.

During analysis, we apply a strict set of criteria to select the optimum splitting results. Only non-null results which meet the following are retained: (i) acceptable signal-to-noise ratio on both horizontal components; (ii) clear elliptical particle motion before analysis; (iii) clear linearisation of particle motion when corrected; (iv) measured source polarisation is within 15° of the CMT-predicted source polarisation; (v) clear minimum on the λ_2 surface. A quality of 1 (excellent) to 4 (very poor) is assigned manually to each measurement. Null measurements are retained, provided the signal-to-noise ratio is adequate and particle motion is clearly linear before analysis, but after correction for receiver anisotropy.

Following analysis, 350 measurements of splitting of 'fair' (3) quality or better beneath 67 events comprise the dataset. Of these, 122 are of quality 'good' (2) or

better. There are 189 null measurements. The events have magnitude range $4.4 \leq M_b \leq 6.7$, and depth range 0–33 km.

3.3 Results

Individual source-side splitting results are given in Tables 3.1 (ridge events) and 3.2 (transform events). The following analysis concentrates in turn on each of the ridge systems investigated.

3.3.1 East Pacific Rise

The EPR is the best-sampled MOR segment in this work. Our results agree excellently with SKS splitting results from ocean-bottom seismometers (OBSs) deployed as part of the MELT and GLIMPSE projects (Wolfe and Solomon 1998; Harmon et al. 2004) (orange bars, Fig. 3.6). Here and in the OBS experiments, ϕ'' or ϕ_{SKS} is approximately parallel to the spreading direction, with δt varying from 1–3 s, depending on distance from the ridge axis. Figure 3.7 shows the variation of splitting parameters with distance for results on the EPR which are classified as 'ridge' events, alongside the MELT and GLIMPSE data.

Away from the straightest segments of the EPR, where frequent fracture zones offset the ridge axis, the pattern of observed splitting is different. There is no clear spreading direction-parallel trend to ϕ'', and the change in δt is also complicated. At about $-5°$ latitude, for example, ϕ'' seems to change over a short distance by $\sim 70°$ from spreading direction-parallel to transform zone-perpendicular. Similarly, the pattern of ϕ'' and δt east of the Pacific–Nazca–Antarctic triple-junction is also complex, with a variation of ϕ'' from parallel to perpendicular to the Challenger Fracture Zone (at about $-35°$ latitude).

3.3.2 Mid-Atlantic Ridge

Events which produced 'good' source-side splitting measurements were limited to latitudes between $-40°$ and $15°$. Very few events of sufficient magnitude are reported in the catalogues along the Reykjanes Ridge, and no 'good' measurements could be made north of the equator. We note that few measured earthquakes occur along clear, linear ridge segments along the MAR, and most seismicity for which we have results is located instead on the transform zones. Nonetheless, the few events clearly beneath ridges (e.g., the stack at $-30°$ latitude) do seem to show spreading direction-parallel ϕ''. This agrees approximately with SKS splitting measurements made at ASCN

Table 3.1 Individual source-side shear wave splitting results beneath mid-ocean ridges

DATE	TIME	EVLAT	EVLON	STA	STLAT	STLON	DEPTH	DIST	AZI	BAZ	FAST	DFAST	DT	DDT	SRCPOL	SR(mm/a)	DIRN(az)	RIDGE strike	LOC	RDIST(km)	AGE(Ma)
1991246	0905	−17.910	−116.016	CCM	38.06	−91.24	9.00	60.11	22.40	207.41	−51.00	4.25	3.03	0.14	3.56	153.74	284.70	191	EPR	280.8	3.83
1991246	1156	−17.948	−116.050	CCM	38.06	−91.24	11.00	60.26	22.38	207.35	−47.00	5.25	3.42	0.33	20.96	153.85	284.70	191	EPR	284.2	3.94
1992090	1809	−17.843	−116.169	CCM	38.06	−91.24	15.00	60.12	22.55	207.61	−41.00	3.50	2.83	0.28	32.17	153.73	284.80	191	EPR	297.4	4.08
1994246	0902	−31.482	−111.125	CCM	38.06	−91.24	7.00	71.51	16.50	197.93	−33.00	6.75	2.60	0.36	33.79	158.11	281.70	186	EPR	68.3	0.89
2000218	0613	−24.455	−112.156	EYMN	47.95	−91.50	15.00	74.34	14.16	199.37	−18.00	6.50	1.95	0.30	143.11	156.65	282.30	189	EPR	21.2	3.04
2004115	2300	−28.937	−112.365	SLM	38.64	−90.24	15.00	70.63	18.36	200.58	81.00	14.00	1.02	0.39	147.35	157.91	282.50	186	EPR	31.7	0.32
2004190	1954	−25.041	−115.959	SLM	38.64	−90.24	12.00	67.67	21.49	205.13	−37.00	10.25	2.28	0.22	99.21	157.12	284.30	189	EPR	19.4	0.17
2007045	0129	−29.520*	−112.080*	ULM	50.25	−95.87	10.00*	80.71	10.46	194.27	−7.00	9.75	2.17	0.33	44.91	157.95	282.20	186	EPR	37.4	0.35
1996249	0814	−22.180	−113.456	STACK03	0.00	0.00	10.00	74.20	0.00	0.00	−43.00	3.25	1.98	0.14	0.00	155.89	283.10	191	EPR	90.5	1.04
2000299	0526	−34.578	−109.659	STACK02	0.00	0.00	12.90	74.68	0.00	0.00	−88.00	8.50	1.82	0.35	0.00	58.81	100.70	186	EPR	28.1	3.00
2002183	1015	−29.867	−112.460	STACK03	0.00	0.00	15.00	73.76	0.00	0.00	76.00	3.00	1.62	0.21	0.00	157.99	282.40	186	EPR	51.1	0.96
2004193	2346	−20.235	−126.911	STACK02	0.00	0.00	12.00	70.30	0.00	0.00	63.00	18.00	1.70	0.54	0.00	156.54	290.00	187	EPR	1178.3	23.23
2005170	0201	−23.959	−111.999	STACK02	0.00	0.00	6.10	69.66	0.00	0.00	15.00	37.00	2.42	0.82	0.00	156.46	282.30	189	EPR	21.5	3.00
2008355	2105	−31.190*	−13.340*	STACK02	0.00	0.00	4.00*	66.56	0.00	0.00	−70.00	5.00	1.57	0.32	0.00	35.80	258.20	172	MAR	4.3	0.53
2009065	1050	80.320*	−1.850*	STACK07	11.65	40.21	9.00*	71.29	0.00	0.00	88.00	16.75	1.18	0.54	0.00	14.36	302.60	139	Gakkel	2.0	6.53
1998080	1633	80.063	2.671	FURI	8.90	38.68	8.00	73.37	141.87	353.89	75.00	18.75	1.35	0.89	100.41	14.25	305.50	134	Gakkel	27.9	24.71
2005065	0501	84.899	99.054	FURI	8.90	38.68	9.90	78.64	241.24	4.60	13.00	15.00	1.15	0.34	139.93	9.35	46.40	128	Gakkel	2.6	1.37
2005065	0521	84.913	99.618	FURI	8.90	38.68	17.20	78.72	241.84	4.56	−46.00	27.50	2.05	0.82	17.58	9.36	47.20	128	Gakkel	3.1	0.24
1999032	1155	85.561	86.684	FURI	8.90	38.68	15.40	78.22	229.07	3.41	−20.00	30.25	1.30	0.88	25.77	9.81	34.20	123	Gakkel	24.4	0.52
2008354	0831	47.000*	−27.290*	MAYE	12.78	39.53	2.00*	64.97	98.21	316.02	69.00	12.25	0.90	0.20	114.92	23.32	278.20	172	Reykjanes	2.8	0.11
2000252	0134	−39.786	41.673	DRV	−66.66	140.00	15.70	57.46	152.15	244.79	35.00	9.25	3.10	0.46	82.22	14.77	190.30	72	SWIR	147.4	48.51

STA: STACKN indicates stacked measurement of N results. AZI and BAZ are given as 0 and 0, and FAST is $-\phi''$ (fast at source), so that $\phi'' = \text{azi} + \text{baz} - \phi$ gives correct result

DIST: epicentral distance (degrees)

FAST: fast shear wave orientation at receiver

SRCPOL: recovered source polarisation from minimum eigenvalue splitting analysis

SR: NUVEL-1A spreading rate

DIRN: NUVEL-1A spreading direction

RIDGE/TRANstr: strike of ridge or transform segment (azimuth)

RDIST: distance to ridge

* denotes ISC location, rather than EHB location

Table 3.2 Individual source-side shear wave splitting results beneath mid-ocean ridge transforms. Headings as explained in Table 3.1

DATE	TIME	EVLAT	EVLON	STA	STLAT	STLON	DEPTH	DIST	AZI	BAZ	FAST	DFAST	DT	DDT	SRCPOL	SR(mm/a)	DIRN(az)	TRAN strike	LOC	RDIST(km)	AGE(Ma)
1997161	2153	−35.747	−108.145	STACK03	0.00	0.00	7.00	77.24	0.00	0.00	−77.00	4.50	1.12	0.07	0.00	59.02	99.50	99	EPR	196.6	5.13
2000299	0526	−34.578	−109.659	STACK02	0.00	0.00	12.90	74.68	0.00	0.00	−88.00	8.50	1.82	0.35	0.00	58.81	100.70	99	EPR	28.1	3.00
1990336	0844	−26.755	−114.171	CCM	38.06	−91.24	2.20	67.94	19.36	202.06	11.00	23.50	1.20	0.97	145.22	157.50	283.40	103	EPR	13.2	1.46
1997149	1702	−35.891	−102.506	SLM	38.64	−90.24	10.00	70.99	8.90	189.66	−22.00	17.50	0.50	0.17	120.35	217.14	283.50	99	EPR	6.4	8.19
1991051	0448	−22.604	−112.956	CCM	38.06	−91.24	18.20	63.74	19.06	202.47	−8.00	6.50	3.20	0.23	41.30	156.02	282.90	88	EPR	39.2	1.61
1990336	0844	−26.755	−114.171	CCM	38.06	−91.24	2.20	67.94	19.36	202.06	11.00	23.50	1.20	0.97	145.22	157.50	283.40	103	EPR	13.2	1.46
1991051	0448	−22.604	−112.956	CCM	38.06	−91.24	18.20	63.74	19.06	202.47	−8.00	6.50	3.20	0.23	41.30	156.02	282.90	88	EPR	39.2	1.61
1997131	2216	−36.481	−97.857	CCM	38.06	−91.24	25.00	73.71	5.19	185.35	−58.00	7.25	2.50	0.67	105.26	58.84	91.30	95	EPR	26.1	2.45
1997149	1702	−35.891	−102.506	SLM	38.64	−90.24	10.00	75.05	9.95	190.31	−14.00	15.75	0.50	0.14	121.66	58.93	95.20	96	EPR	6.4	8.19
1997227	0737	−4.393	−105.759	DRLN	49.26	−57.50	10.00	67.67	31.80	233.33	−34.00	25.00	0.88	0.91	0.01	138.65	279.90	99	EPR	17.5	0.51
1999194	1226	−34.938	−103.616	EYMN	47.95	−91.50	15.00	83.84	8.49	190.32	−6.00	6.00	2.15	0.23	118.62	58.86	96.40	99	EPR	77.0	7.94
2005191	0446	−36.336	−97.312	DRV	−66.66	140.00	11.50	68.90	200.82	133.78	59.00	10.00	0.85	0.24	84.37	58.93	90.30	91	EPR	8.1	0.58
1997161	2153	−35.747	−108.145	STACK03	0.00	0.00	7.00	77.24	0.00	0.00	−77.00	4.50	1.12	0.07	0.00	59.02	99.50	99	EPR	196.6	5.13
2007165	1337	−36.220*	−100.370*	STACK03	0.00	0.00	17.70*	79.62	0.00	0.00	11.00	3.25	2.58	0.12	0.00	58.97	93.50	95	EPR	15.9	10.10
1990224	0035	0.909	−28.801	CCM	38.06	−91.24	12.40	67.95	310.97	106.99	−61.00	6.50	3.08	0.26	86.84	31.79	264.50	89	MAR	29.6	5.88
1995177	2126	7.083	−34.362	CCM	38.06	−91.24	15.80	59.78	310.06	105.81	−44.00	26.00	2.20	0.89	89.81	29.66	267.20	90	MAR	7.4	8.18
1998169	0417	−11.516	−14.092	SCHQ	54.83	−66.83	7.00	79.68	332.01	127.36	−56.00	7.25	1.83	0.34	12.06	35.03	258.20	79	MAR	24.9	5.68
2006156	0634	1.009	−28.156	SCHQ	54.83	−66.83	23.60	62.22	335.88	135.08	20.00	10.00	1.25	0.26	54.50	31.80	264.10	89	MAR	32.7	9.71
2007184	0825	0.720*	−30.270*	AAM	42.30	−83.66	10.00*	63.21	318.16	115.95	0.00	13.50	1.83	0.56	125.10	31.83	265.20	89	MAR	11.4	8.72
2008118	1435	−35.460*	−16.600*	SMRE	13.20	39.21	10.00*	71.59	58.11	225.37	−57.00	3.50	2.50	0.19	69.22	35.49	259.50	83	MAR	2.9	3.42
2008254	1308	8.090*	−38.700*	SLM	38.64	−90.24	9.00*	55.30	311.76	109.43	−33.00	8.25	1.73	0.21	103.56	29.27	269.60	91	MAR	2.5	3.90
2008254	1308	8.090*	−38.720*	MAYE	12.78	39.53	10.00*	76.86	78.75	275.43	−24.00	9.00	3.02	0.55	359.60	29.27	269.60	91	MAR	3.5	4.07
2007124	1206	−1.410*	−14.920*	STACK02	0.00	0.00	7.00*	66.56	0.00	0.00	79.00	18.25	1.32	0.47	0.00	33.02	258.00	78	MAR	106.5	6.89
2007212	2255	−0.160*	−17.800*	STACK03	0.00	0.00	11.00*	68.98	0.00	0.00	19.00	1.75	1.50	0.19	0.00	32.55	259.20	78	MAR	5.5	13.80
2008039	0938	10.670*	−41.900*	STACK02	0.00	0.00	9.00*	79.32	0.00	0.00	53.00	13.25	1.15	0.51	0.00	28.31	271.50	92	MAR	88.9	5.86
2008115	1214	−1.180*	−23.470*	STACK02	0.00	0.00	10.00*	67.68	0.00	0.00	−60.00	14.00	0.90	0.24	0.00	32.57	261.90	86	MAR	4.8	24.90
2008144	1935	7.310*	−34.900*	STACK05	0.00	0.00	9.00*	73.46	0.00	0.00	−20.00	2.25	2.50	0.17	0.00	29.58	267.50	91	MAR	10.1	1.51
2008150	1546	64.000*	−21.010*	STACK02	0.00	0.00	9.00*	67.10	0.00	0.00	−30.00	12.25	1.52	0.40	0.00	19.69	283.30	298	Iceland	14.9	7.56

(continued)

Table 3.2 (continued)

DATE	TIME	EVLAT	EVLON	STA	STLAT	STLON	DEPTH	DIST	AZI	BAZ	FAST	DFAST	DT	DDT	SRCPOL	SR(mm/a)	DIRN(az)	TRAN strike	LOC	RDIST(km)	AGE(Ma)
2008209	2115	−0.250*	−18.290*	STACK02	0.00	0.00	17.00*	73.34	0.00	0.00	52.00	18.25	0.68	0.26	0.00	32.55	259.40	78	MAR	2.1	11.95
2008209	2115	−0.250*	−18.300*	STACK02	0.00	0.00	10.00*	58.60	0.00	0.00	−14.00	5.00	2.52	0.47	0.00	32.55	259.40	78	MAR	1.0	11.95
2008224	2338	−1.020*	−21.840*	STACK06	0.00	0.00	13.00*	62.58	0.00	0.00	−44.00	6.00	1.15	0.09	0.00	32.59	261.10	82	MAR	13.9	24.44
2008327	1849	−1.230*	−13.930*	STACK04	0.00	0.00	10.00*	55.04	0.00	0.00	38.00	2.00	2.50	0.09	0.00	33.02	257.50	77	MAR	96.0	4.61
2004105	2307	71.056	−7.696	FURI	8.90	38.68	14.70	68.69	128.91	345.18	−8.00	20.50	1.15	0.47	110.10	17.32	292.80	124	Gakkel	11.6	14.78
2007097	0709	37.280*	−24.680*	FURI	8.90	38.68	8.60*	63.51	99.30	307.19	66.00	5.75	3.03	0.19	181.38	20.68	103.40	103	Reykjanes	4.7	46.41
1998047	2353	52.688	−33.666	FURI	8.90	38.68	8.00	72.30	98.71	322.52	81.00	20.25	0.85	0.49	235.65	22.44	275.40	93	Reykjanes	5.3	10.34
2003092	0343	35.212	−35.704	FURI	8.90	38.68	9.60	72.21	91.63	304.14	−26.00	16.00	1.00	0.33	30.06	21.93	103.60	103	Reykjanes	5.1	2.57
2008140	0316	−47.780*	31.970*	STACK04	0.00	0.00	10.00*	58.76	0.00	0.00	83.00	4.25	2.65	0.17	0.00	14.64	197.80	207	SWIR	81.0	23.47
2008152	0437	−41.220*	80.510*	STACK09	0.00	0.00	10.00*	64.46	0.00	0.00	11.00	2.75	1.65	0.06	0.00	69.40	44.60	42	SWIR	10.4	2.13
2009056	1608	−41.890*	88.630*	STACK03	0.00	0.00	10.00*	68.58	0.00	0.00	7.00	14.75	0.60	0.16	0.00	71.72	37.90	37	SWIR	7.4	0.48

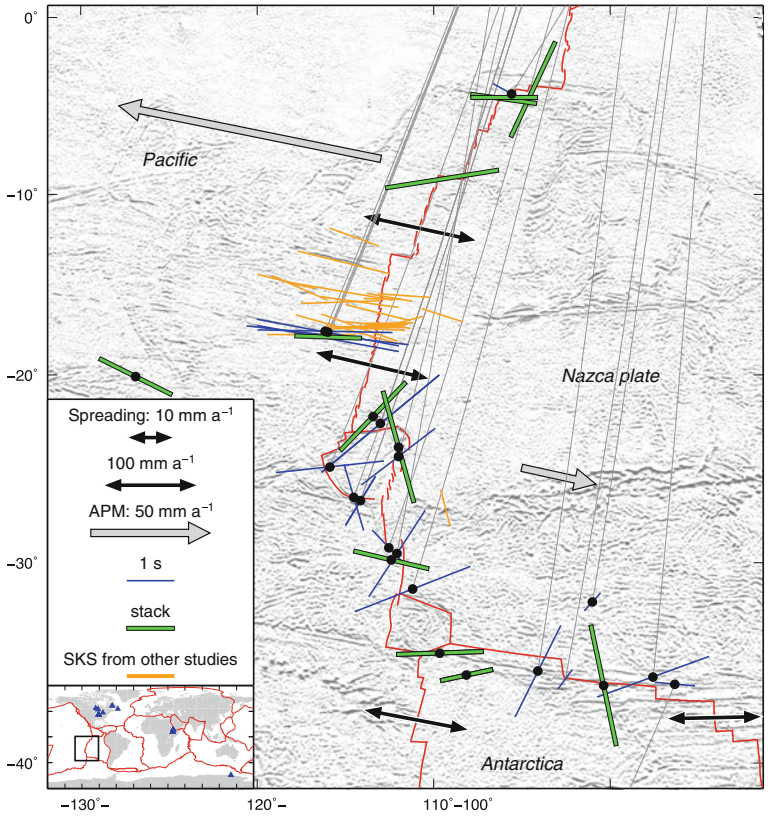

Fig. 3.6 Source-side splitting beneath events on the EPR. Dots show earthquake locations, with *bars* indicating splitting parameters, where the orientation shows ϕ'' and the length δt, as in the legend. *Blue bars* are for single measurements; *green* for stacks. *Orange bars* show SKS splitting parameters from previous studies (Wolfe and Solomon 1998; Harmon et al. 2004). Thin *grey lines* show raypaths to stations (*blue triangles, inset map*). Shading indicates bathymetry (Smith and Sandwell 1997), and *thin red lines* are plate boundaries. *Black double-headed arrows* show base-10 logarithm of NUVEL-1A full spreading rates at selected locations along the ridge. *Grey arrows* show the absolute plate motion (APM) in the HS3 reference frame of the NUVEL-1A model (Gripp and Gordon 2002). The legend indicates spreading and APM rates. Results include stacks from Nowacki et al. (2010)

(Butt Crater, Ascension Island; Wolfe and Silver 1998) and SHEL (Horse Pasture, St. Helena; Behn et al. 2004).

Along transform zones, about half the results show ϕ'' close to the spreading direction, whilst many show large (∼2.5–3 s) δt and ϕ'' roughly perpendicular to the strike of the transform. The dependence of splitting parameters upon distance along the transform zone, away from the nearest ridge segment, is shown in Fig. 3.8. The pattern shows considerable variation near the ends of the transform zones, close to the ridge axes, perhaps related to the complex tectonic environment and resultant

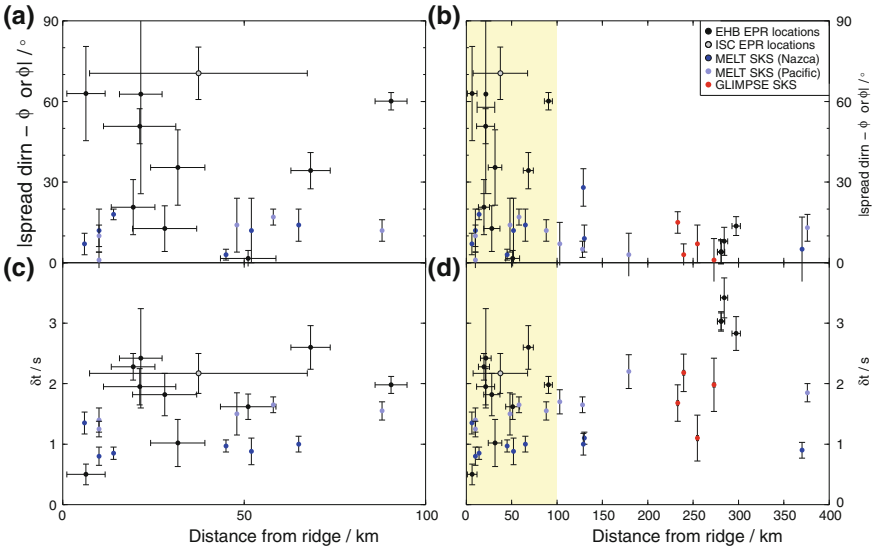

Fig. 3.7 Variation of splitting parameters beneath 'ridge' events with distance away from the axial ridge at the EPR. *Top panel* shows the absolute difference between the spreading direction ('spread dirn') and the fast orientation (ϕ for SKS splitting parameters; ϕ'' for source-side splitting parameters). *Black* and *grey circles* indicate respectively the EHB and standard ISC locations of the events in this study. *Error bars* show 95 % confidence interval in splitting parameters and stated uncertainty in event locations. *Coloured circles* indicate MELT (*blue*) and GLIMPSE (*red*) SKS splitting parameters as shown in the legend, where MELT stations on the Pacific and Nazca plates are coloured lighter and darker respectively. All GLIMPSE stations are on the Pacific plate. Shaded part of panels on right shows regions shown by panels on left. **a** and **b** Modulus of difference in angle between ϕ'' or ϕ_{SKS} and the plate spreading direction (DeMets et al. 1994). **c** and **d** Splitting times for S or SKS

shearing and melt production. However, there is a decrease in the maximum delay time as distance from the ridge axis increases, possibly indicating a reduced contribution from a mechanism of anisotropy arising due to melt or other sub-axial process (Fig. 3.9).

Two events on the MAR gave results at stations in both North America and Ethiopia. In this case, we may examine the azimuthal dependence of the splitting. Figure 3.10 shows equal-area lower-hemisphere stereoplots of the splitting parameters, which are notably different along the two different azimuths. Splitting measured at North American stations for both events has smaller δt (stacked splitting parameters: $\phi'' = (25 \pm 4)°$, $\delta t = (1.9 \pm 0.1)$ s), whereas δt is larger when measured along the other azimuth at Ethiopian stations ($\phi'' = (76 \pm 2)°$, $\delta t = (2.6 \pm 0.1)$ s). At this limited range of slownesses, there is not much variation in the angle away from the vertical for the rays, so the differences primarily arise due to azimuth. The Fresnel zones of the two rays of period 20 s stop overlapping significantly when deeper than ∼200 km, so if heterogeneity were the cause, then the majority of the anisotropy would need to be present below this.

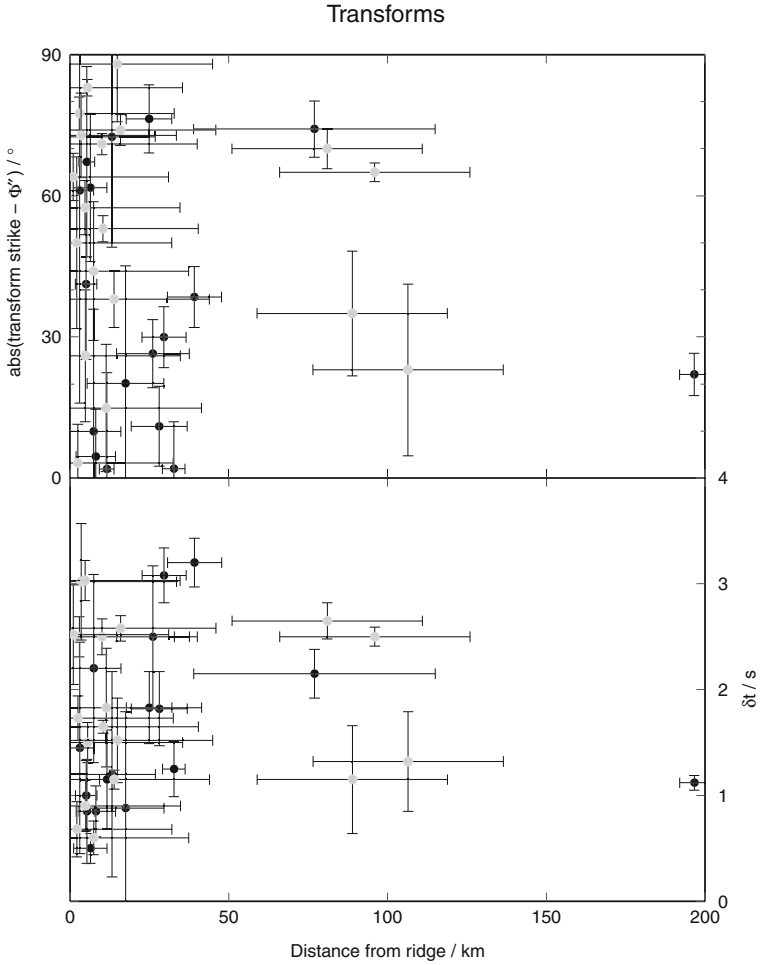

Fig. 3.8 Variation in splitting parameters with distance from nearest ridge segment for events classified as on transforms. *Upper diagram* shows the absolute difference between the source fast orientation, ϕ'', and the strike of the transform. *Dark circles* show EHB relocations; *light circles* represent ISC locations. *Error bars* show published uncertainty in earthquake locations

3.3.3 Gakkel Ridge

Ten results from events on the Gakkel Ridge were of 'good' or better quality, with an equal number of null results. The splitting parameters are shown in Fig. 3.11a. It is notable that most results show a small amount of splitting ($\langle \delta t \rangle = 1.1$ s), and there is a higher proportion of null results than in other regions. The splitting that is present is often ridge-parallel. The spreading rate predicted by NUVEL-1A (DeMets et al. 1994) increases from ~6 to 18 mm a^{-1} from right to left in Fig. 3.11a, however

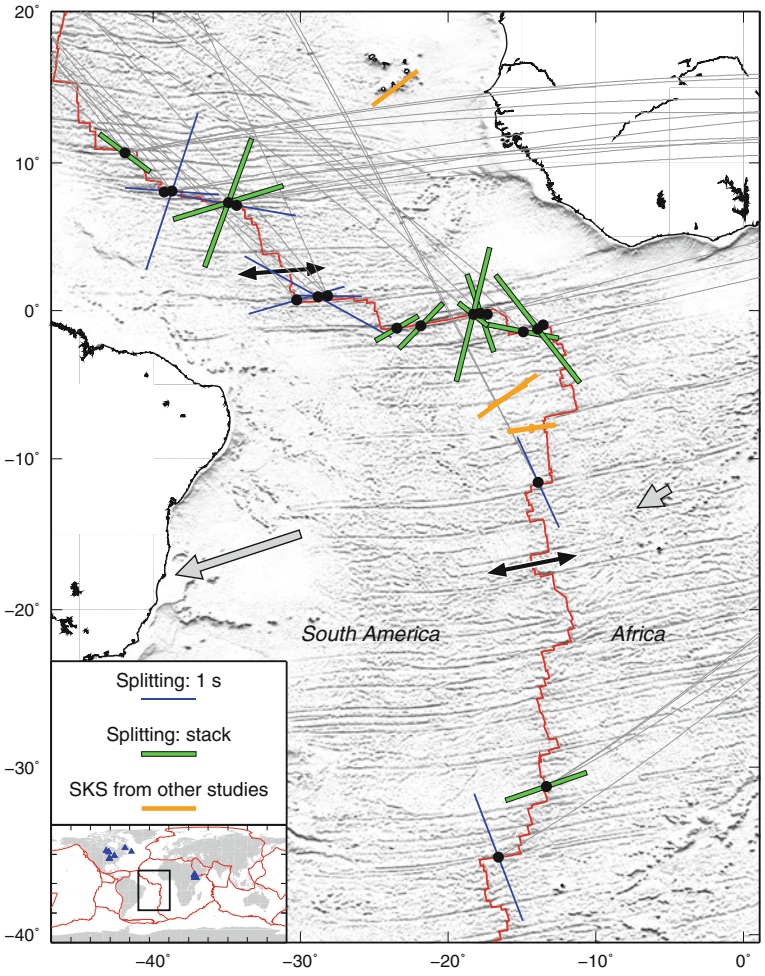

Fig. 3.9 Splitting parameters beneath events on the MAR. Symbols as for Fig. 3.6. *Orange bars* show SKS results of Wolfe and Silver (1998) and Behn et al. (2004). Note that some events are measured at stations in both North America and Ethiopia, in which case stacks of results for both directions are shown. Spreading rates and APM are of same scale as Fig. 3.6

there is no clear corresponding trend in the amount of splitting. There is also no obvious systematic variation of parameters for the cluster of events furthest north (rightmost in Fig. 3.11a, circled) with azimuth. A lower amount of splitting beneath such extremely slow-spreading ridges might be related to reduced melt production caused by slow exhumation of material and a consequently small amount of adiabatic decompression melting. If this is the case, the dominant contribution to seismic anisotropy at teleseismic distances would then be from LPO, yet the axis-parallel fast orientations we observe are hard to explain via mineral alignment.

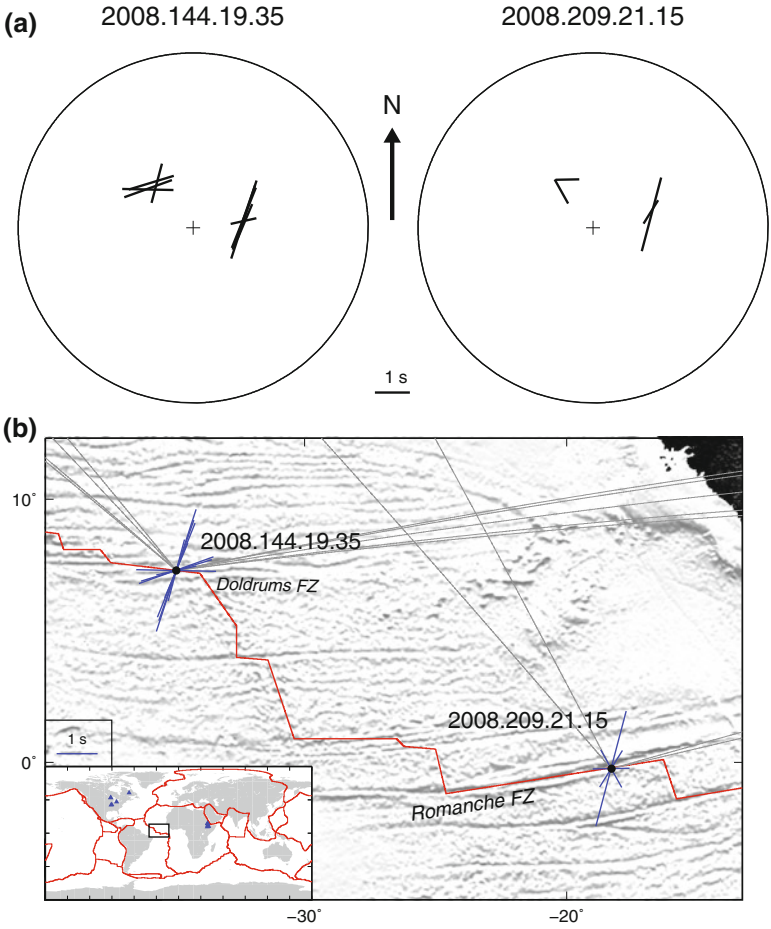

Fig. 3.10 Lower-hemisphere diagrams for splitting parameters measured beneath two events on the MAR. **a** Azimuthal and inclination-dependence of splitting parameters shown on equal-area lower-hemisphere projections. Average inclination of downgoing rays in top 150 km of IASP91 (Kennett and Engdahl 1991) is shown by radial distance (with vertical at the centre). Azimuth corresponds to azimuth at the event. Bar orientation and length corresponds to ϕ'' and δt respectively, as per the scale, centre. The splitting times measured at Ethiopian stations (group on right of hemispheres) are larger for both events, and ϕ'' is also different. **b** Location of events and individual splitting measurements shown at earthquake location. *Bars* correspond to splitting parameters as for previous figures, with delay time indicated by length as per the legend (*left*). *Inset map* show location of larger map by *thick black box*. The raypaths to Ethiopia run along the transform zones, whilst those to North America move away from the transforms

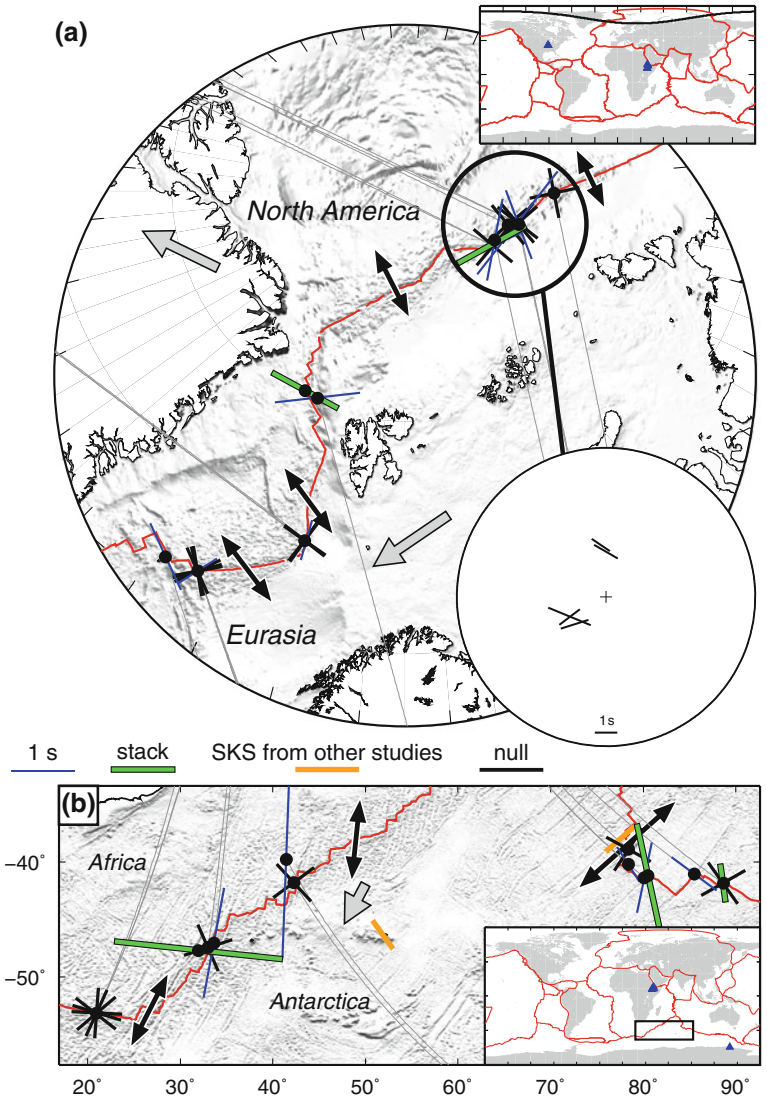

Fig. 3.11 Splitting parameters beneath events on the Gakkel, Southeast and Southwest Indian Ridges. *Symbols* as for Fig. 3.6, except null results are shown by *black* crosses with *bars* parallel to the two null directions. **a** Results for events on Gakkel Ridge. *Thick black circle* shows results included in lower hemisphere stereoplot, *inset* lower right. *Bars* above the centre show measurements made at North American stations; those to the lower left show measurements at Ethiopian stations. Scale indicated at bottom. **b** Results for events on Southwest and Southeast Indian Ridges. SKS splitting at CRZF (Base Alfred Faure, Crozet Islands) and AIS (île Nouvelle-Amsterdam; Behn et al. 2004) is shown by the orange bar. APM is less than 10 mm a^{-1} for African plate, and parallel to spreading direction at ~65 mm a^{-1} for Australian plate (northeast corner, not labelled)

3.3.4 Southwest and Southeast Indian Ridges

Beneath events on the SIRs, 43 individual results, allowing three stacked results, and seven null measurements were made. These are shown in Fig. 3.11b. Again, the pattern is complicated, and few events lie on ridge segments: most are on transforms. The Southwest Indian Ridge shows some of the most oblique spreading of any MOR, so whilst it would be desirable to test whether fast orientations are spreading direction-parallel, or ridge-perpendicular, there are insufficient large earthquakes to make any strong inferences from source-side splitting. Interestingly, all measurements made from beneath the ridge segment at longitude 20° appear to be null. This might result from the absence of anisotropy in the region, but it may also occur if the source polarisation is parallel or perpendicular the local fast orientation of some anisotropy. With only one azimuth of measurements and no other events with different source polarisations, it is not possible to distinguish these scenarios.

3.4 Interpretation

3.4.1 Doldrums FZ Observations

The multi-azimuth observations made beneath earthquakes on the Doldrums Fracture Zone (FZ) in Sect. 3.3.2 allow us to examine the likely style of style deformation here. As a first approximation, we can seek to define an hexagonal symmetry, oriented arbitrarily (called 'tilted transverse isotropy', or TTI). If we assume Thomsen's (1986) anisotropic parameters $\delta = \varepsilon$ (the case of elliptical anisotropy), we can use the two azimuths of observations to find the plane of isotropy, or axis of symmetry, by simple trigonometry (Nowacki et al. 2011). This dips shallowly ($30° \pm 6°$), to the southwest (direction $232° \pm 2°$), as shown by the dashed line in Fig. 3.12. For TTI derived from aligned melt, for instance, this would correspond to penny-shaped inclusions having their short axis aligned about 35° from the vertical, indicated by the solid line in Fig. 3.12. This is in some sense similar to the orientations predicted by simulations (Weatherley and Katz 2010), which suggest melt should be focussed along northwest–southeast flow lines for a transform in this orientation. Intriguingly, it also would be consistent with the suggestion of van Wijk and Blackman (2005), who speculate that the transform fault itself would dip towards the ridge segment near the ends of the transform.

Another likely contributor to seismic anisotropy in the FZ would be the alignment of olivine in response to flow. Natural samples and deformation experiments show that the dominant way in which olivine develops an LPO is by slip in the a-direction, along the $\{0kl\}$ or (010) (b-) planes, known as D- and A-type olivine respectively. We examine the possibility that the observed anisotropy at the Doldrums FZ is caused by olivine LPO by using the method described by Wookey and Kendall (2008) and Nowacki et al. (2010). We use the single-crystal elastic constants of

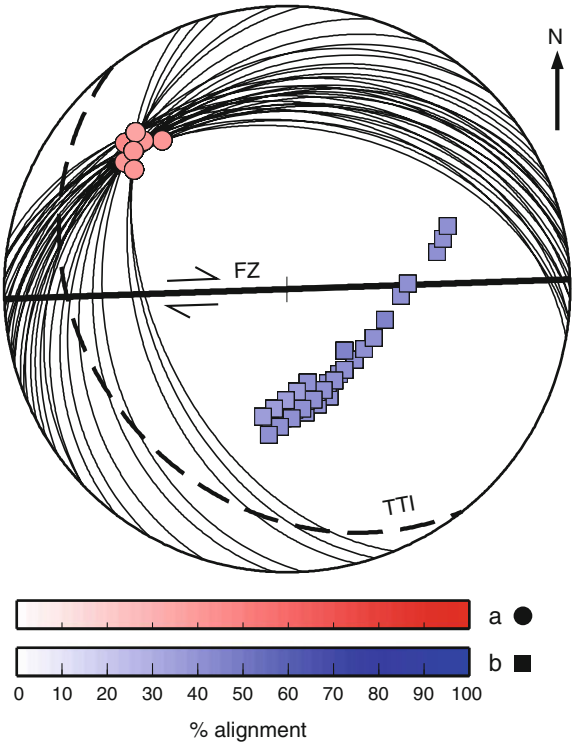

Fig. 3.12 Orientations of olivine a- and b-axes compatible with observations from event 2008.144.19.35 on the Doldrums FZ, MAR. Lower-hemisphere equal area plot shows north upward and the vertical direction out of the page. *Red circles* (*a-axes*) and *blue squares* (*b-axes*) are shaded per the degree of alignment according to the scale below. *Thick black solid line* shows approximate strike of FZ and spreading direction, with strike-slip arrows indicating sense of shear. *Thick dashed line* is best-fitting plane of isotropy from fit of TTI to fast orientations. *Thin solid lines* are crystallographic slip planes (*b-planes*) for the case of 'A-type' olivine LPO

olivine (Abramson et al. 1997) and mix them using Voigt–Reuss–Hill averaging with an isotropic average. The proportion of anisotropic constants in the Voigt–Reuss–Hill mixture approximately corresponds to the strength of LPO in an olivine aggregate. We then rotate these constants to all possible orientations and compute the shear wave splitting accrued over a 200 km thick layer for the two raypaths observed. If in this orientation the constants can reproduce the observations within the uncertainty, they are retained. Figure 3.12 shows the compatible orientations and degree of alignment as the a- and b-axes of the aligned olivine on a lower-hemisphere equal-area projection.

It is clear that the only compatible orientations require the olivine a-axes to line up northwest–southeast, approximately 45° to the FZ strike. For the layer thickness we adopt (200 km), alignments of 35–40 % are required, though there is obviously a trade-off between the two. For the case of A-type olivine LPO, the glide or shear planes (thin black lines, Fig. 3.12) may dip north, northwest, or west, but are all

shallow. In any case, it seems likely that flow is oblique to the direction of shear. Finite-element modelling of ridge transforms (e.g., van Wijk and Blackman 2005; Sparks et al. 1993; Phipps Morgan and Forsyth 1988) suggests that in such left-offset transform zones on north-south striking ridges, the dominant direction of mantle flow should be northwest-southeast, just as we infer. Such modelling, however, indicates that transforms are also the site of the smallest-magnitude flow in the vicinity of MORs, and at this location the half-spreading rate ($\sim$15 mm a^{-1}) is comparable to the absolute plate motion ($\sim$14 mm a^{-1}) (Gripp and Gordon 2002). Given that we infer $\sim$30 % alignment of olivine, which is a significant texturing, one would expect the deformation to be relatively strong, raising further questions in this interpretation. Although these early-stage measurements are insufficient to uniquely characterise the mantle processes at fracture zones, further work has the potential to yield significant information to test hypotheses of oceanic transform dynamics.

3.4.2 Comparison of EPR Observations with Model Predictions

In dynamic models of MOR accretion, spreading rate, asthenospheric viscosity μ, bulk chemistry and relative strength of mineral slip systems are some of the primary controls on the type of flow, and anisotropic structure created by the flow, beneath MORs (Blackman et al. 1996, 2002, Blackman and Kendall 2002; Podolefsky et al. 2004; Nippress et al. 2007). Blackman et al. (1996) investigate the polycrystalline behaviour of an olivine upper mantle under expected conditions of MOR spreading at the ridge axis. They then investigate the splitting caused in vertically propagating S waves (approximating SKS), dependent upon distance from the axis. Later work (Blackman and Kendall 2002) used a 70 % olivine, 30 % enstatite mantle, and also investigated splitting predicted by such models for both vertical and inclined (by 20°, approximating S) shear waves within the ridge-perpendicular plane.

In their models, slow spreading ridges (full-rate $\sim$40 mm a^{-1}) show ridge-parallel splitting within $\sim$20 km from the axis because of the requirement that buoyant flow beneath the ridge axis supplies the upwelling material in a small region. Fast-spreading (full-rate $\sim$140 mm a^{-1}) ridges, by contrast, do not focus material so efficiently towards the centre and should not produce much observable difference in splitting times between the ridge axis and at distance (>50 km). Both cases show $\sim$0.5–1 s of splitting away from the axis. Hence their model predicts there should be little observable difference in splitting in SKS for fast ridges at the axis compared to at distance (>50 km). This agrees with SKS measurements at the EPR (Wolfe and Solomon 1998; Harmon et al. 2004), where full-spreading rates are >60 mm a^{-1}, and on average $\sim$150 mm a^{-1}.

Figure 3.15 shows δt versus the spreading rate for all 'ridge' events in this study; filled circles show events less than 50 km from the ridge axis. Although there is some scatter in the data, it appears that there is not an obvious trend of a decrease in

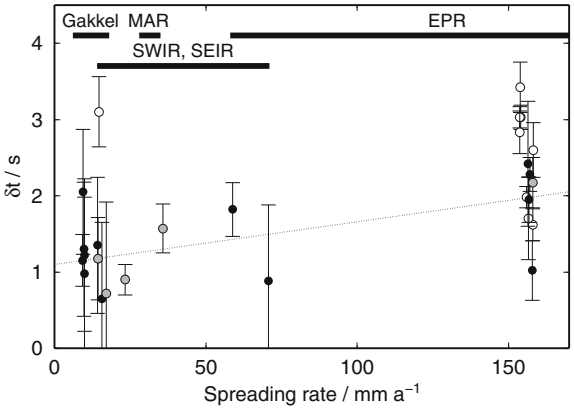

Fig. 3.13 Splitting time versus spreading full-rate beneath all 'ridge' events. *Filled circles* show results less than 50 km from the ridge axis: *black circles* shows events with EHB locations; *grey circles* indicate ISC locations. *Open circles* indicate events >50 km from the axis (all EHB locations). *Thick bars* show range of spreading rates represented by events beneath each MOR in this study. Weighted linear fit to near-axis (*filled circles*) data is shown with thin *dotted line*

maximum splitting time with spreading rate within 50 km of the axis. Rather, there seems to be a weakly positive correlation, if any. (Weighted least-squares linear regression for results <50 km from axis gives $R^2 = 0.42$.)

Whilst most authors predict increased splitting at the slowest MORs, some observations suggest that anisotropy away from the ridge increases with palaeo-spreading rate. P wave anisotropy in the shallow lithosphere beneath the northwest Atlantic (spreading full-rate ~20 mm a^{-1}) is significantly less at ~3 % (Gaherty et al. 2004) than that observed at present-day fast-spreading sites near the East Pacific Rise (~6 %, rate ~100 mm a^{-1}) (Dunn and Toomey 1997) and old lithosphere in the western Pacific (~6 %, palaeo-rate ~60 mm a^{-1}) (Shearer and Orcutt 1986). Such observations constrain the anisotropy in the uppermost mantle, hence probably reflect the effect of 'frozen-in' olivine LPO and processes contemporaneous with lithosphere creation. Gaherty et al. (2004) suggest a spreading rate dependence could be due to slower ridges accommodating more deformation by brittle failure in the crust, leading to reduced LPO in the uppermost mantle. However, our shear wave splitting measurements integrate anisotropy over the complete ray path in the upper mantle, and it is not clear that this effect could cause the change in δt we observe, given the thickness of the brittle crust.

The preceding discussion, however, ignores the effect of a general anisotropy within the model, which will cause the splitting parameters to vary with azimuth and inclination of the up- or down going ray. Blackman and Kendall (2002) explore the effect of inclination within the ridge axis-perpendicular plane and show rays incident at 20° (approximating S) exhibit more splitting. However, they neglect the additional effect of azimuth on the splitting parameters, and for this study we are interested in the downgoing S phase, not upcoming. The backazimuths of the SKS phases used at

the EPR by Wolfe and Solomon (1998) and Harmon et al. (2004) are approximately ridge-perpendicular, whilst the azimuths of the S phases used in this study are close to ridge-parallel. This may then explain the discrepancy between the SKS and S splitting parameters beneath the EPR.

In order to assess the likely impact of the azimuth of waves at MORs on the splitting parameters caused by the anisotropy present, we require an anisotropic seismic model of a MOR. Here, we calculate the splitting predicted by the model of Blackman and Kendall (2002). For fast ridges such as the EPR, we use their texture model for a full-spreading rate of 146 mm a^{-1}, asthenospheric viscosity μ of 10^{20} Pa s, and a 70–30 % mixture of olivine and enstatite. We then calculate the shear wave splitting for S (downgoing, incidence angle $\sim$25°) and SKS (upcoming, incidence angle $\sim$15°) across all azimuths (corresponding to backazimuths for SKS) at various distances from the centre of the model (the ridge axis). We use a ray-theoretical approach, and hence the rays sample a small width. Because the anisotropic model does not vary significantly over scales of $\leq$10 km, this approximation is adequate to asses the impact of variable azimuth and inclination. As the rays traverse the model, the elastic constants at each point are used to predict the local shear wave splitting by solving the Christoffel equation, given the ray's local azimuth and inclination. The fast orientation and delay time are applied in sequence to a synthetic waveform of similar dominant period to that of the data (10 s) in the frequency domain to reduce numerical instability. The final, split waveform is analysed using the method of Teanby et al. (2004) to measure the predicted shear wave splitting that would be observed. More details of the method are given in Sect. 5.2.3 and Appendix B.

Blackman and Kendall (2002) calculate the texture along flow lines which begin at the base of the model and are predictably spaced at this point. However, the calculation points follow the flow field, and thus these paths do not produce elastic constants at regular positions. The model must therefore be regridded for our purposes. To remove artefacts of the gridding procedure, we smooth the discontinuous model using a Gaussian filter with standard deviation $\sigma = 4$ km, where the elastic constants are averaged using Voigt–Reuss–Hill averaging according to the Gaussian filter kernel. The smoothing may also alleviate some of the problems with the ray-theoretical assumption by preventing very close rays from having drastically different splitting parameters.

Figure 3.14 shows the texture model used in the rest of this study. Panel A shows the thermal and flow structure used to calculate the texture from which the elastic constants are calculated for two cases. We use the passive case (left). Panel B shows pole figures for olivine and enstatite at selected points along the texture calculation path lines. Panel C displays the gridded model in the x_1–x_3 plane (x_1 is parallel to spreading, x_3 is upwards, and x_2 is parallel to the ridge axis). The smoothed constants are evaluated on a 4×4 km grid in the x_1–x_3 plane, and at each point the strength of anisotropy is indicated by the value of the universal elastic anisotropy index (Ranganathan and Ostoja-Starzewski 2008; see Appendix A), A^U. This is 0 for isotropic elasticity tensors (white in Fig. 3.14), and increases positively with increasing elastic anisotropy (darker colours).

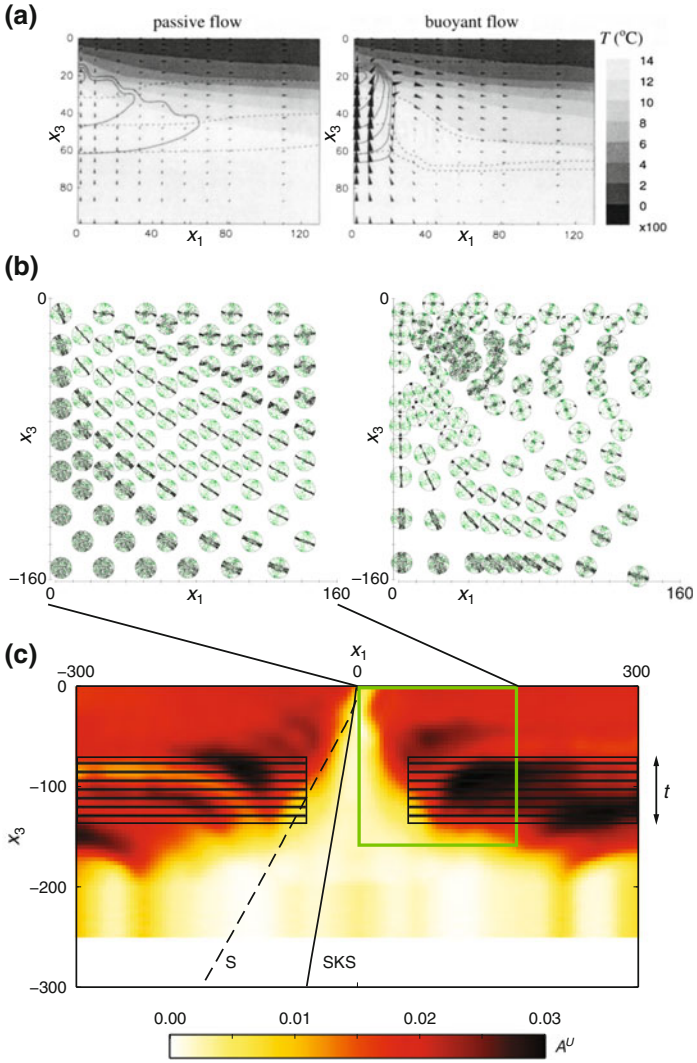

Fig. 3.14 Texture model used in calculating shear wave splitting beneath the EPR. Each subfigure is a depth section taken across the MOR model, parallel to the spreading direction. **a** Thermal (*shading*) and flow (*arrows*) structure of MOR. (*Solid* and *dashed lines* refer to melt and mantle depletion, not present in this model.) Models with passive (*left*) and active upwelling are shown, but only the passive case is considered here. After Blackman and Kendall (1997). **b** Olivine (*black*) and enstatite (*green*) LPO development. Each *circle* is a pole figure with the centre the x_2 axis, showing orientations of [100] axes for 1000-grain aggregates in the texture calculation. Alignment of olivine predominantly determines the local anisotropy. After Blackman et al. (2002). **c** Input elasticity model used in this study. Elastic constants from panel B are shown gridded and smoothed. Colour represents the strength of anisotropy locally by the value of A^U (see text). *Green box* shows location of panel B. *Hashed boxes* show region where VTI is imposed in inversion for elliptical anisotropy, with the layer thickness, t, indicated. Example ray paths for SKS and S travelling perpendicular to the ridge axis are shown. Axes units are km, all shown without vertical exaggeration. $x_1 = 0$ is the ridge axis

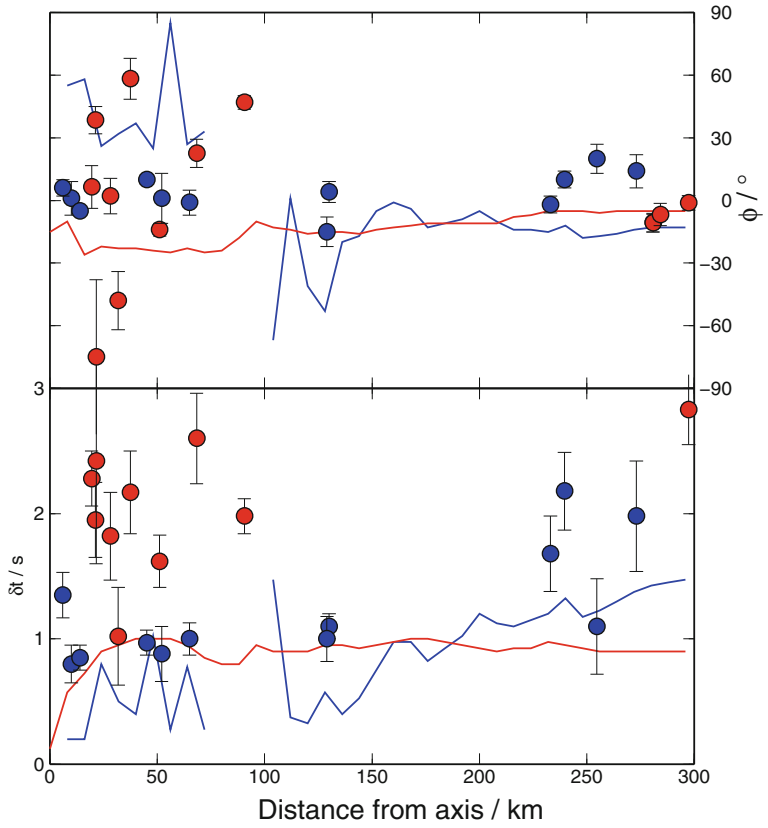

Fig. 3.15 Observed (*coloured circles*) splitting parameters, and those predicted by the MOR LPO-development model of Blackman and Kendall (2002) (*lines*) for downgoing S rays at an azimuth of 20° and upcoming SKS rays at forward azimuth 110° (backazimuth at the station of 290°). *Red circles* and *lines* show S; *blue* represents SKS. The *bottom panel* shows δt, whilst the *top* shows the angle anticlockwise from the spreading direction, from E towards N for the EPR. *Lines* are not drawn where the predicted splitting is classified as null, using an automated null-classification scheme (Wuestefeld et al. 2010). Such null or near-null values may give poorly-constrained splitting parameters

Figure 3.15 shows the predicted pattern of splitting at the EPR for downgoing S rays at an azimuth of 20° from the ridge axis (the mean for our observations) and upcoming SKS rays with a forward azimuth of 110° from the ridge axis (mean for the MELT and GLIMPSE observations), alongside the observed splitting parameters. The uncertainty in the measurements is not insignificant, and obviously our calculations neglect finite-frequency effects, but there remains a clear discrepancy between the model predictions and the actual measurements. This might in part be explained by the specific texture model used for the calculations, such as the asthenospheric viscosity or passive-upwelling assumption. The strength of the texture is likely to increase as the viscosity does, hence this should not affect the style of anisotropy

much. More importantly, although the observations show robustly that the amount of splitting in S becomes almost 1 s larger than that of SKS beyond 200 km, this is not predicted by the texture model. This discrepancy is more probably dependent on the type and orientation of anisotropy than it is on the strength.

3.4.3 Inversion for Elliptical Anisotropy Parameters

One simple mechanism which would introduce an increase in splitting in S but not SKS is vertical transverse isotropy (VTI, also known as hexagonal symmetry where the axis of rotational symmetry is vertical). Because the SKS phase is polarised within the vertical plane, it is not split by this type of anisotropy. Furthermore, in this case we require that near-vertically propagating waves (of inclination $\sim 20°$) experience significant shear wave splitting with fast directions approximately ridge-perpendicular, hence implies the special case of elliptical anisotropy (where Thomsen's (1986) parameters $\delta = \varepsilon$). Whilst elliptical anisotropy is not the only mechanism which can produce compatible observations, it is the simplest and thus the one we test here. It is also important to state that at this stage, our only reason for imposing elliptical anisotropy is as an arbitrary mechanism to explain our observations; interpretation of its meaning is made later.

In order to test if this scenario might be compatible with observations, we construct a simple misfit-minimisation inversion scheme to search the parameter space of a simplistic forward model. We add a layer of vertically transverse elliptical anisotropy with parameters δ, ε $(= \delta)$, γ and layer thickness, t, with the velocity of vertically-polarised shear waves, V_{SV}, given by the PAC06 model of Tan and Helmberger (2007) at that depth everywhere beyond 50 km of the ridge axis. This layer simply replaces the anisotropy previously present in the model due to LPO. The layer shows strongest anisotropy at the top, and decays to nearly isotropic at the bottom according to

$$p' = p \operatorname{erf}\left(\frac{1}{n(1 - z')}\right), \tag{3.1}$$

where erf is the error function, n is a scaling constant, z' is the fractional height within the layer, p is either δ or γ, and p' is the scaled value of p at that height in the layer. Here we use $n = 3$, but the results are not significantly sensitive to it.

In order to be able to better constrain our best-fitting model, we scale the observed δt so that the maximum values at the greatest distances from the ridge match the SKS δt predicted by the original model with no added elliptical anisotropy. This is probably an acceptable compromise, as changing the value of the input texture model's viscosity would likely perform the same function.

Exploratory modelling showed that the depth to the top of this layer does not affect the splitting significantly, and hence we fix the depth at 70 km, an estimate for the top of the low velocity zone observed beneath oceanic plates (e.g., Shapiro and Ritzwoller 2002); the results are similar almost regardless of depth.

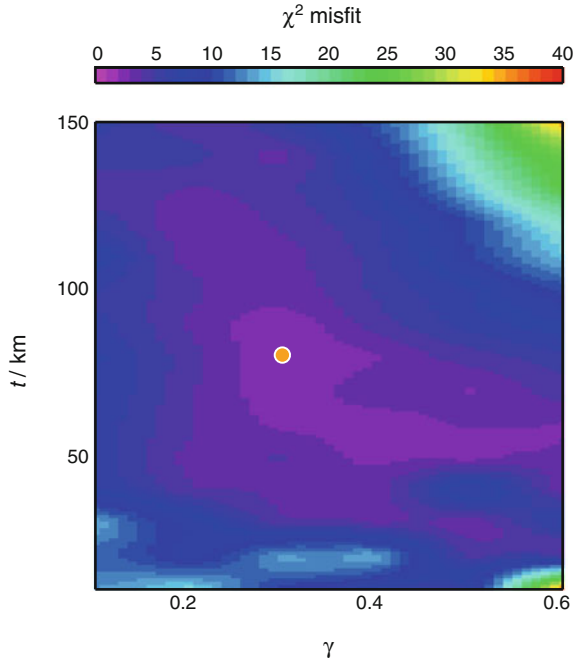

Fig. 3.16 χ^2 misfit surface for the inversion discussed in the main text. The thickness of the layer of elliptical anisotropy, t, is shown against Thomsen's (1986) parameter γ

We perform a grid search over the three independent parameters (δ, γ, t): we construct the model, calculate the splitting parameters along the azimuth and inclination of each observation (our S and SKS from previous studies), apply the splitting operators to synthetic shear waves of the same polarisation as the observations, and measure the resulting splitting as before. The reduced χ^2 misfit for each model, $\chi^2 = (1/\nu)\sum_i^N (\delta t_{\mathrm{obs},i} - \delta t_{\mathrm{syn},i})^2/\sigma^2_{\mathrm{obs},i}$ where $\nu = N - 3 - 1$, and N is the number of observations, is calculated and the minimum is found.

We find the optimum values to be $\gamma \approx 0.3$ and $t \approx 80\,\mathrm{km}$, however there is obviously a tradeoff between the two as one can increase the splitting in S over SKS more by having a thicker layer, or a stronger peak anisotropy. Although the horizontal P wave velocity is determined by δ, the amount of shear wave anisotropy is not affected by it, hence our inversion is not sensitive to this parameter. Figure **??** shows the χ^2 misfit surface for γ and t, showing that a fairly wide range of parameters can match the observations within the 95 % confidence interval ($0.6 \geq \gamma \geq 0.1$ for $20 \leq t \leq 150\,\mathrm{km}$). Figure 3.17 shows the predicted splitting parameters for the optimum model with coloured lines.

3.5 Discussion

In interpreting our results, it is difficult to draw firm conclusions about the behaviour of MORs in general because of poor sampling, arising from the lack of stations outside USA and Ethiopia with comprehensive studies published on the backazimuthal

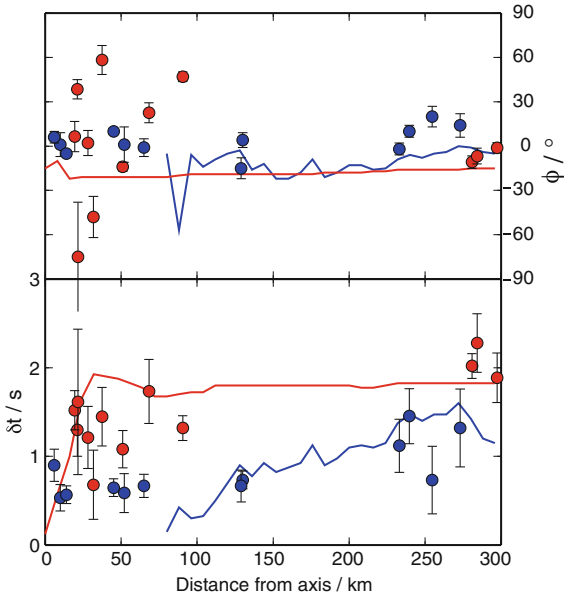

Fig. 3.17 Observed splitting results at the EPR for earthquakes classified as 'ridge' events (*circles* with *error bars*), with the model predictions from the inversion (*lines*). Shown are the fast orientations with respect to the spreading direction, ϕ, and the delay times, δt. In both cases, SKS parameters are shown in *blue*, and S with *red*. At small distances from the ridge axis (0 km), the SKS waveforms produce null splitting results, which are not shown. Optimum model includes as background the texture calculations of Blackman and Kendall (2002), with an imposed 80 km layer of elliptical anisotropy with a vertical symmetry axis, decreasing in strength with $\gamma = 0.4$ at the *top*, and 0 at the *bottom*. See text for further details

variation of SKS splitting parameters. For the purposes of studying relatively small-magnitude earthquakes at teleseismic distances such as is done here, networks of stations with such measurements are necessary to allow stacking of data, especially when fast directions are near the source polarisation. This limitation also means that comparisons between fast and slow ridges are hard to make. However, our measurements do suggest that splitting near the ridge axis is greater beneath fast-spreading ridges (full-rate $> 100\,\mathrm{mm\,a^{-1}}$) than slow-spreading ones.

Our measurements of splitting show ϕ'' to be very similar to the fast orientations observed by regional SKS studies near MORs, but these are extremely limited in coverage because of the practical difficulties in operating such OBS sites. Surface wave studies examining azimuthal anisotropy globally (e.g., Debayle et al. 2005) can provide better coverage near MORs, but limited horizontal resolution means changes over relatively small distances (up to few tens of kilometres and less) cannot be imaged well. Such global measurements tend to show fast orientations approximately parallel to the spreading direction, but this can vary by up to 45° in some places, notably near large fracture zones.

The observations suggest that the style of anisotropy beneath at least the Romanche and Doldrums fracture zones (Fig. 3.10) on the MAR is somewhat complex. Anisotropy dominated by olivine LPO or shape-preferred orientation of melt or other seismically-distinct material would likely be caused by alignment of TTI planes or olivine a-axes along an azimuth of ∼310°, dipping shallowly, which is not inconsistent with predicted mantle flow or melt flow lines from previous modelling (Weatherley and Katz 2010; van Wijk and Blackman 2005; Sparks et al. 1993; Phipps Morgan and Forsyth 1988). Whilst the uncertainty in our measurements is not insignificant, even with more relaxed constraints on the orientations the picture is much the same (Fig. 3.18). We of course neglect other anisotropic phases in this approach, but would expect this to require a stronger texturing in the olivine itself to match observations. Hence further study is needed.

In the previous section, we test the assumption that the variation in splitting beneath the EPR between S and SKS waves is due to the presence of some layer of anisotropy not captured in LPO modelling. We find that the presence of a layer of ∼80 km thickness and peak $\gamma \approx 0.3$ at the top, within a background model of olivine and enstatite LPO, is compatible with observations. This is in accordance with recent studies of the 'LAB' discontinuity seen beneath much of the Earth's oceanic lithosphere at 40–100 km depth (e.g., Rychert et al. 2010; Kawakatsu et al. 2009; Rychert and Shearer 2009), which is sometimes interpreted as being due to the presence of horizontal melt pockets or other seismically distinct material. Furthermore, surface wave studies show at compatible depths the presence of faster velocities in horizontally-polarised S waves compared to those in vertically polarised waves (e.g., Nettles and Dziewoński 2008), which is also consistent with our elliptical anisotropy interpretation. However, it is clearly possible that other features may be responsible. For example, the S waves from events near the axis travel along the ridge axis for some distance, whilst the SKS phases with which we compare them quickly leave the axis region, so there may be some heterogeneous or anisotropic structure which current LPO models of MORs do not adequately recreate. The presence of melt beneath the ridge axis was not included in this analysis, however it is clear that melt focussing towards the axis must be present and would likely lead to additional anisotropic effects. These effects were considered by Blackman and Kendall (1997), but only for vertical waves. Holtzman and Kendall (2010) considered both vertical and horizontal melt beneath the axis and at distance, but only for vertical 'SKS' or horizontal surface waves.

Several studies show that the structure beneath the EPR is asymmetric (e.g., Conder 2007; Podolefsky et al. 2004; Harmon et al. 2004; Wolfe and Solomon 1998), whilst our modelling uses the starting case of symmetrical spreading and assumes asymmetry is a second-order control on the overall style of splitting, hence this might play some part in the observed difference in splitting times between S and SKS phases. However, our data also sample both sides of the ridge, so presumably are also affected by the same asymmetry, yet still consistently show larger splitting in S than SKS. Blackman and Kendall (1997) calculate the splitting times for vertical-incidence shear waves on a suite of asymmetric model of MOR LPO development,

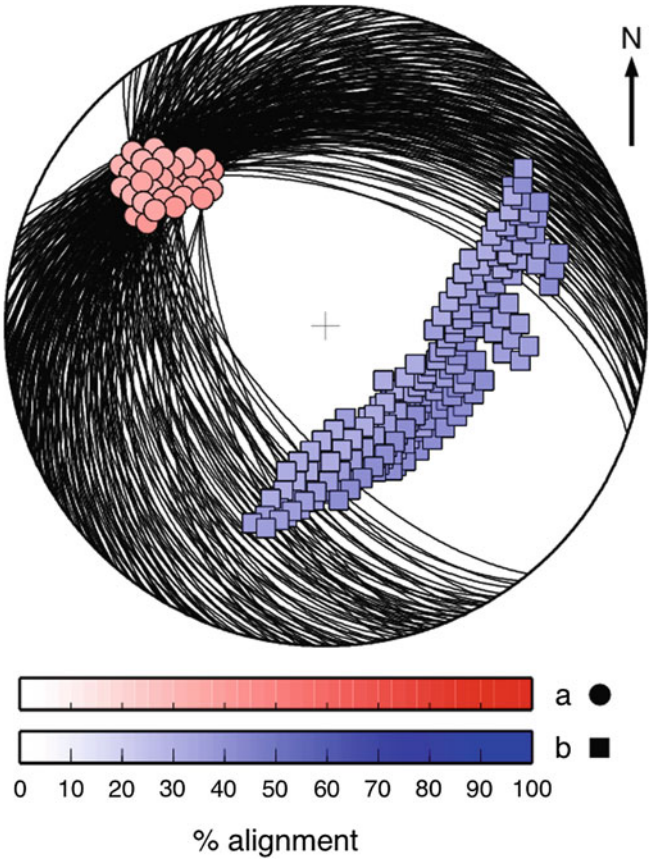

Fig. 3.18 Orientations of olivine a- and b-axes, and b-planes, compatible with observations at the Doldrums Fracture Zone, Mid-Atlantic Ridge. As for Fig. 3.12, except shown are orientations which predict splitting within twice the errors of the shear wave splitting measurements quoted in the main text. The a-axes still predominately trend along an azimuth of ~310°, dipping about 28°. FZ strike and TTI plane not shown

as for the EPR, and for the best-fitting case predict splitting times for SKS of up to 2–3 s on the Pacific plate, and up to 1.5 s on the Nazca plate. This asymmetry is observed to a lesser extent in the data (Fig. 3.7). However, again they did not study the effect of azimuth as we do here.

3.6 Conclusions

We present measurements made using the source-side shear wave splitting technique for the UM beneath MORs around the world. We correct for the UM on the receiver side for seismic stations where the anisotropy beneath is very well characterised, and

can resolve the source anisotropy, subject to a series of rigorous tests. With 122 new observations, the presented dataset adds significantly to the current knowledge of anisotropy beneath MORs, and for the EPR we are able to show that the presence of a layer of elliptical anisotropy which increases in strength towards the top is compatible with our observations when considered as part of a background model of LPO development at a fast-spreading ridge. Assuming the background LPO anisotropy, we find that a layer of 80 km thickness, increasing from isotropic to anisotropic at the top with peak Thomsen's parameter of $\gamma = 0.3$ can reproduce the data. This additional anisotropy might indicate the presence of horizontal layered melt or other seismically distinct material as one possible explanation, compatible with observations of the 'LAB' discontinuity beneath oceanic plates. As further rigorous study of UM anisotropy using SKS phases becomes routine, more stations can be used to measure the seismic shear wave splitting beneath MORs and other remote parts of the Earth where earthquakes occur, and hence our understanding of mantle dynamics in these regions will be vastly improved.

References

Abramson, E., Brown, J., Slutsky, L., & Zaug, J. (1997). The elastic constants of San Carlos olivine to 17 GPa. *Journal of Geophysical Research-Solid Earth, 102*(B6), 12253–12263. doi:10.1029/97JB00682.

Ayele, A., Stuart, G., & Kendall, J. M. (2004). Insights into rifting from shear wave splitting and receiver functions: an example from Ethiopia. *Geophysical Journal International, 157*(1), 354–362. doi:10.1111/j.1365-246X.2004.02206.x.

Barclay, A., & Toomey, D. (2003). Shear wave splitting and crustal anisotropy at the Mid-Atlantic Ridge, 35° N. *Journal of Geophysical Research-Solid Earth, 108*(B8), 2378. doi:10.1029/2001JB000918.

Barruol, G., Helffrich, G., & Vauchez, A. (1997). Shear wave splitting around the northern Atlantic: frozen Pangaean lithospheric anisotropy?. *Tectonophysics, 279*(1–4), 135–148. doi:10.1016/S0040-1951(97)00126--1.

Becker, T. W., Ekström, G., Boschi, L., & Woodhouse, J. H. (2007). Length scales, patterns and origin of azimuthal seismic anisotropy in the upper mantle as mapped by Rayleigh waves. *Geophysical Journal International, 171*(1), 451–462. doi:10.1111/j.1365-246X.2007.03536.x.

Behn, M., Conrad, C. P., & Silver, P. G. (2004). Detection of upper mantle flow associated with the African Superplume. *Earth and Planetary Science Letters, 224*(3–4), 259–274. doi:10.1016/j.epsl.2004.05.026.

Bird, P. (2003). An updated digital model of plate boundaries. *Geochemistry Geophysics Geosystems, 4*, 1027. doi10.1029/2001GC000252.

Blackman, D., & Kendall, J. M. (1997). Sensitivity of teleseismic body waves to mineral texture and melt in the mantle beneath a mid-ocean ridge. *Philosophical Transactions of the Royal Society A, 355*(1723), 217–231.

Blackman, D. & Kendall, J. M. (2002). Seismic anisotropy in the upper mantle 2. Predictions for current plate boundary flow models. *Geochemistry Geophysics Geosystems, 3*, 8602. doi:10.1029/2001GC000247.

Blackman, D., Orcutt, J., Forsyth, D., & Kendall, J. M. (1993). Seismic anisotropy in the mantle beneath an oceanic spreading center. *Nature, 366*(6456), 675–677. doi:10.1038/366675a0.

Blackman, D., Orcutt, J., & Forsyth, D. (1995a). Recording teleseismic earthquakes using ocean-bottom seismographs at mid-ocean ridges. *Bulletin of the Seismological Society of America, 85*(6), 1648–1664.

Blackman, D., Orcutt, J., Forsyth, D., & Kendall, J. M. (1995b). Correction to: 'Seismic anisotropy in the mantle beneath an oceanic spreading center (vol. 366, p. 675, 1993)'. *Nature, 374*(6525), 824.

Blackman, D., Kendall, J. M., Dawson, P., Wenk, H.-R., Boyce, D., & Phipps Morgan, J. (1996). Teleseismic imaging of subaxial flow at mid-ocean ridges: Traveltime effects of anisotropic mineral texture in the mantle. *Geophysical Journal International, 127*(2), 415–426. doi:10.1111/j.1365-246X.1996.tb04730.x.

Blackman, D., Wenk, H.-R., & Kendall, J. M. (2002). Seismic anisotropy of the upper mantle 1. Factors that affect mineral texture and effective elastic properties. *Geochemistry Geophysics Geosystems, 3*, 8601. doi:10.1029/2001GC000248.

Conder, J. A. (2007). Dynamically driven mantle flow and shear wave splitting asymmetry across the EPR, MELT area. *Geophysical Research Letters, 34*(16), L16301. doi:10.1029/2007GL030832.

Debayle, E., Kennett, B., & Priestley, K. (2005). Global azimuthal seismic anisotropy and the unique plate-motion deformation of Australia. *Nature, 433*(7025), 509–512. doi:10.1038/nature03247.

Delorey, A. A., Dunn, R. A., & Gaherty, J. B. (2007). Surface wave tomography of the upper mantle beneath the Reykjanes Ridge with implications for ridge-hot spot interaction. *Journal of Geophysical Research-Solid Earth, 112*(B8), B08313. doi:10.1029/2006JB004785.

DeMets, C., Gordon, R. G., Argus, D. F., & Stein, S. (1994). Effect of recent revisions to the geomagnetic reversal time scale on estimates of current plate motions. *Geophysical Research Letters, 21*(20), 2191–2194. doi:10.1029/94GL02118.

Dunn, R. A., & Toomey, D. (1997). Seismological evidence for three-dimensional melt migration beneath the East Pacific Rise. *Nature, 388*(6639), 259–262. doi:10.1038/40831.

Engdahl, E., van der Hilst, R. D., & Buland, R. (1998). Global teleseismic earthquake relocation with improved travel times and procedures for depth determination. *Bulletin of the Seismological Society of America, 88*(3), 722–743.

Evans, M., Kendall, J. M., & Willemann, R. (2006). Automated SKS splitting and upper-mantle anisotropy beneath Canadian seismic stations. *Geophysical Journal International*, *165*(3), 931–942. doi:10.1111/j.1365-246X.2006.02973.x.

Ferreira, A. M. G., Woodhouse, J. H., Visser, K., & Trampert, J. (2010). On the robustness of global radially anisotropic surface wave tomography. *Journal of Geophysical Research-Solid Earth, 115*, B04313. doi:10.1029/2009JB006716.

Foley, B. J., & Long, M. D. (2011). Upper and mid-mantle anisotropy beneath the Tonga slab. *Geophysical Research Letters, 38*(2), L02303. doi:10.1029/2010GL046021.

Fouch, M. J., Fischer, K. M., Parmentier, E., Wysession, M., & Clarke, T. (2000). Shear wave splitting, continental keels, and patterns of mantle flow. *Journal of Geophysical Research-Solid Earth, 105*(B3), 6255–6275. doi:10.1029/1999JB900372.

Gaherty, J. B. (2001). Seismic evidence for hotspot-induced buoyant flow beneath the Reykjanes Ridge. *Science, 293*(5535), 1645–1647. doi:10.1126/science.1061565.

Gaherty, J. B., Lizarralde, D., Collins, J., Hirth, G., & Kim, S. (2004). Mantle deformation during slow seafloor spreading constrained by observations of seismic anisotropy in the western Atlantic. *Earth and Planetary Science Letters, 228*(3–4), 255–265. doi:10.1016/j.epsl.2004.10.026.

Gripp, A., & Gordon, R. G. (2002). Young tracks of hotspots and current plate velocities. *Geophysical Journal International, 150*(2), 321–361. doi:10.1046/j.1365-246X.2002.01627.x.

Hall, S. A., Kendall, J. M., & der Baan, M. V. (2004). Some comments on the effects of lower-mantle anisotropy on SKS and SKKS phases. *Physics of the Earth and Planetary Interiors, 146*(3–4), 469–481. doi:10.1016/j.pepi.2004.05.002.

Harmon, N., Forsyth, D., Fischer, K. M., & Webb, S. (2004). Variations in shear-wave splitting in young Pacific seafloor. *Geophysical Research Letters, 31*(15), L15609. doi:10.1029/2004GL020495.

Hess, H. (1964). Seismic anisotropy of uppermost mantle under oceans. *Nature, 203*(494), 629–631. doi:10.1038/203629a0.

Holtzman, B. K., & Kendall, J. M. (2010). Organized melt, seismic anisotropy, and plate boundary lubrication. *Geochemistry Geophysics Geosystems, 11*, Q0AB06. doi:10.1029/2010GC003296.

Hung, S., & Forsyth, D. (1999). Anisotropy in the oceanic lithosphere from the study of local intraplate earthquakes on the west flank of the southern East Pacific Rise: Shear wave splitting and waveform modeling. *Journal of Geophysical Research-Solid Earth, 104*(B5), 10695–10717. doi:10.1029/1999JB900046.

Kawakatsu, H., Kumar, P., Takei, Y., Shinohara, M., Kanazawa, T., Araki, E., & Suyehiro, K. (2009). Seismic evidence for sharp lithosphere-asthenosphere boundaries of oceanic plates. *Science, 324*(5926), 499–502. doi:10.1126/science.1169499.

Kendall, J. M. (1994). Teleseismic arrivals at a mid-ocean ridge: Effects of mantle melt and anisotropy. *Geophysical Research Letters, 21*(4), 301–304. doi:10.1029/93GL02791.

Kendall, J.-M., & Silver, P. G. (1998). Investigating causes of D″ anisotropy. In M. Gurnis, M. E. Wysession, E. Knittle, & B. A. Buffett (Eds.), *The core-mantle boundary region,* Geodynamics Series, (pp. 97–118). American Geophysical Union, Washington: USA.

Kendall, J.-M., & Silver, P. G. (2000). Seismic anisotropy in the boundary layers of the mantle, in Earth's Deep Interior: Mineral Physics and Tomography from the Atomic to the Global Scale. In S. Karato, A. Forte, R. C. Liebermann, G. Masters, & L. Stixrude, (Eds.), vol. 117 *Geophysical monograph* (pp. 133–159). American Geophysical Union, Washington: USA.

Kendall, J. M., Guest, W., & Thomson, C. (1992). Ray-theory Green's function reciprocity and ray-centered coordinates in anisotropic media. *Geophysical Journal International, 108*(1), 364–371. doi:10.1111/j.1365-246X.1992.tb00863.x.

Kendall, J. M., Stuart, G., Ebinger, C., Bastow, I., & Keir, D. (2005). Magma-assisted rifting in Ethiopia. *Nature, 433*(7022), 146–148. doi:10.1038/nature03161.

Kennett, B. & Engdahl, E. (1991). Traveltimes for global earthquake location and phase identification, *Geophysical Journal International, 105*(2), 429–465. doi:10.1111/j.1365-246X.1991.tb06724.x.

Kustowski, B., Ekström, G., & Dziewoński, A. (2008). Anisotropic shear-wave velocity structure of the Earth's mantle: A global model. *Journal of Geophysical Research-Solid Earth, 113*(B6), B06306. doi:10.1029/2007JB005169.

Lay, T., Williams, Q., Garnero, E. J., Kellogg, L., & Wysession, M. E. (1998). Seismic wave anisotropy in the D″ region and its implications. In M. Gurnis, M. E. Wysession, E. Knittle, & B. A. Buffett (Eds.), *The core-mantle boundary region,* Geodynamics Series 28. (pp. 299–318), American Geophysical Union, Washington: USA.

Liu, K. H. (2009). NA-SWS-1.1: A uniform database of teleseismic shear wave splitting measurements for North America. *Geochemistry Geophysics Geosystems, 10*, Q05011. doi:10.1029/2009GC002440.

Long, M. D., & Silver, P. G. (2009). Shear wave splitting and mantle anisotropy: Measurements, interpretations, and new directions. *Surveys in Geophysics, 30*(4–5), 407–461. doi:10.1007/s10712-009-9075-1.

Mainprice, D. (2007). Seismic anisotropy of the deep earth from a mineral and rock physics perspective. In G. Schubert (Ed.), *Treatise on geophysics,* vol. 2. (pp. 437–492). Oxford: UK

Meade, C., Silver, P. G., & Kaneshima, S. (1995). Laboratory and seismological observations of lower mantle isotropy. *Geophysical Research Letters, 22*(10), 1293–1296. doi:10.1029/95GL01091.

Montagner, J.-P., & Kennett, B. (1996). How to reconcile body-wave and normal-mode reference earth models. *Geophysical Journal International, 125*(1), 229–248. doi:10.1111/j.1365-246X.1996.tb06548.x.

Nettles, M., & Dziewoński, A. (2008). Radially anisotropic shear velocity structure of the upper mantle globally and beneath North America. *Journal of Geophysical Research-Solid Earth, 113*(B2), B02303. doi:10.1029/2006JB004819.

Nippress, S. E. J., Kusznir, N. J., & Kendall, J. M. (2007). LPO predicted seismic anisotropy beneath a simple model of a mid-ocean ridge. *Geophysical Research Letters, 34*(14), L14309. doi:10.1029/2006GL029040.

Niu, F., & Perez, A. (2004). Seismic anisotropy in the lower mantle: A comparison of waveform splitting of SKS and SKKS, *Geophysical Research Letters, 31*(24), L24612. doi:10.1029/2004GL021196.

Nowacki, A., Wookey, J., & Kendall, J. M. (2010). Deformation of the lowermost mantle from seismic anisotropy. *Nature, 467*(7319), 1091–1095. doi:10.1038/nature09507.

Nowacki, A., Wookey, J., & Kendall, J. M. (2011). New advances in using seismic anisotropy, mineral physics and geodynamics to understand deformation in the lowermost mantle. *Journal of Geodynamics, 52*(3–4), 205–228. doi:10.1016/j.jog.2011.04.003.

Panning, M., & Romanowicz, B. (2006). A three-dimensional radially anisotropic model of shear velocity in the whole mantle. *Journal of Geodynamics, 167*(1), 361–379. doi:10.1111/j.1365-246X.2006.03100.x.

Phipps Morgan, J. (1987). Melt migration beneath mid-ocean spreading centers. *Geophysical Research Letters, 14*(12), 1238–1241. doi:10.1029/GL014i012p01238.

Phipps Morgan, J., & Forsyth, D. (1988). Three-dimensional flow and temperature perturbations due to a transform offset: effects on oceanic crustal and upper mantle structure. *Journal of Geophysical Research-Solid, 93*(B4), 2955–2966.

Podolefsky, N., Zhong, S., & McNamara, A. K. (2004). The anisotropic and rheological structure of the oceanic upper mantle from a simple model of plate shear. *Geophysical Journal International, 158*(1), 287–296. doi:10.1111/j.1365-246X.2004.02250.x.

Ranganathan, S. I., & Ostoja-Starzewski, M. (2008). Universal elastic anisotropy index. *Physics Review Letters, 101*(5), 055504. doi:10.1103/PhysRevLett.101.055504.

Restivo, A., & Helffrich, G. (2006). Core-mantle boundary structure investigated using SKS and SKKS polarization anomalies. *Geophysical Journal International, 165*(1), 288–302. doi:10.1111/j.1365-246X.2006.02901.x.

Russo, R., & Mocanu, V. I. (2009). Source-side shear wave splitting and upper mantle flow in the Romanian Carpathians and surroundings. *Earth and Planetary Science Letters, 287*(1–2), 205–216. doi:10.1016/j.epsl.2009.08.028.

Rychert, C. A., & Shearer, P. M. (2009). A global view of the lithosphere-asthenosphere boundary. *Science, 324*(5926), 495–498. doi:10.1126/science.1169754.

Rychert, C. A., Shearer, P. M., & Fischer, K. M. (2010). Scattered wave imaging of the lithosphere-asthenosphere boundary. *Lithos, 120*(1–2), 173–185. doi:10.1016/j.lithos.2009.12.006.

Savage, M. (1999). Seismic anisotropy and mantle deformation: What have we learned from shear wave splitting?. *Reviews of Geophysics, 37*(1), 65–106. doi:10.1029/98RG02075.

Schoenecker, S., Russo, R., & Silver, P. (1997). Source-side splitting of S waves from Hindu Kush-Pamir earthquakes. *Tectonophysics, 279*(1–4), 149–159. doi:10.1016/S0040-1951(97)00130--3.

Shapiro, N., & Ritzwoller, M. (2002). Monte-Carlo inversion for a global shear-velocity model of the crust and upper mantle. *Geophysical Journal International, 151*(1), 88–105. doi:10.1046/j.1365-246X.2002.01742.x.

Shearer, P. M., & Orcutt, J. (1986). Compressional and shear-wave anisotropy in the oceanic lithosphere—the Ngendei seismic refraction experiment. *Geophysical Journal of the Royal Astronomical Society, 87*(3), 967–1003. doi:10.1111/j.1365-246X.1986.tb01979.x.

Silver, P. G., & Chan, W. W. (1991). Shear-wave splitting and subcontinental mantle deformation. *Journal of Geophysical Research-Solid Earth, 96*(B10), 16429–16454. doi:10.1029/91JB00899.

Silver, P. G., & Savage, M. (1994). The interpretation of shear-wave splitting parameters in the presence of two anisotropic layers. *Geophysical Journal International, 119*(3), 949–963. doi:10.1111/j.1365-246X.1994.tb04027.x.

Smith, W., & Sandwell, D. (1997). Global sea floor topography from satellite altimetry and ship depth soundings. *Science, 277*(5334), 1956–1962. doi:10.1126/science.277.5334.1956.

Sparks, D., Parmentier, E., & Phipps Morgan, J. (1993). Three-dimensional mantle convection beneath a segmented spreading center: implications for along-axis variations in crustal thickness

and gravity. *Journal of Geophysical Research-Solid Earth, 98*(B12), 21977–21995. doi:10.1029/93JB02397.

Tan, Y., & Helmberger, D. V. (2007). Trans-Pacific upper mantle shear velocity structure. *Journal of Geophysical Research-Solid Earth, 112*(B8), B08301. doi:10.1029/2006JB004853.

Teanby, N., Kendall, J. M., & der Baan, M. V. (2004). Automation of shear-wave splitting measurements using cluster analysis. *Bulletin of the Seismological Society of America, 94*(2), 453–463. doi:10.1785/0120030123.

Thomsen, L. (1986). Weak elastic anisotropy. *Geophysics, 51*(10), 1954–1966. doi:10.1190/1.1442051.

Tommasi, A., Tikoff, B., & Vauchez, A. (1999). Upper mantle tectonics: three-dimensional deformation, olivine crystallographic fabrics and seismic properties. *Earth and Planetary Science Letters, 168*(1–2), 173–186. doi:10.1016/S0012-821X(99)00046--1.

van Wijk, J., & Blackman, D. (2005). Deformation of oceanic lithosphere near slow-spreading ridge discontinuities. *Tectonophysics, 407*(3–4), 211–225. doi:10.1016/j.tecto.2005.08.009.

Weatherley, S. M., & Katz, R. F. (2010). Plate-driven mantle dynamics and global patterns of mid-ocean ridge bathymetry. *Geochemistry Geophysics Geosystems, 11*, Q10003. doi:10.1029/2010GC003192.

Wolfe, C., & Silver, P. G. (1998). Seismic anisotropy of oceanic upper mantle: Shear wave splitting methodologies and observations. *Journal of Geophysical Research-Solid Earth, 103*(B1), 749–771. doi:10.1029/97JB02023.

Wolfe, C., & Solomon, S. (1998). Shear-wave splitting and implications for mantle flow beneath the MELT region of the East Pacific Rise. *Science, 280*(5367), 1230–1232. doi:10.1126/science.280.5367.1230.

Wookey, J., & Kendall, J. M. (2008). Constraints on lowermost mantle mineralogy and fabric beneath Siberia from seismic anisotropy. *Earth and Planetary Science Letters, 275*(1–2), 32–42. doi:10.1016/j.epsl.2008.07.049.

Wookey, J., Kendall, J. M., & Rümpker, G. (2005). Lowermost mantle anisotropy beneath the north Pacific from differential S-ScS splitting. *Geophysical Journal International, 161*(3), 829–838. doi:10.1111/j.1365-246X.2005.02623.x.

Wuestefeld, A., Al-Harrasi, O., Verdon, J. P., Wookey, J., & Kendall, J. M. (2010). A strategy for automated analysis of passive microseismic data to image seismic anisotropy and fracture characteristics, *Geophysical Prospecting, 58*(5), 753–771. doi:10.1111/j.1365-2478.2010.00891.x.

Chapter 4
Deformation of the Lowermost Mantle from Seismic Anisotropy

4.1 Introduction

Studies of D″ anisotropy in the Caribbean are numerous (Kendall and Nangini 1996; Kendall and Silver 1998; Lay et al. 1998; Garnero et al. 2004; Maupin et al. 2005; Rokosky et al. 2006), because of an abundance of deep earthquakes in South America and seismometers in North America, and show ∼1 % shear wave anisotropy. These mostly compare the horizontally- (SH) and vertically-polarised (SV) shear waves, assuming a style of anisotropy where the shear wave velocity V_S varies only with the angle away from the vertical (vertical transverse isotropy, VTI). With this assumption, SH leads SV here, corresponding to $\phi' = \pm 90\,^\circ$ in our notation (Fig. 4.1c). A further limitation is using only one azimuth of rays in D″: this cannot distinguish VTI from the case of an arbitrarily tilted axis of rotational symmetry in which wave speed does not vary (tilted transverse isotropy, TTI) when the axis dips towards the receivers or stations. An improvement on this situation can be made by utilising crossing ray paths in D″ (Wookey and Kendall 2008), but this relies on having the correct source-receiver geometry, which is not possible beneath North America using only deep earthquakes. We address this issue beneath the Caribbean by incorporating measurements from shallow earthquakes in our dataset, and thus reduce the symmetry of the anisotropy which must be assumed.

We measure anisotropy in D″ using differential splitting in S and ScS phases using an approach described by Wookey et al. (2005a) and Wookey and Kendall (2008). Both phases travel through the same region of the upper mantle (UM), but only ScS samples D″ (Fig. 4.1a). As the majority of the lower mantle (LM) is relatively isotropic (Meade et al. 1995), by removing the splitting introduced in the UM we can measure that which occurs only in D″. Earthquakes in South and Central America, Hawaii, the East Pacific Rise (EPR) and the Mid-Atlantic Ridge (MAR), detected at North American stations, provide a dense coverage of crossing rays which traverse D″ beneath southern North America and the Caribbean (Fig. 4.1b). Three distinct regions are covered (Fig. 4.13), each sampled along two distinct azimuths. The Caribbean

A. Nowacki, *Plate Deformation from Cradle to Grave*, Springer Theses,
DOI: 10.1007/978-3-642-34842-6_4, © Springer-Verlag Berlin Heidelberg 2013

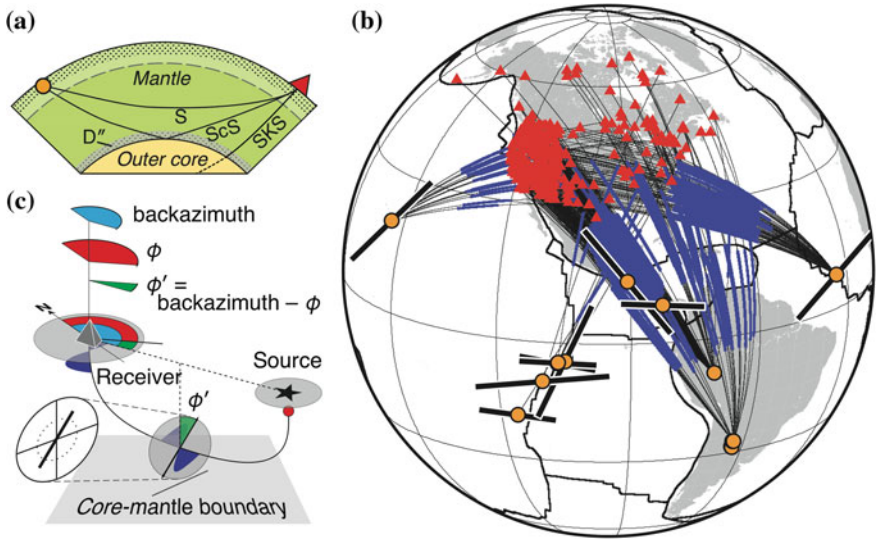

Fig. 4.1 Source–receiver geometry, and explanation of ϕ'. a Earth section with ray paths for S, ScS and SKS phases. The stippled UM and grey D″ are anisotropic. S turns above D″; ScS samples it. **b** Data used in this study: seismic stations (*triangles*); earthquake epicentres (*yellow circles*); ray paths (*thin black lines*); ray paths in a 250 km-thick D″ (*blue lines*); measured source-side shear-wave splitting parameters for shallow earthquakes (*black bars* beneath *circles*: length corresponds to delay time, orientation represents fast direction; largest delay time is 2.4 s). We note that fast orientations of shear-wave splitting in the UM beneath shallow earthquakes on plate boundaries are either generally very closely parallel to the plate-spreading direction (EPR and MAR), or to the subduction zone trench (Central America). **c** Relation of the measured fast directions in the geographic (ϕ) and ray (ϕ') reference frames. Because the ScS phase is nearly horizontal for most of its travel through D″, we define $\phi' =$ backazimuth $- \phi$, which corresponds to the polarisation away from the vertical of the fast shear wave. In terms of TI, $\phi' = \pm 90°$ is compatible with VTI, and $-90° < \phi' < 90°$ implies TTI. This can also be thought of as the plane normal to the rotational symmetry axis being tilted from the horizontal, or dipping, at $(90 - \phi')°$

(region 'S') has been previously well studied (Kendall and Silver 1996; Garnero et al. 2004; Maupin et al. 2005), but the northeast ('E') and southwest ('W') United States have not.

4.2 Methods and Data

4.2.1 S–ScS Differential Splitting

We measured differential shear wave splitting between S and ScS phases recorded at ~500 seismic stations in North and Central America, according to the method of Wookey and Kendall (2008). Events of $M \geq 5.7$ in the distance range 55–82 ° were

Table 4.1 Earthquakes and measured splitting parameters in S after removal of receiver-side splitting

Year-day-time	Locality	Lat (°N)	Lon (°E)	Depth (km)	ϕ''[a] (°)	$\Delta(\phi'')$ (°)	δt (s)	$\Delta(\delta t)$ (s)
1991-246-1156	EPR	−17.92	−115.99	11	−88	8	1.4	0.2
1994-119-0730	Argentina	−28.30	− 63.25	562	NULL	–	–	–
1994-130-0636	Argentina	−28.50	− 63.10	601	NULL	–	–	–
1994-231-1001	Argentina	−26.64	− 63.42	564	NULL	–	–	–
1996-236-2156	EPR	− 4.09	−104.37	10	25	5	2.2	0.2
2003-249-0208	EPR	− 4.62	−106.04	10	82	7	1.4	0.5
2006-265-0232	Argentina	−26.77	− 63.03	577	NULL	–	–	–
2007-164-1929	Guatemala	13.63	− 90.73	65	−39	4	2.4	0.1
2007-202-1327	Brazil	− 8.13	− 71.27	645	NULL	–	–	–
2007-226-0538	Hawaii	19.35	−155.07	9	43	4	2.0	0.1
2008-144-1935	MAR	7.31	− 34.90	9	73	3	2.1	0.1
2008-220-2258	EPR	− 9.14	−109.52	10	81	11	2.4	0.4
2008-262-0141	EPR	− 4.55	−106.00	10	90	8	1.4	0.1
2008-324-0611	Panama	8.27	− 82.97	32	95	5	1.5	0.2

[a] ϕ'' is the projection of the measured geographic fast direction at the station onto the event frame, such that $\phi'' =$ azimuth + backazimuth − ϕ. Where ϕ'' is NULL, no splitting is assumed beneath the event

used (Table 4.1), as the two phases then traverse very similar regions of the upper mantle. All data were bandpass filtered between 0.001 and 0.3 Hz to remove noise. We analysed splitting in the phases using the minimum eigenvalue technique (Silver and Chan 1991), with 100 analysis windows in each case to estimate the uncertainties in ϕ and δt using a statistical F-test (Wolfe and Silver 1998; Teanby et al. 2004). An example is shown in Fig. 4.2.The λ_2 surfaces for measurements along each azimuth are stacked (Wolfe and Silver 1998) in three regions (Fig. 4.13) to greatly reduce the errors.

4.2.2 Correcting for Upper Mantle Anisotropy

We correct for upper mantle (UM) anisotropy using previously published (Evans et al. 2006; Wuestefeld et al. 2009) SKS splitting measurements (distance >90 °) at stations which show little variation of splitting parameters with backazimuth, corresponding to simple UM anisotropy, and where there are measurements made along similar backazimuths to the phases we measure in this study (S, ScS). These provide an estimate of the receiver-side anisotropy, and should eliminate the chance that lateral heterogeneity, or dipping or multiple layers of anisotropy beneath the receiver affect our results. Analysing the splitting in S after applying a receiver-side correction gives an estimate of the source-side splitting beneath the earthquake (Fig. 4.1b; Table 4.1). For nearby stations with no available SKS measurements, measuring splitting in

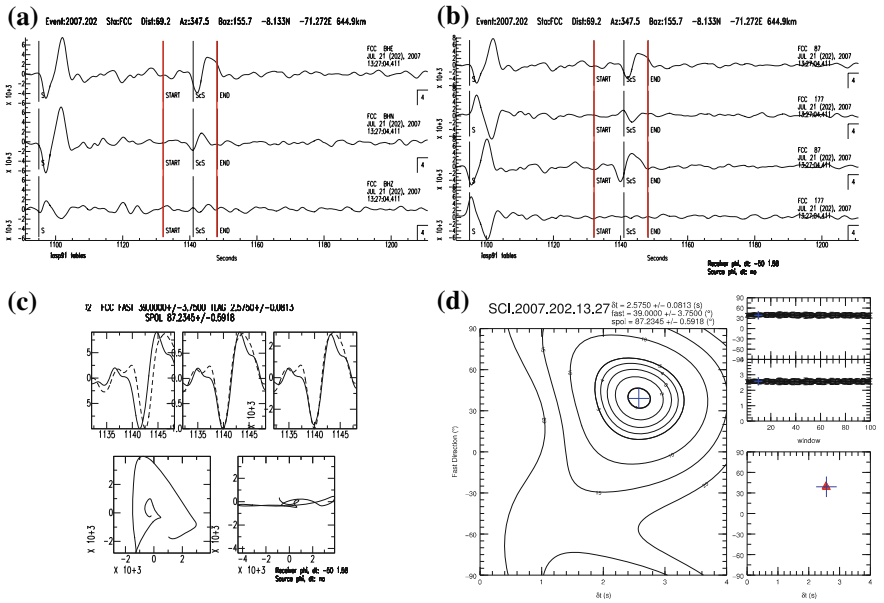

Fig. 4.2 Splitting analysis of ScS phase at station FCC (Fort Churchill, Canada) for a deep event (2007-202-1327, Brazil, depth 645 km). (The waveforms are displayed with a bandpass filter at 0.01–0.2 Hz for clarity of inspection, but the broadband signal is used in the analyses. The same result is found in the case of either filter.) **a** Uncorrected east, north and vertical components of seismogram. Start and end of analysis window giving best linearisation of particle motion are indicated by *red vertical lines*. **b** Uncorrected (*top*) and corrected (*bottom*) radial and transverse components. **c** Uncorrected (*top left*) and corrected (*top right*) fast (*solid*) and slow (*dashed*) waves after rotation to the fast direction. Beneath are uncorrected (*bottom left*) and corrected (*bottom right*) horizontal particle motion. **d** Contour surface of λ_2 (*left*), with the 95 % confidence limit shown by thicker contour. *Blue cross* is the minimum λ_2, corresponding to the values of ϕ and δt which best linearise the particle motion. *Right hand panels* show result of cluster analysis

S whilst correcting for the source anisotropy gives a receiver-side estimate. Both corrections are then applied (for shallow earthquakes; only a receiver-side correction is applied for very deep events >550 km, assuming mantle isotropy below this depth) when analysing ScS, so that the remnant splitting occurs in ScS only, and hence results from anisotropy in D″ alone. An example of a measurement where both source and receiver corrections are applied is shown in Fig. 4.3.

In order to estimate UM anisotropy beneath the Aleutian arc, we make new measurements of SKS splitting at stations in the AK network along similar back-azimuths to the S and ScS phases studied. These are presented in Table 4.2 and shown in Fig. 4.4. Where more than one very good measurement was made, the error surfaces were stacked to improve the estimate of UM splitting. These are listed in Table 4.3. The measurements show a clear trench-parallel trend for most of the arc, with the easternmost measurements becoming less so where a larger strike-slip

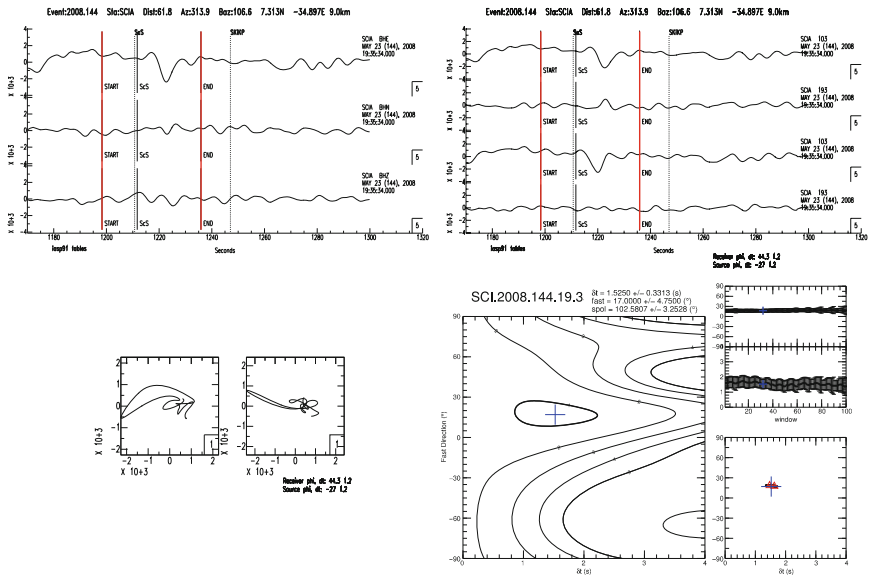

Fig. 4.3 Splitting analysis of ScS phase at station SCIA from Mid-Atlantic Ridge earthquake of 2008-144-1935. Panels as described in Fig. 4.2, except wavelet plots are not shown. The ScS phase is marked by the labelled *solid vertical line* in the *upper* panels. Both a receiver and source correction have been applied. Note that the transverse energy in the uncorrected waveform is removed in the corrected one, and the particle motion is linearised, indicating a good result

Table 4.2 SKS splitting measurements made in this study

Station	Event (year-day-time)	Lat (°N)	Lon (°E)	Depth (km)	Backazimuth (°)	ϕ (°)	$\Delta(\phi)$ (°)	δt (s)	$\Delta(\delta t)$ (s)
AKGG	2007-202-1327	−8.13	−71.27	645	90.96	57.00	8.75	0.88	0.19
ATKA	2003-171-0637	−7.61	−71.72	560	84.82	17.00	12.00	0.80	0.07
BMR	2007-202-1327	−8.13	−71.27	645	108.45	−86.00	10.00	0.32	0.08
EYAK	2007-202-1327	−8.13	−71.27	645	107.44	−34.00	20.75	0.42	0.14
FALS	2007-202-1327	−8.13	−71.27	645	92.95	44.00	8.75	0.50	0.17
PNL	2007-202-1327	−8.13	−71.27	645	112.95	−37.00	12.25	1.20	0.24
RC01	2003-117-2314	−8.20	−71.59	560	104.28	16.00	18.25	0.50	0.56
RC01	2003-171-0636	−7.61	−71.72	560	104.11	29.00	39.50	0.68	0.99
RC01	2007-202-1327	−8.13	−71.27	645	103.97	13.00	6.75	0.60	0.13
SWD	2003-171-0636	−7.61	−71.72	560	104.37	21.00	28.75	0.85	0.88
SWD	2007-202-1327	−8.13	−71.27	645	104.24	−16.00	4.25	1.02	0.03
UNV	2007-202-1327	−8.13	−71.27	645	90.61	53.00	3.75	0.88	0.04

Uncertainties in ϕ, $\Delta(\phi)$, and δt, $\Delta(\delta t)$ are given to the 95 % confidence limit

component in the subduction is apparent (Fig. 4.4). For stations where SKS measurements were not possible within our requirements, we check that the splitting in the S phase (after correction for source anisotropy determined using stations with reliable SKS measurements) agrees with SKS results nearby.

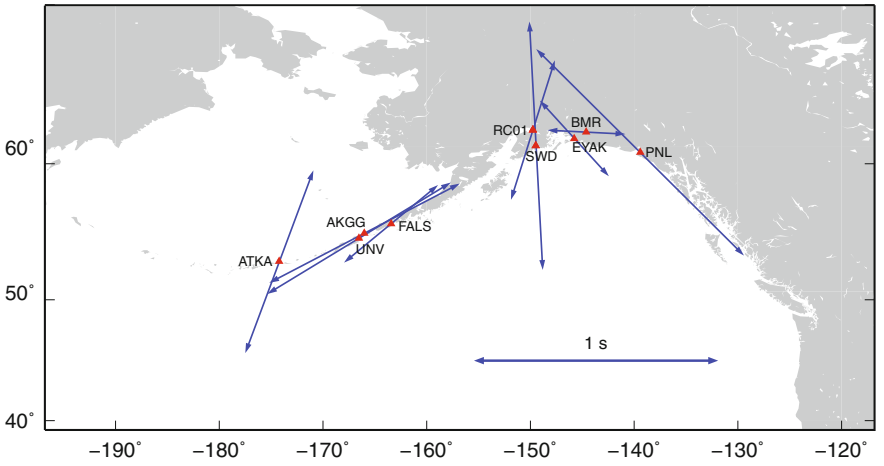

Fig. 4.4 Splitting parameters of SKS at stations in Alaska made in this study. For RC01 and SWD, the stacked measurements are shown. Fast direction ϕ is indicated by orientation of *arrow*; delay time δt is represented by *arrow* length according to the scale

Table 4.3 Stacked measurements of SKS splitting at stations RC01 and SWD, used to assess the validity of nearby SKS measurements

Station	ϕ (°)	$\Delta(\phi)$ (°)	δt (s)	$\Delta(\delta t)$ (s)
RC01	15.00	3.25	0.625	0.075
SWD	−3.00	8.75	1.050	0.313

4.2.3 Testing SKS Splitting Measurements as Upper Mantle Anisotropy Corrections

We test the validity of using SKS measurements as a correction for UM anisotropy. Because the tectonic and geological processes which cause UM anisotropy are unlikely to be determined by structure in D″, we can regard the two as independent. Hence over broad, continental scales, SKS measurements will be oriented approximately randomly, and we can check that the consistency observed in our results is not due to a systematic error being introduced by UM anisotropy. For the MAR event of 2008-144-1935, we analyse the S phase at each station for which we selected reliable SKS measurements, and replace those with others taken at random. The false 'corrections' are determined by allowing the correction fast orientation ϕ_{corr} to vary between 0 and 180°, and the delay time δt_{corr} between the minimum and maximum values for those in SKS measurements used in this study (0–2.5 s). A uniform random distribution is used. Figure 4.5 shows polar histograms of ϕ'', the projected fast orientation at the source, for five of the sets of false 'corrections'. Of these, the smallest sample standard deviation $\sigma_{\phi''} = 47°$. Also shown is that for the

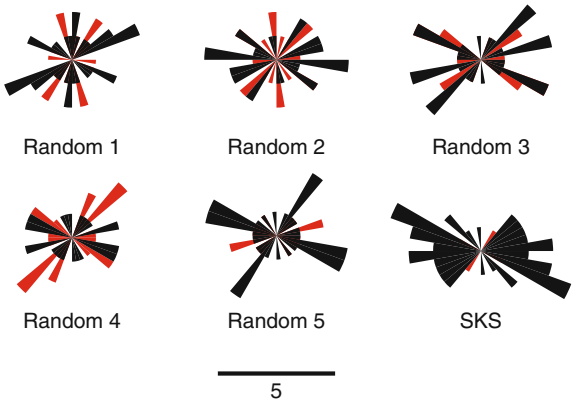

Fig. 4.5 Polar histograms of ϕ'' for five sets of randomised SKS 'corrections' when analysing the S phase for the MAR event of 2008-114-1935; also for the set of SKS actually used in the analyses. ϕ'' is the projection of the measured geographic fast orientation at the receiver back to the source, such that $\phi'' =$ azimuth + backazimuth $- \phi$. *Black bars* show number of measurements in each 10° bin. *Red bars* show bins of null or very large measurements of δt. There is a 180° ambiguity in the measurements. The radial frequency axis is shown by the scale bar, *bottom*. We note that the number of very large or null measurements is smallest by far for the case of using real SKS measurements as receiver corrections

true SKS splitting parameters used ($\sigma_{\phi''} = 33\,^\circ$). Red bars indicate measurements of $\delta t > 3.5$ s, which may correspond to two situations. Firstly, they may be null measurements, which frequently display a minimum λ_2 at the extreme of the permitted δt (here, 4 s). These arise because by chance the 'correction' applied is the same as the total source-side and receiver splitting combined (i.e., $\phi_{\mathrm{SKS}} \approx \phi$ and $\delta t_{\mathrm{SKS}} \approx \delta t$), and by removing the 'correction' there is no remnant splitting. Secondly, the large results may happen when the 'correction' is large and near-perpendicular to the source and receiver splitting at the receiver, leading to very large result, which is extremely unlikely to exist in nature.

It appears that the source side splitting direction (and also delay time; not shown) is most consistent when using SKS measurements to correct for splitting introduced after that beneath the source in S. In addition, ϕ'' is most similar to the plate spreading direction for the SKS-corrected case.

To confirm that applying an SKS measurement as an UM splitting correction is valid, we check that particle motion is linearised and a null (or very small) measurement results from analysing an S wave from a very deep event. This confirms that the S and SKS waves undergo the same splitting whilst travelling in the UM beneath the station, and hence that the SKS correction is valid. For the event 2007-202-1327, Fig. 4.6 shows the splitting in S at station KAPO with no correction applied and with the SKS measurement of Frederiksen et al. (2007) used as a receiver correction ($\phi_{\mathrm{SKS}} = 69°, \delta t_{\mathrm{SKS}} = 0.58$ s). As is evident, with no correction we measure splitting in S to be the same as that in SKS within error. The removal of the splitting leads to a null result, with the particle motion highly linear (Fig. 4.6d).

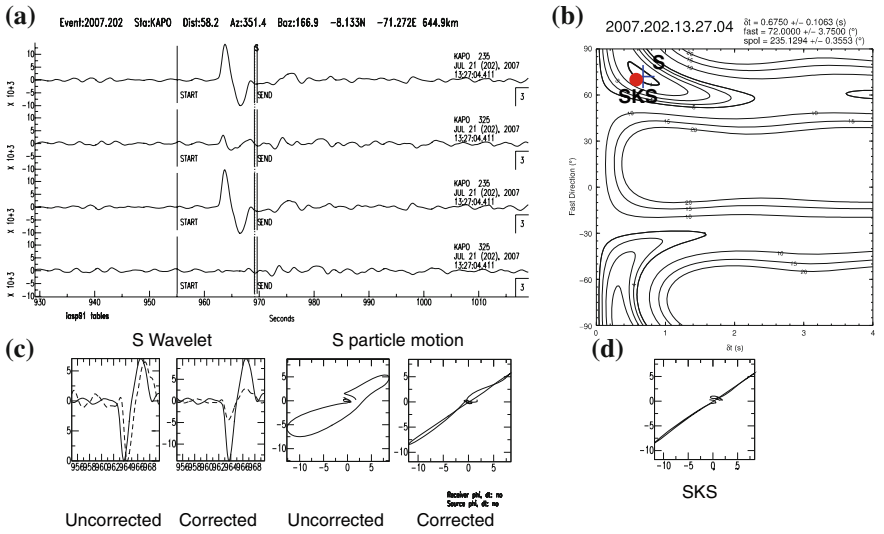

Fig. 4.6 Splitting analysis of uncorrected S wave from event on 2007-202-1327 (Brazil, depth 645 km) at station KAPO (Kapuskasing, Ontario, Canada), compared to SKS (Frederiksen et al. 2007) at the same station. **a** Uncorrected (*top two traces*) and corrected (*bottom traces*) radial and transverse components for S. The transverse energy is well removed by the measurement, which gives the parameters $\phi_S = (72.0 \pm 3.8)\,^\circ$, $\delta t_S = (0.67 \pm 0.11)$ s. **b** λ_2 surface for S result. *Blue cross* shows optimum splitting parameters for S. Also shown is the value obtained for SKS (*red dot*; size is smaller than the uncertainty in the parameters), $\phi_{SKS} = 69\,^\circ$, $\delta t_{SKS} = 0.58$ s. They are the same within error, confirming that there is likely no source-side splitting present in the signal for such deep events. **c** (*Left to right*) Wavelet plots and particle motions for respectively uncorrected and corrected split S waves. The splitting parameters linearise the particle motion well. **d** Particle motion of the SKS phase before analysis, after applying the S splitting parameters (ϕ_S, δt_S) as a receiver correction. As expected, using either to correct the other results in linear particle motion and no splitting (a null result), and confirms that SKS can be used as an UM correction for S

4.2.4 Source-Side Anisotropy Estimates

A further test of the efficacy of correcting for UM anisotropy with SKS measurements, after running the analyses, is to compare the source-side UM splitting that remains after analysing S waves from shallow earthquakes to local splitting measurements. If there is no contamination from unexpected or complicated anisotropy beneath the receiver for which we have not accounted, or for which SKS measurements are not an adequate correction, then source splitting parameters and local ones should be the same. For events at the East Pacific Rise (EPR), we may directly compare ϕ'' with measurements of SKS splitting using ocean bottom seismometers (OBSs) (Wolfe and Solomon 1998). These are shown with ϕ'', δt for the event 1994-246-1156 (Fig. 4.7; Table 4.1). Local splitting and that measured beneath the earthquake are extremely alike. This is also very strong confirmation that the source correction is a true measurement of source-side splitting, and we can thus remove it comprehensively when analysing ScS.

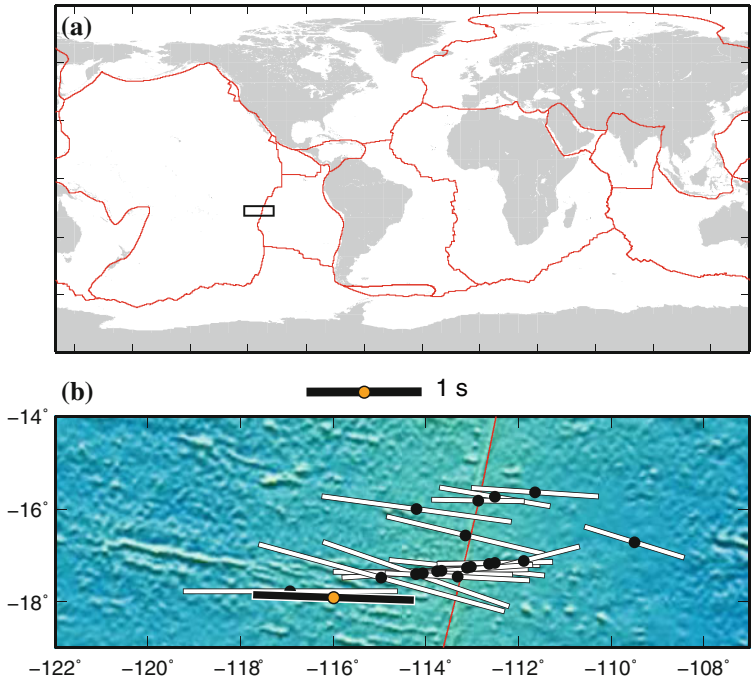

Fig. 4.7 SKS splitting measurements of Wolfe and Solomon (1998) and source-side splitting of earthquake of 1994-246-1156 (Table 4.1) calculated by analysis of direct S phase with SKS measurements used as a receiver-side correction (this study). **a** Index map showing location of (**b**) on the EPR. *Red lines* show major plate boundaries. **b** SKS splitting parameters made at OBSs on the EPR (*white bars* beneath *black circles* for OBS locations: angle is fast orientation; length is proportional to delay time as shown in the key, *middle*). Errors in ϕ_{SKS} are around 5° or more. *Orange circle* is location of event 1994-246-1156; *black bar* orientation shows ϕ''; length is proportional to δt. The measurement of source anisotropy is remarkable in its similarity to the OBS-determined UM anisotropy

4.2.5 Source Polarisation Measurements

Another test of the efficacy of using SKS measurements to correct for receiver-side anisotropy is to compare: the polarisations of the linearised particle motion after applying a correction for receiver-side UM anisotropy and measuring the source-side splitting in S; and the predicted source polarisations of the S wave according to the Global CMT solution for that event. For deep earthquakes, we measure the splitting in S and compare the linearised particle motion with the predicted source polarisation without applying any UM correction; for shallow events we apply a correction using SKS measurements.We find that in no case do the measured and predicted source polarisations differ by more than 20°, and in most cases they are within 10°. Figure 4.8 compares the predicted and measured horizontal particle motions for each earthquake used in this study at an example station.

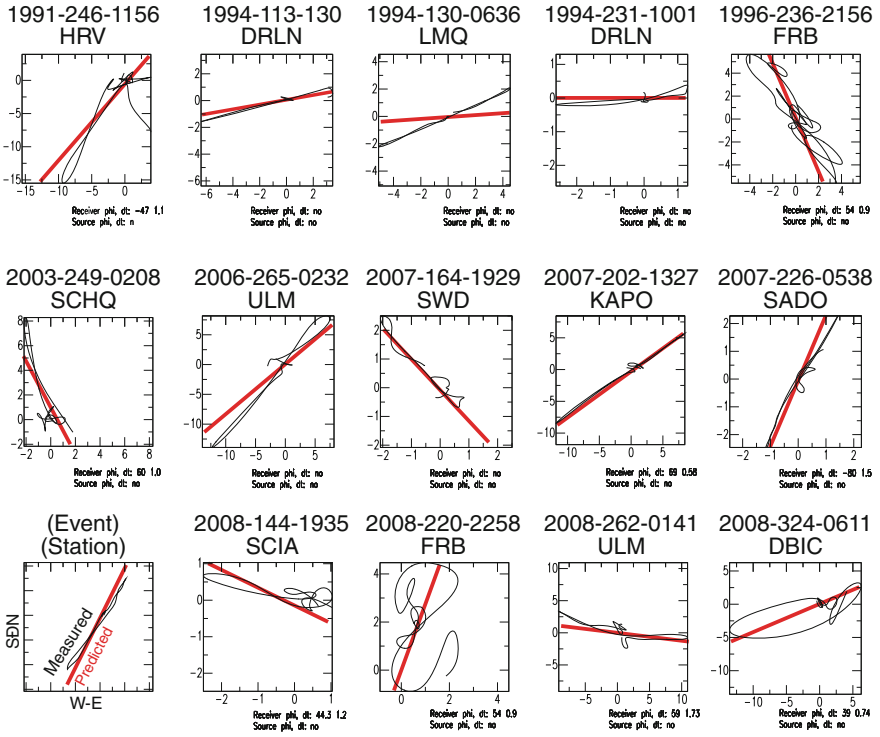

Fig. 4.8 Predicted and measured horizontal particle motion for each earthquake used in this study at an example station, showing the match between measured and predicted source polarisations. The measured (*black*) particle motions are calculated for the corrected S phase after splitting has been measured. For deep events, no source anisotropy correction is made (denoted by 'Receiver phi, dt: no' beneath the subfigure); for shallow events, an SKS correction is applied to remove the receiver UM anisotropy (given in the values beneath the subfigure). The predicted (*red*) particle motions are calculated using the parameters given by the Global CMT solutions for the event, giving a source polarisation that is projected onto the station

4.2.6 S–ScS Splitting from Deep Versus Shallow Earthquakes

As a final check that we adequately remove source-side anisotropy, we compare the results of differential analysis of S and ScS using the 2007–202 event (shown to have no measurable source anisotropy in Fig. 4.6) with those from five shallow earthquakes located nearby (Table 4.4). Hence the ray paths are very similar, and the same region of D″ is sampled. If there is any systematic error in our attempt to remove the source-side splitting, the results will be significantly different.

From a larger group of 25 events located near to event 2007–202 above 100 km depth from 1989 onwards, five were selected for good signal-to-noise ratios for both S and ScS. Using $\phi_{\text{corr}} = 70°$ and $\delta t_{\text{corr}} = 0.63$ s (average of S and SKS splitting parameters; see Fig. 4.6), the procedure outlined above was conducted to

Table 4.4 Shallow earthquakes used to compare ScS splitting parameters for deep (event 2007-202) and shallow earthquakes, measured at station KAPO

Year-day-time	Lat (°N)	Lon (°E)	Depth (km)
2001-186-1353	−16.09	−73.99	62
2003-171-0619	−7.61	−71.72	0
2005-269-0155	−5.58	−76.39	71
2006-293-1048	−13.43	−76.57	33
2007-320-0312	−2.07	−78.20	33

obtain ϕ' and δt. Those ray paths for measurements in the S region which traverse the most similar region in D″ to those from the shallow events were selected for comparison (Fig. 4.9a). Figure 4.9c–d shows polar histograms of the fast direction in the ray frame, ϕ', for the two sets of results, with the near-null results downweighted in the shallow case, as the number of data points is small. Because there are few measurements, there is some spread and the standard deviation is relatively large (both of which is reduced when using larger samples; see for instance Fig. 4.12, eastmost histogram). However for the deep event, $\langle\phi'\rangle \approx 81\,°$, $\langle\delta t\rangle \approx 1.3\,$s; for the shallow events, $\langle\phi'\rangle \approx -84°$, $\langle\delta t\rangle \approx 1.8\,$s. Whilst these are not identical, they are the same within error. The small variation might be due to local variation within D″, as the ray paths do not overlap completely. Where they do, as shown in Fig. 4.9e–f, the results are the same within the 95 % confidence limit, further suggesting that the difference between the two groups is mainly small local variation, not a bias in the shallow or deep source region.

This, and the other tests of the use of source and receiver corrections, compels us to believe that the shear wave splitting we observe in ScS after removing UM anisotropy must be the true signal from a third, intermediate anisotropic region—D″.

4.2.7 Mineral Slip System Fitting

To compare different slip systems in ppv, we calculate the orientations of the shear planes and slip directions which are compatible with our measurements (Fig. 4.10). These orientations are computed by performing a grid search over the elastic constants for the relevant slip systems (Merkel et al. 2007; Yamazaki et al. 2006; Wookey et al. 2005b), which are rotated about the three principal (orthogonal) axes; we scale the elastic constants by linearly mixing the fully anisotropic constants with those of an isotropic average. The amount and orientation of shear wave splitting is computed at each node using the Christoffel equation, and orientations which are compatible with the measured anisotropy (within the errors of the azimuthal stacks; Table 4.5) are plotted. The larger the scaling required to fit the case, the higher degree of ‘strain’ is represented (indicated by colour; Fig. 4.14b–i), and this directly corresponds to the proportion of the material which is a linear mix of the anisotropic and isotropic components (i.e., the relative proportions of oriented and random crystals).

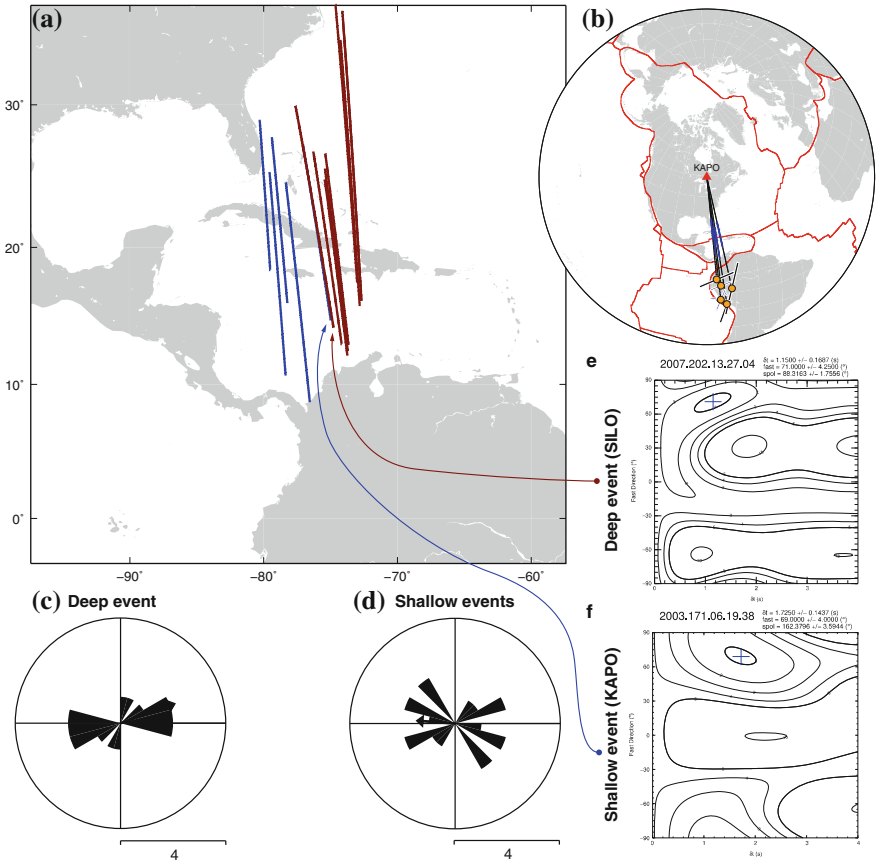

Fig. 4.9 Comparison between corrected ScS ϕ' from deep and shallow events. **a** Map of ray paths in a 250 km-thick D″ for ray from deep (*red*) and shallow (*blue*) events. **b** Shallow event locations with source-side UM splitting (*black bars*; orientation is ϕ'', length shows δt, to maxm. 3 s) and null directions (blue bars). **c** and **d**, polar histograms showing ϕ' for ScS for deep and shallow events respectively. Up is $\phi' = 0°$, as for Figs. 4.12 and 4.13. The latter are recorded at KAPO. *Scale bar* shows radial frequency; near-null directions have been downweighted for the shallow measurements to avoid bias. **e** and **f** Error (λ_2) surfaces for $\phi - \delta t$ in the geographic frame for the most closely overlapping ray paths. **e** is for the deep event recorded at SILO, **f** shows that for shallow event 2003-171-0619. The two are the same within the 95 % confidence limit (*thick black line*)

4.3 Results and Discussion

Stacked results along each azimuth in the three regions give splitting parameters shown in Fig. 4.13 and listed in Table 4.5. We discuss results in terms of the delay time (δt) and ray frame fast orientation (ϕ'; Fig. 4.1c). The primary observation is that D″ everywhere shows anisotropy of between 0.8 and 1.5 % (assuming a uniform 250 km-thick D″ layer). Along south–north (region 'S') and southeast–northwest

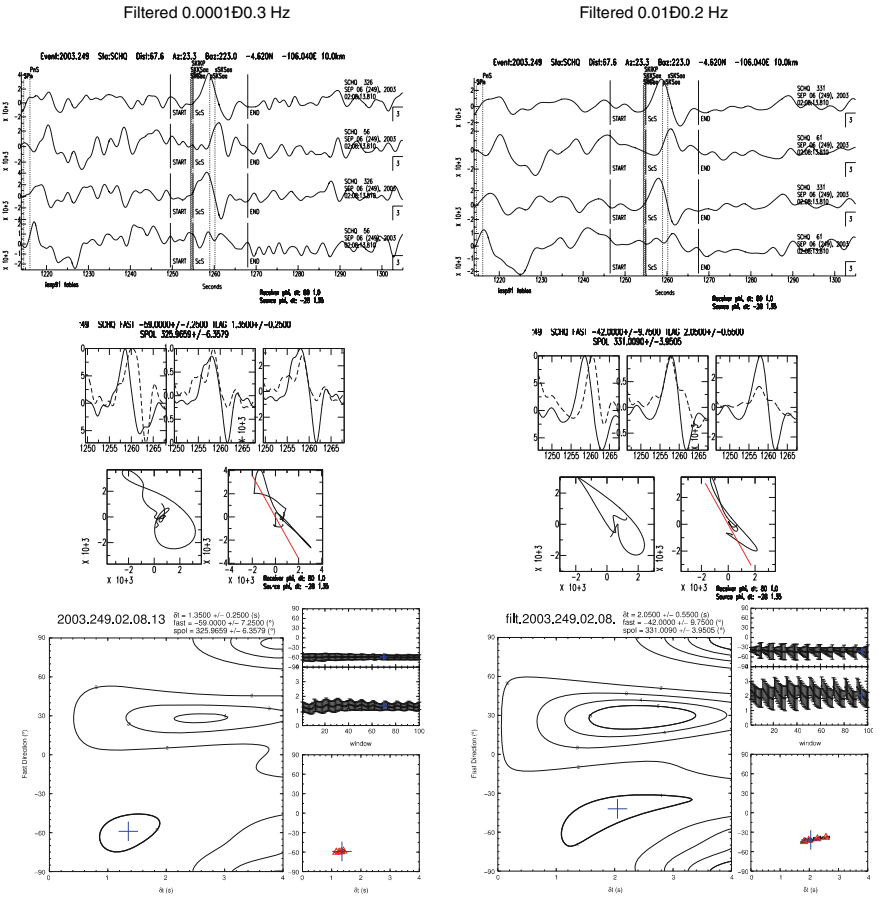

Fig. 4.10 Comparison of splitting results using data filtered in two different pass bands, event 2008-249-0208 recorded at SCHQ (Schefferville, Québec, Canada). The data on the *left* are filtered in the band 0.0001–0.3 Hz; on the *right* between 0.01–0.2 Hz. Although the waveforms on the right appear 'cleaner' and possibly subjectively easier to identify, the nature of the F-test used to calculate the size of the 95 % confidence interval (*thick black line* on λ_2 surface, *bottom*) means that the quoted errors are larger when the frequency content of the signal is narrower. Hence we use the broader-band signal for our analyses. It is important to note that the results are the same within the 95 % confidence interval in any case, which we observe to be generally true

('E') ray paths, from deep South American events (∼200 measurements), $\langle \delta t \rangle = (1.45 \pm 0.55)$ s, implying shear wave anisotropy of ∼0.8 %. Fast orientations are approximately CMB-parallel ($\phi' \approx 90\,^\circ$). This agrees with previous studies made along similar azimuths (Garnero et al. 2004; Kendall and Nangini 1996; Maupin et al. 2005; Rokosky et al. 2006), including the presence of some small variation in ϕ' of up to $\pm 15^\circ$ (Maupin et al. 2005; Garnero et al. 2004). Such variations could be approximated as VTI over the region. Detailed results are shown in Figs. 4.11 and 4.12. Notably, however, oblique to the ∼south–north raypaths in the Caribbean, fast

Table 4.5 Stacked differential S–ScS measurements made in the regions shown in Fig. 4.13

Region	Source	Azimuth (°)	N	ϕ' (°)	$\Delta(\phi')$ (°)	δt (s)	$\Delta(\delta t)$ (s)	ΔV_S (%)
W	Hawaii	66	17	−80	6	1.10	0.04	0.9
W	Central America	318	11	77	10	1.25	0.03	1.5
S	EPR	27	7	−42	4	1.68	0.04	1.2
S	South America	322	191	−84	3	0.90	0.01	0.8
E	South America	355	16	83	8	1.28	0.10	0.8
E	MAR	299	71	45	7	1.78	0.02	1.1

Azimuth is given as mean at ScS bounce point. N is number of measurements. ΔV_s, the shear wave speed variation between the fast and slow wave, is given assuming a uniform 250 km-thick D″ layer and the V_S model SKNA1 (Kendall and Nangini 1996)

directions are at least 40° from CMB-parallel (region S: $\delta t = 1.68$ s, $\phi' = -42°$; region E: $\delta t = 1.28$ s, $\phi' = 45°$). In region 'W', both azimuths show ϕ' about 10–15 ° from the horizontal in D″, with $\delta t \sim 1.2$ s. Hence nowhere are our measurements compatible with VTI, because we do not find $\phi' = \pm 90$ ° within error in both directions for any region.

As Fig. 4.11 shows, there is some small variability of ϕ' and δt within the measurements in the paths. Figure 4.12 shows polar histograms in 15 ° bins for ϕ' along each path. The EPR–North America leg of region S shows very steep fast orientations ($\phi' \approx -10$ °). This is because the three measurements from event 2008-262 are near-null, giving larger uncertainties and results which the analysis places near to the null direction. Stacking the λ_2 surfaces for these alongside the other events leads to a better-constrained result, as the fast direction in D″ is not as close to the source polarisation when projected into the ray frame.

4.3.1 LPO in Post-Perovskite

A likely mechanism for the production of anisotropy in D″ is the lattice-preferred orientation (LPO) of anisotropic mineral phases present above the CMB such as (Mg, Fe)O, and $MgSiO_3$-perovskite (pv) and -ppv. These may give rise to styles of anisotropy more complicated than TTI with lower symmetries, which are compatible with our two-azimuth measurements. We investigate the possibility of LPO in ppv leading to the observed anisotropy rather than other phases because of its likely abundance in seismically fast regions of the lowermost mantle (LMM) beneath North America and its relatively large anisotropy. (Mg, Fe)O and pv seem poor candidates for D″ anisotropy—(Mg, Fe)O is equally abundant in the LM above D″, which appears relatively isotropic (Meade et al. 1995), and pv is the dominant phase there. Whilst (Mg, Fe)O may be strongly anisotropic and mechanically weaker than ppv (Karki et al. 1999; Long et al. 2006; Yamazaki and Karato 2002), and therefore might take up more deformation and align more fully, ppv is also highly anisotropic and is

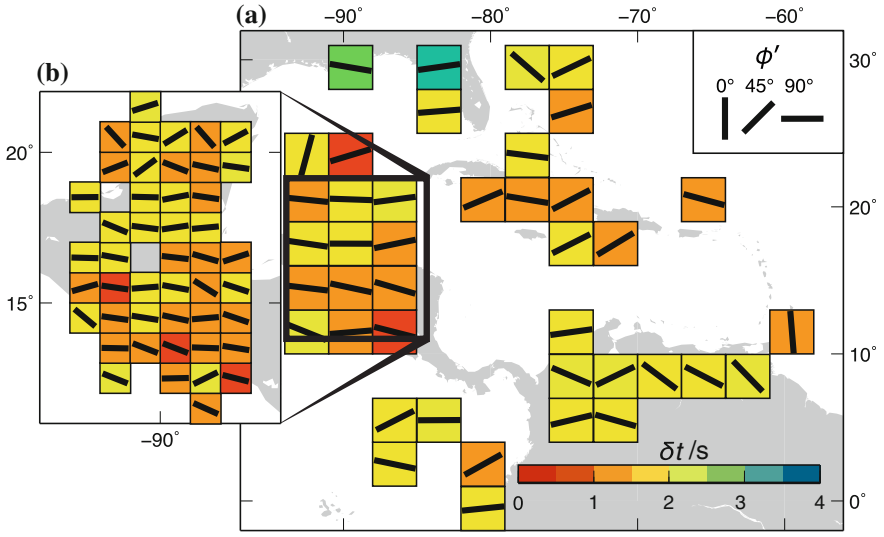

Fig. 4.11 Measurements of shear wave splitting from one azimuth. **a** Results of binning measurements of ϕ' (*thick black lines*; angle corresponds directly to ϕ') and δt (colour as per scale) by ScS CMB bounce point into three-degree blocks (∼150 km at CMB) in the Caribbean, using deep-focus earthquakes in South America. ScS samples D″ from only one azimuth in this case. **b** Enlargement of region beneath Yucatan peninsula binned in one degree blocks (∼50 km at CMB). The zone of sensitivity of ScS at the CMB is less than 10° perpendicular to its propagation direction (∼east-west here)

the most abundant phase, meaning a lower degree of alignment of ppv can produce just as much anisotropy as more alignment of (Mg, Fe)O. Therefore LPO in ppv is our preferred mineralogical mechanism.

Different candidate mechanisms for LPO development in ppv from deformation by dislocation creep have been proposed: slip systems of $[\bar{1}10](110)$ (Merkel et al. 2006, 2007; Oganov et al. 2005) and [100](010) (Carrez et al. 2007; Yamazaki et al. 2006; Iitaka et al. 2004) have been inferred from experimental and theoretical methods. Recent experimental work (Okada et al. 2010) has also suggested that the [100](001) system may be plausible, which is appealing since it appears to best match the first-order anisotropic signature of the lowermost mantle (Stackhouse et al. 2005; Tsuchiya et al. 2004; Wookey et al. 2005b; Wookey and Kendall 2007).

Our results can differentiate between these candidate mechanisms if we assume that most of the measured anisotropy in D″ is a result of deformation-induced LPO in ppv, and we have an accurate estimate of the mantle flow where we measure anisotropy. At present, such models of mantle deformation are in their infancy, but we can nonetheless make inferences from broad-scale trends in subduction and global V_S models. We calculate the orientations of the shear planes and slip directions which are compatible with our measurements for the three slip systems in ppv. Aggregate elastic constants for the $[\bar{1}10](110)$ and [001](010) systems are taken

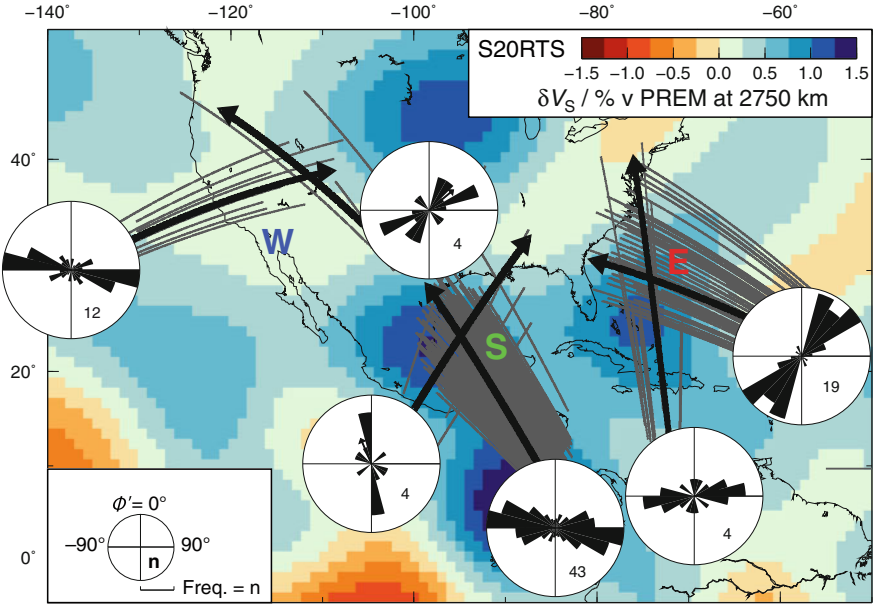

Fig. 4.12 Polar histograms of the ray-frame fast directions (ϕ') of individual measurements of splitting in ScS along each path. The frequency (radial) axis maximum is given by the number n in each histogram. Where visible, the *black arrow* gives the arithmetic mean of ϕ'. δt is not represented in this diagram. Other features as for Fig. 4.13

from deformation experiments (Merkel et al. 2006; Yamazaki et al. 2006); we use single-crystal elastic constants from first-principles calculations (Stackhouse et al. 2005; Wookey et al. 2005b) for the [100](001) system. These planes and directions are plotted in Fig. 4.14. We also produce the shear planes predicted for cases of pv and MgO (Fig. 4.12).

At present, there is some disagreement in detail between different *ab initio* elastic constants for ppv (Stackhouse et al. 2005; Wentzcovitch et al. 2006). We use those of Stackhouse et al. (2005) for consistency with experimental studies. Another source of uncertainty may be the extrapolation of results of deformation experiments (Merkel et al. 2006, 2007; Yamazaki et al. 2006; Okada et al. 2010) to LMM conditions.

To guide our interpretation of the results, we can appeal to the broadly analogous situation of finite strain and olivine LPO associated with passive upwelling beneath a mid-ocean ridge. Models indicate that, near the centre of the upwelling, directions of maximum finite extension dip away from the centre, and become more horizontal with distance from the ridge (Blackman et al. 1996). Corresponding features beneath downwellings are found in convection models of the lower mantle—inclined deformation dipping towards the downwelling centre (McNamara et al. 2003). Regions E and S are either side of the apparent centre of the downwelling Farallon slab (Ren et al. 2007; Ritsema et al. 1999) (Figs. 4.13, 4.14) which strikes roughly northwest-

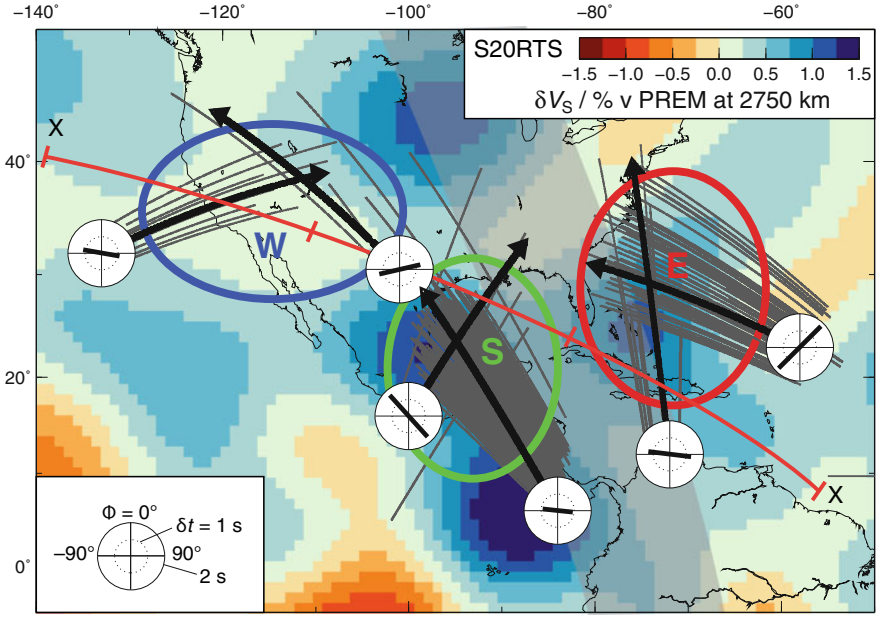

Fig. 4.13 Multi-azimuth stacked shear wave splitting results in each region. Also shown are individual D″ ray paths of ScS phases used in stacks (*thin grey lines*); representative mean ray paths in D″ of stacked measurements (*thick black lines*, *arrows* indicate direction of travel); plots of splitting parameters for each stack at the start of the path (*white circles* with *black bars*, angle indicates ϕ', length indicates δt). Beneath is the variation of V_S at 2750 km depth (∼150 km above CMB) in the S20RTS model (Ritsema et al. 1999). *Thick red line* is cross-section shown in Fig. 4.14a. Shaded region shows approximate strike of Farallon plate predicted at 2500 km (Ren et al. 2007). Three study regions ('W', 'S' and 'E') are indicated by *circled areas*. Figure 4.16 shows the approximate finite-frequency zone of sensitivity for ScS in D″

southeast, hence we postulate northeast-southwest slip directions on inclined shear planes with an opposite sense of dip (i.e., dipping southwest for region E, northeast for region S). Further away from the downwelling, in region W, more horizontal flow is expected and hence a horizontal shear plane with northeast-southwest slip directions.

All three considered slip systems have orientations which can explain the data, however the predictions of the [100](001) slip system (Fig. 4.14) best match the above criteria. The $[\bar{1}10](110)$ system is arguably the least plausible, as it requires complex flow further from the downwelling (region W) where a more simple horizontal flow pattern is expected. We cannot yet completely rule out the [100](010) system; more rigorous flow modelling in the region is required to conclusively resolve this issue.

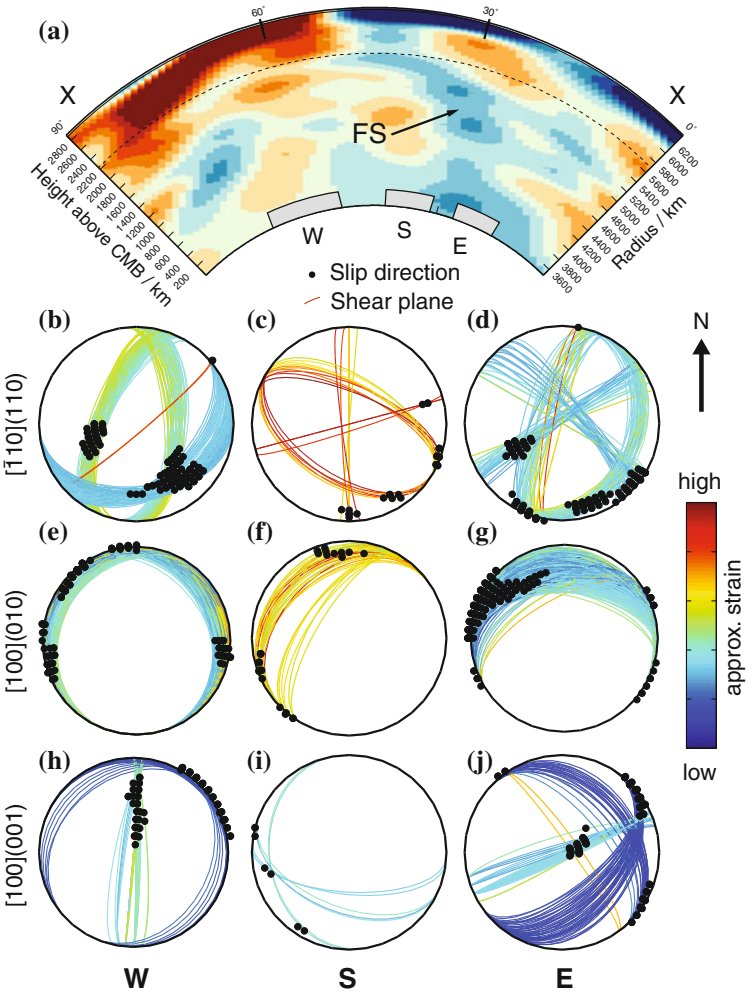

Fig. 4.14 Section through study region and compatible shear planes for candidate ppv slip systems. **a** Cross-section through V_S model S20RTS traversing the study region, as indicated in Fig. 4.13. The approximate regions W, S and E in D″ are drawn. Colours indicate V_S as for Fig. 4.13. The inferred location of the Farallon slab from high V_S is labelled with 'FS'. **b–j** Orientations of potential elastic models which are compatible with the observed anisotropy in D″. Shown are upper hemisphere equal-area projections looking down the Earth radial direction (vertical) of the possible shear planes (*coloured lines*) and slip directions (*black circles*) in ppv for each slip system. The colour of the shear planes indicates the amount of strain required to produce them according to the arbitrary colour scale, *right*. The three slip mechanisms [1̄10](110) (**b–d**), [100](010) (**e–g**) and [100](001) (**h–i**) are tested in each region (*left* to *right*, W, S, E). Up is north. There are usually two sets of planes, because two azimuths of measurements are not sufficient to uniquely define the planes in the orthorhombic symmetry of the models

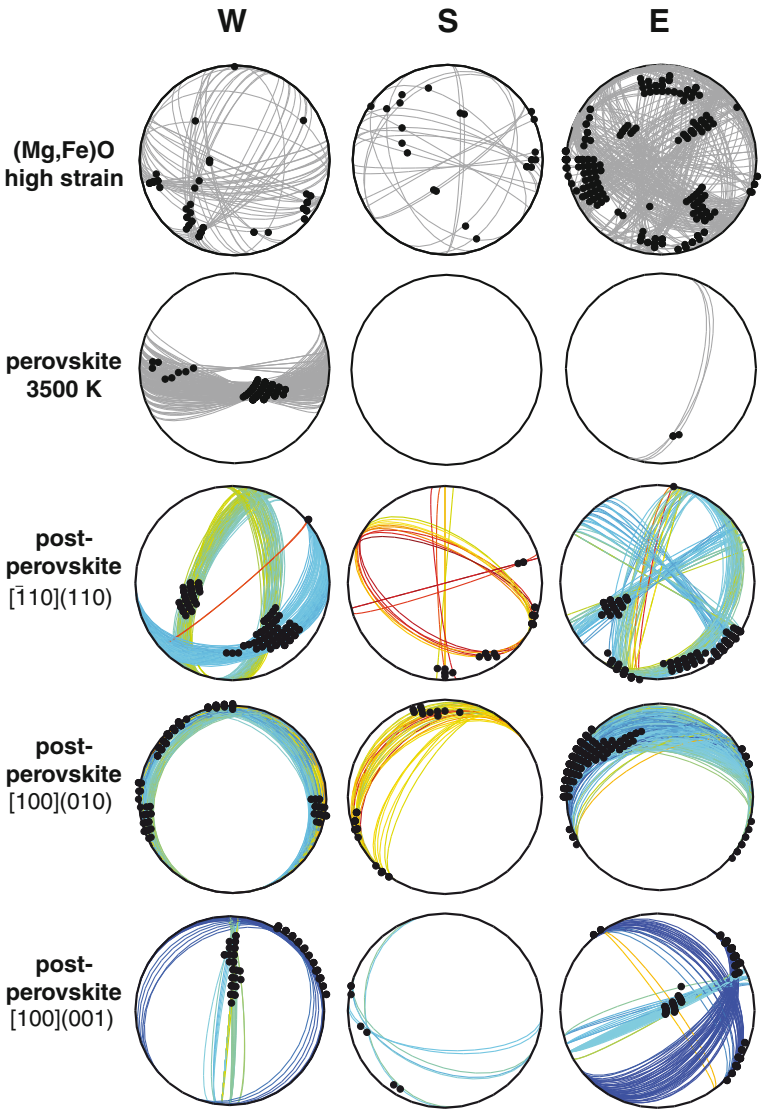

Fig. 4.15 Orientations of shear planes for MgO and perovskite which are compatible with our measurements of anisotropy in D″, alongside those shown in Fig. 4.14 for post-perovskite. Equal-area *upper hemisphere plots* show shear planes (*grey lines*) and slip directions (*black circles*) for the expected slip systems in (Mg, Fe)O (Yamazaki and Karato 2002) and $MgSiO_3$-perovskite (Mainprice et al. 2008) which produce alignment of the mineral phase to produce anisotropy compatible with our measurements. Out of the page is the Earth radial direction, and up is north. The three regions ('W, 'S' and 'E') are labelled

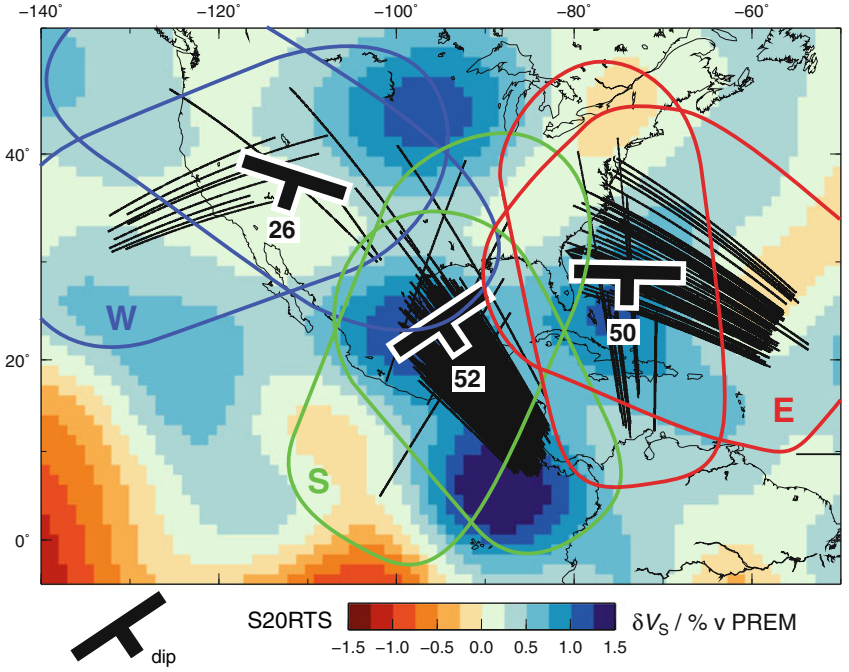

Fig. 4.16 Paths in D″ of ScS rays and best-fitting TTI symmetry planes. Shown are ray paths of ScS in D″, assuming it to be uniformly 250 km thick (*thin black lines*); orientations of best fitting planes normal to axis of rotational symmetry for TTI case of anisotropy (strike and dip symbols); zones of sensitivity of ScS in D″ for each of the sets of crossing paths in the three regions (*blue*, *green* and *red* outlines for 'W', 'S' and 'E' regions respectively). It can be seen that there is considerable overlap in the crossing rays, hence the majority of the signal we observe in the two directions is likely to come from the same area for each region. Plotted beneath is the shear velocity in D″ in the S20RTS model. See Fig. 4.13 for details

4.3.2 LPO in $MgSiO_3$-Perovskite and (Mg, Fe)O

It seems very likely that $MgSiO_3$-post-perovskite (ppv) is the dominant mineral phase at D″ conditions, especially for realistic mantle compositions in terms of Fe and Al (Catalli et al. 2009), hence we believe that anisotropy in aligned ppv is probably the likeliest explanation for the observed shear wave splitting. However, (Mg, Fe)O is also highly anisotropic, and maybe mechanically weaker than ppv (Long et al. 2006; Murakami et al. 2009; Karki et al. 1999; Yamazaki and Karato 2002). Hence it may be the case that MgO dominates the deformation at high strain and may align more than ppv. We test the fit of candidate shear planes and slip directions believed to dominate in MgO (Yamazaki and Karato 2002) to our measurements of shear wave splitting as explained in the Methods section (Fig. 4.15). In this case, we do not show the degree of scaling of elastic constants with colour, though the plots are otherwise the same as Fig. 4.14. Because of MgO's high, cubic symmetry, many planes are compatible with our measurements for some of the regions. We notice, however,

that in region S in particular, there are few shallow-dipping shear planes associated with near-horizontal slip, which seems to be unlikely over a broad scale beneath downwelling. Instead, most planes and slip directions are steeper than for some of the ppv slip systems (Fig. 4.14).

4.3.3 Shape-Preferred Orientation

D″ anisotropy might also arise from shape-preferred orientation (SPO) of seismically distinct material over sub-wavelength scales. This would lead to a TTI-type behaviour (Kendall and Silver 1998), with which our observations are compatible. In this case, we can interpret our results simply by finding the common plane, normal to the rotational symmetry axis, from the two azimuths and ϕ'. These planes are shown in Fig. 4.16.

In each region, the TTI plane dips approximately in the same way as for the [100](010) case, i.e., southwest, southeast and south in regions W, S and E respectively, by between 26–52° (Fig. 4.16). However, there is no constraint on the slip direction, and especially in regions S and E, where the dip is ∼50°, it is hard to correlate the TI planes with a candidate plane of deformation based on V_S, and models of deformation suggest strain in such slab-parallel orientations is unlikely. For this reason and other explanations of D″ properties by the post-perovskite phase (Wookey et al. 2005b), we favour the mineralogical interpretation at present, where all tested ppv mechanisms are in some agreement with our results, and the [100](001) slip system in ppv is most compatible with our observations.

4.4 Conclusion

Using several hundred measurements of differential shear wave splitting in ScS waves beneath the Americas, we have demonstrated that the region displays significant seismic anisotropy in the lowermost mantle. Along one set of paths, our results agree excellently with previous work suggesting that horizontally-polarised shear waves travel faster than vertically-polarised waves in D″. However, measurements along different, crossing paths show that the style of anisotropy in the region is in fact more complicated and cannot be approximated by vertical transverse isotropy. This novel observation is made possible by correcting our measurements for anisotropy beneath the earthquake in the upper mantle, permitting the use of shallow earthquakes which increase our seismic coverage.

We have made significant progress towards using D″ anisotropy to measure deformation in the LMM. Assuming that anisotropy in D″ is caused by the alignment of ppv, we may suggest which slip system dominates LPO, though without more detailed models of mantle flow there is still doubt as to the likely orientation of slip planes and directions in the LMM. As more reliable estimates of the type of deformation

we expect in well-studied regions become available, or conversely as numerical and physical experiments further indicate the mechanisms by which the material in D″ deforms, our observations of seismic anisotropy hold great potential to map dynamic processes at the CMB.

References

Blackman, D., Kendall, J. M., Dawson, P., Wenk, H. -R., Boyce, D., & Phipps Morgan, J. (1996). Teleseismic imaging of subaxial flow at mid-ocean ridges: Traveltime effects of anisotropic mineral texture in the mantle. *Geophysical Journal International*, *127*(2), 415–426. doi:10.1111/j.1365-246X.1996.tb04730.x.

Carrez, P., Ferré, D., and Cordier, P. (2007). Implications for plastic flow in the deep mantle from modelling dislocations in $MgSiO_3$ minerals. *Nature*, *446*(7131), 68–70. doi:10.1038/nature05593.

Catalli, K., Shim, S. -H., & Prakapenka, V.B. (2009). Thickness and Clapeyron slope of the post-perovskite boundary. *Nature*, *462*(7274), 782–785. doi:10.1038/nature08598.

Evans, M., Kendall, J. M., & Willemann, R. (2006). Automated SKS splitting and upper-mantle anisotropy beneath Canadian seismic stations. *Geophysical Journal International*, *165*(3), 931–942. doi:10.1111/j.1365-246X.2006.02973.x.

Frederiksen, A. W., Miong, S. -K., Darbyshire, F. A., Eaton, D. W., Rondenay, S., & Sol, S. (2007). Lithospheric variations across the Superior Province, Ontario, Canada: Evidence from tomography and shear wave splitting. *Journal of Geophysical Research-Solid Earth*, *112*(B7), B07318. doi:10.1029/2006JB004861.

Garnero, E. J., Maupin, V., Lay, T., & Fouch, M. J. (2004). Variable azimuthal anisotropy in Earth's lowermost mantle. *Science*, *306*(5694), 259–261. doi:10.1126/science.1103411.

Iitaka, T., Hirose, K., Kawamura, K., & Murakami, M. (2004). The elasticity of the $MgSiO_3$ post-perovskite phase in the Earth's lowermost mantle. *Nature*, *430*(6998), 442–445. doi:10.1038/nature02702.

Karki, B. B., Wentzcovitch, R. M., de Gironcoli, S., & Baroni, S. (1999). First-principles determination of elastic anisotropy and wave velocities of MgO at lower mantle conditions. *Science*, *286*(5445), 1705–1707. doi:10.1126/science.286.5445.1705.

Kendall, J. M., & Nangini, C. (1996). Lateral variations in D″ below the Caribbean. *Geophysical Research Letters*, *23*(4), 399–402. doi:10.1029/95GL02659.

Kendall, J. M., & Silver, P. G. (1996). Constraints from seismic anisotropy on the nature of the lowermost mantle. *Nature*, *381*(6581), 409–412. doi:10.1038/381409a0.

Kendall, J. -M., & Silver, P. G. (1998). Investigating causes of D″ anisotropy, In M. Gurnis, M. E. Wysession, E. Knittle, & B. A. Buffett (Eds.), *The core-mantle boundary region, geodynamics series* (pp. 97–118). Washington: American Geophysical Union.

Lay, T., Williams, Q., Garnero, E.J., Kellogg, L., & Wysession, M. E. (1998). Seismic wave anisotropy in the D″ region and its implications, In M. Gurnis, M. E. Wysession, E. Knittle, & B. A. Buffett, (Eds.), *The core-mantle boundary region, geodynamics series 28* (pp. 299–318). Washington: USA, American Geophysical Union

Long, M. D. (2009). Complex anisotropy in D″ beneath the eastern pacific from SKS-SKKS splitting discrepancies. *Earth and Planetary Science Letters*, *283*(1–4), 181–189. doi:10.1016/j.epsl.2009.04.019.

Long, M. D., Xiao, X., Jiang, Z., Evans, B., & Karato, S. (2006). Lattice preferred orientation in deformed polycrystalline (Mg, Fe)O and implications for seismic anisotropy in D″. *Physics of the Earth and Planetary Interiors*, *156*(1–2), 75–88. doi:10.1016/j.pepi.2006.02.006.

Mainprice, D., Tommasi, A., Ferré, D., Carrez, P., & Cordier, P. (2008). Predicted glide systems and crystal preferred orientations of polycrystalline silicate Mg-perovskite at high pressure:

Implications for the seismic anisotropy in the lower mantle. *Earth and Planetary Science Letters*, *271*(1–4), 135–144. doi:10.1016/j.epsl.2008.03.058.

Maupin, V., Garnero, E. J., Lay, T., & Fouch, M. J. (2005). Azimuthal anisotropy in the D″ layer beneath the Caribbean. *Journal of Geophysical Research-Solid Earth*, *110*(B8), B08301. doi:10.1029/2004JB003506.

McNamara, A. K., van Keken, P., & Karato, S. (2003). Development of finite strain in the convecting lower mantle and its implications for seismic anisotropy. *Journal of Geophysical Research-Solid Earth*, *108*(B5), 2230. doi:10.1029/2002JB001970.

Meade, C., Silver, P. G., & Kaneshima, S. (1995). Laboratory and seismological observations of lower mantle isotropy. *Geophysical Research Letters*, *22*(10), 1293–1296. doi:10.1029/95GL01091.

Merkel, S., Kubo, A., Miyagi, L., Speziale, S., Duffy, T. S., Mao, H., et al. (2006). Plastic deformation of $MgGeO_3$ post-perovskite at lower mantle pressures. *Science*, *311*(5761), 644–646. doi:10.1126/science.1121808.

Merkel, S., McNamara, A. K., Kubo, A., Speziale, S., Miyagi, L., Meng, Y., et al. (2007). Deformation of (Mg, Fe)SiO_3 post-perovskite and D″ anisotropy. *Science*, *316*(5832), 1729–1732. doi:10.1126/science.1140609.

Murakami, M., Ohishi, Y., Hirao, N., & Hirose, K. (2009). Elasticity of MgO to 130 GPa: Implications for lower mantle mineralogy. *Earth and Planetary Science Letters*, *277*(1–2), 123–129. doi:10.1016/j.epsl.2008.10.010.

Oganov, A., Martonak, R., Laio, A., Raiteri, P., & Parrinello, M. (2005). Anisotropy of Earth's D″ layer and stacking faults in the $MgSiO_3$ post-perovskite phase. *Nature*, *438*(7071), 1142–1144. doi:10.1038/nature04439.

Okada, T., Yagi, T., Niwa, K., & Kikegawa, T. (2010). Lattice-preferred orientations in post-perovskite-type $MgGeO_3$ formed by transformations from different pre-phases. *Physics of the Earth and Planetary Interiors*. *180*(3–4), 195–202. doi:10.1016/j.pepi.2009.08.002.

Ren, Y., Stutzman, E., van der Hilst, R.D., & Besse, J. (2007). Understanding seismic heterogeneities in the lower mantle beneath the Americas from seismic tomography and plate tectonic history. *Journal of Geophysical Research-Solid Earth*. *112*(B1), B01302. doi:10.1029/2005JB004154.

Ritsema, J., van Heijst, H. J., & Woodhouse, J. H. (1999). Complex shear wave velocity structure imaged beneath Africa and Iceland. *Science*, *286*(5446), 1925–1928. doi:10.1126/science.286.5446.1925.

Rokosky, J. M., Lay, T., & Garnero, E. J. (2006). Small-scale lateral variations in azimuthally anisotropic D″ structure beneath the Cocos plate. *Earth and Planetary Science Letters*, *248*(1–2), 411–425. doi:10.1016/j.epsl.2006.06.005.

Silver, P. G. & Chan, W. W. (1991). Shear-wave splitting and subcontinental mantle deformation. *Journal of Geophysical Research-Solid Earth*, *96*(B10), 16429–16454. doi:10.1029/91JB00899.

Stackhouse, S., Brodholt, J. P., Wookey, J., Kendall, J. M., & Price, G. D. (2005). The effect of temperature on the seismic anisotropy of the perovskite and post-perovskite polymorphs of $MgSiO_3$. *Earth and Planetary Science Letters*, *230*(1–2), 1–10. doi:10.1016/j.epsl.2004.11.021.

Teanby, N., Kendall, J. M., & der Baan, M. V. (2004). Automation of shear-wave splitting measurements using cluster analysis. *The Bulletin of the Seismological Society of America*, *94*(2), 453–463. doi:10.1785/0120030123.

Tsuchiya, T., Tsuchiya, J., Umemoto, K., & Wentzcovitch, R. M. (2004). Phase transition in $MgSiO_3$ perovskite in the earth's lower mantle. *Earth and Planetary Science Letters*, *224*(3–4), 241–248. doi:10.1016/j.epsl.2004.05.017.

Wentzcovitch, R. M., Tsuchiya, T., & Tsuchiya, J. (2006). $MgSiO_3$ postperovskite at D″ conditions. *Proceedings of the National Academy of Sciences of the United States of America*, *103*(3), 543–546. doi:10.1073/pnas.0506879103.

Wolfe, C., & Silver, P.G. (1998). Seismic anisotropy of oceanic upper mantle: Shear wave splitting methodologies and observations. *Journal of Geophysical Researh-Solid Earth*, *103*(B1), 749–771. doi:10.1029/97JB02023.

Wolfe, C., & Solomon, S. (1998). Shear-wave splitting and implications for mantle flow beneath the MELT region of the East Pacific Rise. *Science*, *280*(5367), 1230–1232. doi:10.1126/science.280.5367.1230.

Wookey, J. & Kendall, J. -M. (2007). Seismic anisotropy of post-perovskite and the lowermost mantle, In K. Hirose, J. Brodholt, T. Lay, & D. A. Yuen, (Eds.) *Post-Perovksite: The Last Mantle Phase Transition* (Vol. 174, pp. 171–189). Washington, DC: American Geophysical Union Geophysical Monograph.

Wookey, J., & Kendall, J. M. (2008). Constraints on lowermost mantle mineralogy and fabric beneath Siberia from seismic anisotropy. *Earth and Planetary Science Letters*, *275*(1–2), 32–42. doi:10.1016/j.epsl.2008.07.049.

Wookey, J., Kendall, J. M., & Rümpker, G. (2005a). Lowermost mantle anisotropy beneath the north Pacific from differential S-ScS splitting. *Geophysical Journal International*, *161*(3), 829–838. doi:10.1111/j.1365-246X.2005.02623.x.

Wookey, J., Stackhouse, S., Kendall, J. M., Brodholt, J. P., & Price, G. D. (2005b). Efficacy of the post-perovskite phase as an explanation for lowermost-mantle seismic properties. *Nature*, *438*(7070), 1004–1007. doi:10.1038/nature04345.

Wuestefeld, A., Bokelmann, G., Barruol, G., & Montagner, J. -P. (2009). Identifying global seismic anisotropy patterns by correlating shear-wave splitting and surface-wave data. *Physical of the Earth and Planetary Interiors*, *176*(3–4), 198–212. doi:10.1016/j.pepi.2009.05.006.

Yamazaki, D., & Karato, S. (2002). Fabric development in (Mg, Fe)O during large strain, shear deformation: implications for seismic anisotropy in Earth's lower mantle. *Physics of the Earth and Planetary Interiors*, *131*(3–4), 251–267. doi:10.1016/S0031-9201(02)00037-7.

Yamazaki, D., Yoshino, T., Ohfuji, H., Ando, J., & Yoneda, A. (2006). Origin of seismic anisotropy in the D″ layer inferred from shear deformation experiments on post-perovskite phase. *Earth and Planetary Science Letters*, *252*(3–4), 372–378. doi:10.1016/j.epsl.2006.10.004.

Chapter 5
Predicting Lowermost Mantle Anisotropy Using Models of Mantle Flow

5.1 Introduction

Observations of seismic anisotropy in the Earth's lowermost mantle are numerous (Chap. 2), yet at present it is difficult to reconcile these observations across length scales (global versus regional studies) and locations (regions of assumed palaeo-subduction and present-day upwelling). In this study we attempt to assess one hypothesis regarding the cause of anisotropy in the lowermost mantle—also known as D″—and thereby determine if these discrepancies can be addressed.

Since its recent discovery (Oganov and Ono 2004; Iitaka et al. 2004; Murakami et al. 2004), the post-perovskite polymorph of $MgSiO_3$ (ppv) has been proposed as a potential cause for anisotropy in D″, as it exhibits stronger single-crystal anisotropy than the perovskite (pv) polymorph (Wookey et al. 2005b; Tsuchiya et al. 2004; Oganov and Ono 2004; Iitaka et al. 2004; Murakami et al. 2004), and pv is believed to transform into the ppv structure at depths near to the observed D″ discontinuity (see Chap. 2, and references therein). If ppv in D″ develops a lattice-preferred orientation (LPO) sufficiently when deformed, and if it is deformed enough whilst it is stable within the lowermost mantle, it is possible that this may be observed seismically as anisotropy. Attention has focussed on ppv so strongly not only because of its large single-crystal anisotropy, but also because it is more abundant than ferropericlase ((Mg,Fe)O, fpc), so a weaker LPO in ppv can cause the same strength of anisotropy than for other D″ phases. However, so far no data have confirmed that another cause, such as shape-preferred orientation (SPO) of seismically distinct material above the CMB (e.g., Kendall and Silver 1996), is inadequate to explain D″ anisotropy. Here we seek to test ppv LPO as a mechanism, potentially ruling it in or out.

A. Nowacki, *Plate Deformation from Cradle to Grave*, Springer Theses,
DOI: 10.1007/978-3-642-34842-6_5, © Springer-Verlag Berlin Heidelberg 2013

5.1.1 Global Mantle Flow Modelling

One approach to assessing the likelihood that LPO of ppv causes seismic anisotropy in D″ is to calculate the texture of the lowermost mantle that would develop with a hypothetical style of flow based on geodynamic modelling (e.g.,Wenk et al. 2006; Merkel et al. 2007; Wenk et al. 2011). Such studies conclude that for models which include diffusion and dislocation creep, strain rates are highest in the lower mantle in D″, and this is the likely site for dislocation creep, which would lead to LPO development with sufficient deformation(e.g., McNamara et al. 2002, 2003).

An alternative approach is to use recent models of mantle flow which are derived from observables and which seek to most accurately represent the likely flow occurring currently. Recent models (Simmons et al 2007, 2009, 2010) jointly invert S-wave travel times, and mineral-physical density-velocity data, using constraints from the geoid, core-topography observations, glacial rebound and surface plate velocities to obtain velocity, density and viscosity in the mantle. These data are then used to construct a model of current, steady-state flow in the whole mantle. Figure 5.1 shows one such recent model. It is important to note, however, the strong limitations in such modelling. A key parameter in the inversion is the relationship between seismic velocity (V_S here), temperature (T), and the density, ρ. Simmons et al. (2009), for example, use as a starting case values taken from mineral physical experiments and calculations, but as the inversion proceeds, allow this to change to increase the model

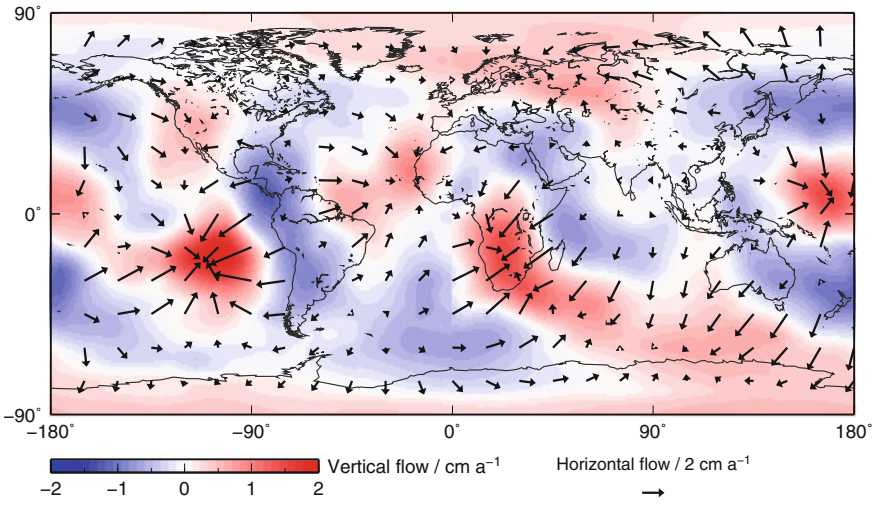

Fig. 5.1 Current steady-state mantle flow 200 km above the core-mantle boundary, in the TX2008 model of Simmons et al. (2009). *Colour scale* shows the vertical flow velocity (*upward* in *red*, *downward* in *blue*); *arrows* show horizontal flow

fit to the observations. They thus obtain a value relating V_S, T and ρ, and retrieve from the model density variations brought about both thermally and athermally (assumed chemically). Using the methods described in Forte and Peltier (1991, 1994) and Forte (2000), one can then derive a map of mantle flow from buoyancy, however the ρ–T–V_S relationship is still rather poorly constrained by independent studies.

Other limitations are inherent in the method, such as the smoothing of the model brought about by inversion regularisation. Hence any such model cannot reproduce what is frequently observed in nature: the partitioning of strain into localised regions, which will likely have a large effect on LPO and SPO. Equally, just as with any V_S tomography, sampling bias introduced by limited source–receiver geometries may lead to uneven coverage.

5.1.2 Texture Modelling

Walker et al. (2011) describe the use of the viscoplastic self-consistent (VPSC) method (Lebensohn and Tomé 1993) to construct a texture map of a purely ppv D″ for a variety of cases. To summarise, the method is as follows:

1. For each desired texture point, take the input flow model and propagate a tracer particle backwards in time, saving a history of the velocity gradients. This is acceptable for a steady-state field.
2. Taking into account the Clapeyron slope of the pv–ppv phase transition as predicted by Oganov and Ono (2004) ($\sim$10 GPa K^{-1}, a probable upper bound), calculate using the geotherm of Stacey and Davis (2008) where a particle first transforms from pv→ppv, and where it turns and rises upwards again, where it transforms from ppv→pv.
3. For a sample of 500 ppv grains, use the velocity gradients between the start and endpoints in the previous step to calculate the texture at each forward time step, using the viscoplastic self-consistent (VPSC) method (Lebensohn and Tomé 1993).
4. Using Voigt–Reuss–Hill averaging, calculate the aggregate elastic tensor for the 500 single-crystal ppv grains at each point, with each grain's constants taken from Stackhouse et al. (2005), using the T and ρ derivatives of Wentzcovitch et al. (2006).
5. The output is combined, producing a volume map of gridded fully anisotropic elastic constants globally. For each grid point, there are 21 independent elastic constants.

Hence these elastic constants can be used to predict wave propagation through a D″ region composed of the same material, and compared to observations of the same. We can therefore test the hypotheses behind their production.

5.1.3 Ppv Slip Systems and Flow Models

As discussed in Chap. 2, there is currently some uncertainty in how ppv deforms: because of the current impossibility of conducting deformation experiments at the strain rates, pressures, crystal sizes and temperatures of the lowermost mantle, and the lack of natural samples, the deformation style of ppv-rich mantle—or even pure ppv aggregates—is unclear. At present, there are three main slip systems suggested by experiments and calculations: (i) slip on (100) or {110} along [010] or ⟨110⟩ respectively (Merkel et al. 2007) (case P100); (ii) slip on (010) along [001] (Carrez et al. 2007a, b; Metsue et al. 2009) (P010); and (iii) slip on (001) along [100] or [010] (Miyagi et al. 2010) (P001). (For further details, see Chap. 2.) Walker et al. (2011) create texture models for each of the three slip systems. For the VPSC calculation, a set of relative slip system activities for each case P100, P010 and P001 is needed. These are shown in their Table 5.1.

The authors also examine two flow models: TX2007 (Simmons et al. 2007) and TX2008 (Simmons et al. 2009); the former is less smoothed than the latter. Additionally, for each case, two different viscosity profiles are used: V1 (higher viscosity) and V2 (lower); these are shown in Fig. 5.2. Hence Walker et al. (2011) produce 12 models. However, they show that the largest differences in the output texture calculations come about between different slip system activity models, rather than between different viscosities (V1, V2) or smoothnesses (TX2007, TX2008).

5.1.4 Global VTI Patterns

Walker et al. (2011) compare global inversions for the VTI parameter $\xi = V_{SH}^2 / V_{SV}^2$ (Kustowski et al. 2008; Panning and Romanowicz 2006; Panning et al. 2010) with the values predicted by their texture modelling. Because the inversions are VTI and the texture modelling produces fully anisotropic constants, Walker et al. convert them to VTI by enforcing rotational symmetry about the vertical axis. They find that the correlation between the tomographic inversions and the predictions for VTI elasticity is strongest for the P100 and P010 slip system cases, with a strong anti-correlation for the P001 case. This is true up to spherical harmonic degree $l = 6$. Above that, the (anti-) correlation becomes weak.

5.1.5 Multi-Azimuth Shear Wave Splitting Predictions

As discussed in earlier chapters, VTI is only an approximation to the true anisotropy present in D″—and in this thesis I already show that in some cases it is a very poor approximation at that. The global tomographic inversions may suffer inevitably from sampling bias, such that certain event-receiver geometries dominate for certain areas

Table 5.1 Event-receiver geometries for shear wave splitting measurements I compare to predictions from the texture model

Label	Event lat (°N)	Event lon (°E)	Depth (km)	Receiver lat (°N)	Receiver lon (°E)	ϕ' (°)	$\Delta(\phi')$ (°)	δt (s)	$\Delta(\delta t)$ (s)
North and Central America									
W1	19.3	−155.0	9	40.7	−86.2	−80	6	1.10	0.04
W2	10.7	−86.5	47	56.3	−151.1	77	10	1.25	0.03
S1	−7.0	−107.7	10	49.3	−74.4	−42	4	1.68	0.04
S2	−8.1	−71.3	645	40.4	−116.6	−84	3	0.90	0.01
E1	−8.1	−71.2	645	53.6	−79.2	83	8	1.28	0.10
E2	7.3	−34.9	9	40.1	−106.5	45	7	1.78	0.02
Siberia									
Sib1	36.5	70.84	183	64.5	−111.0	87	4	2.70	0.18
Sib2	45.2	148.5	130	49.5	8.79	35	11	1.45	0.16
NW Pacific									
P	23.3	142.3	324.5	61.9	−117.1	49	7	2.1	0.4

'Events' and 'receivers' are average (usually median) locations for average (NW Pacific) or stacked measurements of splitting

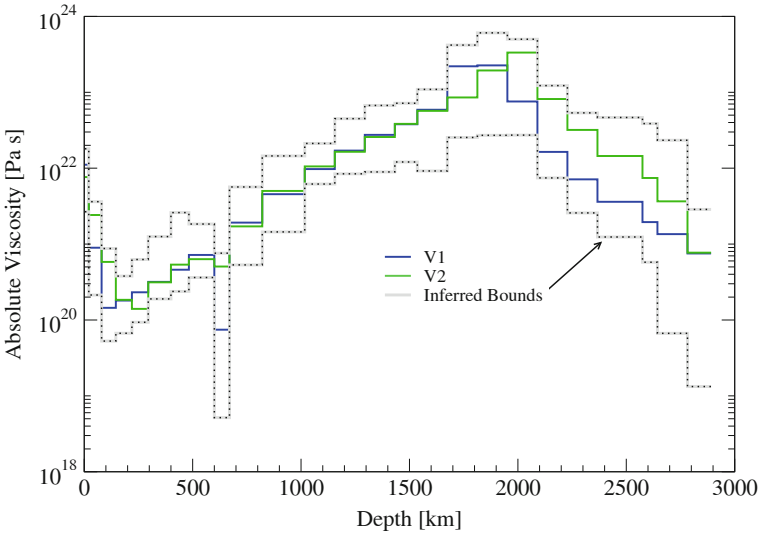

Fig. 5.2 Viscosity profiles V1 and V2 used in the mantle flow models TX2007 and TX2008 used to produce the elastic constants used in this chapter. Figure 2 from Walker et al. (2011)

of the deep mantle, and as such any complicated anisotropy will be determined by only one azimuth, which again we have already seen is inadequate in general. Hence a more potentially insightful test of the hypothesis that deformation-induced LPO in ppv causes seismic anisotropy in D″ is to compare the predictions of Walker et al. with regional multi-azimuth shear wave splitting observations, where no constraints on the anisotropic symmetry are placed in the measurement. Here, I use the observations presented in Chap. 4 and those by Wookey et al. (2005a) and Wookey and Kendall (2008).

5.2 Data and Methods

5.2.1 Previous Observations

The observations of shear wave splitting in D″ we seek to compare with predictions are summarised in Fig. 5.3. There are nine distinct source-receiver geometries which each give a stacked measurement incorporating several seismic stations, and in some cases more than one earthquake. Beneath the measurements is shown the flow predicted by the TX2008 model of Simmons et al. (2009) 200 km above the CMB.

I accrue splitting along the raypaths predicted by the AK135 1D global isotropic model (Kennett et al. 1995) for the event-receiver geometries given in Table 5.1,

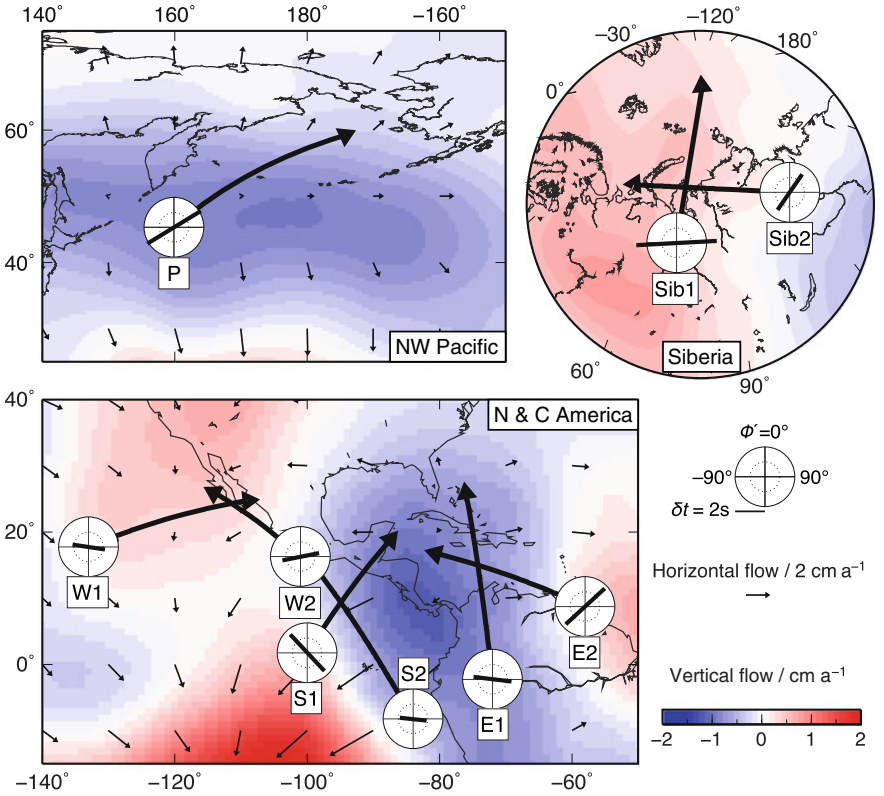

Fig. 5.3 Previous multi-azimuth observations of shear wave splitting in D″, beneath North and Central America, the northwest Pacific and Siberia. Background *colour* and *arrows* (NW Pacific and Americas only) show vertical and horizontal components of flow in the TX2008 model of Simmons et al. (2009), as for Fig. 5.1*Circles with bars* show shear wave splitting observations in ScS phase from Nowacki et al. (2010) (*lower left*), Wookey et al. (2005a) (*upper left*) and Wookey and Kendall (2008) (*right*). Orientation of *bar* corresponds to fast orientation in ray frame, ϕ'; length of *bar* corresponds to delay time, δt (see legend). *Thick blacks lines* are representative ray paths in the *bottom* 250 km of the mantle along which the splitting measurements are made; *arrows* show sense of direction

calculated using the TauP Toolkit of Crotwell et al. (1999). Where several sources or receivers are used and stacked, average source and receiver locations are shown. Using a 1D, isotropic Earth model, rather than explicitly tracing rays through the elastic constants output from the texture calculations, is an acceptable approach, as the input flow model and elastic constants vary very smoothly. Hence any variation in the raypath will not much affect the splitting accrued—the uncertainties in the flow model and texture calculations far outweigh those associated with the approximations of ray-theoretical paths in D″.

The rays are then tracked through the elastic constants (Sect. 5.2.2) and the predicted shear wave splitting calculated.

5.2.2 *Elastic Constants*

For the calculations in this chapter, I use a set of T- and P-dependent elastic constants calculated as in Walker et al. (2011), but with the additional variation of several layers in the lowermost mantle, rather than just one (A.M. Walker, personal communication, 2010). The constants are calculated as previously explained, except the desired endpoints of the flowlines are at a series of radii spaced 50 km apart, starting at 25 km above the CMB; thus giving several 50 km-thick 'layers'. In order to calculate the bulk elastic constants for the multi-grain aggregate, the single-crystal elastic constants are varied according to the T- and P-derivatives given by Wentzcovitch et al. (2006). The density and temperature variation from the TX2008 model is used to locally perturb the geotherm. Isotropy is assumed where the perturbed geotherm locally would mean ppv was not stable. Figures 5.4 and 5.5 show the strength of

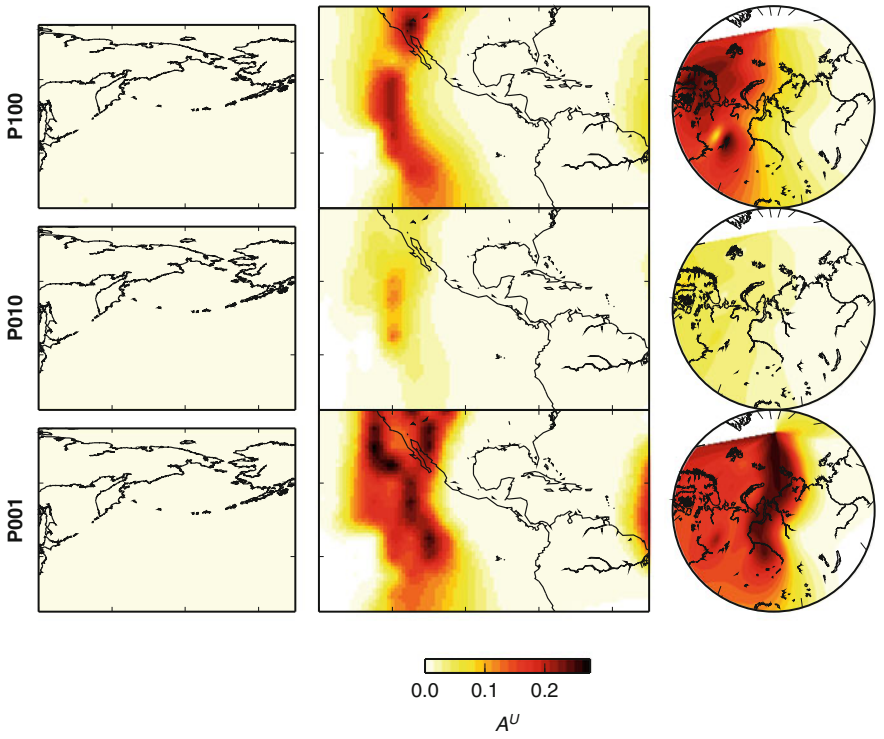

Fig. 5.4 Strength of anisotropy of elastic constants for each plasticity model used in the shear wave splitting calculations at radius 3655 km (175 km above the CMB). Shown are the values of A^U, the universal anisotropy index, for the aggregate elasticity tensors, evaluated each 5° in latitude and longitude. The three plasticity cases, P100, P010 and P001 are shown for the three regions investigated here (*left* Northwest Pacific; *middle* Americas; *right* Siberia). *Black squares* show 5° blocks outside of the ppv stability field, hence no texturing is assumed. *White area* at *top* of Siberia plot show that no constants were evaluated outside the *coloured* area

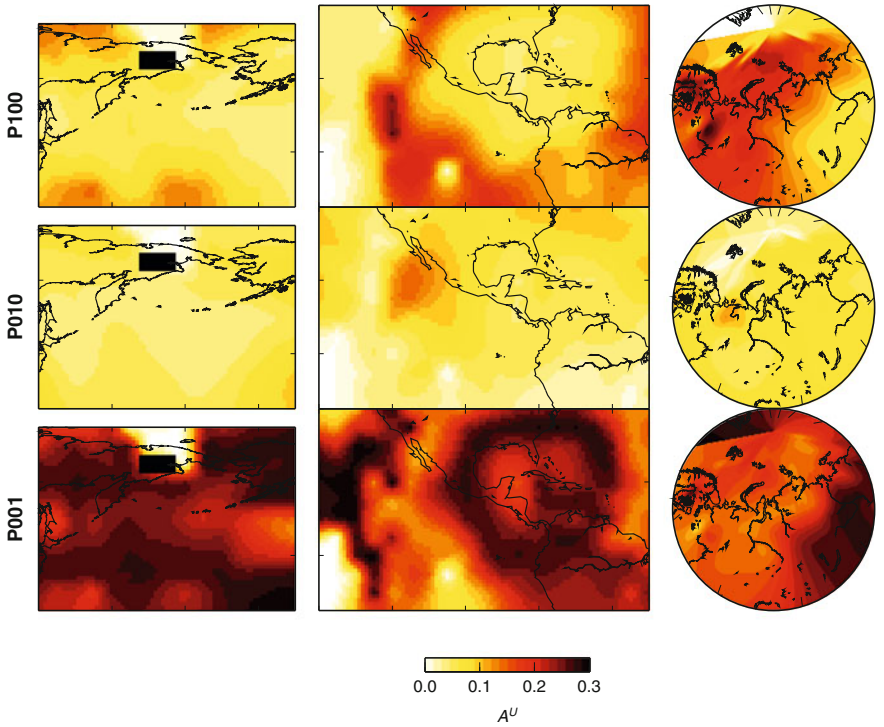

Fig. 5.5 Strength of anisotropy of elastic constants for each plasticity model used in the shear wave splitting calculations at radius 3505 km (25 km above the CMB). Same as for Fig. 5.4. Note that the elevated temperature in the north of the leftmost panels has led to a 'double-crossing' of the pv–ppv phase boundary, so that pv is stable just above the CMB here

anisotropy across the three regions at 175 and 25 km above the CMB respectively. The constants provided are Voigt-Reuss-Hill averages based on 500 grains whose orientations are described by an orientation distribution function (ODF). Hence the single-crystal elastic tensor of each of the 500 grains is rotated to the correct orientation and added to the average, creating an effective elastic tensor for all the grains at that calculation point. An accurate description of the style and strength of anisotropy across the regions in each of the plasticity cases would be to show ODFs at each grid point; however the constants are evaluated on a $5° \times 5°$ latitude–longitude grid, and so depicting this is impractical. Instead, I show the value of the universal anisotropy index, A^U (Ranganathan and Ostoja-Starzewski 2008), which is a measure from 0 upwards of the degree of anisotropy of a single crystal or elasticity tensor. (For example, single-crystal olivine at ambient conditions has $A^U = 0.23$; Abramson et al. 1997; antigorite at 10 GPa and 0 K has $A^U \approx 3.7$; Mookherjee and Capitani 2011. Appendix A gives more details.) Measurements of ppv's single crystal elastic constants (Mao et al. 2010) give $A^U \approx 0.63$, so Figs. 5.4 and 5.5 indicate that in some regions the alignment of the ppv crystals is extremely high. This is for several

reasons, but largely because there is no mechanism included in the VPSC calculations to limit the maximum strength of the texture, such as recrystallisation. Additionally, the assumed relative slip system strengths for the P100 and P001 cases are probably quite unrealistic, and favour slip on one or two planes significantly more than the others, leading to very strong alignment when a crystal is in the correct orientation to deform along that plane. Subsequent deformation then quickly leads to very strong texturing.

The elastic constants are regridded on a 50 km × 50 km × 50 km 3-dimensional grid in Cartesian space. In this convention, the x_1-direction points out from the centre of the Earth along the point where the equator and Greenwich meridian meet (longitude, latitude 0,0); x_2 points out where 90°E and the equator meet (90,0); and x_3 is through the North Pole (thus forming a right-handed set). Because the original constants are evenly spaced in latitude and longitude, rather than Cartesian space, the points are denser near the poles (e.g., in the Siberia region of Wookey and Kendall 2008); regridding at 50 km spacing prevents any texture calculation points overlapping in the Cartesian grid. The gridding is performed by filling vacant boxes with the elastic constants from the nearest full box, provided the box is above the CMB and beneath the top of the anisotropic region; otherwise the box is isotropic and not included in the subsequent calculations. Because the constants vary very smoothly in any case, no smoothing is undertaken to remove large differences between the boxes.

5.2.3 Shear Wave Splitting Calculation

The shear wave splitting is calculated using a ray-theoretical approach, whereby single rays of infinitesimal width represent the earthquake-receiver paths taken by the ScS waves. Rays are followed from their first entry into the anisotropic region bound atop by the limit of the texture-calculated input elastic constants and beneath by the CMB, and whilst they are in the anisotropic region they are propagated forward by a small increment, δs. At each step, i, the local elastic constants at the ray's coordinates, $\mathbf{r}_i$, are used to calculate the shear wave splitting accrued in that step, $\Gamma_i = (\phi'_i, \delta t_i)$, given the ray's azimuth and inclination. The fast orientation in the ray frame, ϕ'_i, is calculated relative to the x_3-direction and then converted to be relative to the Earth radial direction. It is found that as long as δs is about or less than 0.1 of the length of the ray in one anisotropic region (which is at least 50 km and usually more), no significant numerical error is introduced to the size of the delay time predicted due to incomplete traversal of boxes. Hence I use a value of 1 km.

Each step and its associated shear wave splitting values are output and used as the input for the subsequent procedure. Here, a synthetic waveform is created with the same source polarisation as that predicted by the event's Global CMT solution. In some cases, where more than one earthquake was included in the stacked measurement, a 'representative' average source polarisation was used; however, because the earthquakes for one path are usually near to each other, they tend to share a common

tectonic mechanism, hence the source polarisations were not very different in any case. White noise is added to the synthetic waveform with an amplitude of 0.1 of the maximum amplitude of the wave to add random noise to the splitting analysis and provide error bounds. However, even noise amplitudes of 1 times the signal amplitude gave very small errors in the splitting analysis, because the white noise is random and incoherent. The waveforms were not filtered, but tests with synthetics bandpass filtered at the same corner frequencies as the data suggested this made little difference.

This synthetic waveform is then synthetically split many times by the values found in the previous step, Γ_i, in the frequency domain. (See Appendix B for details.) Performing the operation in the frequency rather than time domain reduces numerical noise and avoids the necessity to use very short sampling rates, which would also increase computational time. Tests showed that the shape of the waveform—first-derivative Gaussian, cubic sine or Ricker—had no effect on the results. Initially, a waveform with similar period to the data (∼0.1 Hz) was used, but the splitting predicted by the texture models was in some cases so large that the approximation inherent in the minimum-eigenvalue shear wave splitting technique—that the wave has period much longer than the splitting time—was broken. This would lead to inaccurate measurements of the splitting, as multiple waveforms are created. Instead, where the predicted splitting produced waveforms which were complicated and contained more than one clear impulse, the dominant frequency was adjusted down to a lower limit of 0.01 Hz. Figure 5.6 shows an example of this for 100 random splits of 1 s applied to a wave of period 10 s. As the number of individual splitting operators applied becomes large, and the total splitting exceeds the dominant period of the wave, the particle motion and waveform is extremely complex. Hence the need in some circumstances to increase the period. Waveforms which were still too complicated to yield acceptable results were then rejected.

Finally, the split synthetic waveforms were analysed using the minimum-eigenvalue method (Silver and Chan 1991) to find the total splitting accrued along the ray in the anisotropic region. Pre- and post-analysis waveforms were visually inspected to check the quality of the result and whether any null measurements were made. With synthetic waveforms, errors are generally much smaller than real measurements, however where the waveforms were especially complicated, the result was rejected as unrealistic (Fig. 5.7).

In reality, the ScS phase is not of infinite frequency, hence the ray approximation may not be appropriate. The first Fresnel zone of ScS with dominant frequency 0.1 Hz is approximately 920 km perpendicular to the propagation direction at the CMB in the AK135 model, and the sensitivity of amplitude and phase across this region is complicated, so it is difficult to predict the effect that incorporation of finite-frequency phenomena would have on the following results. However, as long as the elastic constants and splitting parameters do not vary very much along a particular path within the approximate Fresnel zone, then it is probably the case that the finite- and infinite-frequency cases will not differ significantly. I discuss this later.

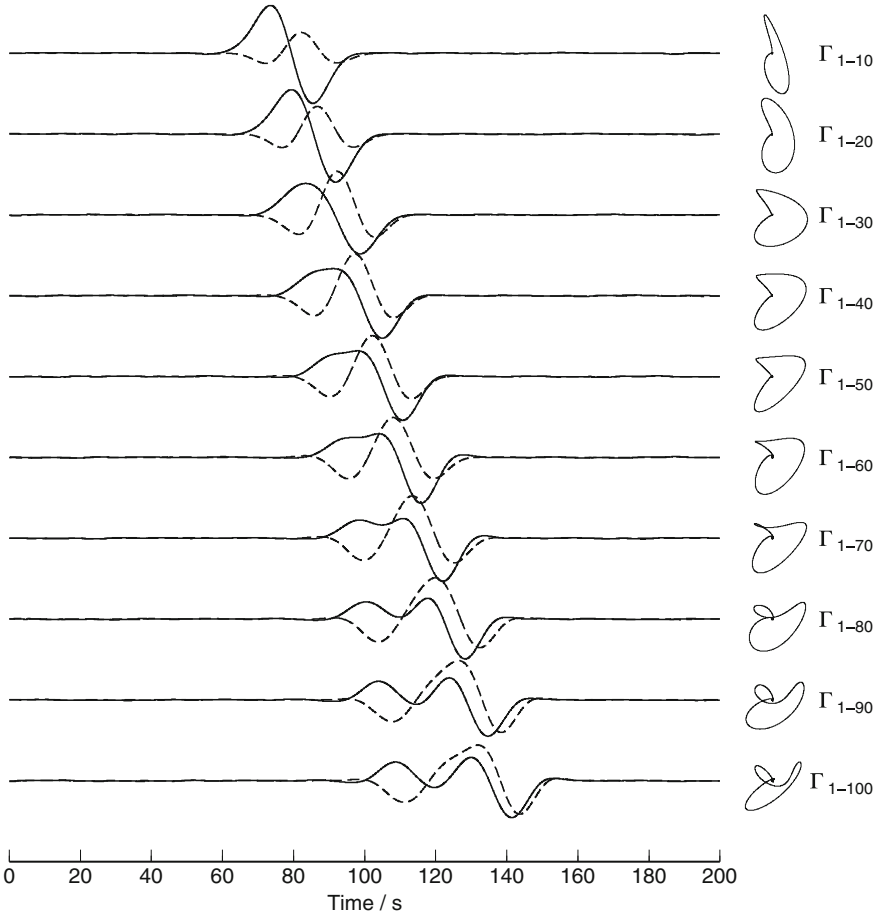

Fig. 5.6 Waveforms progressively split by, in each case, 10 more splitting operators of random orientation. 100 splitting operators (Γ_1 to Γ_{100}) of random orientation (ϕ) and $\delta t = 1$ s are successively applied to an unsplit waveform of dominant period 10 s, polarised 'north'. (*Solid trace* shows 'north–south' component; *dashed line* shows 'east–west' component.) Random noise was applied at 0.1 of the maximum amplitude; the waves were then low-pass filtered at a corner frequency of 10 s. As the splitting operators are applied, the waveform becomes increasingly complicated. Particle motion is shown on the *right* of each trace. Up to Γ_{80}, the motion is still to a good approximation elliptical and the total splitting is not much longer than the period of the wave. Beyond this, however, the particle motion and waveform are very complex. At this point the splitting analysis does a poor job of retrieving a single set of splitting parameters which can linearise the particle motion, and hence for this period of wave, it is not a suitable technique to characterise the splitting experienced by the wave. Usually, increasing the dominant period allows a single apparent splitting operator to be retrieved which describes the particle motion in similar cases

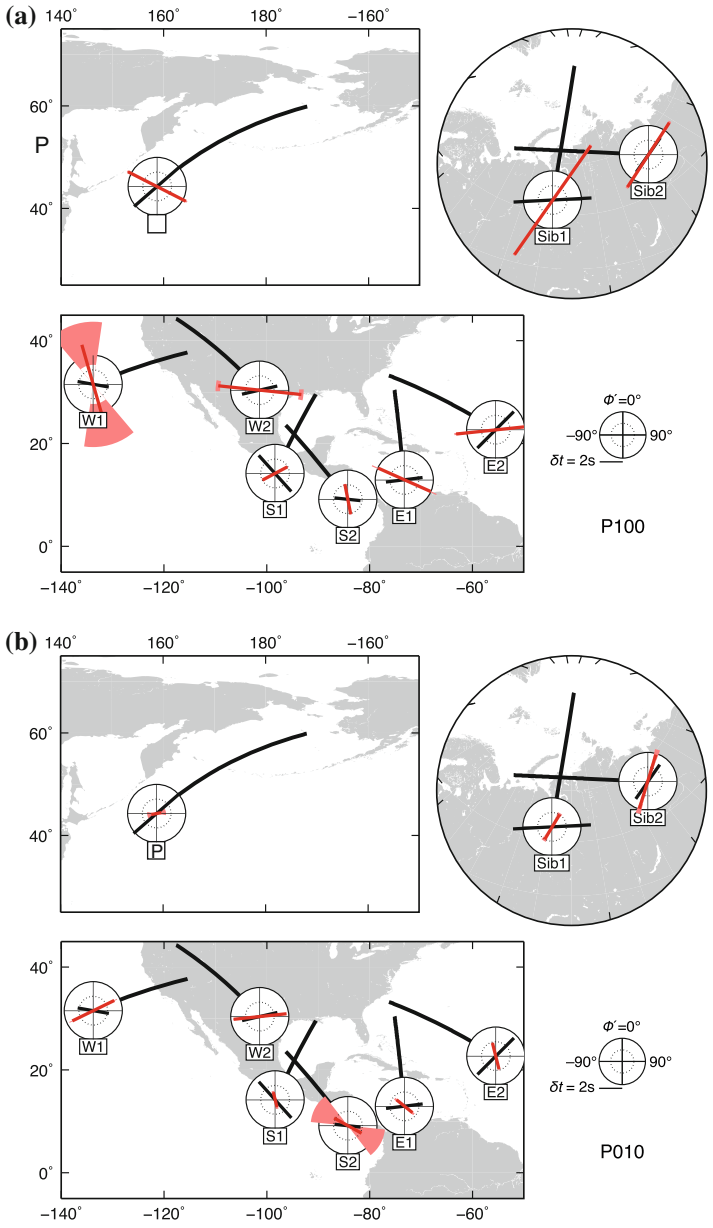

Fig. 5.7 **a** Predicted shear wave splitting from the model P100. *Red bars* show ϕ' and δt as for Fig. 5.3 and as shown by the legend, *lower right*, with the addition of *light red sectors* showing the uncertainties in the splitting parameters. δt is scaled by 0.5 (the Americas and NW Pacific) or 0.2 (Siberia). Where no *red bar* appears, the synthetic splitting measurement was rejected. *Black bars* show observations. **b** Predicted shear wave splitting from the model P010. Features as for **a**. **c** Predicted shear wave splitting from the model P001. Features as for **a**

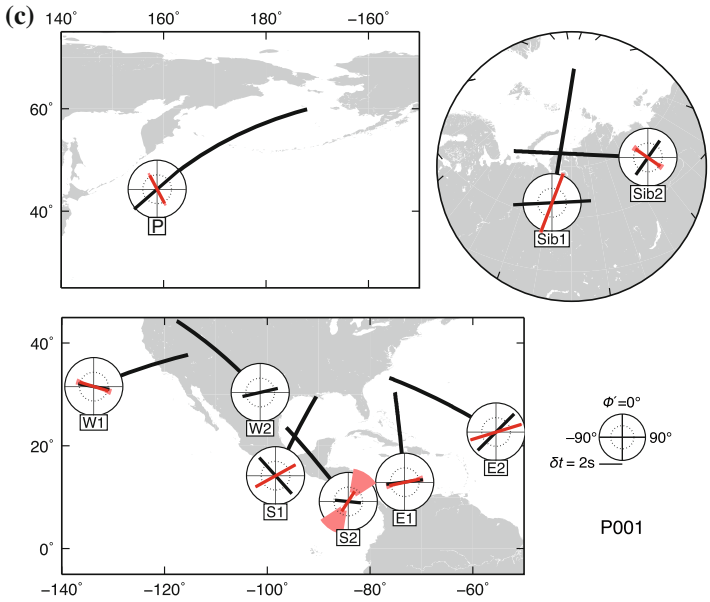

Fig. 5.7 (continued)

5.3 Results and Discussion

Figure 5.7 and Table 5.2 show the results for the nine paths and three different plasticity cases: Figure 5.7 compares the model predictions with the observations. Example synthetic waveforms and λ_2 surfaces are shown in Fig. 5.8.

The modelled splitting times are between 1.1 and 23.0 s, with the strongest variation being between raypaths, and secondarily between plasticity models. Mean delay times, $\langle \delta t \rangle$, are largest for P100 (7.3 s) and smallest for P010 (3.2 s). This reflects the strengths of the texture for the different models, but it is perhaps surprising that P010 is not more dramatically different to the other models, given the physically-derived slip system activities. One explanation may be that most of the paths cross areas of dominantly downward flow (Fig. 5.3), hence texture has not had much time (flowline distance) to develop. The S1, W1 and Siberian paths cross the regions with the strongest textures (Fig. 5.4), and here the values of δt are indeed much larger for the P100 and P001 cases, reflecting the stronger texture which may develop in the more 'arbitrary' models.

Splitting beneath Siberia is predicted to be largest (note that δt is scaled by 0.2 for the Siberia subfigures in Fig. 5.7, rather than 0.5 for the northwest Pacific and the Americas): this is also expected from the strength of texturing in the plasticity models. Conversely the NW Pacific path, P, shows little splitting, reflecting the lower degree of ppv alignment present beneath a downwelling in the TX2008 model (Fig. 5.3).

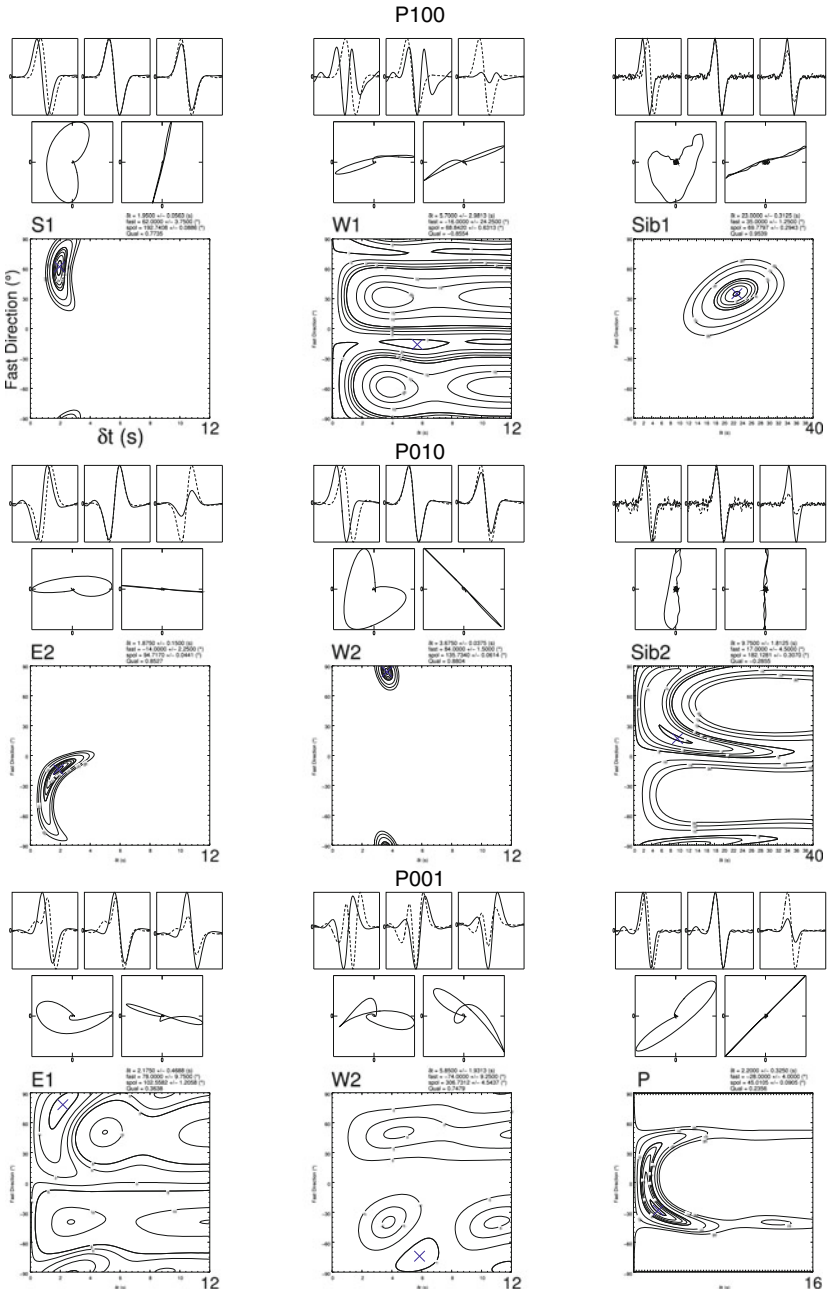

Fig. 5.8 Examples of synthetic split waveforms and minimum-eigenvalue surfaces. Three examples are given for each of the three plasticity models. Maximum δt of λ_2 surfaces shows at *bottom right* of each panel. S1 path for P100 case shows axes labels enlarged for clarity. Note W2 for P001 is excluded from further analysis

Table 5.2 Synthetic shear wave splitting predicted from each plasticity model for each raypath

Model	Path	ϕ' / °	$\Delta(\phi')$ / °	δt / s	$\Delta(\delta t)$ / s	Q	$\langle\delta t\rangle^{a}$ / s
P100	E1	−66.0	1.0	3.98	0.90	−0.87	
	E2	84.0	1.5	5.47	0.26	−0.84	
	S1	62.0	3.8	1.95	0.06	0.77	
	S2	−11.0	4.0	2.10	0.09	0.80	
	W1	−16.0	24.2	5.70	2.98	−0.85	7.3
	W2	−84.0	7.2	5.78	0.32	0.90	
	P	−63.0	1.5	4.50	0.17	0.90	
	Sib1	35.0	1.2	23.00	0.31	0.95	
	Sib2	33.0	2.0	13.25	0.50	0.89	
P010	E1	−51.0	5.5	1.43	0.30	0.00	
	E2	−14.0	2.2	1.88	0.15	0.85	
	S1	−14.0	9.2	1.05	0.23	0.58	
	S2	−61.0	23.2	2.17	2.98	−0.70	
	W1	64.0	1.0	3.23	0.45	−0.94	3.2
	W2	84.0	1.5	3.67	0.04	0.88	
	P	79.0	20.8	0.70	0.63	0.30	
	Sib1	31.0	9.2	5.00	0.56	0.57	
	Sib2	17.0	4.5	9.75	1.81	−0.28	
P001	E1	78.0	9.8	2.17	0.47	0.36	
	E2	73.0	1.5	3.67	0.13	0.88	
	S1	61.0	2.0	3.15	0.06	0.86	
	S2	33.0	23.8	1.65	2.96	−0.53	
	W1	−73.0	10.0	2.10	0.41	s0.69	3.8
	W2	–	–	–	–	–	
	P	28.0	4.0	2.20	0.33	0.24	
	Sib1	21.0	3.5	10.75	0.31	0.84	
	Sib2	−55.0	10.2	5.25	0.94	0.49	

Q is the shear wave splitting quality, as defined by Wuestefeld et al. (2010), where a value of −1 indicates a likely null, 0 a poor measurement, and 1 an excellent positive measurement. Path W2 for the P001 model is excluded

[a] Mean δt given for each plasticity model

The waveforms produced by applying the synthetic splitting procedure are generally simple. Figure 5.8 shows examples of these (e.g., P100: S1, Sib1; P010: E2, W2, Sib2; P001: P). Here, the waveform resulting from the application of many small splitting operators leads to a clear, single recoverable apparent splitting operator. In some cases, the initial polarisation is close to the apparent fast orientation, leading to a minimum-eigenvalue surface which would in real data be classified as a null measurement. However in the case of path W1 for P100, further splitting analysis with different values of the maximum δt in the grid search and inspection of the pre- and post-corrected waveforms confirms that the global minimum λ_2 and best-linearised particle motion is indeed found for the values shown in Fig. 5.8 and Table 5.2. However, such measurements are difficult to compare with observations,

because the uncertainty is large in δt, and it is arguable that any real measurement would be considered null if the true splitting were as for this synthetic example. This specific case highlights one point which the method does not address: the source is very shallow (<200 km) for some of the paths we model here, and hence the waveform would be split, and its polarisation changed, by the significant upper mantle anisotropy beneath the earthquake. The subsequently altered waveform would be split again in D″, and possibly therefore differently to if it were unaffected by any previous layer of anisotropy. However, because of the generally very small errors inherent in this synthetic splitting methodology and the fact that we can recover apparent fast orientations which are within a few degrees of the initial polarisation (as for path W1 for P100), it appears that adding a pre-existing amount of splitting to the initial wave would not change the results significantly.

One path did not yield acceptable recovered splitting parameters: path W2 for P001. Despite using a variety of different dominant frequencies of the starting wave, in each case the final waveforms were too complicated to give a well-linearised particle motion after correction. Figure 5.8 shows the result of the synthetic splitting and analysis with a wave of dominant frequency 0.1 Hz, but frequencies down to 0.01 Hz were also used. The reason for this is not clear: perhaps, as Fig. 5.10 shows, the presence of three partly distinct regions of different ϕ_i' and similar δt_i combine to produce particle motion which cannot adequately be linearised by a single splitting operator. If that were the case, however, this should be addressed by using a wave of longer period, but this does not seem to improve the results.

5.3.1 Circular Misfit

In order in some sense to quantitatively assess the goodness of fit of each of the plasticity models, I propose a 'circular misfit' in analogy to the reduced χ^2 misfit:

$$\chi_{c^2} = \frac{1}{\nu}\sum_{i}^{N}\frac{\sin^2(\phi_{i,\mathrm{obs}} - \phi_{i,\mathrm{syn}})}{\sin^2(\sigma_{i,\mathrm{obs}})}\,, \tag{5.1}$$

where N is the number of data, $\nu = N - 1$ is the number of degrees of freedom, ϕ is the observed or synthetic fast orientation, and σ is the uncertainty in the observed orientations. (The angular quantities ϕ and σ are in radians.) These are orientational rather than directional data, hence observed and synthetic angles of -90 and 90° respectively should give a misfit of 0, as inspection of the form of χ_c^2 shows, because of the squared sine term. Although the values of ϕ_{syn} are themselves somewhat uncertain, incorporating these into the measure is difficult as the range in σ_{syn} is very large (varying from 1.0 to 24.3°, with mean 7.3°). Figure 5.9 shows the value of χ_c^2 for a constant $\sigma_{\mathrm{obs}} = 5$ and 10°.

Using the measure χ_c^2, it is possible to compare model predictions with the observations for the fast orientations, but this does not take into account δt. As previ-

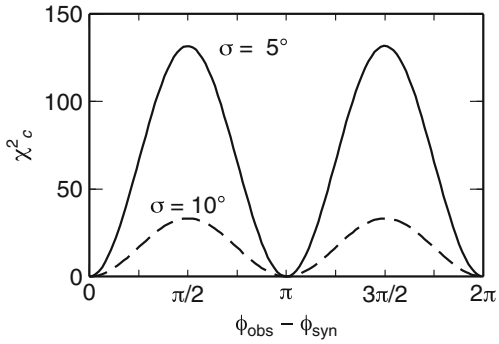

Fig. 5.9 Value of χ_c^2 for all values of $\phi_{obs} - \phi_{syn}$, where σ_{obs} is 5 and 10°. The misfit is 0 where the two angles are the same or 180° apart, which are equivalent for orientational data

ously mentioned, the texture of the elastic constants in the input models is usually unphysically strong, producing delay times far beyond any observations, so none of the models would fit the observed δt at all. Even with some method (inevitably arbitrary) of scaling the textures down to represent realistic anisotropy in D″, any comparisons would be entirely due to the scaling imposed. Hence, with the many assumptions in the texture calculations, it seems that the modelled ϕ values are alone the sensible measurements to compare. Another issue is how to deal with null values or ones discarded because the waveforms are too complicated (the W2 path for the P001 model). In this instance, there is only one value rejected.

Table 5.3 compares the χ_c^2 values for each texture model. It appears that the P010 model best matches the fast orientations overall, whilst the other two models give about the same misfit. It is possible that the exclusion of the W2 path from the P001 model has affected the χ_c^2 value, but given it is highest and the values are all similar, drawing any firm inferences from these values should be treated with caution. To give a sense of the measure for these data, for a model with predicted angles different to the observations by 45° in each case, $\chi_c^2 = 70$; for $\phi'_{i,obs} - \phi'_{i,syn} = 20°$ for all i, $\chi_c^2 = 16$. $\chi_c^2 \approx N$ when $\phi'_{i,obs} - \phi'_{i,syn} \approx 15°$ for all i, which should correspond to a case where the model provides a significantly good fit to the observations. The maximum value of χ_c^2 here is ~140, when all model values are different by 90°. That the value of χ_c^2 here is at least 46 suggests that none of the models predict splitting measurements that are adequately comparable to the observations, at least for this particular synthetic splitting methodology. However, the proviso that the particular forward modelling itself will influence how well the plasticity models predict shear wave splitting is something which much be addressed. I attempt to do so in the following section.

We may also consider if the models fit the data significantly better than would a random set of orientations. Using 500,000 random sets of orientations (all nine paths for models P100 and P010; only eight for P001), the means and standard deviations of the χ_c^2 values are given in Table 5.4. The values show that both the P100 and P001 models are actually worse than a random set of orientations at the 1σ level, marginally, whilst the P010 model is better than random. None of the synthetic χ_c^2

Table 5.3 Misfit of synthetic shear wave splitting fast orientations compared to previous observations for each plasticity model

Model	χ_c^2	χ_c^2 (selection)[a]
P100	104	119
P010	46	45
P001	109	84

[a] For a selection of paths where splitting parameters vary least for each model: see Sect. 5.3.2

Table 5.4 Mean and standard deviations of misfits to data of 500,000 random sets of fast orientations

Model	μ	σ
P100	69.6	21.6
P010	69.6	21.6
P001	77.2	24.7

Values are identical for P100 and P010 models as the distributions are only dependent on which paths are included

are significantly different to those from random orientations at the 2σ level—this requires a χ_c^2 of around 26.

5.3.2 Variation of Splitting Along Paths

As mentioned in Sect. 5.2.3, if the infinite-frequency (ray-theoretical) assumption is to yield results consistent with a finite-frequency approach (likely to better represent the full waveform effects of anisotropy and heterogeneity), then a requirement of this is that the variation of splitting along the path is fairly small, or at least smooth. Figure 5.10 shows how the calculated splitting parameters vary along each of the paths, for each of the plasticity cases.

As is evident, there is some variation between paths and plasticity models in how the local splitting parameters predicted by the models changes along the ray in the anisotropic region. Neglecting the scattering effects that would occur at strong velocity contrasts, strong variations in apparent anisotropy along a seismic wave's propagation would cause complicated waveform changes. Hence the results from the method of forward modelling the waveforms presented here are most likely to be consistent with finite-frequency calculations for paths such as Sib1 for P100. Note that ϕ' varies little, and does so quite smoothly. Other relatively constant paths, such as P for P100, would also likely produce similar results with other methods. By contrast, paths P for P010 or Sib2 for P001 show strong changes in ϕ' and δt along the ray, making the results of ray-theoretical and finite-frequency forward modelling techniques potentially different.

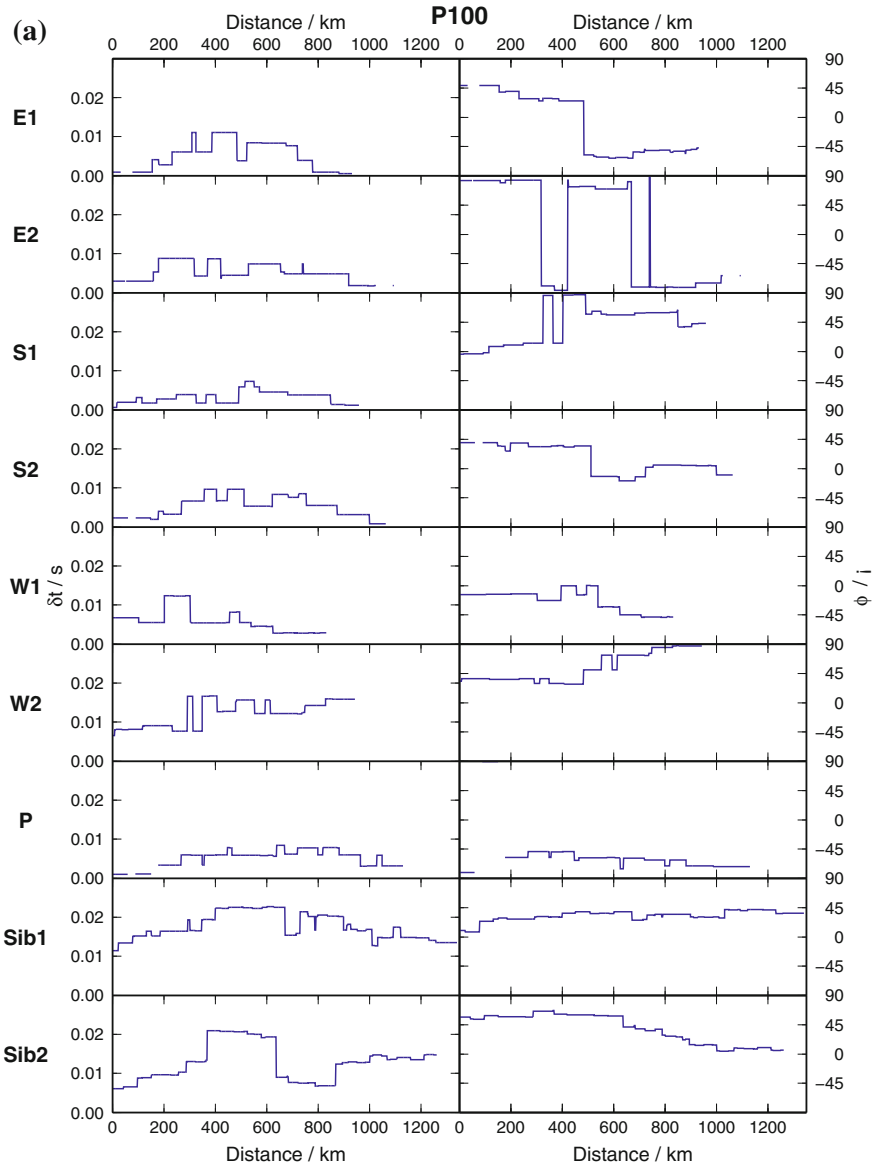

Fig. 5.10 **a** Variation of splitting parameters with distance along each path in the anisotropic region for the P100 plasticity model. Gaps show where ppv is locally unstable and where isotropy is assumed—no splitting occurs in these regions. Note that because of the 180° ambiguity in ϕ', where values change from >-90 to <90 (and vice versa) the change in ϕ' can seem more dramatic than is the case. **b** Variation of splitting parameters with distance along each path in the anisotropic region for the P010 plasticity model. **c** Variation of splitting parameters with distance along each path in the anisotropic region for the P001 plasticity model

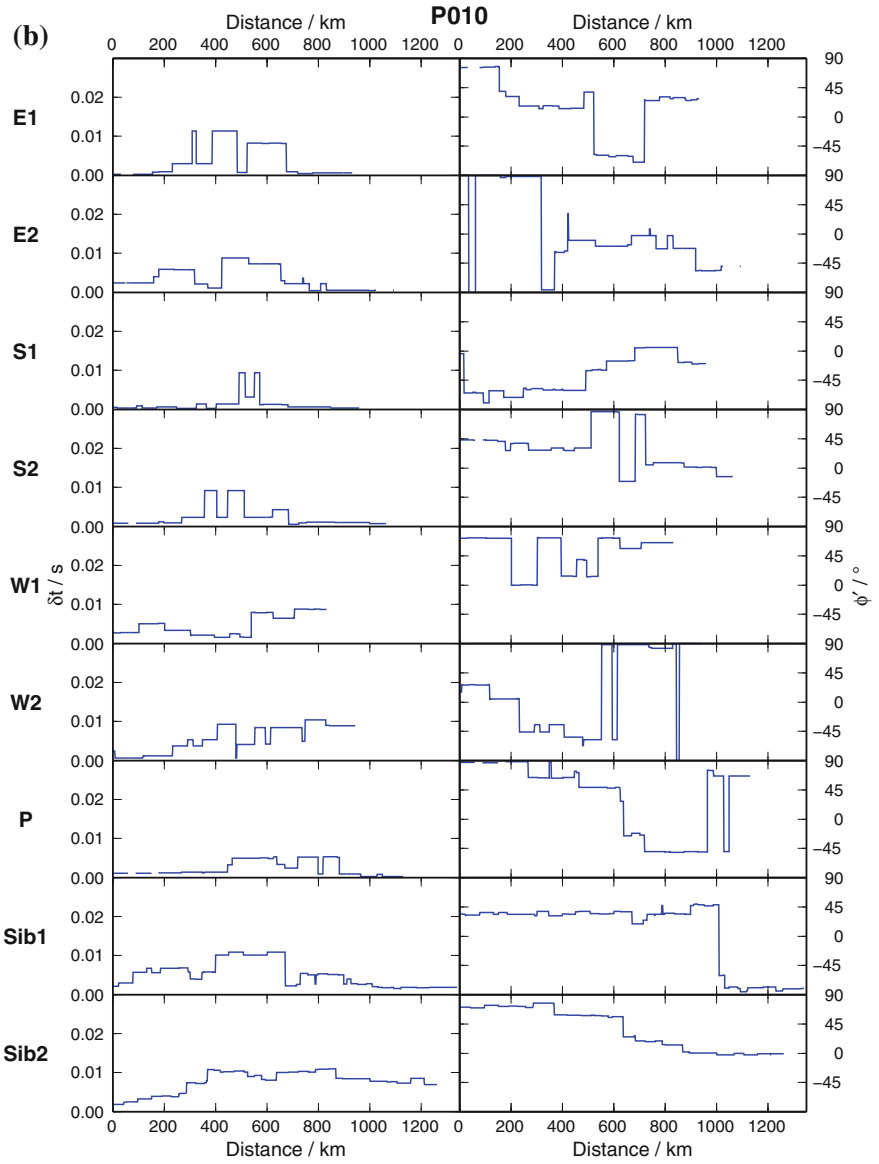

Fig. 5.10 (continued)

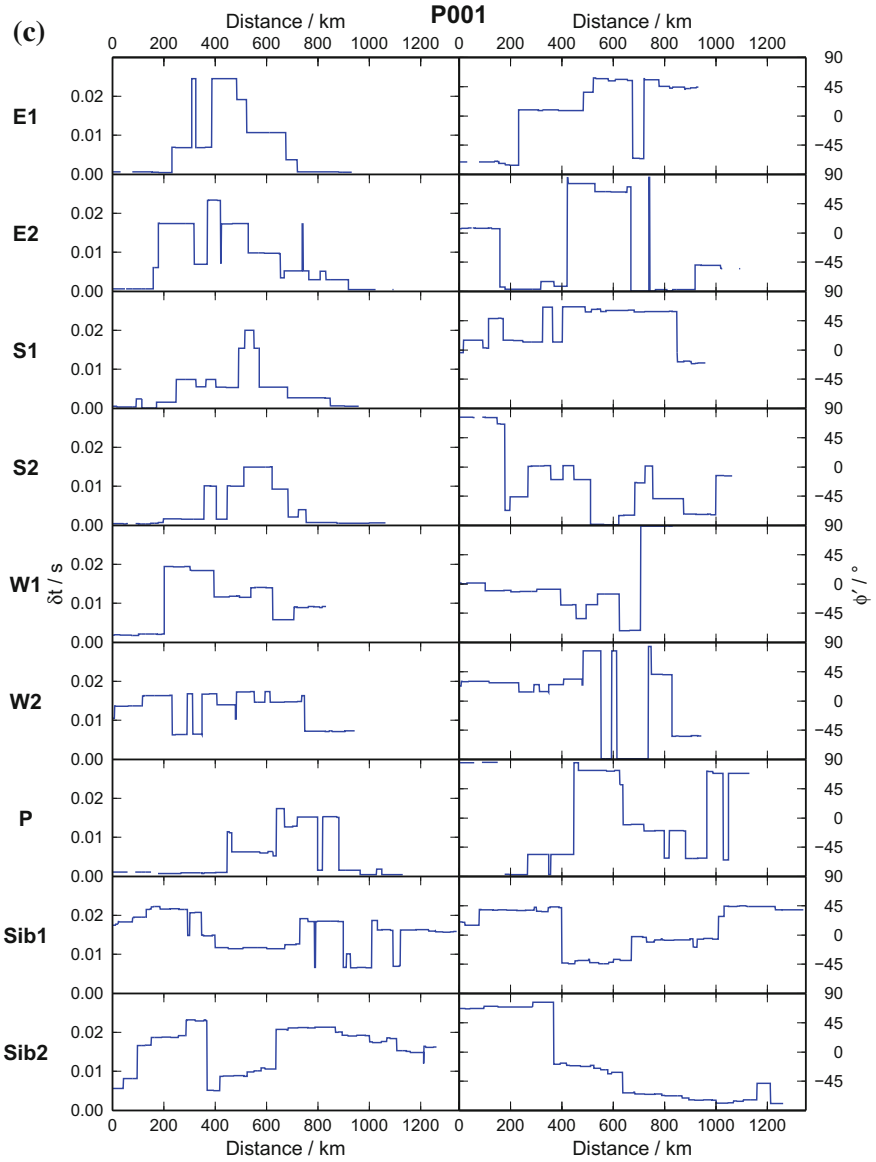

Fig. 5.10 (continued)

Hence some insight may be gained by considering the simplest paths only. A necessarily subjective selection of the paths that show least complex variation along the ray might pick the following: P100: S2, W1, W2 P, Sib1, Sib2; P010: S1, S2, W1, Sib2; P001: E2, W1, P, Sib1. Taking only these paths, a value of χ_c^2 can be calculated—these are also given in Table 5.3. The values are lowered somewhat for the P010 and P001 models, but increased slightly for P100, so that the P010 case seems best to fit the data. However the values are still large and suggest that none of the models are especially good fits. This indicates that, even for paths with the simplest effects of LPO-derived anisotropy, none of the plasticity models adequately predicts the observed splitting in all regions.

5.3.3 Comparison with VTI Patterns

The results presented here use very similar elastic constants to those studied by Walker et al. (2011). They considered only one layer of anisotropy in D″, rather than the several possible here, but in other respects the spatial variation in strength of anisotropy is very similar. The main difference between their work and this is that in order to compare the results with global tomographic inversions for radial anisotropy, they formed a VTI average from the elastic constants. Here we do not impose any symmetry.

Walker et al. (2011) suggest that, by comparison with the models of radial anisotropy (shown in Fig. 1.3), the P100 and P010 plasticity models reproduce observations best. This perhaps indicates that slip on (100) or (010) in ppv in deformation is the dominant cause of anisotropy in the lowermost mantle. This is assuming that the deformation comes from flow similar to that in the flow model we use here. Here, the P010 plasticity model is by far the most consistent with regional shear wave splitting observations, whilst P100 does a poor job. It may be, therefore, that the data tested here provide some extra constraint. This in fact is understandable by considering the ppv phase velocity surface. If slip is mainly vertical near the observations modelled here (as shown in Fig. 5.3), then slip on either (010) or (100) will produce a similar VTI pattern when averaged by rotation. Without this imposition, and with some horizontal component of flow defining a shear plane, the (010) planes, for instance, will align perpendicular to one another, leading to fast orientations which may be very different.

Both studies find a compatible mechanism for anisotropy whereby slip on (010) in ppv due to deformation. This produces, on average, VTI which is compatible with both global radial anisotropy tomography, and local shear wave splitting studies, hence is the strongest candidate to explain our observations.

5.3.4 Discussion

There may be several causes of the difference between the observed shear wave splitting and that predicted by our plasticity models. Perhaps most importantly, it may be that LPO of ppv caused by dislocation creep in response to mantle flow is not the cause of anisotropy everywhere in D″. Hence it may be that in some regions, our modelled splitting is close to the observed values because this is the causative mechanism in this region, whilst for the same plasticity model our predictions disagree with observations elsewhere because this mechanism is not responsible in that region. In this case, we might conclude that in at least some or all of D″, LPO in ppv is not the only cause of anisotropy (if one at all), and other mechanisms such as SPO are responsible.

Another cause of the discrepancy might be inaccuracies and limitations of the flow model. The model used to calculate the texture in ppv varies only slowly spacially, hence does not include any processes such as strain localisation from strain-weakening rheologies (e.g.,Yamazaki and Karato 2001) or strain weakening upon the pv–ppv phase transition itself (e.g., Hunt et al. 2009). These would develop strain and textures along narrow zones on scales much shorter than the resolution of the model, but are not included.

Our lack of knowledge of the deformation mechanism of ppv (or indeed other lowermost mantle phases) means that none of the three plasticity models might be adequate descriptions of ppv's behaviour, even for a completely ppv D″. For instance, point defect motion (Ammann et al. 2010), which would not generate an LPO, is a potential deformation mechanism and cannot at present be excluded from possibility.

A final possibility is also that the forward modelling methodology I employ is only adequate in some cases, and that ray-theoretical calculations are not sufficient to predict the shear wave splitting that would be observed in waves traversing the elastic constants we produce. Equally, the strong texture in the elastic constants might also preclude the forward modelling of waveforms that are similar to those observed—i.e., the lack of a limiting mechanism to the strength of anisotropy might itself prevent us being able to test whether any particular plasticity model and recreate the observations. Further, finite-frequency modelling might be able to address these issues, whilst at the same time, refinement of the texture modelling methods might yet yield different results. By far the largest uncertainty in the calculations is our ignorance of slip systems in ppv at D″ conditions, and indeed our ignorance of deformation mechanisms in the mantle above the CMB at all. Hence until significant progress is made in determining these unknowns, any similar studies to this will still have at least three, and potentially more, candidate deformation processes to test, introducing a large a priori uncertainty into the modelling.

5.4 Conclusions

In this chapter I present the results of forward modelling the shear wave splitting that would be produced by a suite of three models of lowermost mantle anisotropy. The models all assume that D″ is made up purely of ppv, which forms a texture in response to mantle flow by the movement of crystal dislocations on glide planes, but each assumes a different set of slip system activities in ppv. Using the approximation of infinite-frequency rays, I find that the modelled δt are generally much larger than the observations, and vast differences in the splitting parameters are found between plasticity models and ray paths. Whilst none of the models accurately model the data in all regions, the P010 plasticity model (favouring slip mainly on (010) planes) predicts fast orientations which best match the observations, and which do so better than random orientations. This might suggest that anisotropy in D″ is indeed caused mainly by deformation-induced LPO in ppv, where the dominant slip system involves dislocation glide on (010). However, the lack of correlation everywhere between the modelled splitting and observations may also suggest that this mechanism may not be at work everywhere, and other causes might be present in some or all areas. Another explanation might also be that if LPO in ppv is the cause of the observed anisotropy, it develops in a way we have not yet anticipated. Alternatively, there may be incorrect assumptions in the flow model, the texture modelling, or the forward modelling of the split waveforms, all of which can be addressed in future studies. This work shows that our understanding of D″ processes still leaves plenty of room for refinement in our knowledge and scope for new observations to place constraints on the range of possibilities we currently consider; it also shows that we have a powerful way to test hypotheses of formation of anisotropy in D″ and potentially a test of future models of mantle flow.

References

Abramson, E., Brown, J., Slutsky, L., & Zaug, J. (1997). The elastic constants of San Carlos olivine to 17 GPa. *Journal of Geophysical Research-Solid Earth*, *102*(B6), 12253–12263. doi:10.1029/97JB00682.

Ammann, M. W., Brodholt, J. P., Wookey, J., & Dobson, D. P. (2010). First-principles constraints on diffusion in lower-mantle minerals and a weak D″ layer. *Nature*, *465*(7297), 462–465. doi:10.1038/nature09052.

Carrez, P., Ferré, D., & Cordier, P. (2007a). Implications for plastic flow in the deep mantle from modelling dislocations in $MgSiO_3$ minerals. *Nature*, *446*(7131), 68–70. doi:10.1038/nature05593.

Carrez, P., Ferré, D., & Cordier, P. (2007b). Peierls-Nabarro model for dislocations in $MgSiO_3$ post-perovskite calculated at 120 GPa from first principles. *Philosophy Magazine*, *87*(22), 3229–3247. doi:10.1080/14786430701268914.

Crotwell, H., Owens, T., & Ritsema, J. (1999). The TauP Toolkit: Flexible seismic travel-time and ray-path utilities. *Seismological Research Letters*, *70*, 154–160. doi:10.1785/gssrl.70.2.154.

Forte, A. M. (2000). Seismic-geodynamic constraints on mantle flow: Implications for layered convection, mantle viscosity, and seismic anisotropy in the deep mantle. In S. Karato, A. M. Forte, R. C. Liebermann, G. Masters, & L. Stixrude (Eds.), *Earth's Deep Interior: Mineral*

Physics and Tomography from the Atomic to the Global Scale (Vol.117, pp. 3–36). Washington, D.C.: American Geophysical Union Geophysical Monograph.

Forte, A. M. & Peltier, W. (1991). Viscous-flow models of global geophysical observables: 1. Forward problems. *Journal of Geophysical Research-Solid Earth*, *96*(B12), 20131–20159. doi:10.1029/91JB01709.

Forte, A. M., & Peltier, W. (1994). The kinematics and dynamics of poloidal toroidal coupling in mantle flow: The importance of surface plates and lateral viscosity variations. *Advances in Geophysics*, *36*, 1–119. doi:10.1016/S0065-2687(08)60537-3.

Hunt, S. A., Weidner, D. J., Li, L., Wang, L., Walte, N. P., & Brodholt, J. P., et al. (2009). Weakening of calcium iridate during its transformation from perovskite to post-perovskite. *Nature Geoscience*, *2*(11), 794–797. doi:10.1038/NGEO663.

Iitaka, T., Hirose, K., Kawamura, K., & Murakami, M. (2004). The elasticity of the $MgSiO_3$ post-perovskite phase in the Earth's lowermost mantle. *Nature*, *430*(6998), 442–445. doi:10.1038/nature02702.

Kendall, J. M., & Silver, P. G. (1996). Constraints from seismic anisotropy on the nature of the lowermost mantle. *Nature*, *381*(6581), 409–412. doi:10.1038/381409a0.

Kennett, B., Engdahl, E., & Buland, R. (1995). Constraints on seismic velocities in the Earth from travel-times. *Geophysical Journal International*, *122*(1), 108–124. doi:10.1111/j.1365-246X.1995.tb03540.x.

Kustowski, B., Ekström, G., & Dziewoński, A. (2008). Anisotropic shear-wave velocity structure of the Earth's mantle: A global model. *Journal of Geophysical Research-Solid Earth*, *113*(B6), B06306. doi:10.1029/2007JB005169.

Lebensohn, R., & Tomé, C. (1993). A self-consistent anisotropic approach for the simulation of plastic-deformation and texture development of polycrystals–application to zirconium alloys. *Acta Metallurgica Et Materialia*, *41*, 2611–2624. doi:10.1016/0956-7151(93)90130-K.

Mao, W. L., Meng, Y., & Mao, H. (2010). Elastic anisotropy of ferromagnesian post-perovskite in Earth's D″ layer. *Physics of the Earth and Planetary Interiors*, *180*(3–4), 203–208. doi:10.1016/j.pepi.2009.10.013.

McNamara, A. K., van Keken, P., & Karato, S. (2002). Development of anisotropic structure in the Earth's lower mantle by solid-state convection. *Nature*, *416*(6878), 310–314. doi:10.1038/416310a.

McNamara, A.K., van Keken, P., & Karato, S. (2003). Development of finite strain in the convecting lower mantle and its implications for seismic anisotropy. *Journal of Geophysical Research-Solid Earth*, *108*(B5), 2230. doi:10.1029/2002JB001970.

Merkel, S., McNamara, A. K., Kubo, A., Speziale, S., Miyagi, L., & Meng, Y., et al. (2007). Deformation of (Mg, Fe)SiO_3 post-perovskite and D″ anisotropy. *Science*, *316*(5832), 1729–1732. doi:10.1126/science.1140609.

Metsue, A., Carrez, P., Mainprice, D., & Cordier, P. (2009). Numerical modelling of dislocations and deformation mechanisms in $CaIrO_3$ and $MgGeO_3$ post-perovskites–Comparison with $MgSiO_3$ post-perovskite. *Physics of the Earth and Planetary Interiors*, *174*(1–4), 165–173. doi:10.1016/j.pepi.2008.04.003.

Miyagi, L., Kanitpanyacharoen, W., Kaercher, P., Lee, K. K. M., & Wenk, H.-R. (2010). Slip systems in $MgSiO_3$ post-perovskite: Implications for D″ anisotropy. *Science*, *329*(5999), 1639–1641. doi:10.1126/science.1192465.

Mookherjee, M., & Capitani, G. C. (2011). Trench parallel anisotropy and large delay times: Elasticity and anisotropy of antigorite at high pressures. *Geophysical Research Letters*, *38*, L09315. doi:10.1029/2011GL047160.

Murakami, M., Hirose, K., Kawamura, K., Sata, N., & Ohishi, Y. (2004). Post-perovskite phase transition in $MgSiO_3$, *Science*, *304*(5672), 855–858. doi:10.1126/science.1095932.

Nowacki, A., Wookey, J., & Kendall, J. M. (2010). Deformation of the lowermost mantle from seismic anisotropy. *Nature*, *467*(7319), 1091–1095. doi:10.1038/nature09507.

Oganov, A., & Ono, S. (2004). Theoretical and experimental evidence for a post-perovskite phase of $MgSiO_3$ in Earth's D″ layer. *Nature*, *430*(6998), 445–448. doi:10.1038/nature02701.

Panning, M., & Romanowicz, B. (2006). A three-dimensional radially anisotropic model of shear velocity in the whole mantle. *Geophysical Journal International*, *167*(1), 361–379. doi:10.1111/j.1365-246X.2006.03100.x.

Panning, M., Lekić, V., & Romanowicz, B. (2010). Importance of crustal corrections in the development of a new global model of radial anisotropy. *Journal of Geophysical Research-Solid Earth*, *115*, B12325. doi:10.1029/2010JB007520.

Ranganathan, S. I., & Ostoja-Starzewski, M. (2008). Universal elastic anisotropy index. *Physical Review Letters*, *101*(5), 055504. doi:10.1103/PhysRevLett.101.055504.

Silver, P. G. & Chan, W. W. (1991). Shear-wave splitting and subcontinental mantle deformation. *Journal of Geophysical Research-Solid Earth*, *96*(B10), 16429–16454. doi:10.1029/91JB00899.

Simmons, N. A., Forte, A. M., & Grand, S. P. (2007). Thermochemical structure and dynamics of the African superplume. *Geophysical Research Letters*, *34*(2), L02301. doi:10.1029/2006GL028009.

Simmons, N. A., Forte, A. M., & Grand, S. P. (2009). Joint seismic, geodynamic and mineral physical constraints on three-dimensional mantle heterogeneity: Implications for the relative importance of thermal versus compositional heterogeneity. *Geophysical Journal International*, *177*(3), 1284–1304. doi:10.1111/j.1365-246X.2009.04133.x.

Simmons, N. A., Forte, A. M., Boschi, L., & Grand, S. P. (2010). GyPSuM: A joint tomographic model of mantle density and seismic wave speeds. *Journal of Geophysical Research-Solid Earth*, *115*, B12310. doi:10.1029/2010JB007631.

Stacey, F. D. & Davis, P. M. (2008). *Physics of the Earth* (4th edn). Cambridge, U.K.:Cambridge University Press.

Stackhouse, S., Brodholt, J. P., Wookey, J., Kendall, J. M., & Price, G. D. (2005). The effect of temperature on the seismic anisotropy of the perovskite and post-perovskite polymorphs of $MgSiO_3$. *Earth and Planetary Science Letters*, *230*(1–2), 1–10. doi:10.1016/j.epsl.2004.11.021.

Tsuchiya, T., Tsuchiya, J., Umemoto, K., & Wentzcovitch, R.M. (2004). Phase transition in $MgSiO_3$ perovskite in the earth's lower mantle. *Earth and Planetary Science Letters*, 224(3–4), 241–248. doi:10.1016/j.epsl.2004.05.017.

Walker, A. M., Forte, A. M., Wookey, J., Nowacki, A., & Kendall, J. M. (2011). Elastic anisotropy of D″ predicted from global models of mantle flow. *Geochemistry, Geophysics, Geosystems*, *12*(10), Q10006. doi:10.1029/2011GC003732.

Wenk, H.-R., Speziale, S., McNamara, A. K., & Garnero, E. J. (2006). Modeling lower mantle anisotropy development in a subducting slab. *Earth and Planetary Science Letters*, *245*(1–2), 302–314. doi:10.1016/j.epsl.2006.02.028.

Wenk, H.-R., Cottaar, S., Tomé, C. N., McNamara, A. K., & Romanowicz, B. (2011). Deformation in the lowermost mantle: From polycrystal plasticity to seismic anisotropy. *Earth and Planetary Science Letters*, *306*(1–2), 33–45. doi:10.1016/j.epsl.2011.03.021.

Wentzcovitch, R. M., Tsuchiya, T., & Tsuchiya, J. (2006). $MgSiO_3$ postperovskite at D″ conditions. *Proceedings of the National Academy of Sciences USA*, *103*(3), 543–546. doi:10.1073/pnas.0506879103.

Wookey, J., & Kendall, J. M. (2008). Constraints on lowermost mantle mineralogy and fabric beneath Siberia from seismic anisotropy. *Earth and Planetary Science Letters*, *275*(1–2), 32–42. doi:10.1016/j.epsl.2008.07.049.

Wookey, J., Kendall, J.M., & Rümpker, G. (2005a). Lowermost mantle anisotropy beneath the north Pacific from differential S-ScS splitting. *Geophysical Journal International*, *161*(3), 829–838. doi:10.1111/j.1365-246X.2005.02623.x.

Wookey, J., Stackhouse, S., Kendall, J. M., Brodholt, J. P., & Price, G. D. (2005b). Efficacy of the post-perovskite phase as an explanation for lowermost-mantle seismic properties. *Nature*, *438*(7070), 1004–1007. doi:10.1038/nature04345.

Wuestefeld, A., Al-Harrasi, O., Verdon, J. P., Wookey, J., & Kendall, J. M. (2010). A strategy for automated analysis of passive microseismic data to image seismic anisotropy and fracture characteristics. *Geophysical Prospecting*, *58*(5), 753–771. doi:10.1111/j.1365-2478.2010.00891.x.

Yamazaki, D., & Karato, S. (2001). Some mineral physics constraints on the rheology and geothermal structure of Earth's lower mantle. *American Mineralogist*, *86*(4), 385–391.

Chapter 6
Conclusions

The topmost and lowermost few hundred kilometres of the mantle are where the sharpest contrast in material properties occur in the Earth. For this reason, these are the sites of strongest gradients in temperature, forming boundary layers, and are where direct evidence for the movement of the mantle are to be found. Seismic anisotropy has proved to be invaluable in measuring flow in the uppermost mantle, and appears to be the key to understanding the same near the core-mantle boundary. In this thesis I have reviewed previous attempts to understand how and if we can infer flow from measurements of seismic anisotropy, finding that especially for the lowermost mantle, there are still several possibilities to be explored. I present new data which show that some previous assumptions about the style of anisotropy present in the deep Earth need to be revised, and develop models of D'' anisotropy which suggest that we are still some way from being able to confidently claim that the cause of seismic anisotropy there is always the alignment of mineral grains.

Here I present an overview of the main points addressed and answered in the preceding thesis, and briefly discuss some of the implications and future directions prompted by the chapters herein.

6.1 Flow in the Lowermost Mantle: The Cause of Anisotropy?

In Chaps. 4 and 5 I respectively measure and forward model the shear wave splitting in D''. In the former chapter, we show the orientations of shear for several models of mantle deformation which are compatible with our observations. We then go on to speculate that one particular slip system produces the expected shear orientations, by analogy with flow at mid-ocean ridges. However, as I explain in Chap. 2, this first attempt at constraining uncertainty in deformation styles and anisotropy generation is limited. I then go on to test much more 'realistic' models of deformation derived from a mantle flow model in Chap. 5. Here, I show that of the three models of

A. Nowacki, *Plate Deformation from Cradle to Grave*, Springer Theses,
DOI: 10.1007/978-3-642-34842-6_6, © Springer-Verlag Berlin Heidelberg 2013

anisotropy generation in D″ from deformation of post-perovskite by dislocation glide, one where slip is mainly on (010) matches observations better than random data. It is not surprising that the general inference of flow used in Chap. 4—which assumes instantaneous strain will correlate with fast shear wave orientation—suggests a slip system in post-perovskite different to that found later in this thesis.

The main conclusion of this work is that, whilst the best match of the cases we try is where all anisotropy in D″ is due to deformation-induced LPO in post-perovskite with slip on (010), none of the models we test can explain our observations everywhere. Additionally, none of the cases we examine are better than the random case at the 2σ level. This may lead us to reject the null hypothesis that flow, post-perovskite LPO and anisotropy are unrelated in D″. However, at the lower 1σ confidence level, the significantly good match of one model—P010—and the significantly bad match of the others, does suggest that flow-induced alignment of post-perovskite is a strong contributor. When one considers the single-crystal properties of post-perovskite (i.e., its orthorhombic symmetry), and the nature of the three plasticity models I examine (i.e., all accommodate slip mainly on the three principle, orthogonal planes of the crystal), it is perfectly understandable that this positive and dual-negative correlation should present itself. It may even be that this correlation is some evidence that the cause of anisotropy in D″ is post-perovskite LPO, or some other mechanism related to flow which produces an orthorhombic anisotropy. In order to support or refute this inference, future studies are needed in the fields of seismology, geodynamics, mineral physics and other areas, which I discuss shortly in these conclusions.

6.2 Summary of Main Conclusions and Original Contributions

6.2.1 Review of Observations and Explanations of Boundary Layer Anisotropy

I have reviewed the previous observations of seismic anisotropy in the upper and particularly the lowermost mantle, discussing primarily body-wave seismic methods, but also touching on surface wave (upper mantle) and normal-mode (D″) studies. Whilst in the upper mantle, flow-induced lattice-preferred orientation (LPO) of olivine is widely seen as the primary cause of seismic anisotropy—at least in regions away from subduction—there is still much uncertainty in the reason for the numerous observations of D″ anisotropy. I discuss potential methods of inferring the direction and strength of flow from the observed anisotropy, and this depends entirely on how we believe deformation occurs in this region. To that end, I also summarise the extensive mineral physical work which has gone into pinning down slip systems active in dislocation creep in $MgSiO_3$ post-perovskite. Global studies of the lowermost mantle necessarily impose certain approximations on the symmetry of the anisotropy, whilst recent advances can relax these assumptions. I show these methods, employed in this

thesis, have the potential to resolve whether we can indeed link mantle flow in D″ to anisotropy in the deep Earth.

6.2.2 Mantle Anisotropy Beneath Mid-Ocean Ridges and Oceanic Lithosphere

In studies of anisotropy in the deep Earth, one incredibly important and large source of seismic energy is usually overlooked: the mid-ocean ridges. In order to expand the area we can image seismically, it is necessary to make use of earthquakes on oceanic plate boundaries. Not only can they be used to image deeper, the seismic waves from earthquakes here also contain much information about the structure of mid-ocean ridges themselves. As the site of the creation of oceanic lithosphere, the dynamic processes at constructive margins are of great interest, and these can be revealed by the seismic anisotropy they produce. I have investigated the dynamics of ridges by making many shear wave splitting measurements in S waves beneath the source region, correcting for the upper mantle beneath the seismic station. These more than double the number of shear wave splitting measurements beneath ridges. I have shown that for most ridges, previous ideas hold true: it appears that flow-induced alignment of olivine explains the broad pattern of anisotropy, predicting spreading-direction-parallel fast orientations in vertical shear waves, and increasing delay times with distance from the ridge axis. However, ultraslow ridges such as the Gakkel Ridge are not well understood and do not produce the expected splitting from current models; instead they may deform so slowly as to not form the expected LPO which contributes to anisotropy elsewhere. Even beneath the East Pacific Rise, which is the only ridge to have previously been studied for teleseismic anisotropy, LPO of olivine alone is not sufficient to fully predict the new observations I have made. These show that the amount of splitting in S waves increases with distance from the ridge axis faster than for SKS waves, beyond that merely due to their differing incidence angles. I have suggested that a layer of radial anisotropy—such as that generated by a layer of horizontal melt pockets at the base of the lithosphere—is needed to reconcile models and observation, and that this is in agreement with recent studies of the ‘lithosphere–asthenosphere boundary’ discontinuity.

6.2.3 Multi-Azimuth Observations of D″ Anisotropy Beneath the Americas

Shear wave splitting provides perhaps the most unambiguous indicator of the presence of seismic anisotropy, and offers the advantage over other methods that it does not itself impose any particular symmetry on the anisotropy present. I have made several hundred observations of shear wave splitting in D″ beneath North and

Central America from ScS waves, correcting for the splitting in the upper mantle, and exploiting shallow earthquakes as well as deep. This provides ray paths which cross each other along different azimuths, letting me interpret the anisotropy in terms of the orientation of a range of candidate lowermost mantle mineral phases, or more generally as caused by transverse isotropy. In the latter case, the planes of isotropy must dip southwards beneath the Caribbean, and southwest beneath the western USA. If anisotropy is caused by aligned material such as melt pockets, this implies north–south flow directions. One particular style of anisotropy which is often assumed, radial anisotropy, cannot explain the observations and this shows that future studies must allow for more complicated types of anisotropy in the lowermost mantle. Making arguments about the dominant flow regime expected beneath a palaeo-subduction zone, I have suggested that one particular deformation mechanism in post-perovskite—slip on (001) planes—appears to be the most likely cause for anisotropy in D″.

6.2.4 Shear Wave Splitting Predicted by Models of Post-Perovskite Texture in D″

The most-commonly held explanation for anisotropy in D″—the alignment of ppv by dislocation glide in response to mantle flow—is merely one of many possibilities which cannot at present be ruled out. However, models of mantle flow have recently been made by inversion of geophysical and mineral physical data which can be used to test this hypothesis. Using one such model and a range of possible deformation mechanisms in ppv in D″, we have tracked the path taken by packets of mantle material globally in the lowermost mantle. These paths drive a viscoplastic-self-consistent (VPSC) description of deformation in a multigranular, monomineralic ppv sample, which develops LPO as it is tracked. At present, the active slip systems in ppv are poorly constrained, so I test three different plasticity models of ppv. Using the same ray paths as those observations I have made in this thesis, and others previously presented elsewhere, I model the shear wave splitting which such an LPO-controlled lowermost mantle would create. I have described a method of doing this by application of successive splitting operators to a synthetic waveform in the frequency domain, with the modelled splitting measurements made in a typical way for real data. These were then compared to the observations. I have shown that none of the models of D″ elasticity reproduce the observations well everywhere, although in some cases the infinite-frequency, ray approximation may not be appropriate and lead to results which would differ from a finite-frequency approach. Nonetheless, even for ‘simple’ paths, I have suggested that deformation-induced LPO in ppv (or at least that along slip systems we currently believe to be likely candidate ones) cannot be the cause everywhere of anisotropy in D″. It seems that some other cause in at least some regions must be investigated.

6.2.5 *Workflows, Codes and Algorithms*

During the course producing the work outlined above, I have developed several novel techniques and implemented them with my own code. I have also designed workflows for the processing of data and calculation of synthetics which are generalisable.

- I designed a novel method of measuring seismic anisotropy from shear wave splitting in the source region, rather than the receiver, improving on previous work. I used receiver stations with very well known sub-station shear wave splitting, which minimises the uncertainty in the source measurements (c.f. Russo et al. 2010), and report wherever possible stacked measurements whose uncertainty is least.
- To allow the use of shallow seismic sources (typically, tens of km deep) for source-side shear wave splitting measurements, I developed routines which used the event's source parameters (longitude, latitude, depth, time) and event-receiver parameters (azimuth, backazimuth, distance) to search the GlobalCMT database and retrieve the event's moment tensor. These routines then calculate the predicted polarisation at the receiver, and overlay the result on a standard shear wave splitting analysis diagnostic plot. The user can instantly see if the analysis window unintentionally incorporates surface-reflected phases, making the results invalid, as a deviation of the linearised particle motion from that predicted by the software. The code is a combination of Fortran and shell scripts, also containing scripts to automatically retrieve the CMT databse from the GlobalCMT's web server, called CMT2pol.
- For source-side measurements, in order to more accurately stack the output of shear wave splitting analysis, the λ_2 surfaces, I implemented a source-frame method of doing so, an adaptation of the SHEBA program (J. Wookey, pers. comm.).
- Several new scripts and compiled codes were developed to automatically request, retrieve and process data downloaded from IRIS and the CNDC. These are useful to anyone using the WEED or JWEED programs, or sending mailed requests to the CNDC.
- To interpret measurements of shear wave splitting made in several directions, I wrote fit_orientations, a shared-memory parallel Fortran code which tests an arbitrary number of splitting observations with all rotations of an arbitrary elasticity tensor, reporting which orientations can reproduce the observations. Inspired by the method of Wookey et al. (2005), it can be used for any input data and elastic constants, and can test all proportions of mixtures of the elastic constants with an isotropic average using Voigt–Reuss–Hill averaging.
- split_rays_cart and split_rays_global are Fortran codes which were used to perform the forward modelling in Chaps. 3 and 5. They respectively read local and spherical Cartesian grids of elastic constants and predict the splitting experienced by a ray traversing a given path through the model. This is done by splitting a waveform (chosen by the user in terms of parameters such as style—Ricker, Gaussian, and so on—, period and polarisation) progressively at each model grid-point in the frequency domain, compounding the splitting accrued to give a total

'effective splitting'. The waveforms are then analysed using a modularised version of the SHEBA routines from within the same program. A data format for the potentially large grid files, and plotting and gridding codes make up the package.
- The code used in Chap. 3 to invert for elliptical anisotropy parameters, EA_invert_3d, incorporates much of split_rays_cart, but with the addition of the calculation of elasticity tensors for various effective-medium models and descriptions of types of anisotropy. These are available in the Fortran module anisotropy_ajn.

The workflow which I designed for the processing of seismic data from both the IRIS and CNDC data centres, and from experiments run by Bristol around Hudson Bay and Ethiopia, are briefly described here.

1. For studies involving shallow earthquakes, use previous SKS splitting measurements to find stations with excellent and consistent SKS splitting beneath them. Use these in any case for waves from deep events to determine whether they also contain splitting.
2. Obtain processed data for the stations using custom scripts:
    a. Retrieve data automatically from IRIS or CNDC data centres using my tools JWEED_extract or CNDC_extract. (This step skipped for other data sources.)
    b. Add header information to SAC files.
    c. Remove seismograms with gaps where the gap would fall in the analysis windows.
    d. Detrend, taper and band-pass filter the traces.
    e. Trim components to be the same length.
    f. Sort into directories by event.
    g. Add header information for predicted phase arrivals of interest (e.g., S, ScS, SKS).
3. For each event-receiver pair:
    a. Correcting for the receiver, measure splitting in S. For source-side studies this is the output data for further analysis. Reject measurements where:
        - Signal-to-noise ratio is acceptable on both horizontal components;
        - CMT-predicted source polarisation and that retrieved by the analysis differ by more than 15°;
        - Particle motion is not clearly elliptical before and linear after analysis.
    b. Correcting for the source and receiver, analyse splitting in ScS. For D″ studies this is the output for further analysis. The same quality assessment criteria are applied.

6.3 Future Work and Avenues of Exploration

6.3.1 The Upper Mantle Beneath Mid-Ocean Ridges

The observations made of shear wave splitting beneath mid-ocean ridges are only the first step towards an improved understanding of the anisotropy, structure and dynamics in these regions. The seismic stations I use to investigate ridges are only on a tiny fraction of the Earth's surface (mainly North America and Ethiopia): the same source-side splitting techniques I demonstrate are equally applicable from any station with demonstrably simple sub-station anisotropy. I expect that future studies of SKS splitting beneath other stations globally—potentially using novel, automated methods (Teanby et al. 2004; Wuestefeld et al. 2010)—will allow more of the constructive plate boundaries to be studied in greater detail. Thus, more azimuths of data can be found, more tightly defining the style of anisotropy present, and hence its cause. There is much scope thereafter to incorporate these measurements into future mineral textural (e.g., Blackman 2007) and melt-porosity (e.g., Katz 2010) models, which should eventually allow for inversion of ridge structure by forward modelling of wave propagation through such models.

Another benefit of progress in this area is that future studies of anisotropy elsewhere in the Earth can be improved and uncertainty reduced with a fuller understanding of anisotropy beneath the oceanic upper mantle. The inversion technique I outline for estimating radial anisotropy parameters of the so-called 'LAB' region can easily be extended to include other observations of isotropic and anisotropic sublithospheric structure, such as surface waves (e.g., Gaherty 2001). Indeed, joint inversion of multi-azimuth shear wave splitting observations and surface waves is an ongoing topic of interest (e.g., Long et al. 2008), and perhaps relatively simple oceanic lithosphere will prove to be an effective 'test bed' of the method before more complex regions like subduction zones are fully characterised.

6.3.2 The Lowermost Mantle

A multitude of potential avenues of exploration present themselves as a result of the work done in this thesis. To begin with, further data analysis on a global basis of splitting in ScS—not just that beneath the Americas—would yield an invaluable database of observations with which to compare the current texture models of LPO in ppv in D″. Again, this perhaps may require automated methods, as the publicly-available dataset is huge and ever-growing, but would add significantly to current global datasets, which limit the type of anisotropy to TI.

Another obvious course to follow is to incorporate other fabric generation mechanisms into our models of mantle flow. For example, it would be possible to test in a similar way as for ppv LPO whether shear banding and SPO in a multiphase D″ is compatible with observations of splitting. Because this would also cause TI, not radial

anisotropy in general, a large database of shear wave splitting observations would again be invaluable. The method I describe for predicting shear wave splitting would be easily applicable to these situations, however there is still scope to more accurately model the anisotropy experienced in D″ by core-reflected waves. Finite-frequency modelling using techniques such as the finite-element, spectral-element and finite-difference methods can accurately model generally heterogeneous, anisotropic wave propagation, and though computationally expensive, should best afford the ability to compare our models of D″ anisotropy with observations. Adaptation of currently-available codes should yield synthetic waveforms similar to those modelled in this thesis, but with more realistic sensitivity to CMB structure: this will allow us to more rigorously test future hypotheses of deformation in the mantle and mechanisms of anisotropy generation.

These methods will also enable us to study more seismic phases which traverse D″, such as SK(K)S, S_{diff}, as at present interpretation of these waves is difficult without being able to predict their sensitivity to lowermost mantle and outer core structure, let alone anisotropy. This opens up the possibility of radically enlarging the datasets and regions of the Earth which will be visible to us, as S_{diff}, for instance, has a very broad sensitivity. We may also be able to use Earth's free oscillations to better probe structure in D″. Continuous, long-period records are becoming much easier to obtain, hence new normal mode studies looking at the lowermost mantle may be able to confirm or refute some of our current ideas. In particular, testing our models by forward modelling normal modes for a heterogeneously anisotropic D″ is a challenging prospect.

Current knowledge of the rheology and phase stability of the D″ region is still in its early days, but this thesis demonstrates that we are already in a position to in some senses test different hypothesis of deformation in the lowermost mantle. However, it is still true that we await the results of future experiments (perhaps distant) to determine the polymineralic behaviour of a mantle-like rock at the conditions present in D″. Without such experiments, or equally numerical simulations, we are left to make informed guesses as to how to interpret our seismic observations. This is evidenced in Chaps. 4 and 5, where the uncertainty in the slip system of post-perovskite is by far the largest unknown in our interpretations.

Whilst the upper mantle might appear well-characterised, new questions appear as soon as old ones are addressed. As the various fields of study converge on ever more accurate descriptions of how the mantle flows, our observations in turn will become more useful in describing the mantle's movement and the processes which shape the top and bottom of the Earth's rocky innards.

References

Blackman, D. (2007). Use of mineral physics, with geodynamic modelling and seismology, to investigate flow in the Earth's mantle. *Reports Progress Physics*, *70*(5), 659–689. doi:10.1088/0034-4885/70/5/R01.

Gaherty, J. B. (2001). Seismic evidence for hotspot-induced buoyant flow beneath the Reykjanes Ridge. *Science*, *293*(5535), 1645–1647. doi:10.1126/science.1061565.

Katz, R. F. (2010). Porosity-driven convection and asymmetry beneath mid-ocean ridges. *Geochem Geophy Geosystems*, *11*, Q0AC07. doi:10.1029/2010GC003282.

Long, M. D., de Hoop, M. V., & van der Hilst, R. D. (2008). Wave-equation shear wave splitting tomography. *Geophysical Journal International*, *172*(1), 311–330. doi:10.1111/j.1365-246X.2007.03632.x.

Russo, R., Gallego, A., Comte, D., Mocanu, V. I., Murdie, R. E., & VanDecar, J. (2010). Source-side shear wave splitting and upper mantle flow in the Chile Ridge subduction region. *Geology*, *38*(8), 707–710. doi:10.1130/G30920.1.

Teanby, N., Kendall, J. M., & der Baan, M. V. (2004). Automation of shear-wave splitting measurements using cluster analysis. *B Seismol Society American*, *94*(2), 453–463. doi:10.1785/0120030123.

Wookey, J., Kendall, J. M., & Rümpker, G. (2005). Lowermost mantle anisotropy beneath the north Pacific from differential S-ScS splitting. *Geophysical Journal International*, *161*(3), 829–838. doi:10.1111/j.1365-246X.2005.02623.x.

Wuestefeld, A., Al-Harrasi, O., Verdon, J. P., Wookey, J., & Kendall, J. M. (2010). A strategy for automated analysis of passive microseismic data to image seismic anisotropy and fracture characteristics. *Geophysical Prospecting*, *58*(5), 753–771. doi:10.1111/j.1365-2478.2010.00891.x.

Appendix A
The Universal Elastic Anisotropy Index

I use a general measure of the anisotropy of a single crystal of any crystal class, the universal elastic anisotropy index, A^U. For isotropic crystals, $A^U = 0$. Larger values of A^U indicate stronger anisotropy of a crystal, or indeed any elasticity tensor. It is defined by:

$$A^U = \mathbf{C}^V : \mathbf{S}^R - 6 = 5\frac{G^V}{G^R} + \frac{K^V}{K^R} - 6 \geq 0, \tag{A.1}$$

where $\mathbf{C}$ and $\mathbf{S}$ are the fourth-order stiffness and compliance tensors respectively, G is the shear modulus, K is the bulk modulus, the superscript V and R denote the Voigt and Reuss bounds for the ensemble averaged quantities over the crystal, and : denotes the tensorial inner product.

Note that isotropic crystals (where the Voigt and Reuss bounds give the same values for G and K) have A^U of zero, and this is the only case where $\mathbf{C}^V = \left(\mathbf{S}^R\right)^{-1}$.

A. Nowacki, *Plate Deformation from Cradle to Grave*, Springer Theses,
DOI: 10.1007/978-3-642-34842-6, © Springer-Verlag Berlin Heidelberg 2013

Appendix B
The Frequency-Domain Splitting Operator

Forward modelling of shear wave splitting may be done in the time-domain, but it is frequently practical to do so instead in the frequency domain. Here I note the method of applying shear wave splitting 'operators' to discrete time-series data.

A discrete time series, f, consists of N points. This can be expressed in the frequency domain using the discrete Fourier transform:

$$F_k = \sum_{i=0}^{N-1} f_i e^{-j2\pi\frac{k}{N}i} \,, \tag{B.1}$$

where $j = \sqrt{-1}$ and k is the wavenumber. The frequency-domain trace, F, can be represented in the time domain using the inverse discrete Fourier transform:

$$f_i = \frac{1}{N} \sum_{k=0}^{N-1} F_k e^{j2\pi\frac{k}{N}i} \,. \tag{B.2}$$

The splitting operator, $\Gamma(\phi, \delta t)$, acts on two traces, f^1 and f^2, which are assumed to be orthogonal to each other. In this work, it represents a delay of the slow component (oriented arbitrarily compared to the actual trace orientations) relative to the fast of δt. (This is in contrast to Silver and Chan (1991), who define a forward shift of the fast and backward of the slow components by $\delta t/2$ in each case). The fast orientation, measured clockwise from a reference orientation in the plane containing the two components, is termed ϕ'.

To apply the frequency-domain splitting operator to discrete time-series data, the following operations are needed:

- Fourier transform the time-domain traces.
- Rotate the frequency-domain traces, F^1 and F^2, by ϕ into the fast and slow orientations, F^{fast} and F^{slow}.
- Multiply the slow trace by a phase shift, Φ, corresponding to δt.
- Rotate the traces back into the original orientation.

A. Nowacki, *Plate Deformation from Cradle to Grave*, Springer Theses,
DOI: 10.1007/978-3-642-34842-6, © Springer-Verlag Berlin Heidelberg 2013

- Transform the frequency-domain traces back into the time domain.
  Rotation of the traces is achieved simply by application of a rotation matrix **R** to the real and imaginary parts separately:

$$\mathbf{R}_\phi = \begin{bmatrix} \cos\,\phi & \sin\,\phi \\ -\sin\,\phi & \cos\,\phi \end{bmatrix}, \tag{B.3}$$

$$\begin{pmatrix} \Re\{F^{\text{fast}}\} \\ \Re\{F^{\text{slow}}\} \end{pmatrix} = \mathbf{R}_\phi \begin{pmatrix} \Re\{F^1\} \\ \Re\{F^2\} \end{pmatrix}, \tag{B.4}$$

$$\begin{pmatrix} \Im\{F^{\text{fast}}\} \\ \Im\{F^{\text{slow}}\} \end{pmatrix} = \mathbf{R}_\phi \begin{pmatrix} \Im\{F^1\} \\ \Im\{F^2\} \end{pmatrix}. \tag{B.5}$$

The slow trace may then be shifted by Φ to give the delayed slow trace, $F^{slow,\,shifted}$:

$$\Phi_k = -2\pi \frac{\delta t}{\Delta} \frac{k}{2N}, \tag{B.6}$$

$$F_k^{\text{slow, shifted}} = F_k^{\text{slow}}\, e^{j\,\Phi_k}, \tag{B.7}$$

where Δ is the sampling rate of the trace. Rotation back by multiplication by the matrix $\mathbf{R}_{-\phi}$ returns the traces to their original orientation. The frequency-domain splitting operator therefore combines rotation, shifting and backrotation. Additional operators may then be applied before performing the inverse discrete Fourier transform.

Appendix C
Shear Wave Splitting Analysis with Source Correction

In this thesis, extensive use is made of shear wave splitting measurements where the source-side anisotropy is corrected for and removed from the analysis. This appendix explains in basic terms how this is done, given the non-commutativity of the operators, and the meaning of the source correction.

The time-domain discrete traces f^1 and f^2 are split by three distinct splitting operators, Γ_1, Γ_2 and Γ_3 (Fig. C.1), perhaps corresponding to anisotropy in the source region, D″ and the receiver region. This produces the split traces

$$\begin{pmatrix} f^{1,\,split} \\ f^{2,\,split} \end{pmatrix} = \Gamma_3 \Gamma_2 \Gamma_1 \begin{pmatrix} f^1 \\ f^2 \end{pmatrix} . \tag{C.1}$$

Hereafter, we drop the explicit writing of the traces f.

If we wish to recover the second splitting operator, Γ_2 (that is, it is unknown), given knowledge of what the first and third are, Γ_1 and Γ_3, then we must correct for the latter operators in the splitting analysis. However, because the operator is in general not commutative, matters are complicated.

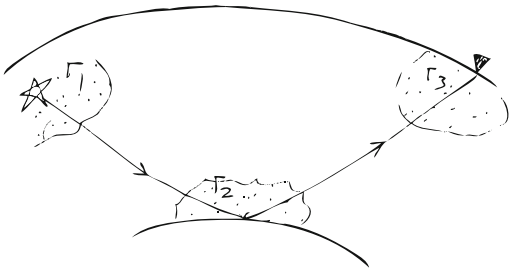

Fig. C.1 Schematic of a shear wave split by three splitting operators. The *star* represents the source and the inverted triangle the surface receiver. The solid line with arrows is the ray path of the shear wave. Stippled regions show the regions where splitting operators Γ_1 to Γ_3 affect the wave

A. Nowacki, *Plate Deformation from Cradle to Grave*, Springer Theses,
DOI: 10.1007/978-3-642-34842-6, © Springer-Verlag Berlin Heidelberg 2013

Correcting for Γ_3 is straightforward: apply the inverse operator before any splitting analysis, leaving only the source (Γ_1) and D″ (Γ_2) splitting:

$$\Gamma_3^{-1}\,\Gamma_3\,\Gamma_2\,\Gamma_1 = \Gamma_2\,\Gamma_1\ . \tag{C.2}$$

This step may be done before any splitting analysis and requires only one operation.

The method of shear wave splitting analysis employed by Silver and Chan (1991) and used in this thesis performs a grid search over a set of trial splitting operators to find that which best linearises the particle motion on the two traces. N trial operators Γ_i', $i = 1\ldots N$, are preapplied in turn. In order to recover an estimate of the unknown Γ_2, therefore, correction for the source (Γ_1^{-1}) must be applied after each trial operator:

$$\Gamma_1^{-1}\,\Gamma_i'\,\Gamma_2\,\Gamma_1\ .$$

When Γ_i' is equal to Γ_2, the forward and inverse Γ_1 and Γ_1^{-1} cancel leaving linear, unsplit particle motion. This means, however, that plotting 'pre-corrected' waveforms when applying a source correction is not meaningful, as $\Gamma_1^{-1}\,\Gamma_2\,\Gamma_1$ does not represent the splitting only present because of Γ_2, again on account of the operators' non-commutativity.

Bibliography

Silver, P.G., & Chan, W.W. (1991). Shear-wave splitting and subcontinental mantle deformation. *Journal of Geophysical Research-Solid Earth, 96*(B10), 16429–16454. doi: 10.1029/91JB00899.